Synthesis and Properties of Low Band Gap Organic Semiconductors for Solar Cell Applications

İlke Yücekan

Submitted to the

Institute of Graduate Studies amd Research
in partial fulfillment of the requirements for the Degree of

Doctor of Philosophy
in
Chemistry

Eastern Mediterranean University
June 2013
Gazimağusa, North Cyprus

Approval of the Institute of Graduate Studies and Research

_____
Prof. Dr. Elvan Yılmaz
Director

I certify that this thesis satisfies the requirements as a thesis for the degree of Doctor of Philosophy in Chemistry.

_____
Prof. Dr. Mustafa Halilsoy
Chair, Department of Chemistry

We certify that we have read this thesis and that in our opinion it is fully adequate in scope and quality as a thesis for the degree of Doctor of Philosophy in Chemistry.

_____
Prof. Dr. Huriye İcil
Supervisor

Examining Committee
_____

1. Prof. Dr. Metin Balcı   _____

2. Prof. Dr. Huriye İcil   _____

3. Prof. Dr. Turan Öztürk   _____

4. Assoc. Prof. Dr. Hamit Caner   _____

5. Asst. Prof. Dr. Nur P. Aydınlık _____

ABSTRACT

The development of new PV technology is essential with increasing consumption of fossil fuels and seems to be the only way to cover energy demand. The primary objective should be accomplished efficiency between cost and power conversion efficiency. Moreover, the applicability of new materials is primarily determined by their balanced electrical, thermal, physical and chemical properties.

In this thesis, a new series of low band gap aromatic polyimides were successfully synthesized to be used in photovoltaic applications as next generation organic semiconductor material. To this purpose, chitosan biopolymer based two aromatic polyimide functionalized with commercially available perylene and naphthalene organic semiconductors and previously synthesized high molecular weight naphthalene based polyimide have been characterized in detail by studying their , photophysical, thermal and electrochemical properties through the data obtained from NMR, FTIR, GPC, UV-vis, Fluorescence, DSC, TGA and CV and SQWV.

Incorporation of the hydrophobic chromophore units within the hydrophilic polymeric backbones yielded a network-like structure and maintained good solubility. The compounds showed extraordinary thermal stabilities and high molar absorption coefficients. They possessed excimer type emission and aggregation formation which confirmed the electroactive species both in ground and excited state. The products showed outstanding electrochemical stability and also undergoes only one reversible reduction and oxidation in solid state which make them candidate as Donor/Acceptor polymer for PV technology.

Keywords: Perylene, Naphthalene, Donor/Acceptor Polymer, High Molar Absorptivity

ÖZ

Fosil yakıtlarının artan tüketimi karşısında, yeni PV teknolojilerinin geliştirilmesi zaruridir ve enerji talebinin karşılanması için tek kurtuluş yolu olarak gözükmektedir. Birincil amaç, maliyet ve güç dönüşüm verimliliği arasındaki tutarlılığın gerçekleştirilmesidir. Ayrıca, elektriksel, ısı, fiziksel ve kimyasal özellikleri bakımından dengeli yeni materyallerin uygulanabirliği belirlenmelidir.

Bu tezde, fotovoltaik uygulamalarda yeni nesil organik yarı-iletken malzeme olarak kullanılmak üzere düşük bant aralığına sahip aromatik poliimidlerin sentezi gerçekleştirilmiştir. Bu amaçla, ticari olarak temin edilebilen naftalin ve perilen organik yarı iletkenler ile fonksiyonlandırılmış kitozan tabanlı iki aromatik poliimid ile daha önce sentezlenmiş olan naftalin esaslı yüksek molekül ağırlıklı poliimidin fotofiziksel, termal ve elektrokimyasal özellikleri NMR, FTIR, GPC, UV-vis, Fluoresans, DSC, TGA ve voltametri ölçümleri ile karakterize edilmiştir.

Sentezlenen maddeler, hidrofobik kromofor birimlerinin hidrofilik yapıdaki polimerlere dahil edilmesiyle ağ-benzeri bir yapı oluşturmuş olup iyi bir çözünürlüğe sahiptirler. Her bir polimer, yüksek molar soğurma katsayısına ve olağanüstü termal kararlılıpa sahiptir. Poliimidler eksimer tipi emisyon ve aggregasyon oluşumuna sahip olduklarından hem temelde hem de uyarılmış halde elektroaktif türlere sahiptirler. Sentezlenen ürünler, elektrokimyasal kararlılığa sahip olup, katı halde geri dönüşümlü oksidasyon ve redüksiyon potansiyeline sahiptir. Bu özellikleri sayesinde, PV teknolojisi için elektron donör/akseptör polimer olarak potansiyel birer adaydırlar.

Anahtar Kelimeler: Perilen, Naftalin, Donör/Akseptör Polimer, Yüksek Molar Soğurum

To my wife and my family!!!

ACKNOWLEDGMENTS

TABLE OF CONTENTS

LIST OF TABLES

LIST OF FIGURES

LIST OF SCHEMES

LIST OF ABBREVIATIONS

A   : Absorption

Anal.   : Analytical

AU   : Arbitrary unit

Avg.   : Average

c   : Concentration

calcd.   :Calculated

^{13}C NMR   :Carbon- 13 nuclear magnetic resonance spectroscopy

CB   : Conduction band

CH   : Chitosan

CHL   : Chloroform

CIGS   : Copper indium gallium diselenide

CV   : Cyclic voltammetry

δ : Chemical shift

Da   : Dalton

DCM   : Dichloromethane

DMF   : N,N'-Dimethylformamide

DMAc   : Dimethylacetamide

DMSO   : Dimethylsulfoxide

DSC   : Differential scanning calorimetry

DSSC   : Dye sensitized solar cell

ε : Extinction coefficient

ε_{max} : Molar asbsortivity / Maximumextinction coefficient

eV   : Electron volt

$E_{1/2}$:Half-wave potential

E_g : Band gap energy

E_{ox}	: Oxidation potential
ΔE_p	: Separation of peak potentials
E_{pa}	: Anodic peak potential
E_{pc}	: Cathodic peak potential
Equn.	: Equation
EM	: Emission spectrum
E_{red}	: Reduction potential
E_s	: Singlet energy
ES	:Excitation spectrum
f	: Oscillator strength
Fc	: Ferrocene
FET	: Field-effect transistors
Fig.	Figure
FT-IR	: Fourier transform infrared spectroscopy
GPC	: Gel permeation chromatography
h	: Hour
$h\nu$	: Irradiation
^{1}H NMR	: Proton nuclear magnetic resonance spectroscopy
HOMO	: Highest occupied molecular orbital
i_p	: Peak current
i_{pa}	: Anodic peak current
i_{pc}	: Cathodic peak current
IPC	: Inorganic photovoltaic cell
IR	: Infrared spectrum/spectroscop
ITO	: Indium tin oxide
kDa	: kilo Daltons
k_f	: Fluorescence rate constant

l	: Path length
LED	: Light emitting diodes
LUMO	: Lowest unoccupied molecular orbital
M	: Molar concentration
M_n	: Number average molecular weight
M_w	: Weight average molecular weight
max	: Maximum
MHz	: Megahertz
min	: Minute
mmol	: Millimole
mp	: Melting point
mV	: Millivolt
$[\eta]$	: Intrinsic viscosity
η_{sp}	: Specific viscosity
η_{red}	: Reduced viscosity
$NaBF_4$	: Sodium tetrafluoroborate
NDA	: 1,4,5,8-naphthalenetetracarboxylic dianhydride
NDI	: Naphthalene diimide
NMP	: *N*-methylpyrrolidinone
NMR	: Nuclear magnetic resonance spectroscopy
OPC	: Organic photovoltaic cell
Φ_f	: Fluorescence quantum yield
PC	: Photovoltaic cell
PCE	: Power conversion efficiency
PDA	: Perlylene 3,4,9,10- tetracarboxylic dianhydride
PDI	: Perlylene diimide
PDI	: Polydispersity index

PNI	: Poly naphthalene imide
PPI	: Poly perylene imide
PV	: Photovoltaic
TBAPF$_6$	: Tetrabutylammoniumehexafluorophosphate
TGA	: Thermogravimetric analysis
THF	: Tetrahydrofuran
SQWV	:Square wave voltammetry
τ_0	: Theoretical radiative lifetime
τ_f	: Fluorescence lifetime
t	: Time
TCE	: 1,1,2,2-Tetrachloroethane
TFAc	: Trifluoroacetic acid
TGA	: Thermogravimetric analysis
u	: Unknown
μ	: Micro
UV-vis	: Ultraviolet visible light absorption
VB	: Valance band
vs.	Versus
λ	: Wavelength
λ_{exc}	: Excitation wavelength
λ_{em}	: Emission wavelength
λ_{max}	: Maximum wavelength

Chapter 1

INTRODUCTION

The development of new solar cell technology is fundamental with rapidly increasing consumption of fossil fuels and seems to be the only way to cover future energy demand. The primary objective is accomplished efficiency between cost and power conversion efficiency. The important part of the cost of solar panels are coming from their materials and manufacturing procedure. Currently, commercial inorganic solar cells, mostly based on silicon, require a thick layer of silicon to capture light effectively. The fabrication is complicated and production of silicon crystal is laborious and long-lasting process. Organic photovoltaic cells (OPCs) are good candidates for the next generation of solar cell. Compare to the silicon based inorganic photovoltaic cells (IPCs), OPCs have the advantages of lightweight, flexible, easily fabricated at low temperatures and they have a less negative impact to the environment [1]. The development of organic based semiconductors for optoelectronic devices e.g. photovoltaic cells (PCs), emitting diodes (LEDs), or field-effect transistors (FETs) is a challenging task of current research [2] and their main advantages are tunability of their optical and electron transport properties by chemical synthesis [3]. Well established balance between the device performance, ease of fabrication and operational stability allows us to get electro active, low band gap semiconductors for the desired applications [4].

1.1 Photovoltaic Cell

Photovoltaic (PV) cell, also called solar cell, is a device that converts solar energy into electric current. In general, PV cell is defined as a system where light falling on a solid or liquid system and produce electrical current between two electrodes. All of the photovoltaic material practically consist of a semiconductor material and a p-n junction that photocurrent generated along the surface. PV cells are located inside a panel where electrically connected with each other, so-called photovoltaic panel. Photovoltaic panels have a sheet of translucent glass surface and this surface protects semi-conductive material against impact and abrasion. In order to capture a reasonable amount of sunlight, currently available photovoltaic cells should have a thick layer between 180-240 μm and made up of bulk materials such as silicon derivatives (amorphous silicon, mono or poly crystalline silicon), the III-V compounds and alloys (cadmium telluride, CdTe) and the chalcopyrite compound (copper indium gallium diselenide, CIGS) [5]. The last group consists of the nanocrystals and used as quantum-dots. Other materials are organic dyes and organic polymers that forming thin-film layers.

1.2 Configuration of Photovoltaic Cell

To make an efficient solar device, photon absorption and electron mobility should be effective also. Because of different physical properties of inorganic and organic molecules, the configuration of photovoltaic cell based on each technology is significantly different also.

Commercial silicon based photovoltaic panel consist of many photovoltaic cells and each cell made up of positive layer (n-type), which has free electrons, and negative layer (p-type), which is lacking free electrons, to create electric field. When the

surface of the cell is exposed to electromagnetic radiation, the photons of the sun-light are absorbed by the n-type semiconductor. This energy causes the electrons of n-type semiconductor to become free and excite from valance band to the conduction band. The electrons starts to flow from through n-type part to p-type part of the cell through a metal wire, transfer energy while moving around the electrical field, and then back into its initial position. This movement of electrons in photovoltaic cell generates electricity.
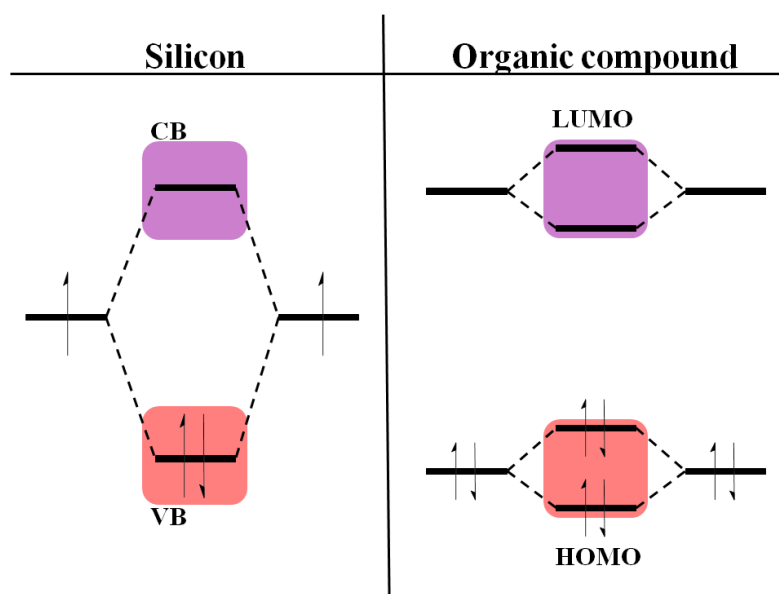
Figure 1.1: Schematic Band Structure and Molecular Orbital Diagram for Silicon and Organic Compound as Examples of Inorganic and Organic Semiconductors, respectively.

Working principle of OPCs is quite different on a light absorption. OPCs do not directly create free charge carriers in contrast to IPCs; instead, bound electron–hole pairs called excitons are generated by photoexcitation in the organic material. As a result of OPCs are excitonic, when sun-light is absorbed, an electron is excited form HOMO energy level to the LUMO energy level forming an exciton. In order to generate an electric current, these photogenerated excitons must be diffused to

3

donor-acceptor interface, where dissociate into free electrons and holes. Electrons are collected at the aluminium electrode and holes are introduced at the ITO electrode. Excitons have only few order of 10nm diffusion lengths, therefore absorption layer should be very thin for all excitons to reach the interface. However, for most OPCs, the film thickness is in the range of 100 nm. Different approaches have been studied to overcome this problem. Nowadays, the most popular strategy, donor and acceptor material blended into each other to provide proper movement [6].

The importance of the use of solar energy is growing a little more with each passing year with the depletion of hydrocarbon based fuels and global warming. Today, scientific studies about photovoltaic cells were mainly divided into two groups including inorganic and organic base; the inorganic photovoltaic cells (IPCs) and organic based organic photovoltaic cells (OPCs).

1.3 Inorganic Photovoltaic Cells (IPCs)

The first generation photovoltaic technology was started by discovering of photovoltaic effect (light induce voltage) by E. Becquerel in 1839. C. Fritts showed first solid-state photovoltaic cell in 1883 by depositing a thin gold layer on selenium semiconductor. The semiconductor was used for light absorption and charge separation was occurred at the internal electric field. These two fundamental processes are the basis of today's silicon-based photovoltaic cells. The first modern photovoltaic cell was patented in 1946 by Ohl and demonstrated in 1954 at Bell Laboratories. This cell constructed with mono crystalline silicon for light absorption and a p-n junction for charge separation, with a power conversion of ~5% [7]. With that innovation, remarkable attention has been directed towards to develop the silicon technology up to date.

The IPCs use inorganic semiconductors include amorphous silicone, mono or poly crystalline silicone, microcrystalline silicone, and cadmium telluride, and copper indium gallium diselenide. Other cell types (thin film photovoltaic cells) have been developed to compete with silicon based cells either in terms of low cost of production or in terms of advanced efficiencies. All of these materials have energy band gaps varying from 1.1 eV to about 1.7 eV, which it is quite close to the optimum energy band gap (1.5 eV).

Although improving efficiency in last fifty years (up to ~25% for crystalline silicon and ~40% for tandem cells) and 90% of the solar cell industry dominated by IPCs, developments in silicon technology can not reach to an adequate level. In the case of silicon based photovoltaic cells, the biggest problem is manufacturing cost; Solar

cells require a relatively thick layer of well-processed silicon for a consistent amount of photon capture and silicon purification is very expensive process. There is also other limitations exist about silicon technology such as, material inconsistencies, toxicity, poor solubility in solvents, and inability to directly melt process. Because of these problems, improvements in silicone technology were not impressive in last decades. Despite there have been many studies done to find the solution, notably thin-film fabrication technologies and multi-junction approach, there are several practical problems about application [8].

Thin-film based IPCs describes a solar cell technology that is based on use compounds made of III-V elements in the periodic table, for instance; GaAs, GaSb, and InP, as a single or multiple junctions (sometimes refer to as tandem junctions) semiconductor layer to absorb sunlight nearly all off the spectrum, thus convert into electricity as much as possible. These materials have strong absorption, have near optimum band gap energies around 1.4 eV, and also have excellent charge carrier properties. This makes them attractive materials for second generation semiconductors.

Single-junction photovoltaic cells generally composed of GaAs and InP that have conversion efficiencies 25.8% and 21.9%, respectively. In a single-junction IPCs, a very high percentage of the usable energy is lost, because photons which have lower energy than band gap are not absorbed and photons which have higher energy than band gap is lost as heat energy. A series of studies have demonstrated that using tandem photovoltaic cells, such loses may be minimized causing much higher efficiency solar cells. IPCs based on multiple-junction thin films contain more than one junction ($Ga_xIn_{1-x}As$ or $Ga_yIn_{1-y}P$ with different ratio) and each junction has

different energies of band gap which is responsible for light absorption in a particular region of the solar spectrum. Under one-sun illumination, the performance of this tandem cells is around 34%. Beside other silicon based IPCs, some tandem technologies have been commercialized including silicon in either amorphous or crystalline form with about 12-20% efficiency.

A well-proven approach to improve photovoltaic cell technology is the using of tandem cell structure. By far the main drawback with using III-IV compounds in solar cell devices is the astronomical cost of manufacturing process and expensive materials. This is because these metals rarely occur in the nature; consequently large amount of metal required by solar industry also creates shortage of raw materials. Deformations in crystal structure and unwanted impurities gravely reduce cell performances and alternative low-cost deposition methods can not be utilized, because of electrical properties of each layer has to be well matched. These cells are also not mechanically strong as silicon-based solar cells and are easily cleaved. Another issue is the use and recycling of highly toxic metals (such as cadmium), thus this technology is not environmentally friendly. These disadvantages have led to tandem solar cells not being considered as a promising candidate for terrestrial photovoltaic cells. Multiple junction IPCs generally find applications in producing energy for aerospace applications and concentrator systems [9].

1.4 Organic Photovoltaic Cells (OPCs)

An Organic Photovoltaic Cell (OPC) is a group of solar cell that based on organic electronics for light absorption and charge transport. PCs are actually composed of many components, which includes metal cathode and ITO anode, but essentially organic semiconductors. This is because organic semiconductor is an active element. Small organic chromophores or large organic polymers forming the electron donor and acceptor materials of OPCs which optical absorption and charge transfer depend on a partially delocalized π–π conjugated systems. A π–π conjugated system is a system of covalently bonded carbon atoms with ranging from single and double bonds sequentially. These systems possessing delocalized π electrons that result from hybridization of carbon π orbitals and forming the delocalized bonding π orbital with a π^* antibonding orbital. The band gap energy between HOMO and LUMO determines which wavelength of sunlight can be absorbed by OPC.
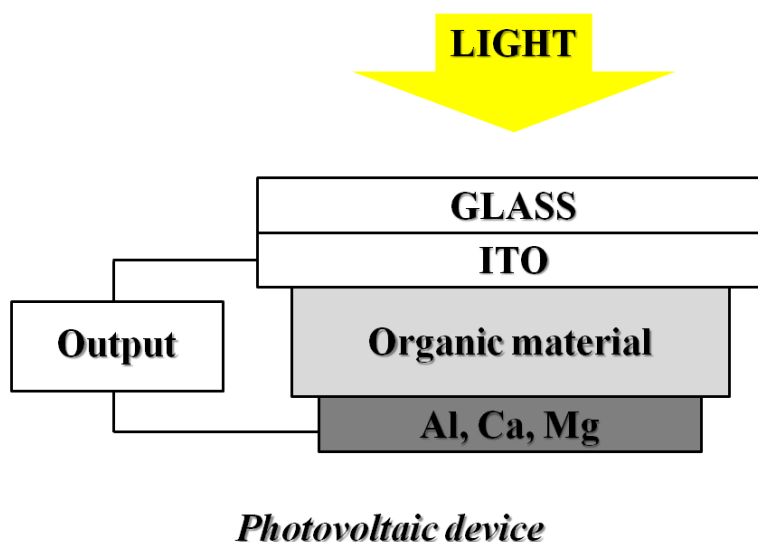
Figure 1.2: Typical Organic Photovoltaic Device

The worldwide application of photovoltaic cells demands competitive efficiency, cost and stability. OPCs systems are promising candidates over IPCs in a cost-effective way with state of art PCE (power conversion efficiencies) approaching 8%. The aim for the OPCs so called third generation photovoltaic cells is to produce electricity at a large scale with competitive price [10-11]. Extensive research in this field has been carried out by the intrinsic advantages of organic materials; high light absorption, tunability by chemical tailoring to incorporate suitable electronic features, ease of processing in large area as well as low manufacturing cost and they are replacing ISCs in most cases [12-15].

To obtain effective photo-electric conversion in OPCs, various types of organic materials have been used for the manufacture of organic solar cell active layers either small molecule [16], combination of small molecule / conjugated polymer [17], conjugated polymers [18-19], non conjugated polymers [1], or combination of inorganic / organic hybrid materials [20]. Although small molecules have certain advantages over polymer counterparts regarding well defined molecular structure and weight, and high purity [21], they show restricted solubility in common solvents and are usually deposited by vacuum deposition techniques where polymeric materials can be deposited in thin films by many cheap techniques such as spray coating, screen printing, spin-coating [22.]. In contrast to small molecules, organic polymers have attracted more and more consideration for solar cell applications due to their strong absorption ability, good film forming ability, easy processability, etc. [23].

The performance of charge generation in OPCs has been reported to be due to several factors, including cell morphology, the existence of electric field, the dielectric constant of the donor/acceptor blend film, the mobility of charge carrying

species, the free-energy difference forcing charge separation, the strength (durability) of electronic interactions at junction interface [24]. It is an extremely crucial task to increase the charge-generation efficiency that based on the presence of Coulombically bound charge transfer species at junction points. The dissociation of exciton particles into free charge carriers, shown in Figure 1.3, is an essential parameter for determine the PCE. Some small molecules and polymers with flat structures such as anthracene [25], pyrene [26], naphthalene [27], and perylene [28] have been reported to form excimers or aggregates by π–π interactions. In OPCs, excimer formation could altered the fluorescence emission properties of molecules and polymers, thus, excimer or exciplex formation indicates important charge transportations between low-band gap organic polymers. Enhanced π–π interactions could improve their charge-carrier ability, and thus enhance the power conversion efficiency.

1.4.1 Basic parameters in OPCs

Organic charge transporting materials can be categorized as electron- or hole-transport materials based on π-conjugated compounds (molecular or polymeric) where migrate under the effect of an electric field. These materials results from by removing/adding electrons from filled and empty molecular orbitals, respectively [29]. In usually, for a successful organic photovoltaic cell three important parameters have to be optimized to obtain highly efficient photovoltaic cell i) Photon Absorption, ii) Charge Generation and Diffusion, and iii) Charge Transportation and Collection [30-31].

Photon Absorption: To create an electric current in any photovoltaic cell, the photons of light must be collected efficiently. To maximize photon collection, the absorption

spectrum of n-type material should be sufficiently matched with the solar emission spectrum and the wideness of the photoactive layer should be thick to absorb the entire incident light. N-type semiconductor needs a minimum energy, named as band gap energy, to excite its electrons to higher energy levels. HOMO-LUMO band gap is equivalent to the energy required to free a valance's electron from its orbit and to become a mobile charge carrier. The band gap is a major factor determining the electrical conductivity and feasibility of any photovoltaic cell. Only photons of sunlight are able to provide this energy, or more. To a better overlap with the electromagnetic spectrum is achieved by lowering the HOMO/LUMO band gap of n-type semiconductor. Therefore, it is highly preferable to synthesize photoactive chemicals with broader light absorption through lowering the optical band gap without sacrificing molar extinction coefficient and charge transport abilities. The semiconductors commonly used in solar cells have band gap within the range 0.5-3.0 eV. Increasing the thickness of the layer is advantageous for the absorption of light, but the charge transport is hampered.

Charge Generation and Diffusion: During the conversion of light into electrical energy, charge generation and diffusion are also one of the key criteria in the photovoltaic devices. To create a working solar cell, n-type and p-type semiconductors are sandwiched between two electrodes to collect charges. After the absorption of sunlight, OPCs generate neutral charges and strongly bound electron-hole pairs, named as exciton. Since excitons are neutral their transport is not affected by any electric field. Charge diffusion, or exciton diffusion, can be regard as a series of successful hopping transfer steps between molecular and polymeric repeating units. The characteristic exciton diffusion length of OPCs is ~10-20 nm and these

photogenerated charges have to transport to the electrodes without recombination in order to generate photocurrent. Additionally, some of the sun-light energy is wasted via radiative or non-radiative ways. Therefore, it is important that formation of photogenerated charges need to be thermodynamically and kinetically favourable. In this manner, the length of the potential intermolecular barriers can be shortened with close packing of the molecules and planar molecular framework will lead to better exciton diffusion properties than the bulky molecular structures.

Charge Transportation and Collection: During the hopping transport process, the photogenerated charges (holes and electrons) have disassociated at the semiconductor/electrode surface and then they start to localize their corresponding electrodes and should enter to the external circuit without any interface problems. The ability of the charge collection process at the electrodes can not be easy due to complexity of electrode/semiconductor interface layer.
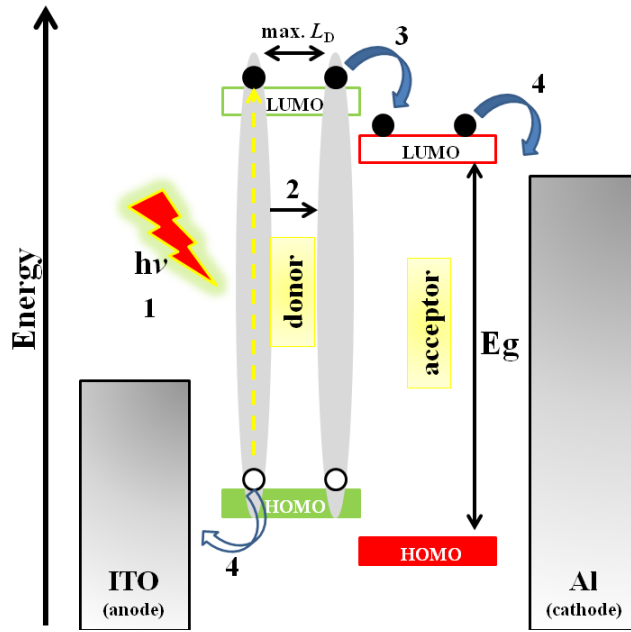
Figure 1.3: Fundamental Steps Occuring in PV Cell; 1-Generation of exciton by photoexcitation of donor, 2- Exciton diffusion to the Donor/Acceptor junction, 3-Dissociation of bound excitons to form geminate electron-hole pair at Donor/Acceptor interface, 4-Charge transportation and collection at external electrodes (electrons are collected at the Al electrode and holes are collected at ITO electrode) (E_g: optical band gap, L_D: longer diffusion length)

Chapter 2

THEORETICAL

2.1 Organic/Polymer Photovoltaic Cells

One new major photovoltaic technology, organic polymer solar cell, is based on conjugated or non-conjugated organic polymer molecules. This technology has attracted remarkable attention in the last decade owing their as a promising approach. Due to the differences in mechanism between OPCs and IPCs, the size of OPC needs to be naturally different from counter part. Inorganic materials generally possess thick layer (micro-scale size). However, the layer thickness of most organic semiconductors can be kept thin (nano-scale size) with preserving high absorption capacity and good charge transport properties [32]. OPCs systems have advantage over IPCs in cost but efficiency remain too low. OPCs will take place IPCs sooner or later in solar cells as they have been gradually started to replace IPCs in many areas such as light-emitting diodes, laser printers, and photocopiers that depends a combination of flexibility, low cost, and large area. [33-34]. Although IPCs are too expensive to fabricate, OPCs have low cost production in high volumes due to flexibility of organic materials [35]. This feature of organic molecules makes them strongly fruitful for novel phototechnologic applications. One alternative is a next generation of photovoltaic cells, based on organic/polymer photovoltaic cells. Conjugated and non-conjugated polymers can be tailored at molecular level to alter their properties. By extension of π- π system and/or adding functional groups to the organic polymers can lower the band-gap energy level of the solar cell that gives the

chance of achieving reasonably high power conversion efficiency. Therefore, there is a growing interest to the engineering new organic optoelectronic devices; particularly polymer based solar cells that provide structurally controllable properties including low band gap light absorption, high conductivity, charge transport, ionic interactions and aggregation phenomena.

In a very short time, the development of polymeric devices has reached 7.4% with a rapid increase in power conversion efficiencies and they become as an alternative route to the new organic photovoltaic technology, to design novel devices to compensate high optical absorption and enhance electron mobility. Moreover, polymer based OPCs have direct band gap of energy generally ranging from 1.5 to 3 eV. Exteremely high molar excinction coefficient of organic semiconductors represents possibility for fabrication of very thin OPCs (100-150 nm) and therefore, only very few amount of these materials is required for production of PV cell [36-38].

2.1.1 Aromatic Polyimides

Amongst many kinds of conjugated polymers that have been worked, polythiophene, poly(p-phenylenevinylene and poly(alkylfluorene) derivatives are typical electron donor (p-type) semiconductors. On the other hand, the power conversion efficiency of solar cells with these polymers is limited due to their relatively high band gap energies. To most preferred way to overcome this challenge is attached n-type semiconductor to the system. By utilizing internal-charge transfer from p-type (electron donating) to n-type (electron accepting) moiety leads to low-band gap photovoltaic cells. Light absorption of conjugated polymers are usually strong in the visible region, unfortunately fullerene molecules, the most widely used class of n-

type semiconductor, have fairly poor absorption in the visible spectral range. Thus, instead of fullerene molecules using brand new n-type electron acceptor will enhance light absorption of organic solar cell devices [39-40].

Aromatic polyimides (PIs) were produced by first time by Marston Bogert in 1908. The first synthesized high molecular weight aromatic polyimides were obtained by two step polycondensation reaction of pyromellitic dianhydride with diamines in 1955. Since then, intense research works have been focused on the development of new aromatic PIs based on organic compounds for electronic and optoelectronic devices due to their unique electrical properties, high mechanical strength, thermo-oxidative stability, and high radiation and solvent resistance. As a result of highly symmetrical plane and highly polar groups, aromatic PIs were equipped with rigid chains and strong inter- and intra- molecular interactions, which results charge transfer complex formation and electronic polarization. Moreover, it is possible to use PIs for long term applications at temperatures up to 200 °C, whereas short-tem operations are possible up to 480°C. Furthermore, PIs display also exceptional physico-mechanical properties in a wide temperature range and have excellent great radiation resistance and dominant semiconductor characteristics. These features allow PIs to dominate in a diverse range of applications; as heat-resistant polymers in high temperature plastics, dielectrics, photoresists, adhesives, nonlinear optical materials, Langmuir–Blodgett (LB) films, and membrane materials for separation; as electroactive components in the field of defense, aerospace, opto-electronics, electroluminescent devices, electrochromic materials, liquid crystal alignments, composites, polymer electrolyte fuel cells, fiber optics, polymer memories, etc. [41-42].

Materials that possess low band gap energy are being developed to alter silicon dioxide in semiconductor industry. Designing PIs with low band gap energy, good processability, and high thermal stability is of real interest in the area of electronic industry. Polymers with low band gap energy (<3eV) can be used in large scale integration or integrated circuits. The low band gap energy is one of the most charming properties of PI materials for electronic applications. In order to achieve polymer architecture with low band gap energy, incorporating aromatic rings into flexible polymer chain can be lowered band gap energy [43]. Aromatic PIs, considering the structure of imide component, are divided into two classes; namely compounds with five- and six-membered imide rings. Polynaphthaleneimides (PNIs) and polyperyleneimides (PPIs) are the polymers with six-membered imide rings. When compared with conventional five-membered phthalic PIs, they denote enhanced thermal and chemical resistance under harsh conditions. Among the types of PIs studied, commonly obtained from 1,4,5,8-naphthalene tetracarboxylic dianhydride (NDA) and 3,4,9,10-peryelene tetracarboxylic dianhydride (PDA), have alerted considerable interest in years. [44-46].

2.1.2 Perylene Polyimides

Perylene based colorants have received extensive attention in academic as well as industrial dye and pigment research. Perylene diimides (PDIs) initially applied for industrial purposes, such as red vat dyes, and several members of perylene diimide derivates, as dye pigment, have started to use for automotive industry after 1950s. In recent years, applications of functionalized PDIs and their polymeric derivatives have attracted significant interest in the field of electronic materials. They act as an important class of n-type organic semiconductors, because of easily reduction at low potential. This n-type semiconductivity of Perylene dyes is associated with their high

electron affinity, which makes them most promising for application in PV technology. Due to the encouraging combination of optical, redox and stability properties of PDIs and lately PPIs were extensively studied. They exhibit high extinction coefficient (extinction coefficient, ε, is ~80000 M^{-1} cm^{-1} in comparison to that of P3HT ~ 20000 M^{-1} cm^{-1}), high fluorescence quantum yield up to 100% with outstanding thermal and photochemical stability [47]. Contrast to inorganic based semiconductors, PDIs can be used for low-cost operations like spin-coating, evaporating and printing and used in fabricating a variety of optoelectronic devices [48]. Perylene based-polymers are potential canditates as electron transporting components in OLEDs (organic light emitting diodes) [49], semiconductive material for OFETs [50], as photovoltaic material for solar energy conversion [39], as fluorescent labelling dye for bio-imaging [51].

The evolution of current solar cell based on organic molecules and polymers will come true with the design of new functional units for the purposes of charge generation/transfer and charge collection at the electrodes [*52*]. One of the biggest attractive properties of PDIs and PPIs is their versatile optical and electrochemical properties. This is because; PDIs and PPIs can be readily designed not only at the anhydride oxygen groups but also its α-position and β-position of "bay region" of the aromatic core that provides the tunability of the photo electronic properties of perylenes. Functionlization in anhydride position can be easily achieved by the imidization of aromatic perylene core using a wide variety of amines but has limited impact upon the optical and electrochemical properties. Derivatization of perylene core can be altered also via the formation of halogenated perylene species at the bay region (1, 6, 7 and/or 12 positions) of the aromatic core and subsequent replacement

of the halide groups with a diversity of chemical functionalities. Modifications on bay area can dramatically tuned the optical and electrochemical properties [*53*]. Consequently, the modification of these positions varies the absorption of the light from near ultra-violet up to the near infrared region. Most perylene derivatives, particularly PPIs, also demonstrate the ability of self-assemble formations via amphiphilic interactions as well as π-π stacking. Different orientations, such as H- or J- aggregations, may be occurred and promotes enhanced electronic communication with the neighbouring chromophore and this event may have caused the improvement of electron mobilities and/or charge transport on the whole molecule. To prevent electrical shortcuts in devices, smooth and pinhole free films are essential. For that reason, polymeric forms of organic semiconductor employ to develop the film forming ability of the device and also its attachment to other PV cell layers.

From the application viewpoint, blending of perylene chromophore into a polymer would be obtain mechanically strong materials with the attractive properties and increase the lifetime of the organic based electronic device. An exciting application of such a promising material for OPCs is to replace expensive and bad film-forming fullerene derivatives [54]. As a second aspect, usually the planarity of the perylene core is retained if the polymer attached to the carbocyclic scaffold. To design efficient OPC, charge transport should be concerned. As a consequence, the formation of extended PDI stacks that exhibit excimer like emission pronounced efficient charge transportation along the columnar pathway [55].

2.1.3 Naphthalene Polyimides

Unlike the higher analogues of the imide substituted rylene dyes like perylene, terrylene and quaterrylene, naphthalenecarboxylicdiimide derivatives absorb light below 400 nm and as result they possess low fluorescence quantum yield (Φ_f) and weakly emit in the visible region of the spectrum. They are neutral, planar and chemically redox- active materials with high thermal stabilities [56]. However, with the extensive studies on high performance (high-mobility, environmentally stable) polymers, naphthalene based polyimides with an extended $\pi-\pi$ surface become one of the most potential n-type semiconductors class for designing conducting organic materials, due to their low dielectric constants, high thermal stabilities and good mechanical properties [57]. One method to obtain both thermally stable and highly processable naphthalene polyimide is to interpenetrate naphthalene chromophore into a polymer network. Functionalization of naphthalenediimide into a polymer expanded the scope of application of these molecules such as for OFETs (organic field effect transistors) and solar cells due to their highly favourable $\pi-\pi$ stacking properties, strong absorption and fluorescence and upgraded charge carrier mobilities [58]. Due to efficient intermolecular $\pi-\pi$ electron delocalization, the charge carrier mobility of materials that assemble from planar chromophores is generally maximized by the $\pi-\pi$ stacking and hence conductivity increases [59]. The different types of supramolecular forces such as $\pi-\pi$ stacking, hydrogen bonding have been applied to develop highly ordered supramolecular architectures. Because of these non-covalent interactions, these well organized molecules can be find applications in electronic devices.

In summary, all the studies performed up to date on PPI and NPI based OPCs have shown that use of this kind of materials are promising for PV technology due to following reasons: (i) high molar extinction coefficient in the visible region makes it good light harvester (ii) the high stabilities against light and heat are expected to meet the necessity of a realistic outdoor operating solar cell in the future (iii) the molecular frame can be altered easily at different positions by bearing substituents and therefore their charming properties can be tuned further by structure variation.

2.1.4 Application of Perylene and Naphthalene Polyimides

Perylene and Naphthalene polyimides are members of high-performance aromatic polyimides that have received widespread attention in both acedemic and industrial centres because of their specific properties, that is, excellent thermal stability, electrical property, and mechanical strength. Moreover, PPIs and NDIs are worthy due to their photo-stabilities, photo-chemical behaviour, photo-conductive and good electron acceptor properties [60]. These compounds are highly efficient in terms of prospective applications in organic molecular electronics and related areas, exemplary as materials for developing high efficiency PV cells [61], for fabrication of light-emitting diodes (OLEDs) [62] or organic fied effect transistors (OFETs) [63-64], as organic cation exchange membrane for polymer electrolyte fuel cell [41,65].

Bulk heterojunction (BHJ) photovoltaic cells incorporating polyimide-based acceptor polymers are amongst the most effective all polymer photovoltaic cells to be reported. Thelaktat and co-workers synthesized donor-acceptor diblock polyacrylate polymers carrying with pendant PDI units and triphenylamine as electron- and hole-transporting components respectively [66]. Similarly, NIU Hai-jun et al. reported

novel linear-star shaped triphenylamine containing naphthalene polyimide to exhibit the effect of topological architecture on the photophysical performance of BHJ [61].
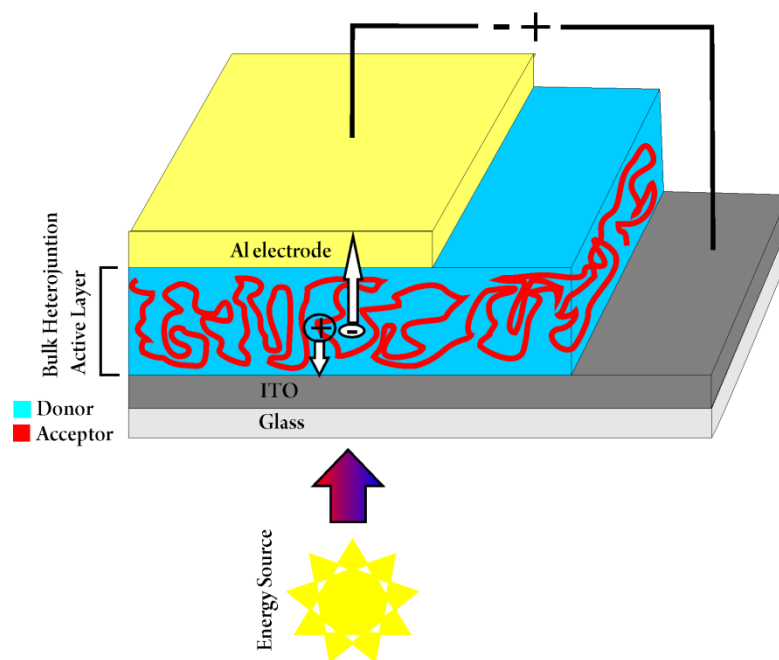
Figure 2.1: Configuration of Bulk Heterojunction (BHJ) Solar Cell

There are challenging published examples of polymer based on imide-functionalized π-system for light emitting diodes (LEDs). Ego et al., developed several polymer light emitting diodes (PLEDs) by blending perylene chromophore on polyfluorene backbone, at the chain termini, or as side chains which leads to tuning of emission colour [62]. H.-K. Shim et al., also developed various fully conjugated carbazole and naphthalene based copolymers by incorporating naphthalene units into polymer chain, which can emit white light electroluminescent emission originating from excimer formation [67].

Such polyimides are generally investigated to meet the key requirements of OFETs, such as excellent charge transport ability, chemical stability, solubility in most of the common solvents, and inexpensive solution or low temperature processing. Facchetti

et al. synthesized naphthalenedicarboxyimide based n-type polymer molecule and successfully deposited into organic thin film transistor, which possess high electron mobilities up to ~0.45–0.85 $cm^2V^{-1}s^{-1}$ in ambient conditions [63]. Wang et al. designed and fabricated a novel perylene polyimide derivative with amphipilic character, into an OFET device by Langmuir-Blodgett technique and shows much more better performance than its monomeric derivative because of face to face structure of perylene molecules in polymer [64].

Nowadays, Nafion, is a perfluorosulfanicacid polymer, used for electrode coating in fuel cell technologies. Because of its limitations, aromatic polyimides have been commonly investigated as potential proton exchange membrane material as a solid polyelectrolyte. Liu et al. reported the synthesis and properties of two series of sulfonated naphthalene polyimide derivatives carrying $-CF_3$ units on the naphthalimide. A polymer which incorporated with 50% sulfonated monomer denotes approximately two times more performance than Nafion membranes [68].

2.1.5 Non-covalent interactions in aromatic polyimides

Transfer of solar energy into an electrical current is a fundamental aspect of photoconversion in OPCs. The mechanism of the photoconversion is still not well understood. But like nature, with the absorption of light in OPCs energy is transferred as excitons to the junction point where mobile excitons finally dissociate into electron-hole pairs. Strong intermolecular non-covalent interactions and geometrically and also energetically well organized chromophores tend to promote movement of excitons [69]. Multichromophoric arrays, that absorb sun light and transmit the excitation energy quickly and effectively to a designated acceptor point, are of great attention for probing the mechanisms of energy migration among

chromophores. To achieve this, a deeply effective cooperation is required between the chromophores that are arranged in well-define geometries. This can be utilized by non-covalent interactions such as π–π stacking, hydrogen bonding interactions, and solvophonic effects [70].

In recent years, the latest fashion in the construction of new multichromophoric systems is integration of chromophores into polymer. The role of polymer is very important, acts like bridge that anchors the chromophores and controls the displacement of the rings and let them to communicate electronically. The bridge, that provides structural motif, mediates not only π–π stacking but also formation of weak electronic coupling by non covalent hydrogen bonding interactions between the chromophores [71]. This new technology opens the way to development of innovative supramolecular systems and also to enhancement of the energy displacement of the photoactive entities in the array. By altering the individual properties of both chromophore and polymer may result wider absorption range and a better control on the energy transfer flow.

2.1.5.1 π–π Stacking System

In the field of OPCs e.g. photogenerating dyes for photoconductors, the π–π interactions between organic planar π–conjugated molecules play a crucial role and this aggregation phenomena initially affects performance by changing absorption and fluorescence spectra and also alters the power conversion efficiency and charge mobilities [72-73]. One of the most remarkable features of PDI and NDI derivatives is their tendency to self assemble in π-stacks. The π–π interactions of the PDIs and NDIs are the dominant driving forces leading to the aggregation of the chromophores to create photo physically active assemblies. While the π–π stacking facilitate the

molecular aggregation of these dyes, the nature of the aggregation can be modulated by integration of these chromophores into polymeric cage which capacitate the efficient conduction of excitons within the aggregates and the features of the OPC commonly enhance with increasing structural order [74-75]. From the application point of view, polymer based OPCs should be highly promising devices for photofunctional applications thus may overcome obstacles arising from morphological problems encountered in OPCs.

Lately, B. Y. Liu et al. constructed a nanoscopic supra-molecular aggregate result from perylene diimides bridged cyclodextrin conjugates, a class of cyclic oligosaccharides, via π–π stacking interactions. The π–stacking behaviour of self-assembly was studied with UV-vis, fluorescence and ^{1}H NMR spectrophotometer in various organic and aqueous solvents. The distance between π–π stacking units calculated as 4.02 Å according to the X-ray powder measurements which is higher than common π–π aggregating distance (~3.50 Å) of PDIs [76]. The nematic ordered perylene containing polyimides, in which perylene containing main-chain folded by strong intermolecular π–electron delocalization between adjacent perylene diimide moieties described by Sundararajan and coworkers [77].

E. Schab-Balcerzak et al. synthesized and characterized novel two low band gap poly(azomethine-naphthalene diimide) compounds with thiophene and bithiophene rings in the range from 1.31 to 1.37 eV that could from highly delocalised π-system [78]. P. Piyakulawat et al. also reported another low bandgap copolymer comprise of NDI and thiophene derivative and fabricated into BHJ solar cell with 0.40% power conversion efficiency under the illumination of AM 1.5 (100mW/cm^2) [79].

G. Qi et al. developed a series of linear perylene tetracarboxylic mono-anhydride derivatives for DSSCs with high molar extinction coefficients. Because of the extended π-conjugation, the energy transfer performance from donor segment to acceptor segment are almost 100% estimated from fluorescence quenching that improves the solar energy conversion [80].

2.1.5.2 H-bonding System

Besides the traditional intrinsic π–π interactions between dyes backbones, one field of intense interest in last years has been the improvement of other intermolecular forces that can orient the formation of fascinating supramolecular architectures with encouraging outcomes. H-bonding is selective, more specific and moderately strong and that makes it powerful tool for modelling larger motifs from small building blocks. [81]. Hydrogen bonds have higher binding energies than other bonds (π–π stacking, Van der Waals forces and dipole–dipole interactions) and are considered as one of the most significant forces to be used for the construction of various molecular aggregates [82]. In conjunction with aromatic π-stacking, weak non-covalent interactions like aromatic C–H ••• π and aromatic C–H ••• O interactions take a role in directing self assembly of molecular strands [83;]. The appropriate combinations of molecular assemblies with π–π stacking and hydrogen bonding interactions affect the orientation and closeness of these materials. A smoot, well-ordered film with intermolecular actions is beneficial to manifold the charge mobility in OPCs by creating new excitonic states [84.]. The geometrically arrangement of NDIs or PDIs in polymeric network structure could favour the H-bond formation which enabling weak electronic coupling between the dye molecules to construct different types of aggregates.

Lately, Y. Jung et al. synthesized uniform and highly ordered semiconducting nano/macro wire patterns of tridodecyloxyphenyl-functionalized perylene dyes which demonstrates strong self assembling tendency originating from augmented intermolecular H-bonding interactions. Electrical conductivities of these nano/macro wire arrays measured as 1.93 ± 0.47 x 10^{-6} S cm^{-1} [85]. The mutual effects of hydrogen bonding and π–π stacking on self organization of arylene dyes was studied by Jancy and Asha. The presence of hydrogen bonding force between aromatic cores affects the mechanism of π–π stacking of the polymer at low and high incorporation of diimides [60]. Self assembled naphthalenebisimide based heterodimer was reported with improved charge mobilities for OFETs due to hydrogen bonding between the aminoimide groups [86]

2.1.5.3 Ambipolar Charge Trasport

Organic compounds have commonly used as unipolar materials and this limits their feasibility for photonic applications. Ambiphilic polymers which are usually composed of covalently attachment of hydrophobic chromophores into hydrophilic polymers have interesting properties worth of study. These are electrochemically reduced and oxidized to carbo-anions and carbo-cations, respectively. Since they have ability to transport both hole and electrons, they can be used as n-type and p-type charge carriers to develop optoelectronically active polymeric materials [87]. One of the most favourite approaches to fabricate low band gap polymers is the utilization of the ambipolar charge transfer interactions between electron-rich donor and electron-deficient acceptor in the polymer backbone. However, a very few of examples of organic polymer semiconductors capable of ambipolar charge transport have been reported in the literature. The copolymers based on PDI units attached in bay areas with oligothiophene units, which is suitable for donor-acceptor polymeric

PV systems have been described by Kazma et al and showed ambipolar electrochemical properties [88]. Watson and co-workers reported a series of nine NDI based ambipolar polymers in order to study charge transport properties for OFETs by varying HOMO/LUMO energy levels. Only two of them showed ambipolar transport characteristics with mobilities of $>10^{-3}$ $cm^2V^{-1}s^{-1}$ and 0.006-0.02 $cm^2V^{-1}s^{-1}$ for holes and electrons respectively [58].

2.1.5.4 Solvophobic interactions

Solvophobic effect describes the interactions between polar solvents which carrying spatial H-bond network, and non-polar solutes. The solvophonic effect usually involves two phenomena: solvophonic solvation and solvophonic interaction. In the first phenomena-solvophonic solvation- solvophonic part of solutes surrounded by solvent molecules which cause to stabilization of solute species. The second phenomena-solvophonic interaction- refers to aggregation behaviour of non-polar part of solute in solutions [89]. The energy level of organic compounds could affect not only by the solvent polarity but also by their degree of polarizability. Thus, both position and spectral shape of absorption and emission band of compounds may varied. Very recently, solvent dependent fluorescent colour tunable oligomer carrying hydrophilic hexa(ethylene glycol) unit and hydrophobic naphthalene-bisimide dye has been reported by Icil and Bodapati. That oligomer emits yellow and blue light in chloroform and methanol, respectively [90]. The arylene polymers (PPIs/PNIs) are known to form π–π aggregates in different solvents. Self-assembled aggregates of arylene polymers can upgrade with exploiting solvophobic forces [84]. Studies have also revealed that the morphology and microstructure of amphiphilic compounds have also varied by polarity of solvent. Chen and co-workers have observed the effect of solvent on the morphology and structure of self assembling of amphiphilic PDI-nanostructures. The self assemblies of PDI derivatives in methanol and n-hexane result nanobelts and nanoleaves/sheets, respectively [91]. Lately, aqueous supramolecular polymer formed from an amphiphilic perylene monomer has been described by Wintgens and co-workers [92]

2.2 Biopolyelectrolytes in Optoelectronics

Nowadays, there is a growing interest to the photoactive polymers (polyelectrolytes) which have electrolyte units in the repeating order. There are two major classes of polyelectrolytes; natural (polynucleotides, polypeptides and polysaccharides) and synthetic polyelectrolytes (specific chromophores or π-conjugated polymers). They are considered as important part of the photoactive devices, such as light-emitting devices, nano tubes, biosensors, or solar energy conversion systems, which is arising from the synergistic effect of dual functionality of ionizable electrolyte groups. Polyelectrolytes provide unique set of properties, such as ionic conductivity, water solubility, strong intra- and inter-chain interactions, interactions with ions in solution, surface activity and a propensity to adsorb at interfaces. Recently, polyelectrolytes have been applied in the formation of new type of thin film materials known as polyelectrolyte multilayers (PEMs). PEMs can be constructed by using layer-by-layer deposition technique. These thin films decreases the thickness of solar cells to the single-nanometer scale [93]. Furthermore, natural polyelectrolytes, especially polysaccharides, have become more and more important over synthetic polymers for their unique chemical, physical and biological properties [94].

2.2.1 Chitosan

Last studies of chitosan have received much great attention from academia and industry due to their low cost and rich renewable resources. Chitosan, consisting partly of $\beta(1\rightarrow4)$-2-acetamido-2-deoxy-D-glucopyranose and mostly $\beta(1\rightarrow4)$-2-amino-2-deoxy-D-glucopyranose units, is the second most abundant linear polysaccharide based biopolymer in the nature. Chitosan is commercially obtained by partially de-acetylation of chitin. Chitosan and its derivatives can be employed in many areas, such as optical and biomedical applications, environmental protection,

waste water treatment, industrial, food processing and also agriculture [95-96]. Owing to its distinctive properties such as non-toxicity, biodegradability, biocompatibility, and antibacterial properties, it is a "popular" biomaterial and used in the field of optical, biosensing and biomedical research as "carrier" in gene delivery and/or drug targeting systems, as "bio-imaging agent" to increase the absorption of biotherapeutics [97-98]. Nowadays, it is frequently started to use for photovoltaic applications, for instance as film forming material in PV cell [99], as photoconductive resin [100], as proton exchange membrane in fuel cell [101]. Chitosan is an electron donating bio-polyelectrolyte which presents a range of functional ionizable groups; free amine groups on deacetylated units, the hydroxyl groups on the carbons and carboxyl groups on the acetylated units, aimed at participating in energy or electron transfer processes. Thus, chitosan as an electrically sensitive cationic polymer is potential polyelectrolyte for solar cells and may forms highly conductive composite films for photovoltaic systems, especially for carbon nanocomposites [102-103]. Despite the high-energy conversion efficiency of DSSCs based on liquid electrolytes that has reached 11% under irradiation of AM 1.5, there are still important problems to be solved. The cationic character of chitosan also offers good opportunities as solid electrolyte to enhance the conductivity and film forming ability. With this way it can be prevent the problems in liquid electrolyte PV cells such as high-temperature instability, electrolyte leakage and solvent evaporation [104-105]. Furthermore, the attachment of chromophore functionalized biopolyelectrolyte is a great oppurtinity for many applications. It was expected that introducing an aromatic ring on chitosan biomaterial will improve its conductivity by doping the aromatic proton conductors and also will balance its hydrophilic-hydrophobic character. To do this, it will afford a highly stable proton

exchange membrane for direct methanol fuell cells with good chemical and thermal staillities [101]. Additionally, chitosan films have been announced to display good mechanical properties. Chitosan polymers demonstrate a semi-interpenetrating polymer-network system through the strong electrostatic and hydrogen bonding interactions between amino, hydroxyl and carboxyl groups and forms high stable framework [106].

Chapter 3

EXPERIMENTAL

3.1 Materials

A naphthalene-1,4,5,8-tetracarboxylic dianhydride (NDA), perylene-3,4,9,10-tetracarboxylic dianhydride (PDA), low molecular weight chitosan (CH), zinc acetate, isoquinoline and m-cresol were purchased from Aldrich. Sodium tetrafluoroborate (NaBF$_4$) and ferrocene were supplied from Fluka. For studying of photophysical measurements, pure spectroscopic grade organic solvents used directly without any further purification. All the other chemicals and reagent grade solvents were employed as received without further purification, unless stated otherwise.

3.2 Instruments

^{1}H and ^{13}C NMR spectra were obtained on a Burker AVANCE-500 spectrometer operating at 400 MHz in CDCl$_3$ + CF$_3$COOD with TMS (tetramethylsilane) as an internal reference. Infrared spectra of the samples in the transmission mode were measured as potassium bromide (KBr) pellets on a Mattson Sattelite FT–IR spectrometer in the range of 4000 to 400 cm $^{-1}$. UV-vis absorption spectra of the solutions were examined on a Varian Cary-100 spectrophotometer and UV-vis spectra of solid-states were recorded using a Perkin-Elmer UV/VIS/NIR Lambda 19 spectrometer, provided with solid-state accessories, in thin films. Emission and photoexcitation spectra, and also fluorescent quantum yield of the CH-PPI using dodecyl PDI (Φ_f = 1.00) as reference by exciting at 485 nm in chloroform and fluorescent quantum yield of the CH-PNI using anthracene (Φ_f = 0.27) as reference

by exciting at 360 nm in ethanol, were registered with Varian-Cary Eclipse Fluorescence spectrometer. Elemental analyses were conducted with a Thermo Finnigon Flash EA 112 model CHN elemental analyzer. Thermogravimetric analysis (TGA) was performed using a Perkin-Elmer, TGA, Model, Pyris–1; the glass transition temperature (T_g) values of the compounds were determined at a heating rate of 10 K min^{-1} under oxygen and nitrogen atmosphere. Differential scanning calorimetry (DSC) was undertaken using a Perkin-Elmer, DSC Model, Jade DSC instrument; melting points (mps) were obtained at a heating rate of 10 K min^{-1} in nitrogen. The weight-average molecular weight (M_w) and number-average molecular weight (M_n) of the polymers were determined by gel permeation chromatography (GPC) using column (PSS GRAM, 10 μm, 100Å, ID 8.0 mm x 300 mm), with TSP P1000 HPLC pump, in a combination with a detector Shodex Differentialrefractometer RI 71. The calculation of the molecular masses were done by PMMA-equivalents using PSS-Win GPC UniChrom Version 8.0 program. The samples of polymers were to run in DMSO / 0.1 M LiCl and calibrated with polymethylmethacrylate (PMMA) standard at 70 °C. The polymers were partly soluble and solved in DMSO at 50 °C by shaking for one day. The solutions of polymers were filtrated with a 1μm one-time filter. The intrinsic viscosity [η] measurements of the polymers were carried out in dimethyl acetamide and N-methylpyrrolidinone at 26 °C with a calibrated Ubbelholde viscometer. The intrinsic viscosity [η] was determined from specific viscosity [$η_{sp}$] at five different concentrations, by plotting log($η_{sp}$/c) vs c and extrapolating to origin measure. The redox properties of the polymers in solvents were recorded on "The Gamry Instruments, REFERENCE 600 Potentiostat/Galvanostat/ZRA" and were performed by using a three-electrode cell with 2 mm Pt as working electrode and polished

glassy carbon as counter one. Ferrocene was utilized as internal reference.The solutions (10^{-5} M) were in electroactive material and 0.1 M in supporting electrolyte, $NaBF_4$. The frequency of 25-2000 Hz and the scan rate of 50-1000 mV^{-1} were employed for square-wave and cyclic voltammetries, respectively. The square-wave and cyclic voltammetries in solid state were performed for CH-PPI on Eco Chemie Autolab PGSTAT30 Potentiostat/Galvanostat and for CH-PNI and ENPI on "The Gamry Instruments, REFERENCE 600 Potentiostat/Galvanostat/ZRA" employing glassy carbon (as an auxiliary electrode) and Ag/AgCl electrode (as a reference electrode). The solution of 1M HCl was employed as a supporting electrolyte. Carbon paste (as the working electrode) was obtained by pressing 25mg graphite powder and with 10 µL paraffin oil mixture in a holed Teflon tip. The solid polymer was immobilized to the surface of carbon paste with a diameter of 5 mm by scratching. The frequency 25-2000 Hz and the scan rate of 50-1000 mV^{-1} were employed for solid state square-wave and cyclic voltammetries, respectively.

3.3 Methods of Syntheses

Despite many advantages of OPCs, the most important advantage is their tunability on the molecular level that gives the possibility of achieving reasonably high power conversion efficiency. There is a growing interest to the engineering new organic optoelectronic devices; particularly polymer based solar cells that provide structurally controllable properties including low band band gap light absorption, high conductivity, charge transport, ionic interactions and aggregation phenomena. In a very short time, the power conversion efficiencies of polymeric solar cells have reached 5% and they become as an alternative route to the new organic photovoltaic technology, to design novel devices to compensate high optical absorption and enhance electron mobility, due to their versatility and potential applications in many areas.

Nowadays, there is a growing interest to the photoactive polymers (polyelectrolytes) which have electrolyte units in the repeating order. They are considered as important part of the photoactive devices, such as light-emitting devices, nano tubes, sensors, or solar energy conversion systems, which is arising from the synergistic effect of dual functionality of ionizable electrolyte groups with the inclusion of specific chromophores or π-conjugated systems. Polyelectrolytes provide unique set of properties, such as water solubility, ionic conductivity, strong intra- and interchain interactions, interactions with ions in solution, surface activity and a propensity to adsorb at interfaces.

To make an efficient solar device, donor and acceptor material should blend into each other to provide proper movement. Perylene and naphthalene diimides have strong absorption ability and electric transport mobility, respectively. Derivatization

of dyes in chitosan polymer molecules leads to considerable rigid and planar frameworks of ladder conjugated oligomers or polymers which facilate electron delocalization and enhance conductivity. Therefore, the synthesis and investigation of such polyimides are of considerable interest due to advantages of photophysical and photochemical properties.

The synthetic routes, which were illustrated in Scheme 3.1 to Scheme 3.3 is used for the synthesis of new low band gap polyimides. The syntheses of chitosan substituted naphthalene and perylene polymers were successfully accomplished by substitution reaction between commercially available chitosan biopolymer (CH) and industrial dyes, perylene dianhydride (PDA) and naphthalene dianhydride (NDA), using m-cresol and isoquinoline as solvent mixture. All of the synthesized polyimides were fully characterized by Fourier transform infrared spectra (FTIR) and, hydrogen- and carbon-nuclear magnetic resonance (^{1}H and ^{13}C NMR) as well as via elemental analysis. The electrochemical thermal, photochemical, and optical properties of low molecular weight chitosan based naphthalene and perylene polyimides have been explored in detail.

Additionaly, high molecular weight naphthalene polyimide with long alkoxy chains was also synthesized according to do the Mustafa E Ozser procedure (Ozser, Yucekan, Bodapati, Icil in press) in order to explore in detail photophysical and photochemical properties of ENPI (Scheme 3.3).

3.3.1 Synthesis of Poly[bis-*N,N'*-1,4,5,8-naphthalenetetracarboxydiimide conjugated chitosan, CH-PNI
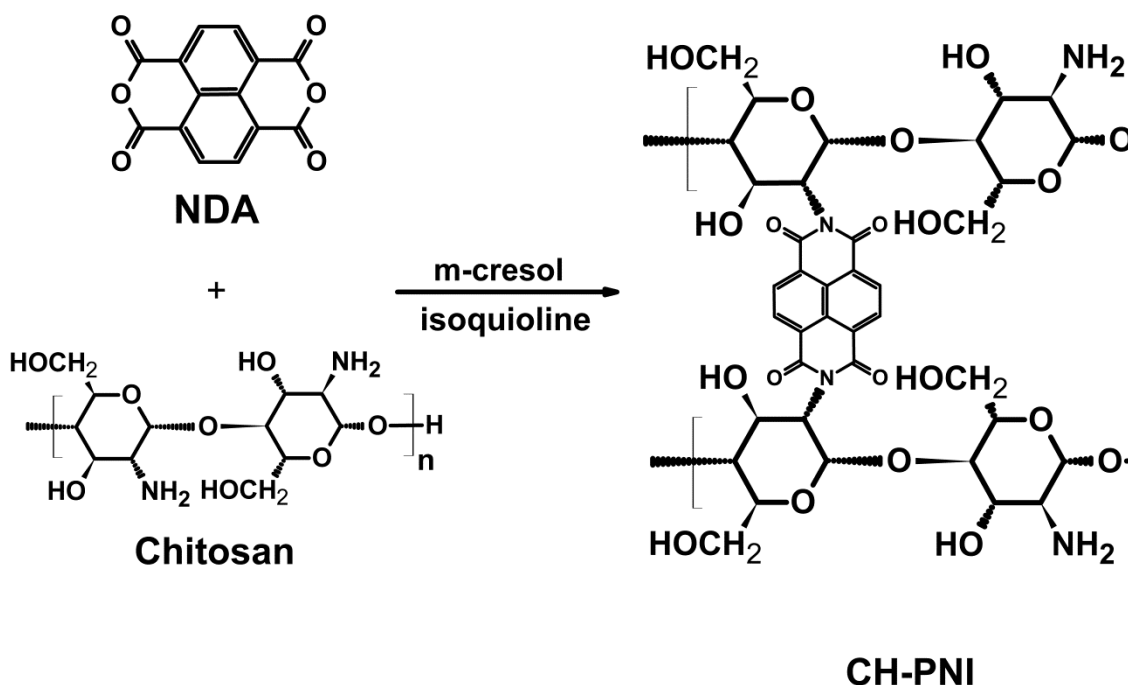
Scheme 3.1: Synthesis of Chitosan Substituted Naphthalene Polyimide, CH-PNI

A mixture of naphthalene-1,4,5,8-tetracarboxylic acid dianhydride (0.268 g, 1.0 mmol), low molecular weight chitosan (0.805 g, 5.00 mmol) were heated in dried solvent mixture (10 mL isoquinoline and 40 mL m-cresol) under argon atmosphere at 80 °C for 2 h, at 120 °C for 4 h and finally at 160 °C for 6 h. The solution was allowed to cool up to 50-60°C and was poured into cold methanol solution (~400mL) to solidify the compound over the night. The precipitate was filtered off by vacuum filtration by washing with 1 % acetic acid and water, and then purified by soxhlet extraction with chloroform during one day in order to remove unreacted compounds, the catalyst zinc acetate and high-boiling point solvents. The crude product termed as CH-PNI was then dried at 110 °C under vacuum.

^{13}CNMR OF CH-PNI(400 MHz, $C_2F_3O_2D$ + $CDCL_3$ (1:1)) δ (ppm): 67.80 (4 CH_2, C (6), C (6'), C (12), C (12')), 102.96 (4 CH, C (1), C (1'), C (7), C (7'), 142.49-122.05 (10 Ar (C), C (13-20) , C (25), C (26),), 162.14 (4 C=O, C (21), C (22), C (23), C (24)). ^{1}HNMR OF CH-PNI(400 MHz, $C_2F_3O_2D$ + $CDCL_3$ (1:1)) δ (ppm): 1.27 (t, J = ? Hz, 4 CH, H-C (4), H-C (4'), H-C (7), H-C (7')), 2.14 (s, 4CH, H-C (2), H-C (2'), H-C (9), H-C (9')), 2.37 (s, $2NH_2$, H-N (9), H-N (9')), 2.67 (s, 8OH, OH-C (3), OH-C (6), OH-C (3'), OH-C (6'), OH-C (8), OH-C (12), OH-C (8'), OH-C (12')), 2.88 (d, J = ? Hz, 4CH, H-C (3), H-C (3'), H-C (8), H-C (8')), 3.92 (s, 4 CH, H-C (5), H-C (5'), H-C (11), H-C (11')), 4.27 (q, J = ? Hz, $4CH_2$, H-C (6), H-C (6'), H-C (12), H-C (12')), 4.33 (q, J = ? Hz, 4CH, H-C (1), H-C (1'), H-C (10), H-C (10')), 9.48-7.85 (m, 4 Ar-H, H-C (14), H-C (15), H-C (18), H-C (19)). IR (KBr, cm^{-1}) : ν =3436, 3058, 2922,1707,1589, 1440, 1365, 1155, 1038, 754. UV-vis (chloroform): $λ_{max}$ (ε) = 414 (101300), 396 (102500), 371 nm (88500). Anal. calcd for $(C_{38}H_{48}N_4O_{22})_n$, $(912.80)_n$: C, 50.00; H, 5.30; N, 6.14. Found: C, 60.95; H, 4.15; N,8.32.

3.3.2 Synthesis of Poly[bis-*N*,*N*'-3,4,9,10-perylenetetracarboxydiimide conjugated chitosan, CH-PPI
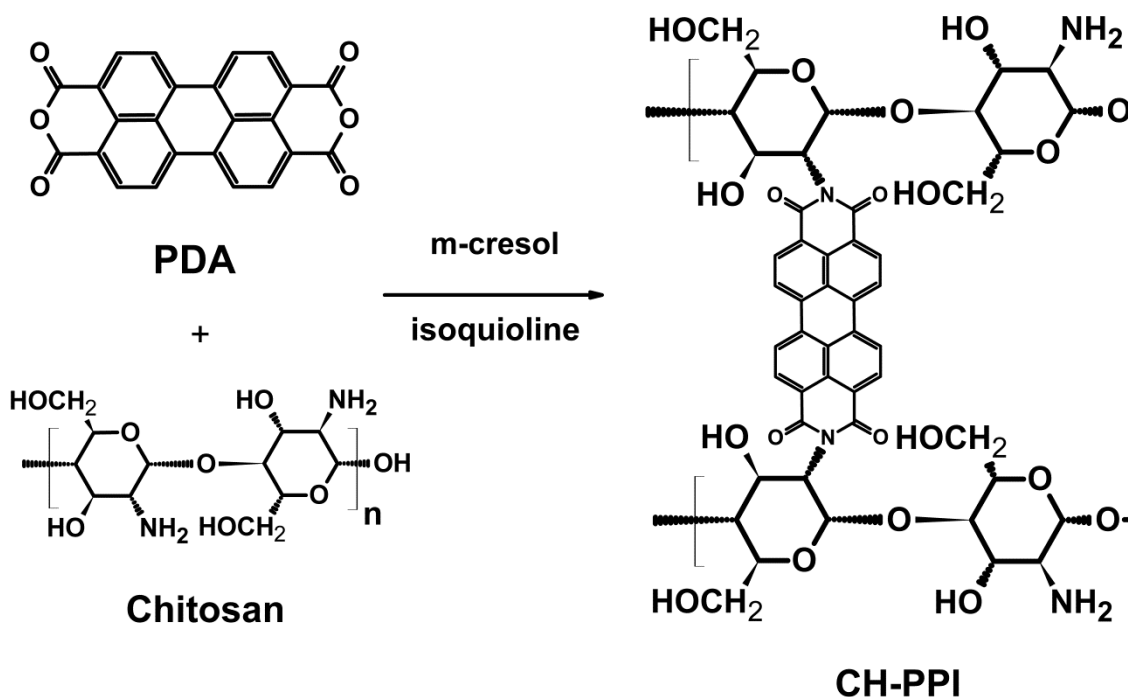
Scheme 3.2: Synthesis of Chitosan Substituted Perylene Polyimide, CH-PPI

Under argon atmosphere, a mixture of PDA (0.3928 g, 1.0 mmol), commercial CH (0.805 g , 5.0 mmol) as an amine and zinc acetate dihydrate (0.1814 g, 0.82 mmol) as a catalyst was stirred well at 80 °C for 2 h, at 120 °C for 4 h and complete the reaction by mixing at 160 °C for 6 h in a mixture of m-cresol and isoquinonline (v/v, 5:1). After being cooled to the room temperature, the reaction mixture was poured into 400 mL chilled methanol. The precipitate was filtered off by suction filtration by washing with 1 % acetic acid and water, and then purified by soxhlet extraction with chloroform during one day in order to remove unreacted compounds, the catalyst zinc acetate and high-boiling point solvents. The crude product was then dried at 110 °C under vacuum. The compound termed as CH-PPI was obtained as a pure, dark brown powder in 60% (0.25 g) yield.

^{13}C NMR (400 MHz, $C_2F_3O_2D$ + $CDCl_3$ (2:3), δ): 65.09 (4 CH_2, C (6), C (6'), C (12), C (12')), 104.29 (4 CH, C (1), C (1'), C (7), C (7'), 147.01-120.07 (20 Ar (C), C (13-24)), 165.66 (4 C=O, C (25), C (26), C (27), C (28)). ^{1}H NMR (400 MHz, $C_2F_3O_2D$ + $CDCl_3$ (2:3), δ): 1.42 (t, J = ? Hz, 4 CH, H-C (4), H-C (4'), H-C (7), H-C (7')), 2.17 (s, 4CH, H-C (2), H-C (2'), H-C (9), H-C (9')), 2.22 (s, 2NH$_2$, H-N (9), H-N (9')), 2.35 (s, 8OH, OH-C (3), OH-C (6), OH-C (3'), OH-C (6'), OH-C (8), OH-C (12), OH-C (8'), OH-C (12')), 2.40 (d, J = ? Hz, 4CH, H-C (3), H-C (3'), H-C (8), H-C (8')), 4.02 (s, 4 CH, H-C (5), H-C (5'), H-C (11), H-C (11')), 4.25 (q, J = ? Hz, 4CH$_2$, H-C (6), H-C (6'), H-C (12), H-C (12')), 4.48 (q, J = ? Hz, 4CH, H-C (1), H-C (1'), H-C (10), H-C (10')), 8.91-7.37 (m, 8 Ar-H, H-C (13), H-C (14), H-C (17), H-C (18), H-C (19), H-C (20), H-C (23), H-C (24)); IR (KBr): ν = 3450, 3163, 3050, 2847, 1690, 1591, 1402, 1362, 1273, 1180, 1030, 812; UV-vis (chloroform): λ_{max} (ε) = 526 (100020), 489 (76542), 460 nm (35414). Anal. Calcd. for $C_{48}H_{52}N_4O_{22}$: C: 55.60%; H: 5.05%; N: 5.40%; found: C: 65.02%; H: 4.00%; N: 7.48%.

3.3.3 Synthesis of Poly[bis-*N*,*N*'-(3-(2-(2-(3-aminoproxy)ethoxy)ethoxy)propyl)-1,4,5,8-naphthalene imide], ENPI
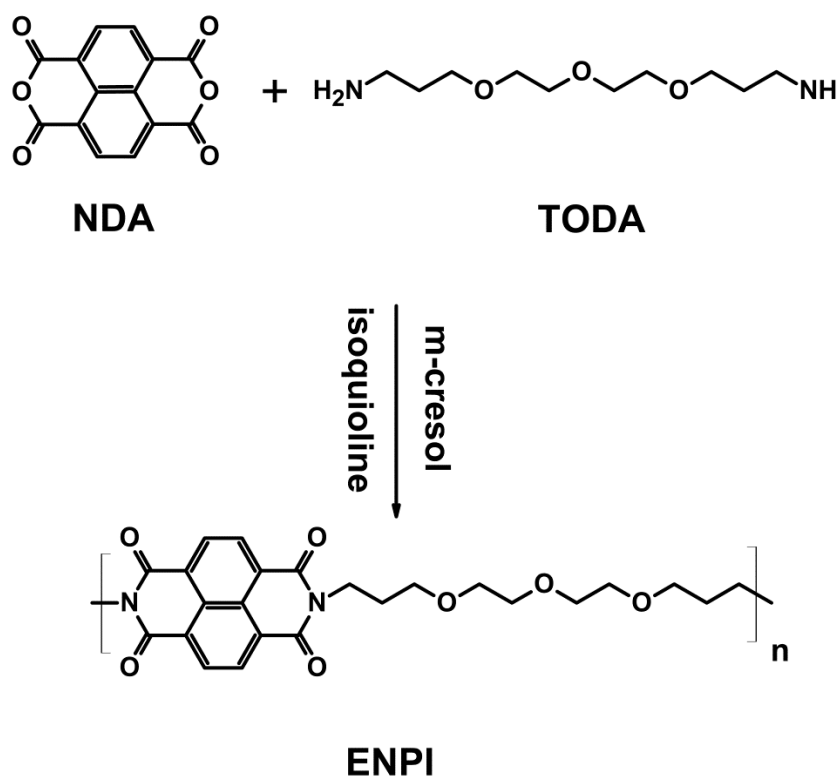
Scheme 3.3: Synthesis of High Molecular Weight Naphthalene Polyimide, ENPI

The high molecular weight 1,4,5,8-naphthalene polyimide (ENPI) was synthesized by Mustafa E. Özser by the one step polycondensation reaction between 4,7,10-trioxa-1,3-tridecanediamine (TODA) and 1,4,5,8-naphthalenetetracarhoxylic dianhydride (NDA).

Chapter 4

DATA AND CALCULATIONS

4.1 Determination of Molecular Weights (M_w)

The weight-average molecular weight (M_w) and number-average molecular weight (M_n) of CH-PPI, CH-NPI and chitosan polymers were determined by gel permeation chromatography (GPC). The intrinsic viscosities [η] of the molecules were measured using an Ubbelohde viscometer. The intrinsic viscosities [η] of the compounds were determined from specific viscosity [η_{sp}] at five different concentrations, by plotting $\log(\eta_{sp}/c)$ vs c and extrapolating to origin measure.

4.1.1 Measurement of Intrinsic Viscosity [η]

Intrinsic Viscosity of CH-PNI

The intrinsic viscosity [η] of CH-PNI was calculated by measuring specific viscosity (η_{sp}) at five different concentrations (*c*) in NMP solvent and applied Huggins equation, plotting $\log(\eta_{sp}/c)$ vs. *c* and extrapolating to zero concentration. Each measurement was repeated at least three times and the average efflux time was regarded for calculation of the intrinsic viscosity. Table 4.1 depictes the efflux times of solvent and CH-PNI, respectively.the efflux time of CH-PNI.

Table 4.1: Data of Efflux Times of NMP at 26°C

Solvent	Efflux Time (sec)	Avg. Efflux Time (sec)
DMAc	1447	1447
	1450	
	1444	

Similarly, the average efflux times of CH-PNI in NMP were tabulated below for five

different concentrations (c).

Table 4.2: Average Efflux Times Data of CH-PNI at 26°C

Concentration (g/dL)	Avg. Efflux Time (sec)
0.0500	1549
0.0250	1537
0.0125	1526
0.0050	1486
0.0025	1470

According to the formulae showing below, all the viscosity parameters for each

concentration were calculated and illustrated in the table 4.4.

$$\eta_{relative} = \frac{t}{t_0} = \frac{\text{efflux time of solution}}{\text{efflux time of solvent}}$$

$$\eta_{specific} = \eta_{relative} - 1$$

$$\eta_{inherent} = \frac{\ln(\eta_{relative})}{c}$$

$$\eta_{reduced} = \frac{\eta_{specific}}{c}$$

Table 4.3: Viscosity Parameters of CH-PNI

Concentration (g/dL)	$\eta_{relative}$	$\eta_{specific}$	$\eta_{reduced}$	$\log(\frac{\eta_{specific}}{c})$
0.0500	1.0705	0.0705	1.41	0.1492
0.0250	1.0622	0.0622	2.49	0.3962
0.0125	1.0546	0.0546	4.37	0.6405
0.0050	1.0270	0.0270	5.40	0.7324
0.0025	1.0159	0.0159	6.36	0.8035

According to Huggins equation,

$$\log\frac{\eta_{specific}}{c} = \log[\eta] + k'\,[\eta]c$$

(Equn. 4.1)

Where, k': The Huggins constant for moderate concentrations

[η] : Intrinsic viscosity in dLg^{-1}

44

The intrinsic viscosity of the solution was determined by the intercept "log[η]" of the

linear fit plot of $\log\left(\frac{\eta_{specific}}{c}\right)$ vs. c (Figure 4.1).
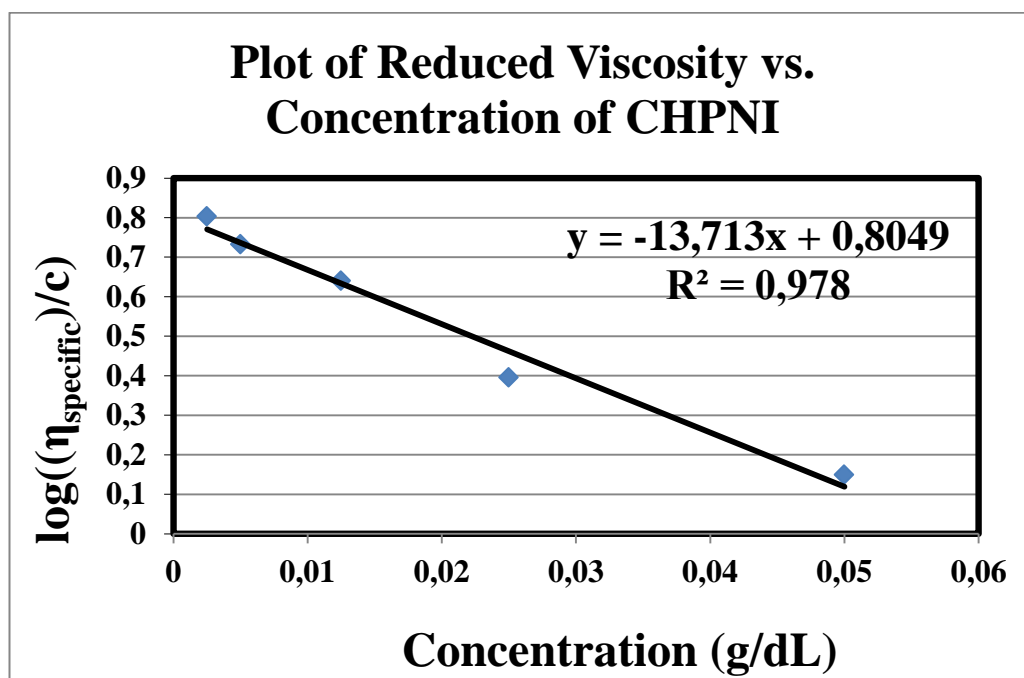
Figure 4.1: Plot of Reduced Viscosity vs. Concentration of CH-PNI

The equation of the plot found as "y = -13,713x + 0,8049" and the intercept of the

plot found from Figure 4.1 at zero concentration (x=0), is +0.8049.

$\log[\eta] = +0.8049$

$[\eta] = 10^{+0.8049} = 6.38 \; dLg^{-1}$

$[\eta] = 6.38 \; dLg^{-1}$

In the similar way, intrinsic viscosities of CH-PPI and chitosan were calculated at

26°C and their data was tabulated below (Table 4.4).

Table 4.4: Intrinsic Viscosities of the Synthesized Compounds

Compound	Solvent	$[\eta]$ (dLg^{-1})
CH-PNI	NMP	6.38
CH-PPI	DMAc	8.71
CH*	0.1 M NaCl/0.1 % TFAc	4.00

4.2 Calculations of Photophysical Parameters

The photophysical, which are UV-vis absorption, fluorescence emission and excitation, parameters of the synthesized perylene and naphthalene based polyimides were analysed by UV-vis and emission spectroscopies in both solution and solid state.

4.2.1 Maximum Extinction Coefficient (ε_{max})

According to the Lambert-Beer's Law;

At λ_{max}

$$\varepsilon_{max} = \frac{A}{cl}$$

(Equn. 4.2)

Where,

ε_{max}: Maximum extinction co-efficient in L. mol^{-1}. cm^{-1} at λ_{max}
A: Absorbance
c : concentration of solution
l : cell length

ε_{max} **Calculation of CH-PNI:**
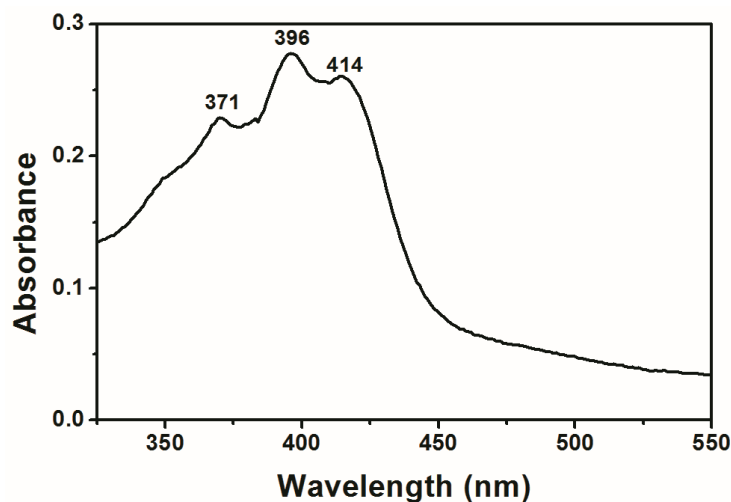
Figure 4.2: Absorption Spectrum of CH-PNI in Chloroform
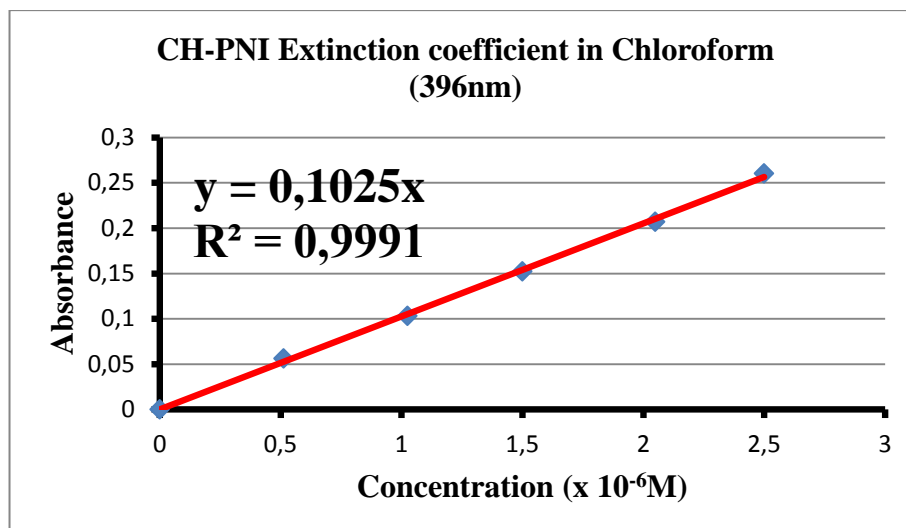
Figure 4.3: Plot of Maximum Absorbance vs. Concentration of CH-PNI at 396 nm.

The maximum extinction coefficient (ε_{max}) of CH-PNI was calculated by measuring maximum absorbance respecting to the maximum absorption wavelength at five different concentrations (c) in chloroform and plotting absorbance (at 396nm) vs. concentration and extrapolating to zero concentration. The linear fit plot of maximum absorbance vs. concentration (Figure 4.3) gives the equation of the plot as "y = 0,1025x" which provides the maximum absorbance of solution at 390nm as 0.1025 when the concentration of solution was 1 X 10^{-6} M.

By applying Lambert-Beer's Law;

$$\varepsilon_{max} = \frac{0.1025}{1.0 \times 10^{-6}\text{M} \times 1\text{ cm}} = 102500 \text{ L. mol}^{-1}. \text{ cm}^{-1}$$

E_{max} of CH-PNI=102500 L. mol^{-1}. cm^{-1}

ε_{max} Calculation of ENPI:

As can be seen from Figure 4.4, the molar extinction coefficients of ENPI were obtained by the slope of plots of the absorption bands at 344, 361 and 382 nm, respectively at five different concentrations.
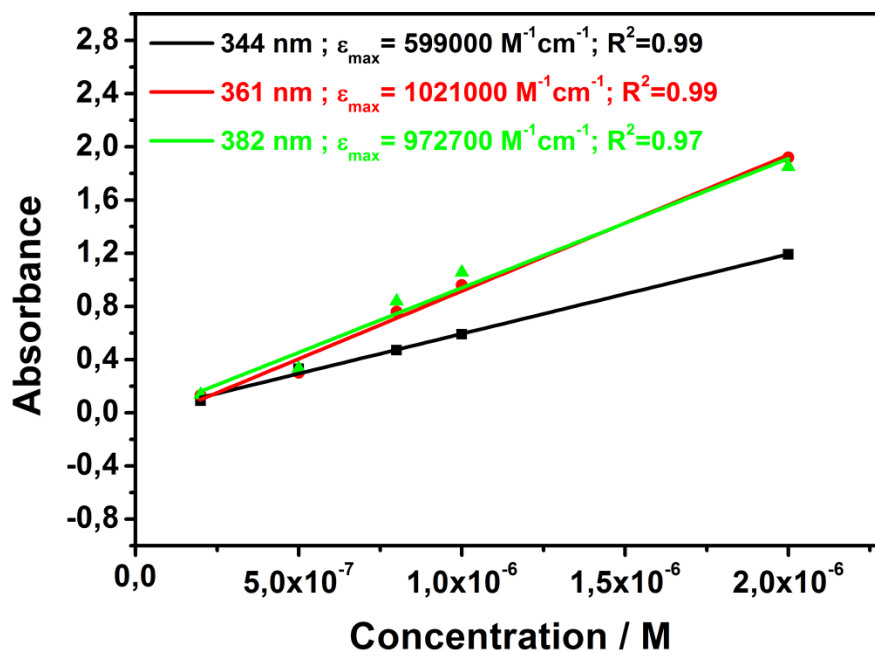
Figure 4.4 : Plot of Maximum Absorbance vs. Concentration of ENPI at 344, 361and 382 nm.

In the similar manner, the molar absorptivity of the CH-PNI, CH-PPI and ENPI (only in TCE) were calculated and tabulated in the Table 4.5 in different solvents from the plots of absorbance vs. concentration.

Table 4.5: Molar Absorptivity Data of Compounds in Different Solvents

Compound	Solvent	Concentration	Absorbance	λ_{max}	ε_{max}
CH-PNI	$CHCl_3$	1×10^{-6} M	0.1025	390 nm	102500 L. mol^{-1}. cm^{-1}
	THF	1×10^{-6} M	0.1049	394 nm	104900 L. mol^{-1}. cm^{-1}
	NMP	1×10^{-6} M	0.1683	390 nm	168300 L. mol^{-1}. cm^{-1}
	DMF	1×10^{-6} M	0.2480	392 nm	248000 L. mol^{-1}. cm^{-1}
	DMAc	1×10^{-6} M	0.1814	367 nm	181400 L. mol^{-1}. cm^{-1}
	DMSO	1×10^{-6} M	0.2231	391 nm	223100 L. mol^{-1}. cm^{-1}
	Ac. acid	1×10^{-6} M	0.2745	354 nm	274500 L. mol^{-1}. cm^{-1}
	NaOH	1×10^{-6} M	0.2235	401 nm	223500 L. mol^{-1}. cm^{-1}
CH-PPI	$CHCl_3$	1×10^{-5} M	1.0002	526 nm	100020 L. mol^{-1}. cm^{-1}
	Acetone	1×10^{-5} M	1.2830	517 nm	128300 L. mol^{-1}. cm^{-1}
	DMAc	1×10^{-5} M	0.3071	513 nm	30710 L. mol^{-1}. cm^{-1}
ENPI	TCE	1×10^{-6} M	0.1000	344 nm	599000 L. mol^{-1}. cm^{-1}
	TCE	1×10^{-6} M	0.1000	361 nm	1021000 L. mol^{-1}. cm^{-1}
	TCE	1×10^{-6} M	0.1000	382 nm	972700 L. mol^{-1}. cm^{-1}

4.2.2 Fluorescence Quantum Yields (Φ_f)

Fluorescence Quantum Yield of CH-PPI

The fluorescence quantum yield, Φ_f of CH-PPI is calculated by using below formula

$$\Phi_f(U) = \frac{A_{std}}{A_U} \; x \; \frac{S_U}{S_{std}} \; x \; \left[\frac{n_U}{n_{std}}\right]^2 x \; \Phi_{std}$$

(Equn. 4.3)

Where,

$\Phi_f(U)$:Fluorescence quantum yield of CH-PPI

Φ_{std} :Fluorescence quantum yield of standard (Dodecyl PDI)

A_{std} :Absorbance of the standart at the excitation wavelength

A_U :Absorbance of the CH-PPI at the excitation wavelength(λ_{exc}= 485nm)

S_{std} :The integrated emission area across the band of the standart

S_U :The integrated emission area across the band of CH-PPI

n_{std} :Refractive index of standart solvent

n_U :Refractive index of unknown solvent

Dodecyl PDI was taken as standart since it has similar absorption range of the CH-PPI and the excitation wavelength was 485 nm. The integrated emission area is given by emmission spectra at 485 nm extitation wavelength. Since solvents of Dodecyl PDI and N,N'-bis(chitosan)-3,4,9,10-perylenetetracarboxydiimide were different from each other it is necessary to use refractive indexes of solvents. There are two reason to use refractive index correction. First, as irradiation passes from the solution into air (i.e. from high to low index region), its intensity changes because of the refraction. Second, internal reflection within a cell can occur. In the literature, the fluorescence quantum yields of naphthalene based compounds are generally low, for comparison, the measurements of CH-PNI were carried out by using Anthracene as standard ($\Phi_f = 0.27$) by exciting at 360 nm in ethanol.

Emission of CH-PPI   **Emission of Dodecyl-PDI**
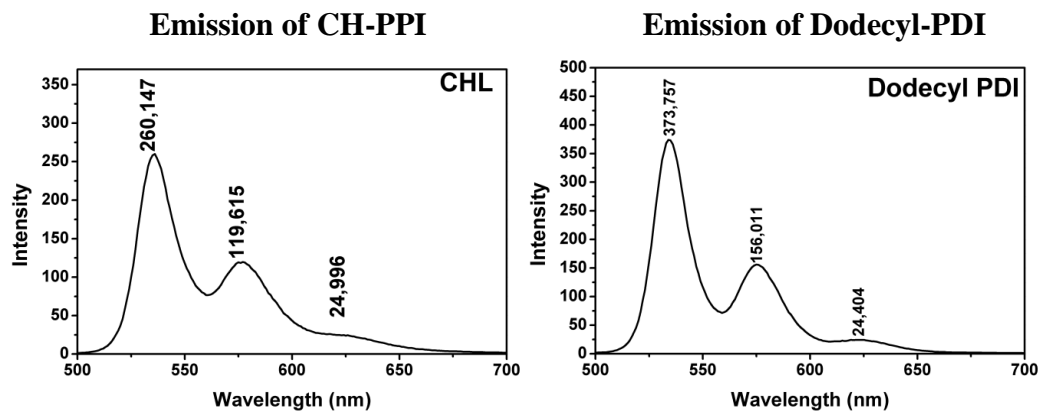
A_{std}= 0.1072, A_{CH-PPI}=0.1053, S_{std}= 13465, S_{CH-PPI}=11302, n_{std}= 1,4459,

n_{CHL}=1,4459, Φ_{std}= 1.00, $\Phi_{f}(CH$-$PPI)$;

From Equation 4.3;

$$\Phi_{f}(CH\text{-}PPI)=\frac{0.1072}{0.1053} \text{ x } \frac{11302}{13465} \text{ x } \left[\frac{1.4459}{1.4459}\right]^{2} \text{ x } 1 = 0.86$$

$\Phi_{f}(CH\text{-}PPI) = 0.86$

The fluorescence quantum yields of CH-PPI and CH-PNI in other solvents were measured by the same method described above and were tabulated in the Table 4.6.

Table 4.6: Fluorescence Quantum Yields of CH-PPI and CH-PNI in Different Solvents

Solvent	CH-PPI Φ_f	CH-PNI Φ_f
CHCl$_3$	0.86	0.011
Ethyl acetate	0.87	0.013
CH$_2$Cl$_2$	0.87	0.011
Acetone	0.88	0.010
THF	–	0.012
EtOH	0.59	0.005
MeOH	0.51	0.007
NMP	–	0.030
DMF	0.73	0.011
CH$_3$CN	0.89	0.012
DMAc	0.59	0.010
DMSO	0.38	0.009
Acetic acid	–	0.019
KOH	–	0.004
NaOH	–	0.005

4.2.3 Calculation of Optical Properties

4.2.3.1 Determination of Theoretical Radiative Lifetime (τ_0)

The theoretical radiative lifetimes of the new compounds were calculated by using following equation 4.4 (Turro, 1965);

$$\tau_0 = \frac{3.5 \times 10^8}{\bar{v}_{max}^2 \, \varepsilon_{max} \, \Delta\bar{v}_{1/2}}$$

(Equn. 4.4)

where;

τ_0 : Theoretical radiative lifetime (sec)

$\bar{v}_{max}$: Mean frequency for the absorption band (cm^{-1})

ε_{max} : Molar Extinction coefficient at the selected absorption wavelength (L. mol^{-1}. cm^{-1})

$\Delta\bar{v}_{1/2}$: Half-width of the selected absorption (cm^{-1}).

Half-width of the absorption ($\Delta\bar{v}_{1/2}$):
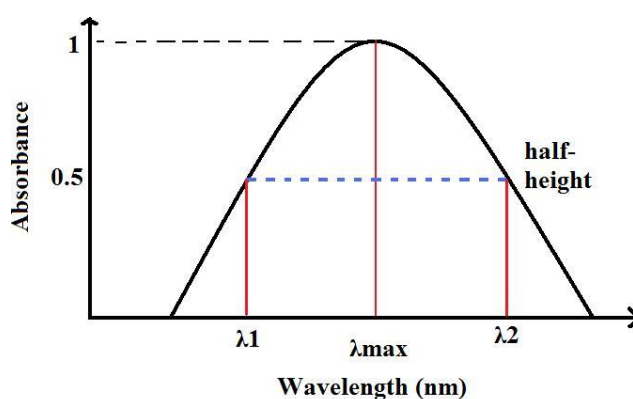
Figure 4.5: Half Bandwidth of the Absorption Spectrum

The half-widths of the molecules are necessary to determine the theoretical lifetime. The spectral half bandwidth of the absorption is defined as the width of the band of light at

53

the wavelength of maximum absorption (λ_{max}) at half maximum (Figure 4.5) and was determined by using equation 4.5 .

$$\Delta\bar{\nu}_{1/2} = \bar{\nu}_1 - \bar{\nu}_2$$

(Equn. 4.5)

Where,

$\bar{\nu}_1$, $\bar{\nu}_2$:   the frequencies from the absorption spectrum (cm^{-1})

$\Delta\bar{\nu}_{1/2}$:   the half width of the selected absorbtion (cm^{-1})

Generally, it is difficult to decide λ_1 and λ_2 for most of the perylene and naphthalene dyes. To find out half-width of the absorption of CH-PPI in chloroform, the λ_1 and λ_2 were determined by following the steps in Figure 4.6;

1.step: Decide the λ_{max} of the perylene

2.step: Make a intersection points. Draw a horizontal line where it pass from the half maximum of the λ_{max} and draw it up to intersects with the curve.

3.step: Decide the λ_1. Draw a vertical line from the intersection to the x-axis to decide the λ_1.

4. step: Decide the λ_2. Draw a vertical line from the intersection to the x-axis to decide the λ_2.
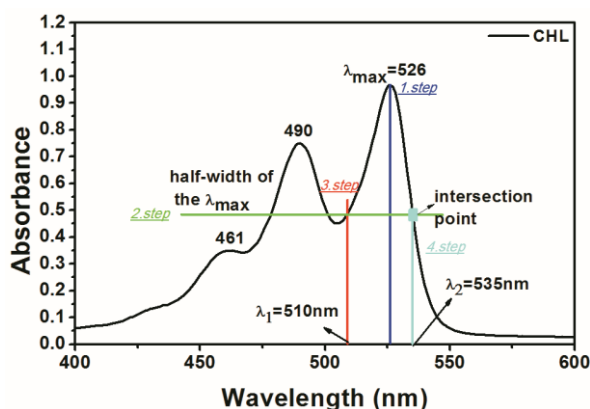
Figure 4.6: A Representative Figure to Calculate the Half-width of the CH-PPI in Chloroform

From the Figure 4.6,

λ$_{max}$ = 526 nm

$$\lambda_{max} = 526 \text{ nm} \times \frac{10^{-9} \text{m}}{1 \text{ nm}} \times \frac{100 \text{ cm}}{1 \text{ m}} = 5.26 \times 10^{-5} \text{ cm}$$

$$\bar{\nu}_{max} = \frac{1}{\lambda_{max}} = \frac{1}{5.26 \times 10^{-5} \text{ cm}} = 19011.40 \text{ cm}^{-1}$$

λ$_1$ = 509 nm

$$\lambda_1 = 509 \text{ nm} \times \frac{10^{-9} \text{m}}{1 \text{ nm}} \times \frac{100 \text{ cm}}{1 \text{ m}} = 5.09 \times 10^{-5} \text{ cm}$$

$$\bar{\nu}_1 = \frac{1}{\lambda_1} = \frac{1}{5.09 \times 10^{-5} \text{ cm}} = 19646.36 \text{ cm}^{-1}$$

λ$_2$ = 535 nm

$$\lambda_2 = 535 \text{ nm} \times \frac{10^{-9} \text{m}}{1 \text{ nm}} \times \frac{100 \text{ cm}}{1 \text{ m}} = 5.35 \times 10^{-5} \text{ cm}$$

$$\bar{\nu}_2 = \frac{1}{\lambda_2} = \frac{1}{5.35 \times 10^{-5} \text{ cm}} = 18691.59 \text{ cm}^{-1}$$

From Equation 4.5,

$$\Delta\bar{\nu}_{1/2} = \bar{\nu}_1 - \bar{\nu}_2$$

$$\Delta\bar{\nu}_{1/2} = 19646.36 - 18691.59$$

$$\Delta\bar{\nu}_{1/2} = 954.77 \text{ cm}^{-1}$$

Now, the theoretical radiative lifetime of CH-PPI can be calculated from Equation 4.4

$$\tau_0 = \frac{3.5 \times 10^8}{\bar{\nu}_{max}^2 \; \varepsilon_{max} \; \Delta\bar{\nu}_{1/2}}$$

$$\tau_0 = \frac{3.5 \times 10^8}{(19011.40)^2 \times 100020 \times 954.77}$$

$$\tau_0 = 10.18 \times 10^{-9} \text{ sec} \times \frac{1 \text{ ns}}{10^{-9} \text{ sec}} \cong 10.18 \text{ ns}$$

$$\tau_0 = 10.18 \; ns$$

In the similar manner, the theoretical radiative lifetimes of the CH-PPI and CH-PNI in different solvents were calculated and the data presented below in Table 4.7.

Table 4.7: Theoretical Radiative Lifetimes of CH-PPI and CH-PNI in Different Solvents

		CH-PPI			
Solvent	λ_{max} **(nm)**	ε_{max} **(L. mol^{-1}. cm^{-1})**	$\bar{\nu}^2_{max}$ **(cm^{-2})**	$\Delta\bar{\nu}_{1/2}$ **(cm^{-1})**	τ_0 **(ns)**
CHCl$_3$	526	100020	3.61×10^8	954.77	10.18
Acetone	517	128300	3.74×10^8	1100.68	6.63
DMAc	513	30710	3.80×10^8	1247.93	24.03
		CH-PNI			
Solvent	λ_{max} **(nm)**	ε_{max} **(L. mol^{-1}. cm^{-1})**	$\bar{\nu}^2_{max}$ **(cm^{-2})**	$\Delta\bar{\nu}_{1/2}$ **(cm^{-1})**	τ_0 **(ns)**
CHCl$_3$	414	102500	5.83×10^8	1566.58	3.74
THF	414	104900	5.83×10^8	1894.29	3.02
NMP	390	168300	6.57×10^8	4628.39	68.39
DMF	392	248000	6.51×10^8	3720.24	58.27
DMAc	391	181400	6.54×10^8	4370.53	67.50
DMSO	391	223100	6.54×10^8	4349.69	55.15
Ac. acid	393	274500	6.47×10^8	2785.85	70.74
NaOH	401	223500	6.22×10^8	5284.00	47.65

4.2.3.2 Determination of Theoretical Fluorescence Lifetime (τ_f)

Fluorescence lifetime was calculated using the formula shown below;

$$\tau_f = \tau_0 \cdot \phi_f$$

<div align="right">(Equn. 4.6)</div>

Where

τ_f : Fluorescence lifetime

τ_0 : Theoretical radiative lifetime (ns)

ϕ_f : Fluorescence quantum yield

Theoretical Fluorescence Lifetime of CH-PPI:

$\tau_f = \tau_0 \times \phi_f$

The theoretical fluorescence lifetime of CH-PPI in chloroform was calculated from the data calculated above by using Equations 4.3 and 4.4

$\tau_f = 10.18$ ns $\times 0.86$

$\tau_f = 8.75$ ns

Table 4.8: Theoretical Fluorescence Lifetimes Data of CH-PPI and CH-PNI

Solvent	**CH-PPI**		
	Φ_f	τ_0 (ns)	τ_f (ns)
$CHCl_3$	0.86	10.18	8.75
Acetone	0.88	6.63	5.83
DMAc	0.59	24.03	14.18
Solvent	**CH-PNI**		
	Φ_f	τ_0 (ns)	τ_f (ns)
$CHCl_3$	0.011	3.74	0.041
NMP	0.012	3.02	0.036
DMF	0.030	68.39	2.05
DMAc	0.011	58.27	0.64
DMSO	0.010	67.50	0.68
Ac. acid	0.009	55.15	0.50
NaOH	0.019	70.74	1.34
$CHCl_3$	0.005	47.65	0.24

4.2.3.3 Determination of Fluorescence Rate Constants (k_f)

The fluorescence rate constant can be calculated by using Turro's equation given below,

$$k_f = \frac{1}{\tau_0}$$

<div align="right">(Equn. 4.7)</div>

Where; k_f : Theoretical Fluorescence Rate Constant (sec^{-1})

τ_0 : Theoretical radiative lifetime (sec)

Fluorescence Rate Constants (k_f) of CH-PPI:

$$k_f = \frac{1}{\tau_0}$$

$$k_f = \frac{1}{10.18 \times 10^{-9} sec}$$

$$k_f = 0.98 \times 10^8 \, s^{-1}$$

In the following table with similar manner, fluorescence rate constants were determined for the products in different solvents and the values were demostrated in Table 4.9.

Table 4.9: Fluorescence Rate constants Data of CH-PPI and CH-PNI

Solvent	CH-PPI	
	τ_0 (ns)	k_f (s^{-1})
CHCl$_3$	10.18	0.98 x 10^8
Acetone	6.63	1.51 x 10^8
DMAc	24.03	0.42 x 10^8
Solvent	**CH-PNI**	
	τ_0 (ns)	k_f (s^{-1})
CHCl$_3$	3.74	2.67 x 10^8
NMP	3.02	3.31 x 10^8
DMF	68.39	0.15 x 10^8
DMAc	58.27	0.17 x 10^8
DMSO	67.50	0.15 x 10^8
Ac. acid	55.15	0.18 x 10^8
NaOH	70.74	0.14 x 10^8
CHCl$_3$	47.65	0.21 x 10^8

4.2.3.4 Determination of Rate Constants of Radiationless Deactivation (k_d)

The rate constants of radiationless deactivation of the compounds were calculated using equation shown below,

$$k_d = \left(\frac{k_f}{\phi_f}\right) - k_f$$

(Equn. 4.8)

Where,

k_d : Rate constant of radiationless deactivation (sec^{-1})

k_f : Theoretical Fluorescence Rate Constant (sec^{-1})

ϕ_f : Fluorescence quantum yield

Rate Constants of Radiationless Deactivation (k_d) ofCH-PPI:

$$k_d = \left(\frac{k_f}{\phi_f}\right) - k_f$$

$$k_d = \left(\frac{0.98 \times 10^8}{0.86}\right) - 0.98 \times 10^8$$

$$k_d = 0.16 \times 10^8 \, s^{-1}$$

According to the Equation 4.8, the rate constants of radiationless deactivation of CH-PPI and CH-PNI were calculated in different solvents and given in the following table.

Table 4.10: Rate Constants of Radiationless Deactivation Data of CH-PPI and CH-PNI

	CH-PPI		
Solvent	Φ_f	k_f (s^{-1})	k_d (s^{-1})
CHCl$_3$	0.86	0.98 x 10^8	0.16 x 10^8
Acetone	0.88	1.51 x 10^8	0.21 x 10^8
DMAc	0.59	0.42 x 10^8	0.29 x 10^8
	CH-PNI		
Solvent	Φ_f	k_f (s^{-1})	k_d (s^{-1})
CHCl$_3$	0.011	2.67 x 10^8	240.1 x 10^8
NMP	0.012	3.31 x 10^8	272.5 x 10^8
DMF	0.030	0.15 x 10^8	4.85 x 10^8
DMAc	0.011	0.17 x 10^8	15.28 x 10^8
DMSO	0.010	0.15 x 10^8	14.85 x 10^8
Ac. acid	0.009	0.18 x 10^8	20.00 x 10^8
NaOH	0.019	0.14 x 10^8	7.23 x 10^8
CHCl$_3$	0.005	0.21 x 10^8	41.79 x 10^8

4.2.3.5 Determination of Singlet Energies (E$_s$)

The equation 4.9 below is used to calculate singlet energies, E$_s$ (kcal.mol^{-1}), of the compounds

$$E_s = \frac{2.86 \times 10^5}{\lambda_{max}}$$

(Equn. 4.9)

where

E$_s$: Singlet Energy (kcal.mol^{-1})

λ_{max} : Maximum absorption wavelength (Å)

Singlet Energy of CH-PPI

$\lambda_{max} = 526 \text{ nm} \times \dfrac{10^{-9}\text{m}}{1 \text{ nm}} \times \dfrac{1 \text{ Å}}{10^{-10}\text{m}} = 5260 \text{ Å}$

$E_s = \dfrac{2.86 \times 10^5}{\lambda_{max}}$

$E_s = \dfrac{2.86 \times 10^5}{5260}$

$E_s = 54.4 \text{ kcal. mol}^{-1}$

The singlet energies of CH-PPI and CH-PNI were determined in the similar way and the datas were tabulated in the following Table 4.11.

Table 4.11: Singlet Energies Data of CH-PPI and CH-PNI

	CH-PPI	
Solvent	λ_{max} (Å)	E_s(kcal mol^{-1})
CHCl$_3$	5260	54.4
Acetone	5170	55.3
DMAc	5130	55.8
	CH-PNI	
Solvent	λ_{max} (Å)	E_s(kcal mol^{-1})
CHCl$_3$	4140	69.1
NMP	4140	69.1
DMF	3900	73.3
DMAc	3920	73.0
DMSO	3910	73.1
Ac. acid	3910	73.1
NaOH	3930	72.8
CHCl$_3$	4010	71.3

4.2.3.6 Determination of Oscillator Strengths (f)

The oscillator strengths of the compounds were calculated using the equation shown

below

$$\mathbf{f} = \mathbf{4.32} \times \mathbf{10^{-9}} \times \Delta\bar{\mathbf{v}}_{1/2} \times \mathbf{\varepsilon_{max}}$$

(Equn. 4.10)

Where,

f :	Oscillator Strength
$\Delta\bar{v}_{1/2}$:	Half-width of the selected absorption (cm^{-1})
ε_{max} :	The maximum extinction coefficient at the maximum absorption wavelength (L. mol^{-1}. cm^{-1})

Oscillator Strength of CH-PPI

$\mathbf{f} = \mathbf{4.32} \times \mathbf{10^{-9}} \times \Delta\bar{\mathbf{v}}_{1/2} \times \mathbf{\varepsilon_{max}}$

$f = 4.32 \times 10^{-9} \times 954.77 \times 100020$

$\mathbf{f} = \mathbf{0.41}$

The oscillator strengths were calculated in the similar manner for CH-PPI and CH-

PNI and the data was given in the Table 4.12.

Table 4.12: Oscillator Strengths Data of CH-PPI and CH-PNI

	CH-PPI		
Solvent	$\Delta\bar{v}_{1/2}$ (cm^{-1})	ε_{max} (L. mol^{-1}. cm^{-1})	f
CHCl$_3$	954.77	100020	0.41
Acetone	1100.68	128300	0.61
DMAc	1247.93	30710	0.17
	CH-PNI		
Solvent	$\Delta\bar{v}_{1/2}$ (cm^{-1})	ε_{max} (L. mol^{-1}. cm^{-1})	f
CHCl$_3$	1566.58	102500	0.69
THF	1894.29	104900	0.86
NMP	4628.39	168300	3.37
DMF	3720.24	248000	3.99
DMAc	4370.53	181400	3.43
DMSO	4349.69	223100	4.19
Ac. acid	2785.85	274500	3.30
NaOH	5284.00	223500	5.10

4.2.3.7 Optical Properties

Table 4.13: Maximum Absorption Wavelength λ_{max} (nm), Extinction Coefficients ε_{max} (L mol^{-1} cm^{-1}), Oscillator strength f, Fluorescence Quantum Yields ϕ_f (λ_{exc} = 485 nm and 360nm), Radiative Lifetimes τ_0 (ns), Fluorescence Lifetimes τ_f (ns), Fluorescence Rate Constants k_f, Rate Constant of Radiationless Deactivation k_d and Singlet Energy E_s (kcal mol^{-1}) Data of CH-PPI, CH-PNI and ENPI.

	λ_{max}	ε_{max}	f	ϕ_f	τ_0	τ_f	k_f	k_d	E_s	E_g
CH-PPI										
CHCl$_3$	526	100020	0.41	0.86	10.18	8.75	0.98 x 10^8	0.16 x 10^8	54.4	2.28
Acetone	517	128300	0.61	0.88	6.63	5.83	1.51 x 10^8	0.21 x 10^8	55.3	2.32
DMAc	513	30710	0.17	0.59	24.03	14.18	0.42 x 10^8	0.29 x 10^8	55.8	2.28
CH-PNI										
CHCl$_3$	414	102500	0.69	0.011	3.74	0.041	2.67 x 10^8	240.1 x 10^8	69.1	2.72
THF	414	104900	0.86	0.012	3.02	0.036	3.31 x 10^8	272.5 x 10^8	69.1	2.67
NMP	390	168300	3.37	0.030	68.39	2.05	0.15 x 10^8	4.85 x 10^8	73.3	2.45
DMF	392	248000	3.99	0.011	58.27	0.64	0.17 x 10^8	15.28 x 10^8	73.0	2.58
DMAc	391	181400	3.43	0.010	67.50	0.68	0.15 x 10^8	14.85 x 10^8	73.1	2.53
DMSO	391	223100	4.19	0.009	55.15	0.50	0.18 x 10^8	20.00 x 10^8	73.1	2.51
Ac. acid	393	274500	3.30	0.019	70.74	1.34	0.14 x 10^8	7.23 x 10^8	72.8	2.73
NaOH	401	223500	5.10	0.005	47.65	0.24	0.21 x 10^8	41.79 x 10^8	71.3	2.87
ENPI										
TCE	382	972660	5.22	0.020	0.52	0.008	2.38 x 10^9	1.16 x 10^{11}	74.9	

4.3 Determination of Electrochemical Properties

The electrochemical parameters of compounds were characterized in detail using cyclic and square-wave voltammetries in both solution and solid state by determining redox potentials, band gap energies (E_g), HOMO (highest occupied molecular orbital) and LUMO (lowest unoccupied molecular orbital).

4.3.1 Redox Potentials ($E_{1/2}$)

The redox potentials of the compounds can be determined by using the Equation 4.11 from cyclic voltammogram according to internal reference.

$$E_{1/2} = \frac{E_{pc} + E_{pa}}{2}$$

(Equn. 4.11)

where,

$E_{1/2}$: half-wave potential (V)

E_{pc} : cathodic peak potential (V)

E_{pa} : anodic peak potential (V)

From the cathodic and anodic peak potentials, the peak potential separation, ΔE_p, can be estimated for the reversible couples by applying the following Equation 4.12 where n is the number of electrons

$$\Delta E_p = E_{pa} - E_{pc} = \frac{0.059}{n} \text{ V}$$

(Equn. 4.12)

The oxidation potential of Ferrocene (Fc) as internal reference was estimated as 0.270 V and redox potentials of the compounds can be expressed with Equation 4.13 relative to the Fc potential;

$$E_{red,1/2} \text{ vs.Fc} = \left(E_{red,\frac{1}{2}} \text{ vs. Ag/AgCl} \right) - (E_{ox} \text{ vs. Ag/AgCl})$$

(Equn. 4.13)

4.3.2 Determination of LUMO Energy Levels

According to the Bredas and co-workers, LUMO energy levels of the compounds were expressed by using following equation with respect to the vacuum level.

$$E_{LUMO} = - (4.8 + E_{1/2})$$

(Equn. 4.14)

where;

E_{LUMO} **:** Energy of LUMO level (eV)

$E_{1/2}$: half-wave potential ($E_{1/2}$ **vs. Fc**) (V)

4.3.3 Determination of Band Gap Energies (E_g)

The optical band gap energies (E_g) of compounds was calculated from their UV-visible spectra using the following equation (Equn 4.15).

$$E_g = \frac{1240 \text{ eV nm}}{\lambda}$$

(Equn. 4.15)

where;

E_g **:** Band gap energy (eV)

λ **:** Cut-off wavelength of the absorption band (nm) where it is found by extrapolating maximum absorption band to zero absorbance.

4.3.4 Determinaton of HOMO Energy Levels

The HOMO energy values of compounds were expressed by the equation shown below;

$$E_{HOMO} = E_{LUMO} - E_g$$

(Equn. 4.16)

where;

E_{HOMO} **:** Energy of HOMO level (eV)

E_{LUMO} **:** Energy of LUMO level (eV)

E_g **:** Optical Band Gap energy (eV)

All the electrochemical properties of all the compounds were found by using the above equations from 4.11 to 4.16 and tabulated in the tables from 4.14 to 4.23.

Table 4.14: Cylic Voltammetry[a] Data and Band Gap Energy E_g, HOMO, LUMO Values of CH-PPI at Different Scan Rates

	E_{pc}/V	E_{pa}/V	ΔE_p/mV	$E_{1/2}$ vs. (Ag/AgCl)/V	E_{Fc} vs. (Ag/AgCl)/V	$E_{1/2}$ vs. Fc/V	LUMO/eV	E_g^{b}/eV	HOMO/eV
100mV	-0.29	-0.37	80	-0.33	0.57	-0.90	-3.90	2.28	-6.18
	-0.54	-0.62	80	-0.58	0.57	-1.15	-3.65	2.28	-5.93
	-0.75	-0.83	80	-0.79	0.57	-1.36	-3.44	2.28	-5.72
	-1.27	-1.36	90	-1.32	0.57	-1.89	-2.91	2.28	-5.19
200mV	-0.31	-0.38	70	-0.35	0.57	-0.92	-3.88	2.28	-6.16
	-0.51	-0.64	130	-0.58	0.57	-1.15	-3.65	2.28	-5.93
	-0.76	-0.84	80	-0.80	0.57	-1.37	-3.43	2.28	-5.71
	-1.25	-1.39	140	-1.32	0.57	-1.89	-2.91	2.28	-5.79
500mV	-0.49	-0.70	210	-0.60	0.57	-1.17	-3.63	2.28	-5.91
	-0.76	-0.87	110	-0.82	0.57	-1.39	-3.41	2.28	-5.69
	-1.24	-1.43	190	-1.34	0.57	-1.91	-2.89	2.28	-5.17

[a] Supporting electrolyte: 0.1 M sodium tetrafluoroborate ($NaBF_4$)

[b] In DMAc

Table 4.15: Cylic Voltammetry[a] Data of CH-PPI at Different Scan Rates

Scan Rate (mVs^{-1})	E_{pc}^{red} (V)	E_{pa}^{red} (V)	ΔE_{p}^{red} (mV)	i_{pa}^{red} (µA)	i_{pc}^{red} (µA)	$i_{pa}^{red} / i_{pc}^{red}$
100	-0.29	-0.37	80	0.81	0.78	1.04
	-0.54	-0.62	80	1.08	1.20	0.90
	-0.75	-0.83	80	2.80	1.24	2.26
	-1.27	-1.36	90	4.50	2.42	1.86
200	-0.31	-0.38	70	2.10	2.18	0.96
	-0.51	-0.64	130	2.67	2.68	1.00
	-0.76	-0.84	80	4.68	4.42	1.01
	-1.25	-1.39	140	6.17	3.78	1.63
500	-0.49	-0.70	210	2.93	2.75	1.07
	-0.76	-0.87	110	3.77	3.62	1.04
	-1.24	-1.43	190	7.07	4.10	1.72

[a] Supporting electrolyte: HCl

Table 4.16: Solid State Cylic Voltammetry[a] Data of CH-PPI at Different Scan Rates

Scan Rate (mVs^{-1})	E_{pc}^{ox} (V)	E_{pa}^{ox} (V)	ΔE_p^{ox} (mV)	i_{pa}^{ox} (µA)	i_{pc}^{ox} (µA)	i_{pa}^{ox}/i_{pc}^{ox}	E_{pc}^{red} (V)	E_{pa}^{red} (V)	ΔE_p^{red} (mV)	i_{pa}^{red} (µA)	i_{pc}^{red} (µA)	$i_{pa}^{red}/i_{pc}^{red}$
50	0.352	0.625	273	2.78	3.23	0.86	-0.349	-0.226	123	0.65	0.65	1.00
100	0.319	0.650	331	4.13	4.78	0.86	-0.348	-0.247	101	0.72	0.72	1.00
200	0.289	0.687	398	7.27	8.82	0.82	-0.353	-0.247	106	0.89	0.76	1.17
300	0.265	0.711	446	10.82	11.97	0.90	-0.351	-0.267	84	0.96	0.86	1.12
400	0.239	0.737	498	12.74	14.30	0.89	-0.365	-0.291	74	1.34	1.00	1.34
500	0.224	0.760	536	14.14	16.48	0.86	-0.365	-0.321	44	1.44	1.36	1.06
750	0.190	0.808	618	19.26	22.42	0.86	-0.379	-0.340	39	2.32	1.98	1.17
1000	0.159	0.839	680	24.39	25.39	0.96	-0.384	-0.348	36	3.53	3.12	1.13

[a] Supporting electrolyte: HCl

Table 4.17: Solid State Cyclic[a] Voltammetry Data and Band Gap Energy E_g, HOMO, LUMO Values of CH-PPI

	ΔE_p^{ox} (mV)	ΔE_p^{red} (mV)	$E_{1/2}^{ox}$ vs. Ag/AgCl (V)	$E_{1/2}^{red}$ vs. Ag/AgCl (V)	E_{Fc} vs. Ag/AgCl (V)	$E_{1/2}^{ox}$ vs. Fc (V)	$E_{1/2}^{red}$ vs. Fc (V)	$E_g^{opt\,b}$ (eV)	$E_g^{CV\,c}$ (eV)	HOMO[d] (eV)	LUMO[e] (eV)
CH	483	—	0.488	—	0.270	0.218	—	—	—	−5.12	—
CH-PPI	331	101	0.485	−0.298	0.270	0.215	−0.568	1.91 (2.28)[f]	0.783	−5.02 (−6.14)[g]	−4.23

[a] Supporting electrolyte: HCl and scan rate of 100 mVs^{-1}

[b] $E_g^{opt} = 1240/\lambda$ in solid state UV

[c] $E_g^{CV} = E_{1/2}^{ox} - E_{1/2}^{red}$

[d] HOMO $= -(4.8 + E_{1/2}^{ox})$ eV

[e] LUMO $= -(4.8 + E_{1/2}^{red})$ eV

f $E_g^{opt} = 1240/\lambda$ in chloroform

[g] HOMO $=$ LUMO $- E_g^{opt}$

$$E_{1/2}^{ox} = 0.215V \text{ vs. Fc}$$
$$E_{1/2}^{red} = -0.568 \text{ V} vs. \text{ Fc}$$

Table 4.18: Cyclic Coltammetry[a] Data and Band Gap Energy E_g, HOMO, LUMO Values of CH-PNI at Different Scan Rates

	E_{pc}/V	E_{pa}/V	ΔE_p/mV	$E_{1/2}$ vs. (Ag/AgCl)/V	E_{Fc} vs. (Ag/AgCl)/V	$E_{1/2}$ vs. Fc/V	LUMO/eV	$E_g{}^b$/eV	HOMO/eV
50mV	-0.43	-0.70	270	-0.57	0.57	-1.14	-3.66	2.45	-6.11
100mV	-0.45	-0.71	260	-0.58	0.57	-1.15	-3.65	2.45	-6.10
200mV	-0.44	-0.72	280	-0.58	0.57	-1.15	-3.65	2.45	-6.10
300mV	-0.45	-0.72	270	-0.59	0.57	-1.16	-3.64	2.45	-6.09
500mV	-0.45	-0.73	280	-0.59	0.57	-1.16	-3.64	2.45	-6.09
750mV	-0.45	-0.75	300	-0.60	0.57	-1.17	-3.63	2.45	-6.08
1000mV	-0.49	-0.74	250	-0.62	0.57	-1.14	-3.66	2.45	-6.11

[a] Supporting electrolyte: 0.1 M sodium tetrafluoroborate (NaBF$_4$)

[b] In NMP

Table 4.19: Cylic Voltammetry[a] Data of CH-PNI at Different Scan Rates

Scan Rate (mVs^{-1})	E_{pc}^{red} (V)	E_{pa}^{red} (V)	ΔE_p^{red} (mV)	i_{pa}^{red} (μA)	i_{pc}^{red} (μA)	$i_{pa}^{red} / i_{pc}^{red}$
50	-0.43	-0.70	270	0.82	0.78	1.05
100	-0.45	-0.71	260	1.19	1.08	1.10
200	-0.44	-0.72	280	1.76	1.76	1.00
300	-0.45	-0.72	270	2.12	2.25	0.94
500	-0.45	-0.73	280	4.07	3.96	1.03
750	-0.45	-0.75	300	4.21	4.29	0.98
1000	-0.49	-0.74	250	9.52	8.89	1.07

[a] Supporting electrolyte: HCl

Table 4.20: Solid State Cyclic[a] Voltammetry Data and Band Gap Energy E_g, HOMO, LUMO Values of CH and CH-PNI

	ΔE_p^{ox} (mV)	ΔE_p^{red} (mV)	$E_{1/2}^{ox}$ vs. Ag/AgCl (V)	$E_{1/2}^{red}$ vs. Ag/AgCl (V)	E_{Fc} vs. Ag/AgCl (V)	$E_{1/2}^{ox}$ vs. Fc (V)	$E_{1/2}^{red}$ vs. Fc (V)	$E_g^{opt\,b}$ (eV)	$E_g^{CV\,c}$ (eV)	HOMO^d (eV)	LUMO^e (eV)
CH	483	—	0.488	—	0.270	0.218	—	—	—	−5.12	—
CH-PNI	249	100	0.485	−0.260	0.270	0.215	−0.530	1.97 $(2.72)^f$	0.745	−5.02 $(−6.24)^g$	−4.27

[a] Supporting electrolyte: HCl and scan rate of 100 mVs^{-1}

[b] $E_g^{opt} = 1240/\lambda$ in solid state UV

[c] $E_g^{CV} = E_{1/2}^{ox} - E_{1/2}^{red}$

[d] HOMO $= -(4.8 + E_{1/2}^{ox})$ eV

[e] LUMO $= -(4.8 + E_{1/2}^{red})$ eV

f $E_g^{opt} = 1240/\lambda$ in chloroform

g HOMO $=$ LUMO $- E_g^{opt}$

$$E_{1/2}^{ox} = 0.215V \text{ vs. Fc}$$
$$E_{1/2}^{red} = -0.530V vs. \text{ Fc}$$

Table 4.21: Solid State Cylic Voltammetry[a] Data of CH-PNI at Different Scan Rates

Scan Rate (mVs^{-1})	E_{pc}^{ox} (V)	E_{pa}^{ox} (V)	ΔE_p^{ox} (mV)	i_{pa}^{ox} (µA)	i_{pc}^{ox} (µA)	i_{pa}^{ox}/i_{pc}^{ox}	E_{pc}^{red} (V)	E_{pa}^{red} (V)	ΔE_p^{red} (mV)	i_{pa}^{red} (µA)	i_{pc}^{red} (µA)	$i_{pa}^{red}/i_{pc}^{red}$
50	0.596	0.410	186	2.04	1.82	1.12						
100	0.609	0.360	249	2.68	2.47	1.09	-0.210	-0.310	100	0.61	0.41	1.49
200	0.649	0.340	309	4.35	3.95	1.10	-0.220	-0.310	90	0.89	0.76	1.17
300	0.689	0.320	369	5.64	4.99	1.13						
400	0.689	0.300	389	6.58	5.82	1.13						
500	0.719	0.280	439	7.21	6.11	1.18	-0.230	-0.320	90	1.15	1.22	0.94
750	0.739	0.250	489	9.11	7.11	1.28						
1000	0.789	0.210	579	15.44	13.23	1.17	-0.240	-0.290	50	2.60	3.43	0.76

[a] Supporting electrolyte: HCl

Table 4.22: Cylic Voltammetry Data and Band Gap Energy E_g, HOMO, LUMO Values of ENPI in Chloroform and Solid state

In chloroform	E_{pc}/V	E_{pa}/V	ΔE_p/mV	$E_{1/2}$ *vs.* (Ag/AgCl)/V	E_{Fc} *vs.* (Ag/AgCl)/V	$E_{1/2}$ *vs.* Fc/V	LUMO/eV	E_g/eV	HOMO/eV
20mV	−0.966	−0.907	59	−0.94	0.47	−1.41	−3.39	3.18	−6.57
	−0.760	−0.832	72	−0.79	0.47	−1.26	–	–	–
	−0.645	−0.474	171	−0.56	0.47	−1.03	–	–	–
100mV	−1.018	−0.862	156	−0.60	0.47	−1.07	−3.73	3.18	−6.91
	−0.742	−0.459	283	−0.94	0.47	−1.41	–	–	–
In Solid State	E_{pc}/V	E_{pa}/V	ΔE_p/mV	$E_{1/2}$ *vs.* (Ag/AgCl)/V	E_{Fc} *vs.* (Ag/AgCl)/V	$E_{1/2}$ *vs.* Fc/V	LUMO/eV	E_g/eV	HOMO/eV
20mV	−0.315	−0.289	26	−0.30	0.30	−0.60	−4.20	–	–
	−0.239	−0.165	74	−0.20	0.30	−0.50	–	–	–
100mV	−0.320	−0.280	40	−0.30	0.30	−0.60	−4.20	–	–

Table 4.23: Solid state Cylic Voltammetry Data of ENPI at Different Scan Rates

Scan Rate (mVs^{-1})	$E_{pc}{}^{red}$ (V)	$E_{pa}{}^{red}$ (V)	$\Delta E_p{}^{red}$ (mV)	$i_{pa}{}^{red}$ (μA)	$i_{pc}{}^{red}$ (μA)	$i_{pa}{}^{red} / i_{pc}{}^{red}$
100	-0.32	-0.28	40	0.18	0.27	0.67
200	-0.33	-0.29	40	0.24	0.35	0.69
300	-0.32	-0.29	30	0.37	0.44	0.84
500	-0.32	-0.29	30	0.62	0.62	1.00
700	-0.32	-0.28	40	0.81	0.82	0.99
800	-0.32	-0.29	30	0.91	0.91	1.00
1000	-0.32	-0.29	30	1.15	1.07	1.07
1500	-0.33	-0.29	40	1.74	1.59	1.09
2000	-0.33	-0.28	50	2.29	2.11	1.09
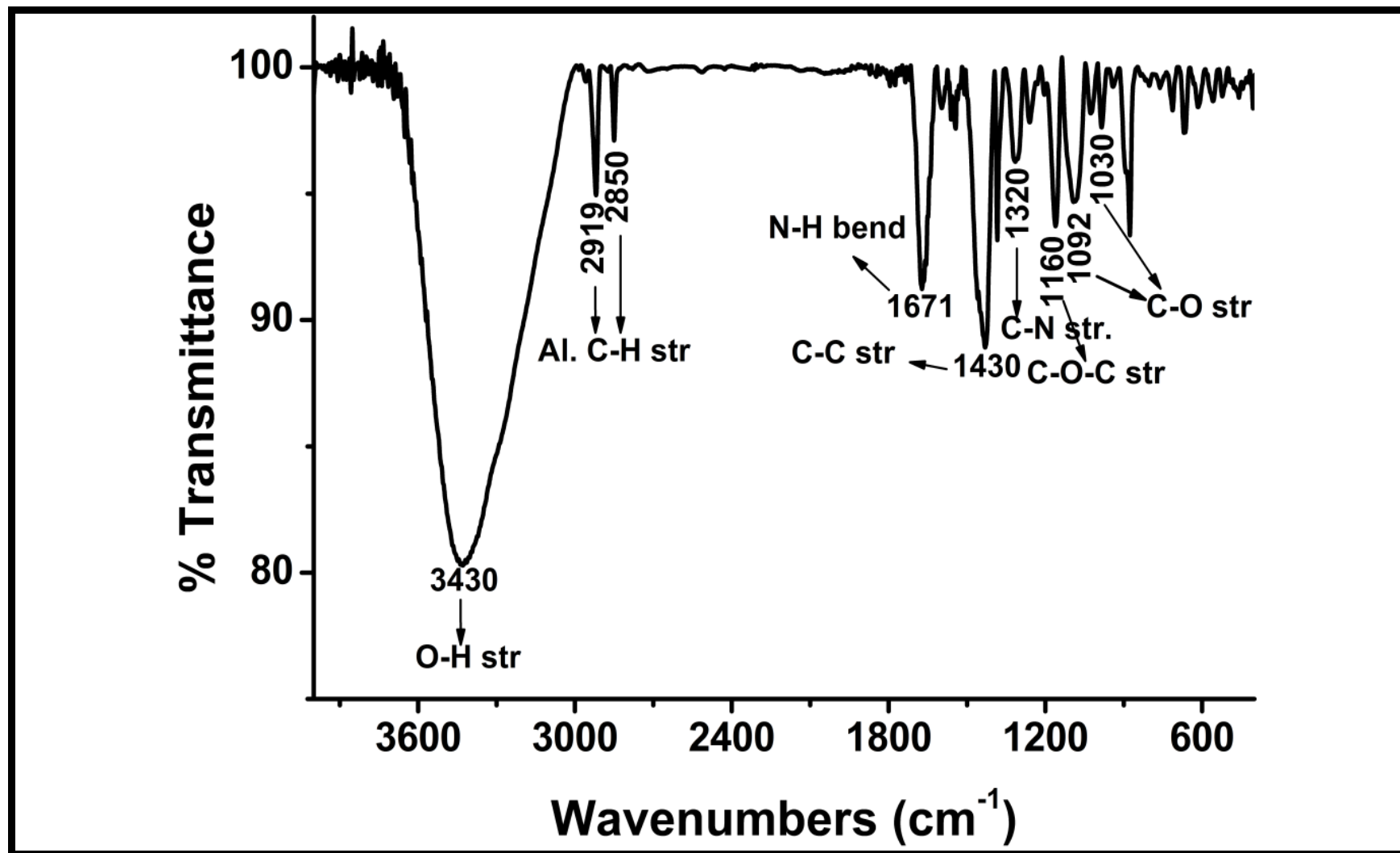
Figure 4.7: FTIR Spectrum of CH at solid state (KBr)
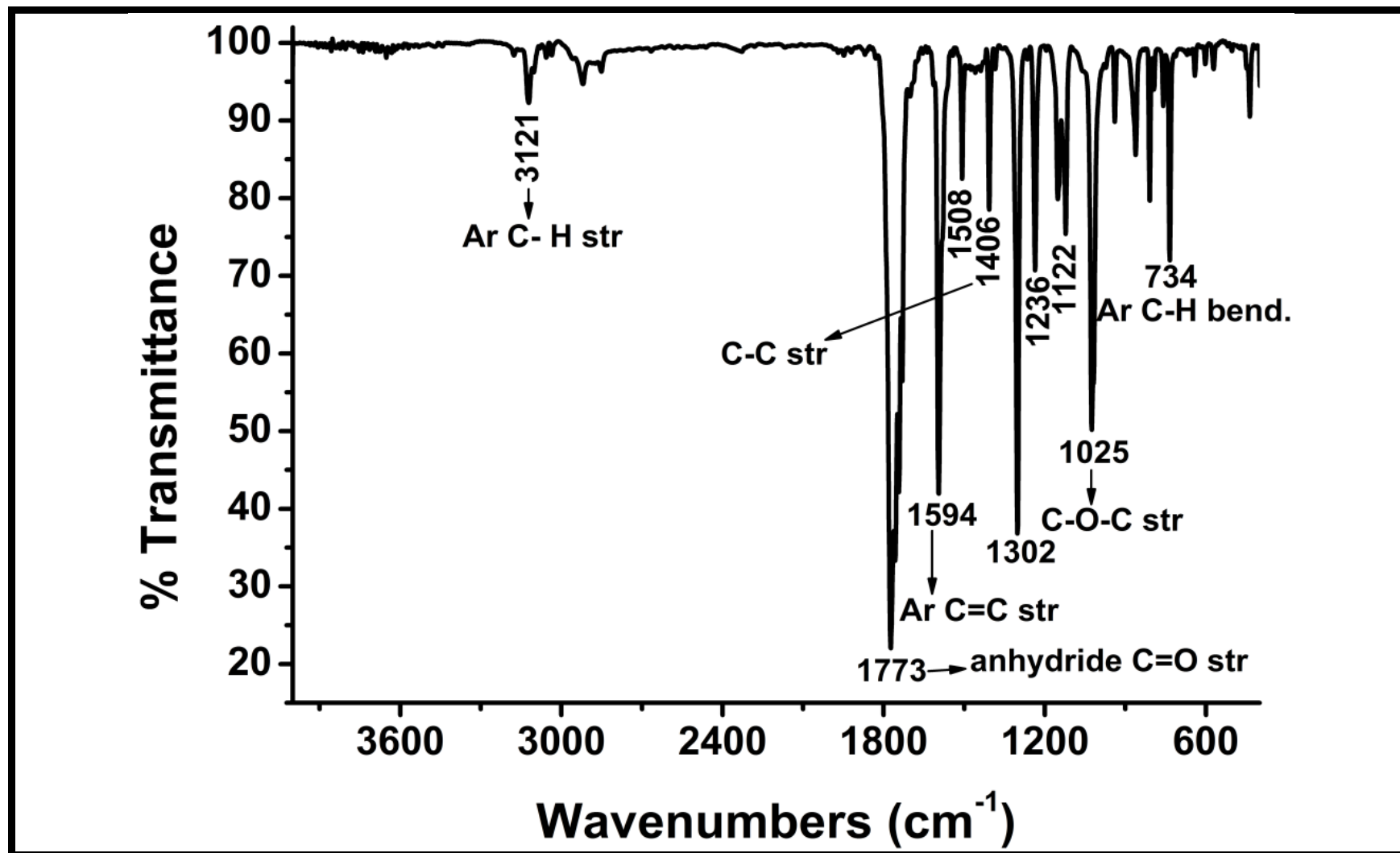
Figure 4.8: FTIR Spectrum of PDA at Solid State (KBr)
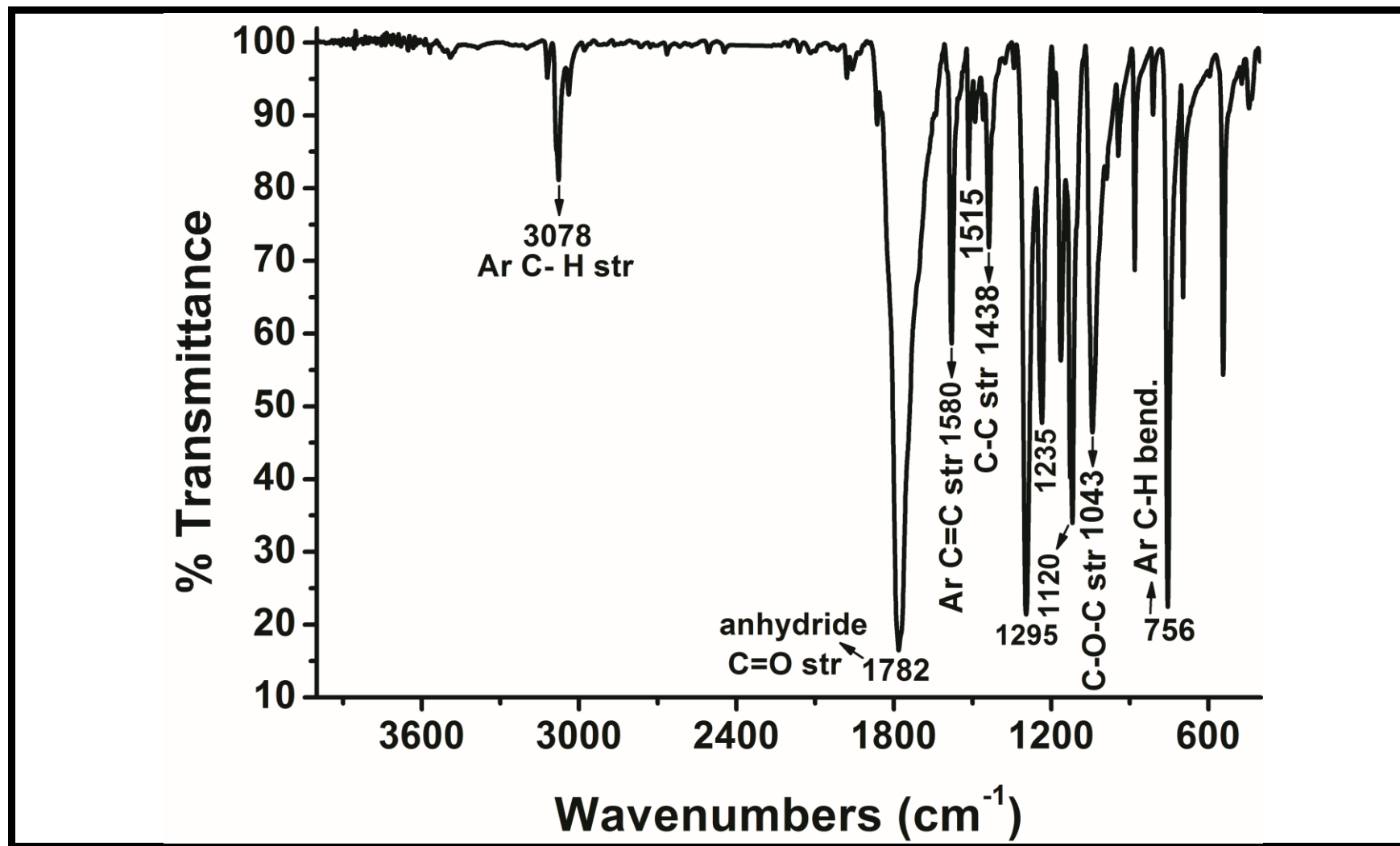
Figure 4.9: FTIR Spectrum of NDA at solid state (KBr)
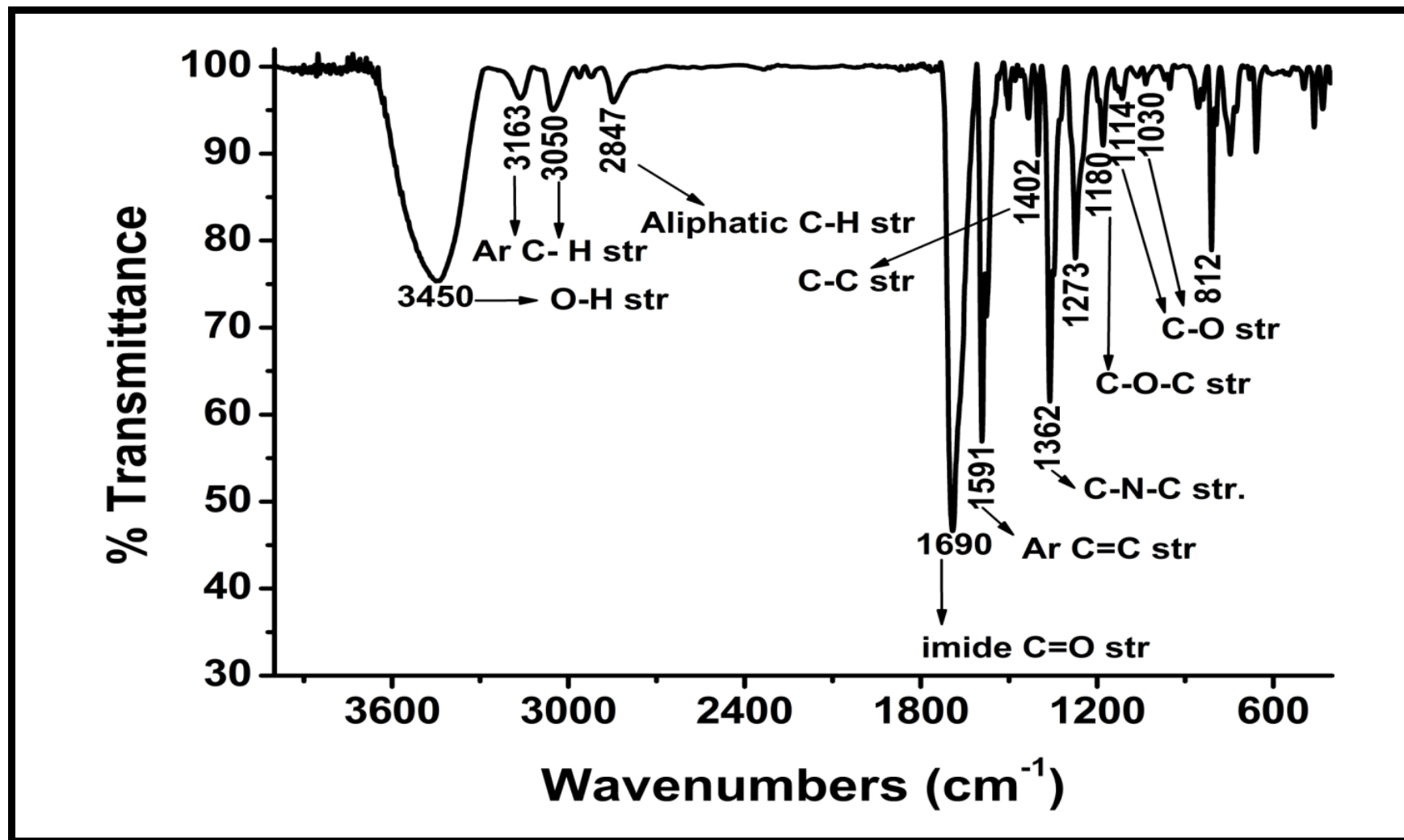
Figure 4.10: FTIR Spectrum of CH-PPI at Solid State (KBr)
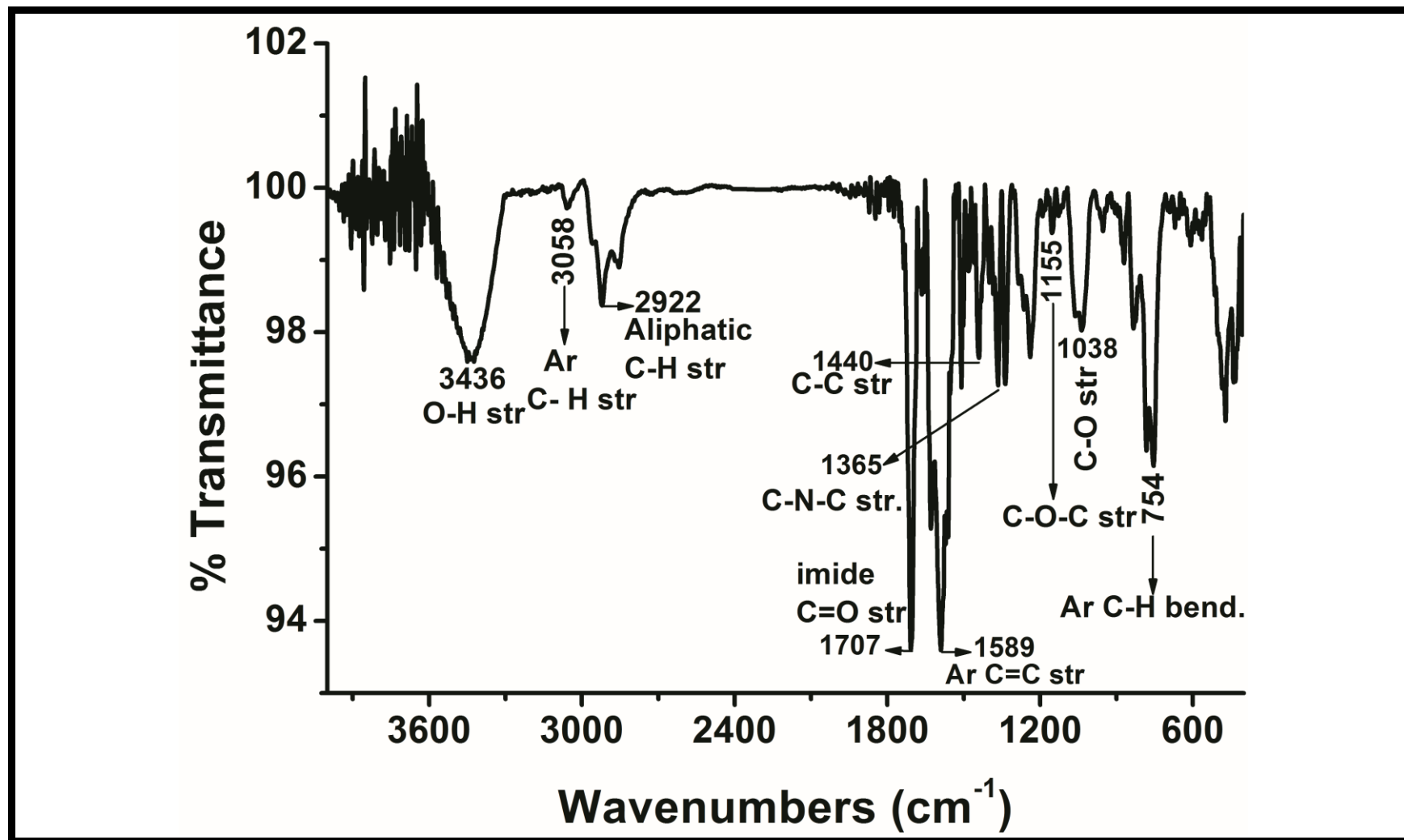
Figure 4.11: FTIR Spectrum of CH-PNI at Solid State (KBr)
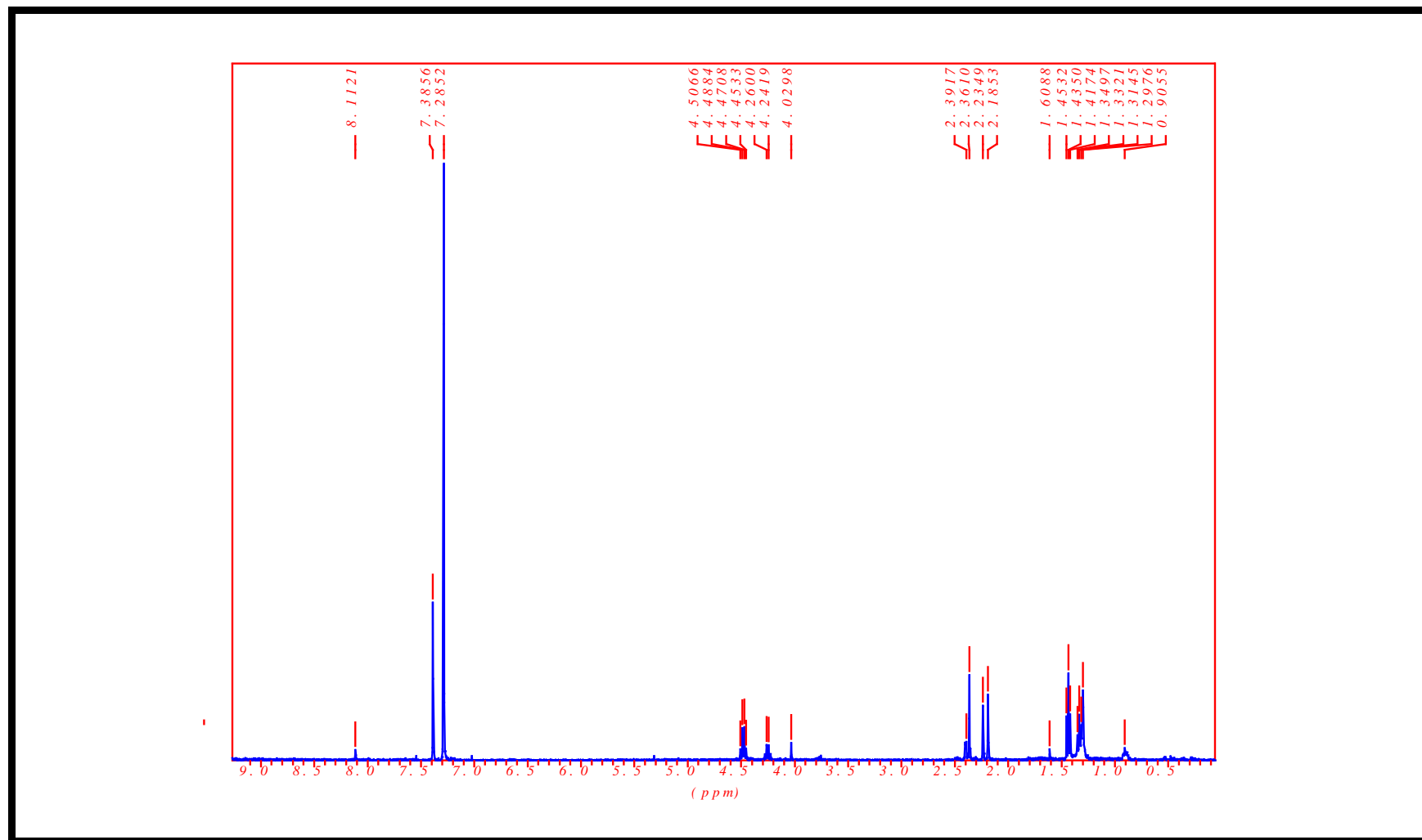
Figure 4.12: ^{1}H NMR Spectrum of CH in CDCl$_3$+CF$_3$COOD (1:1 by volume) (400 MHz)
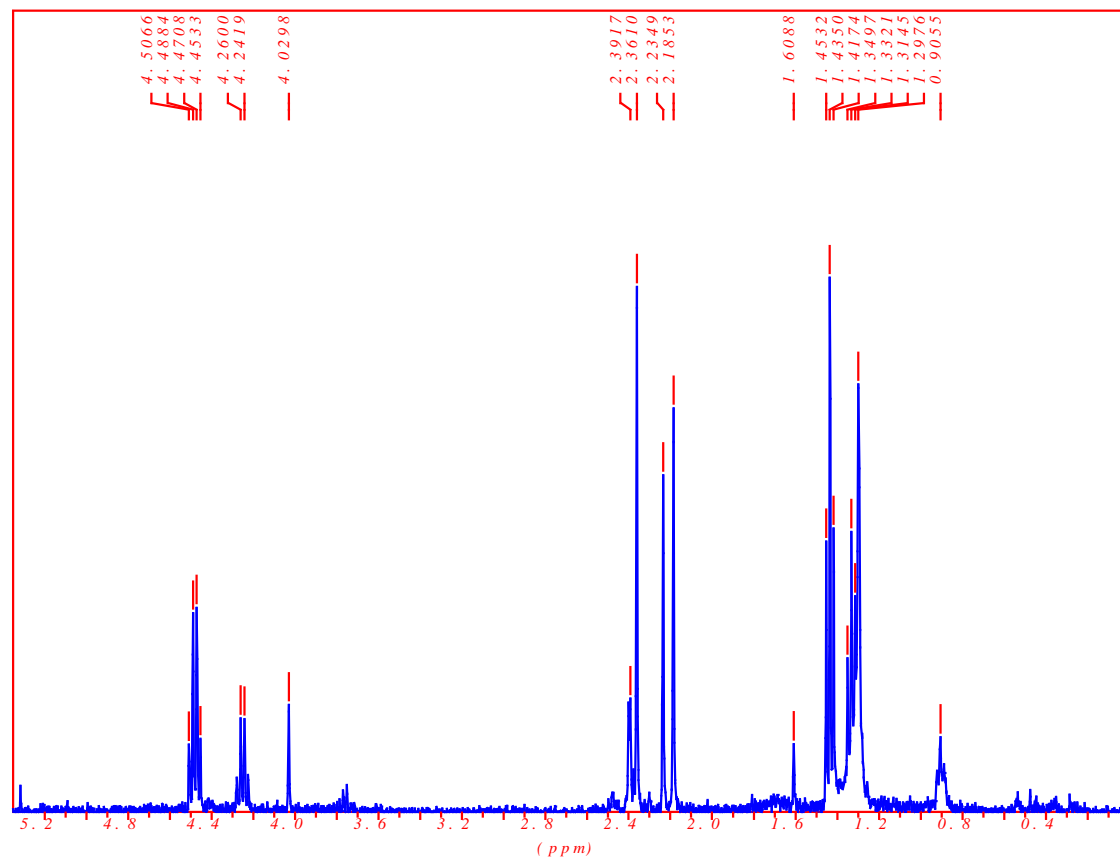
Figure 4.13: ^{1}H NMR Spectrum of CH in $CDCl_3+CF_3COOD$ (1:1 by volume) (400 MHz)
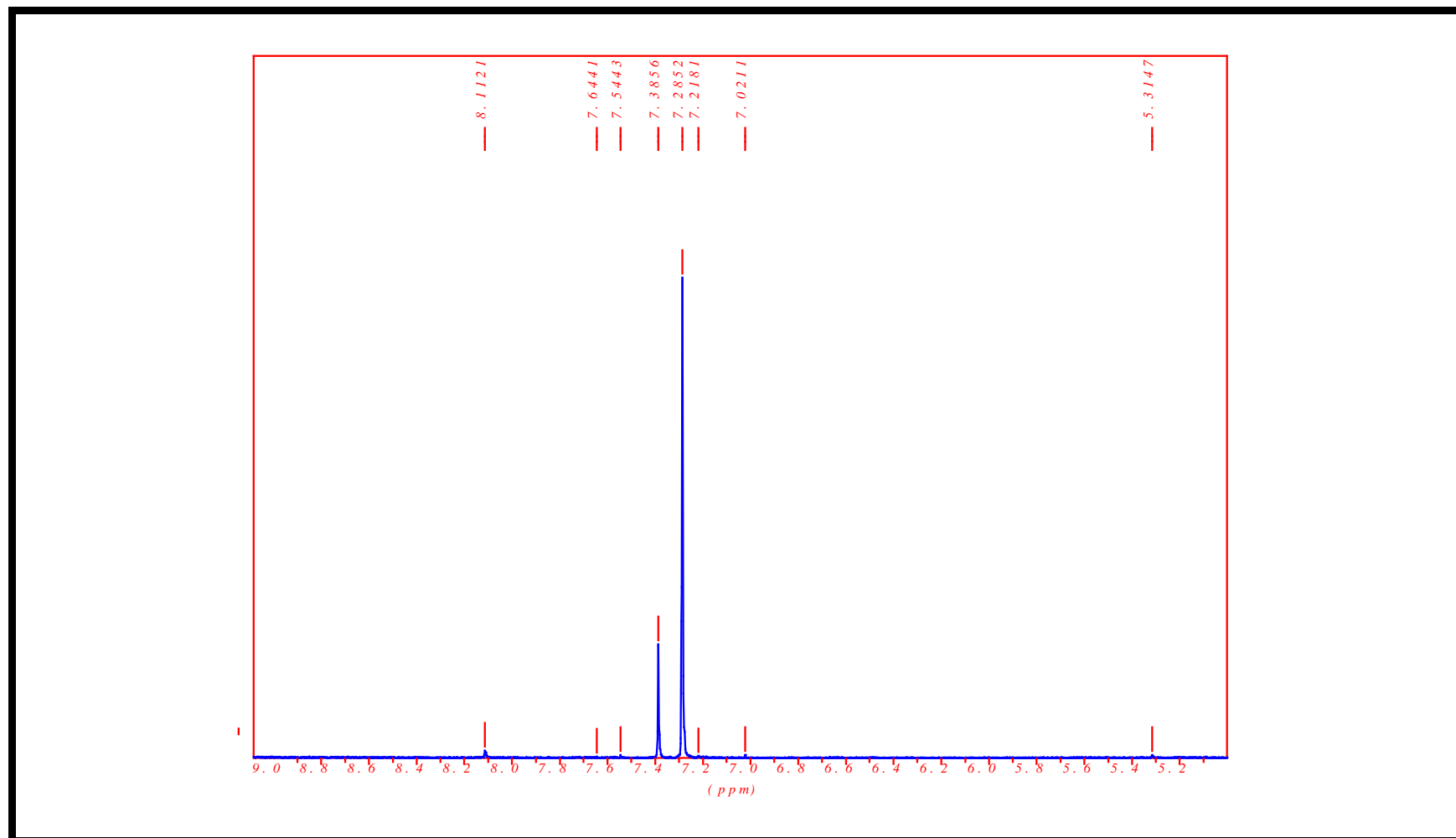
Figure 4.14: ^{1}H NMR Spectrum of CH in CDCl$_3$+CF$_3$COOD (1:1 by volume) (400 MHz)
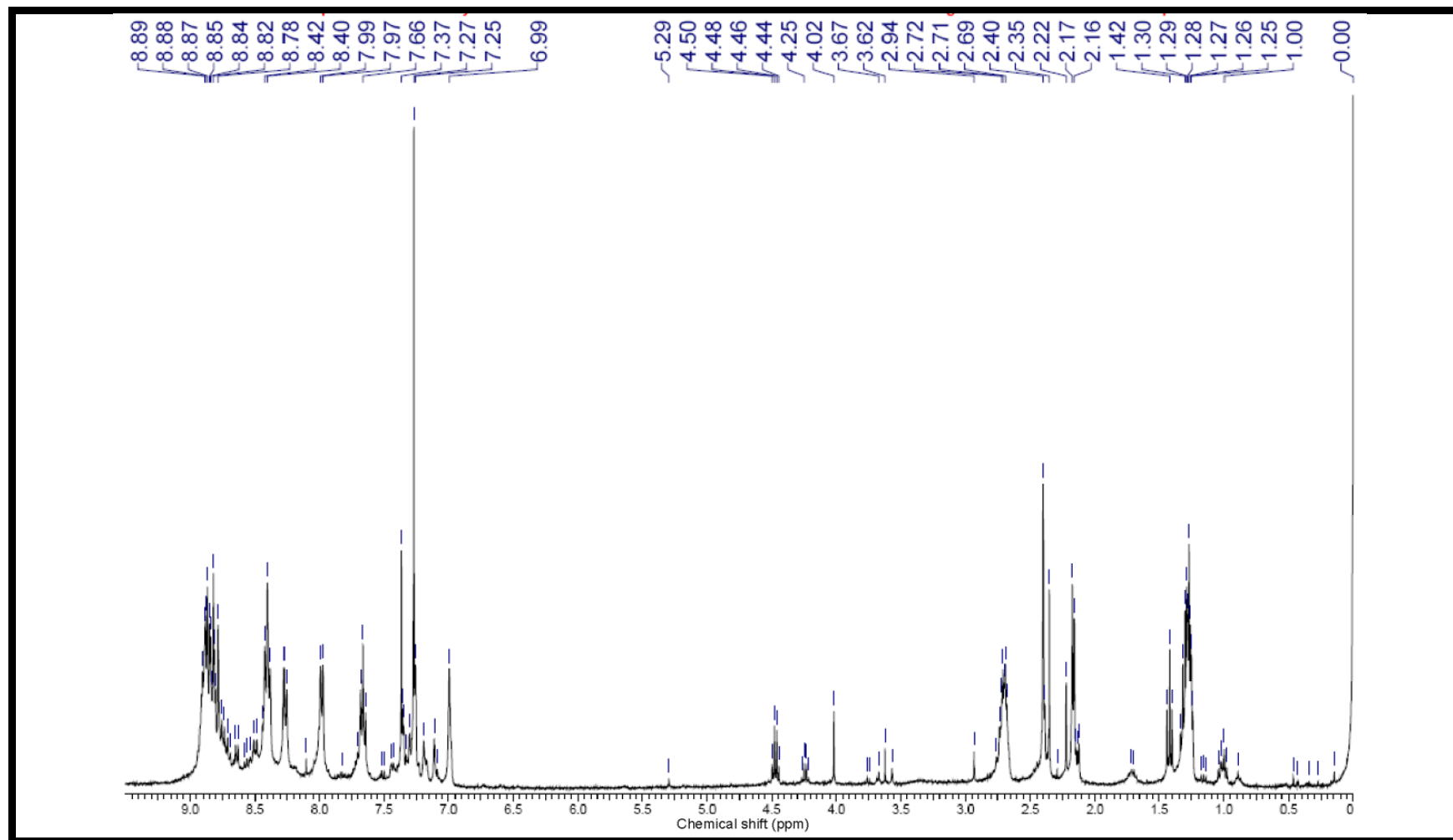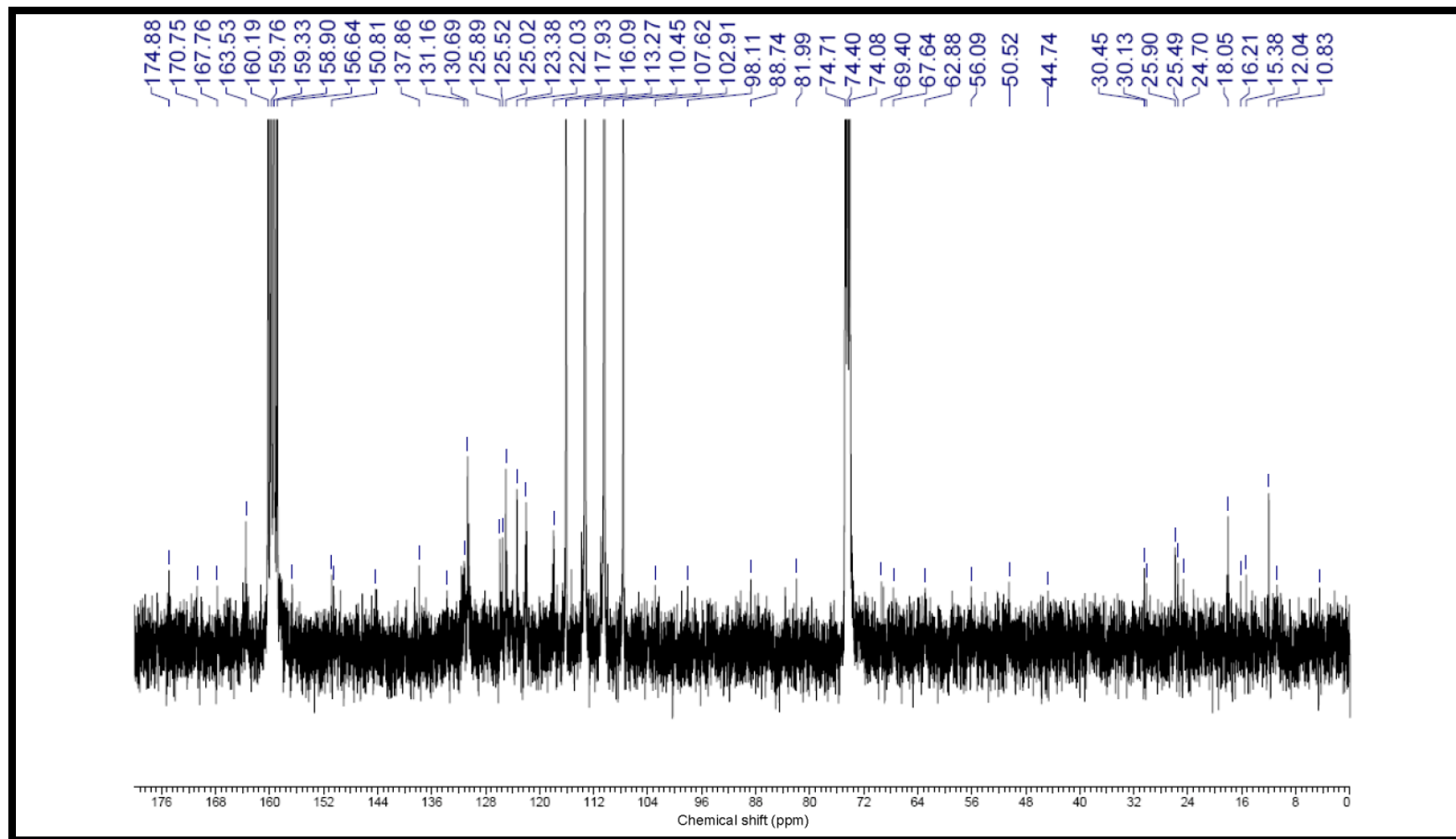
Figure 4.15: ^{1}H NMR Spectrum of CH-PPI in CDCl$_3$+CF$_3$COOD (3:2 by volume) (400 MHz)
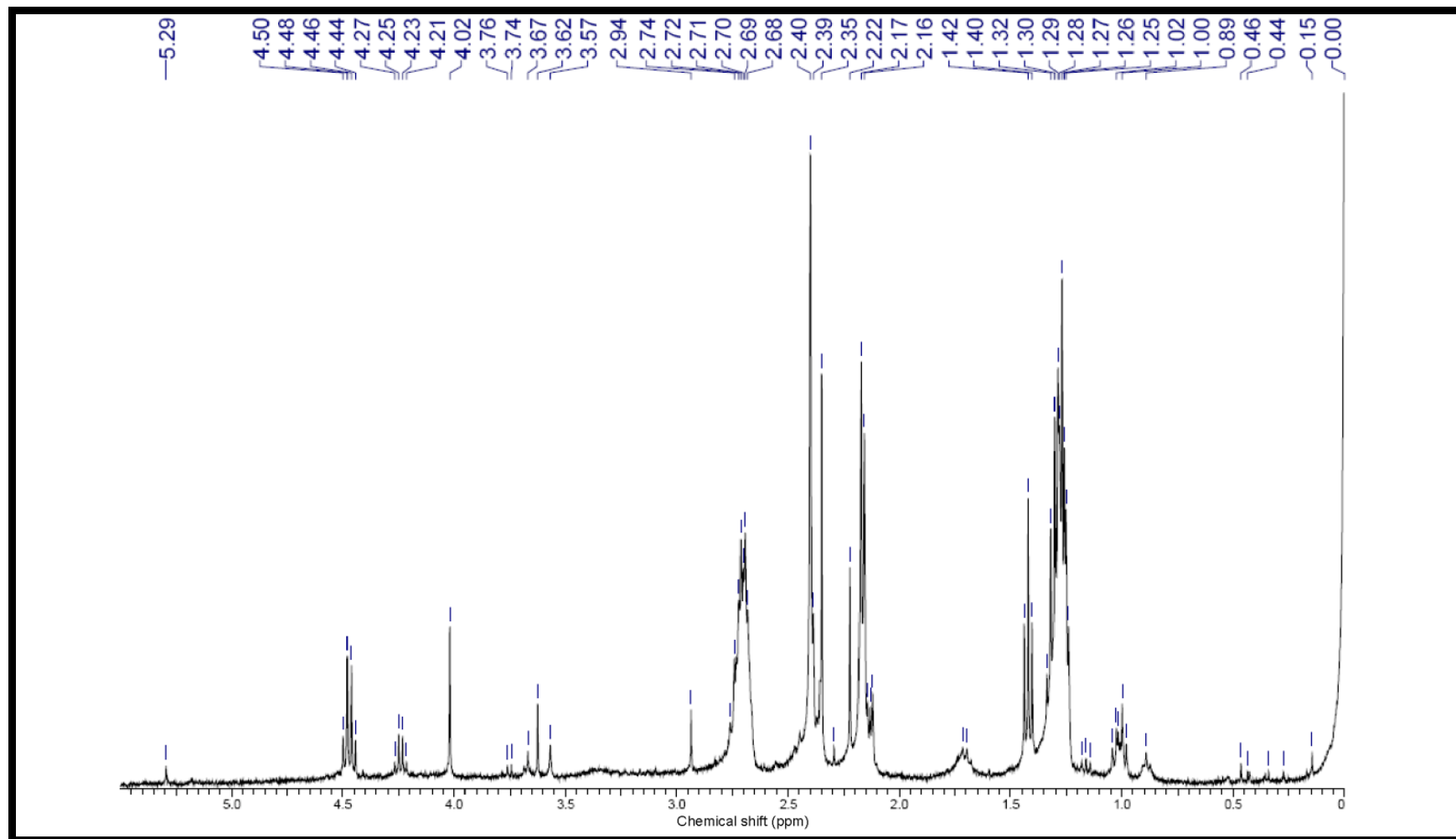
Figure 4.16: ^{1}H NMR Spectrum of CH-PPI in CDCl$_3$+CF$_3$COOD (3:2 by volume) (400 MHz)
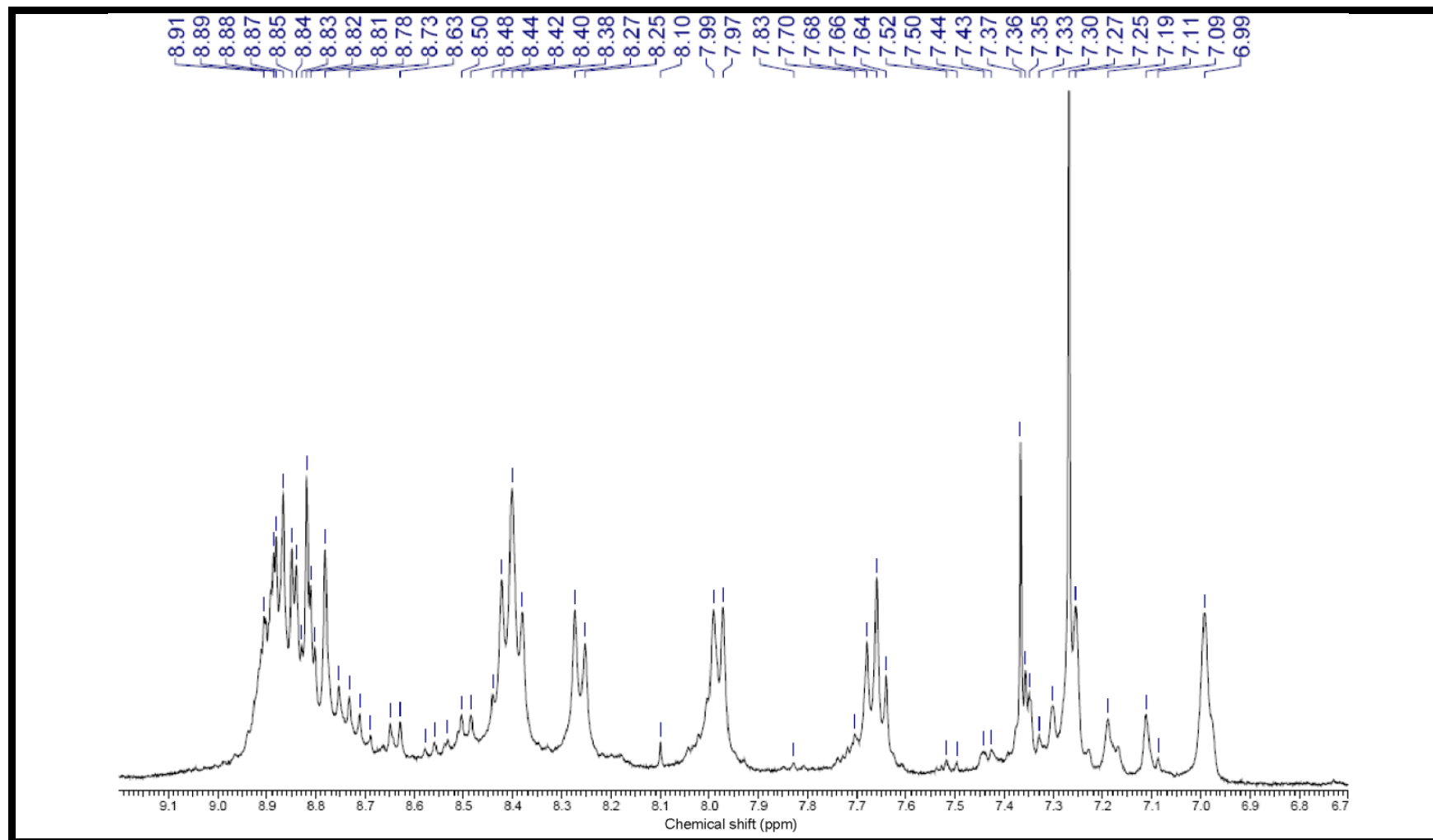
Figure 4.17: ^{1}H NMR Spectrum of CH-PPI in CDCl$_3$+CF$_3$COOD (3:2 by volume) (400 MHz)
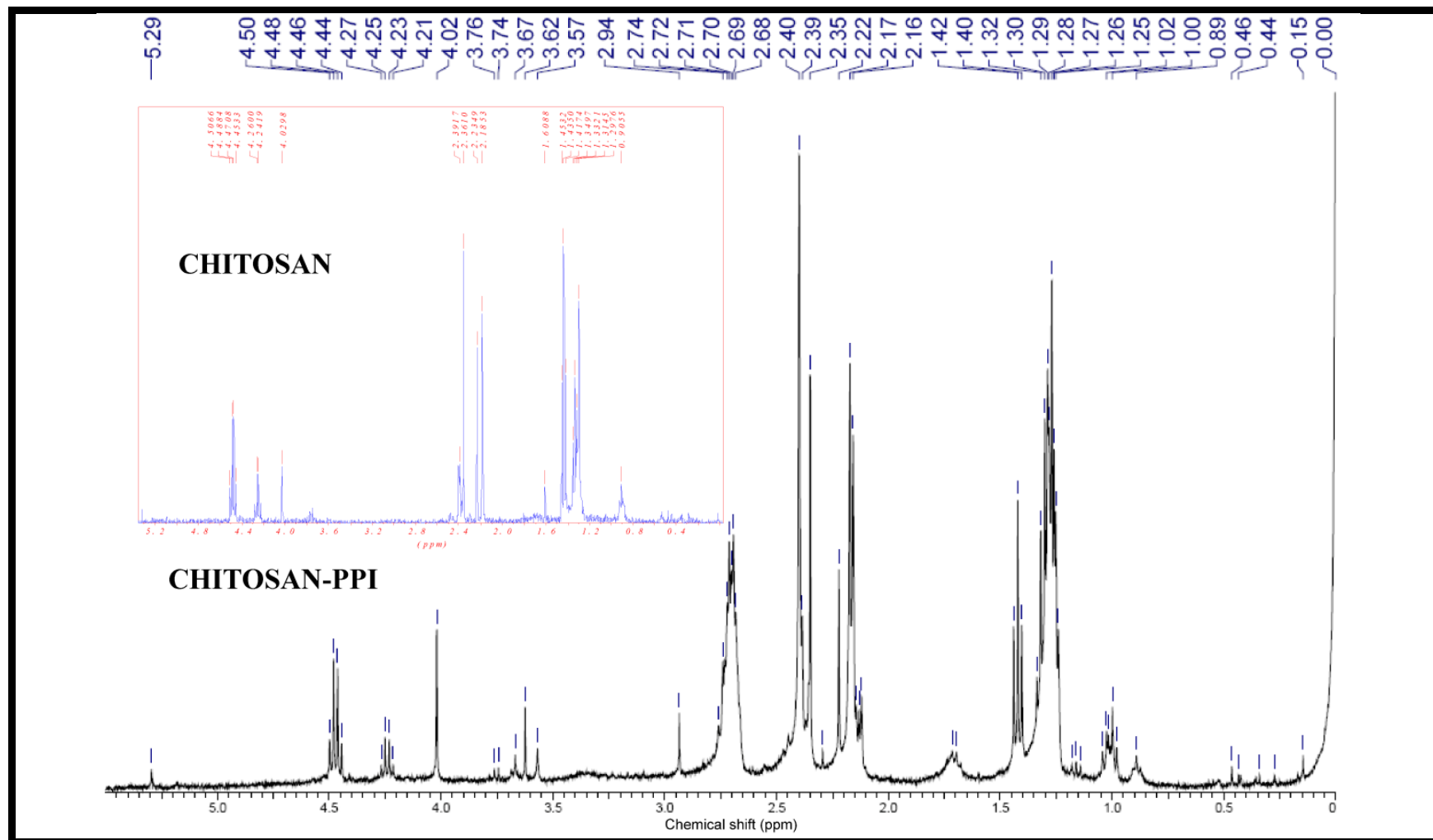
Figure 4.18: Comparison of ^{1}H NMR Spectra of CH and CH-PPI
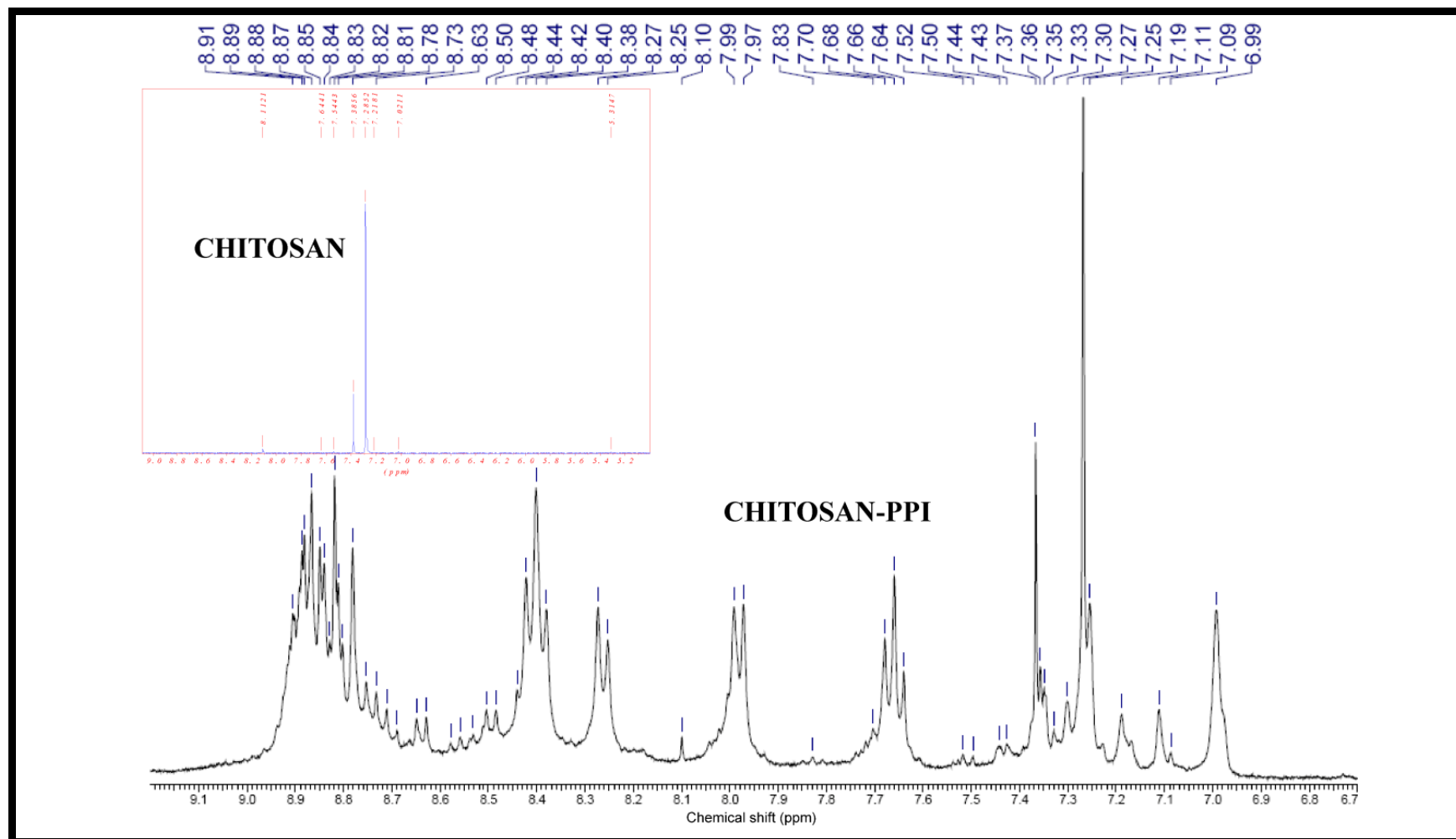
Figure 4.19: Comparison of ^{1}H NMR Spectra of CH and CH-PPI
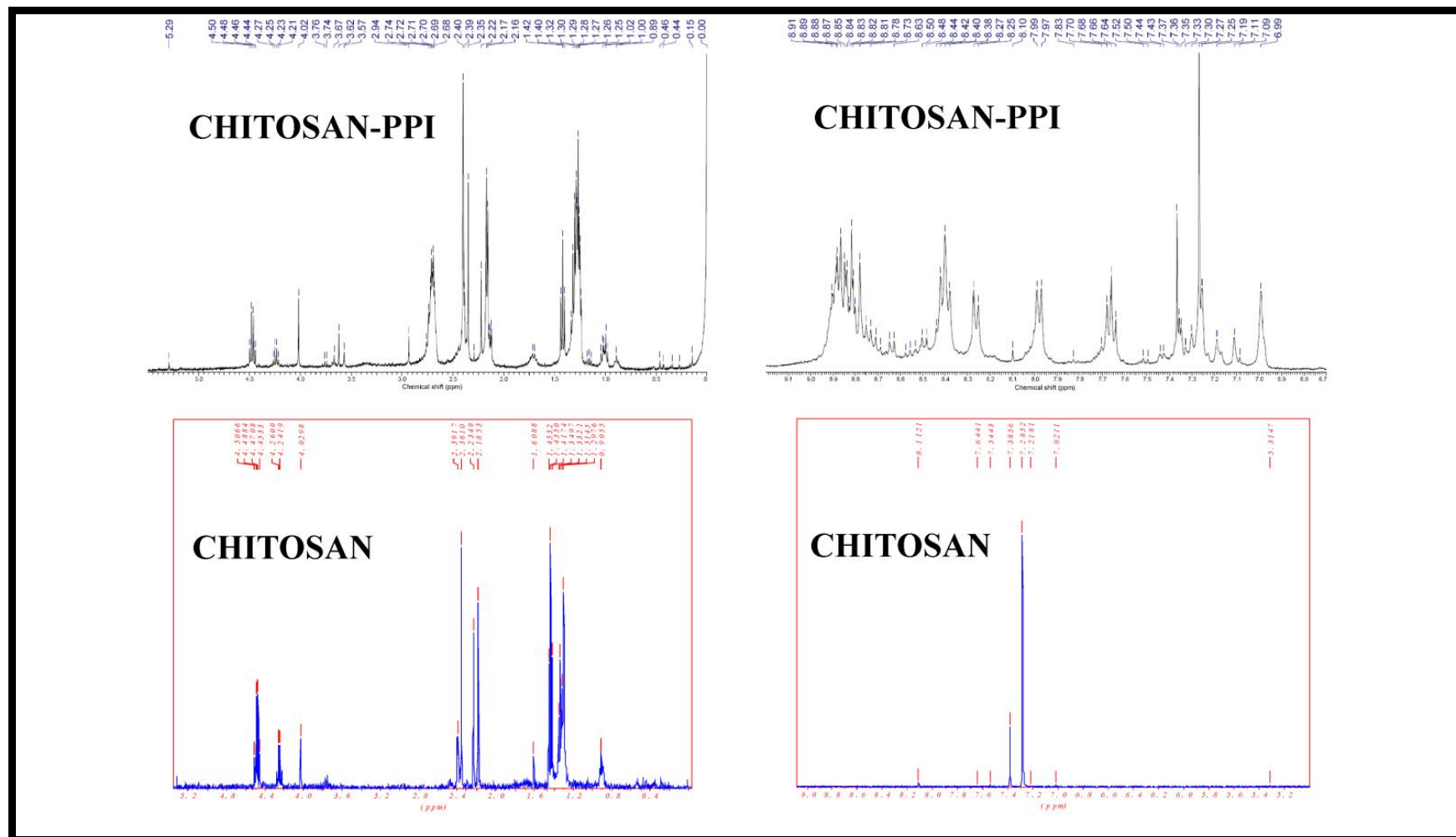
Figure 4.20: Comparison of ^{1}H NMR Spectra of CH and CH-PPI

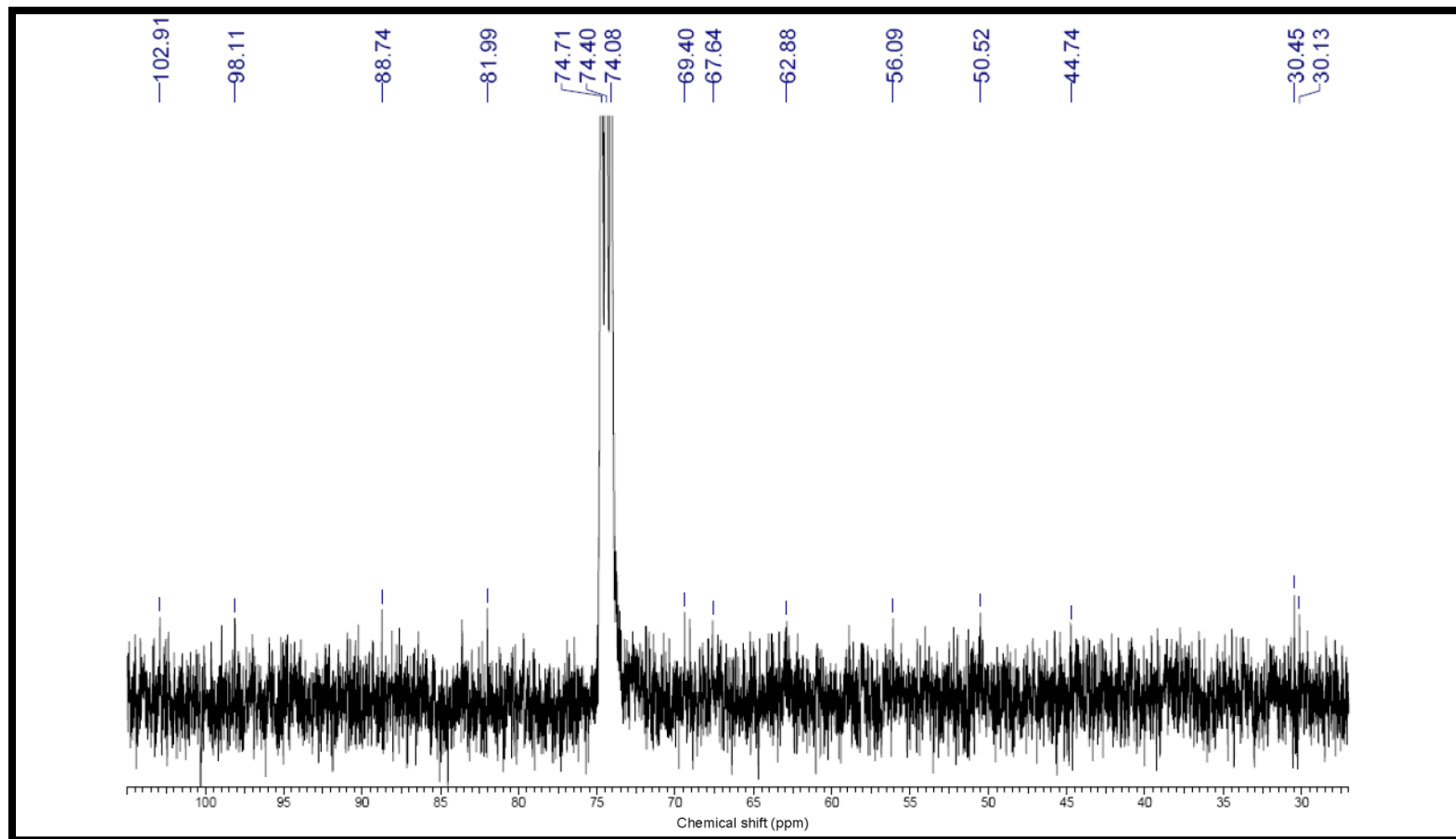Figure 4.21: ^{13}C NMR Spectrum of CH-PPI in $CDCl_3+CF_3COOD$ (3:2 by volume) (400 MHz)

Figure 4.22: ^{13}C NMR Spectrum of CH-PPI in $CDCl_3+CF_3COOD$ (3:2 by volume) (400 MHz)

Figure 4.23: ^{13}C NMR Spectrum of CH-PPI in CDCl$_3$+CF$_3$COOD (3:2 by volume) (400 MHz)

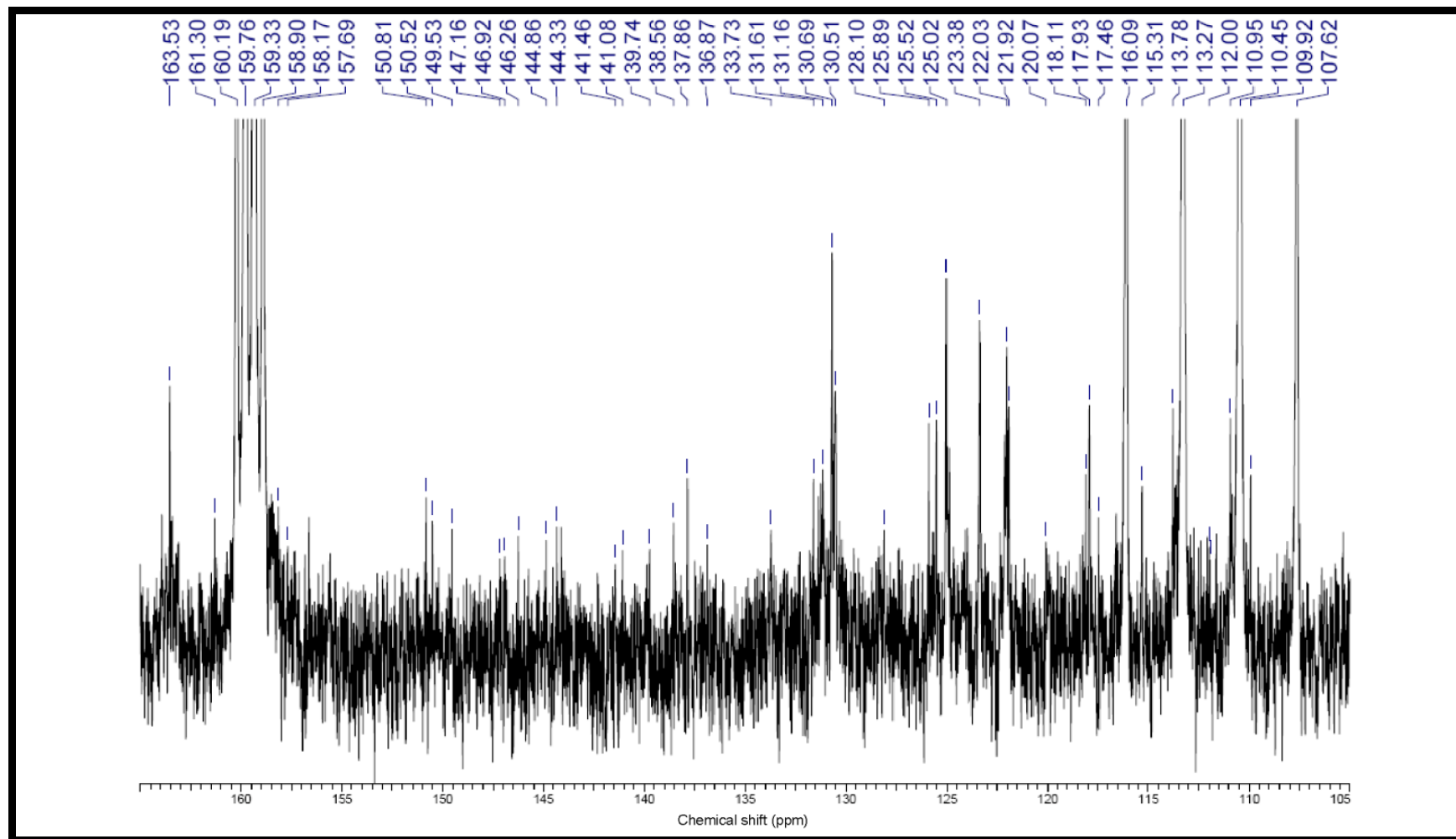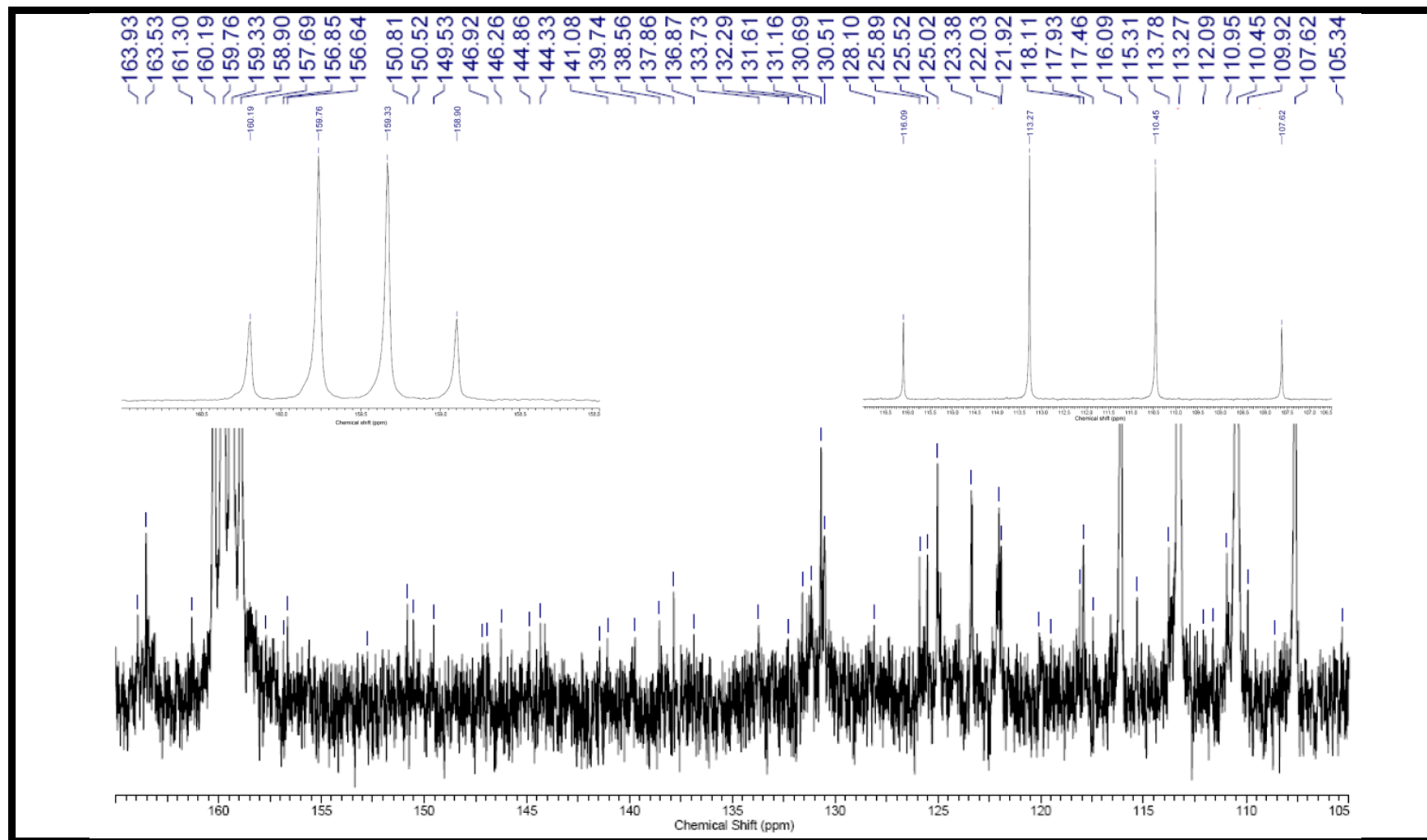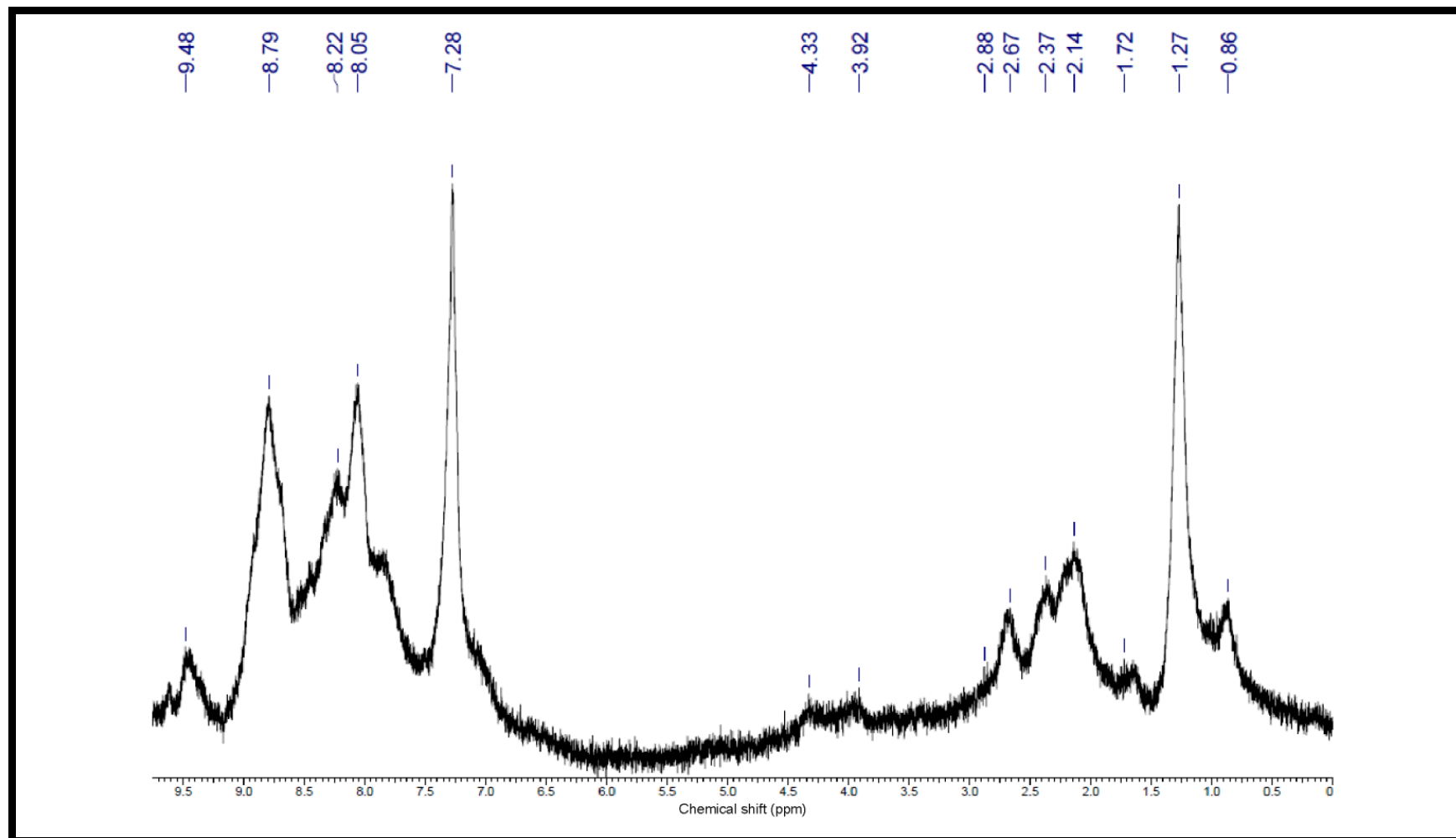Figure 4.24: ^{13}C NMR Spectrum of CH-PPI in $CDCl_3+CF_3COOD$ (3:2 by volume) (400 MHz)

Figure 4.25: ^{1}H NMR Spectrum of CH-PNI in CDCl$_3$+CF$_3$COOD (1:1 by volume) (400 MHz)

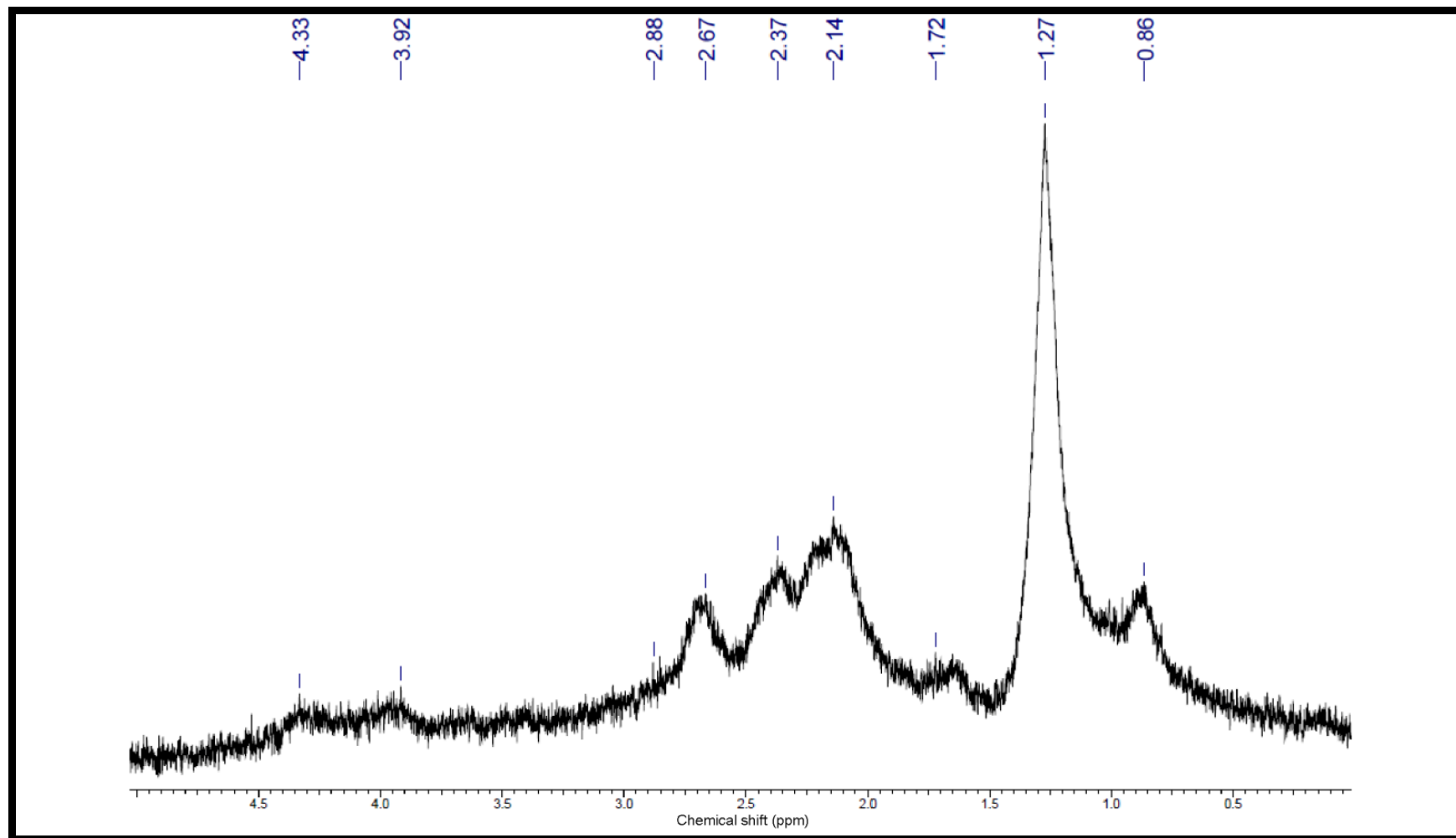Figure 4.26: ^{1}H NMR Spectrum of CH-PNI in $CDCl_3+CF_3COOD$ (1:1 by volume) (400 MHz)
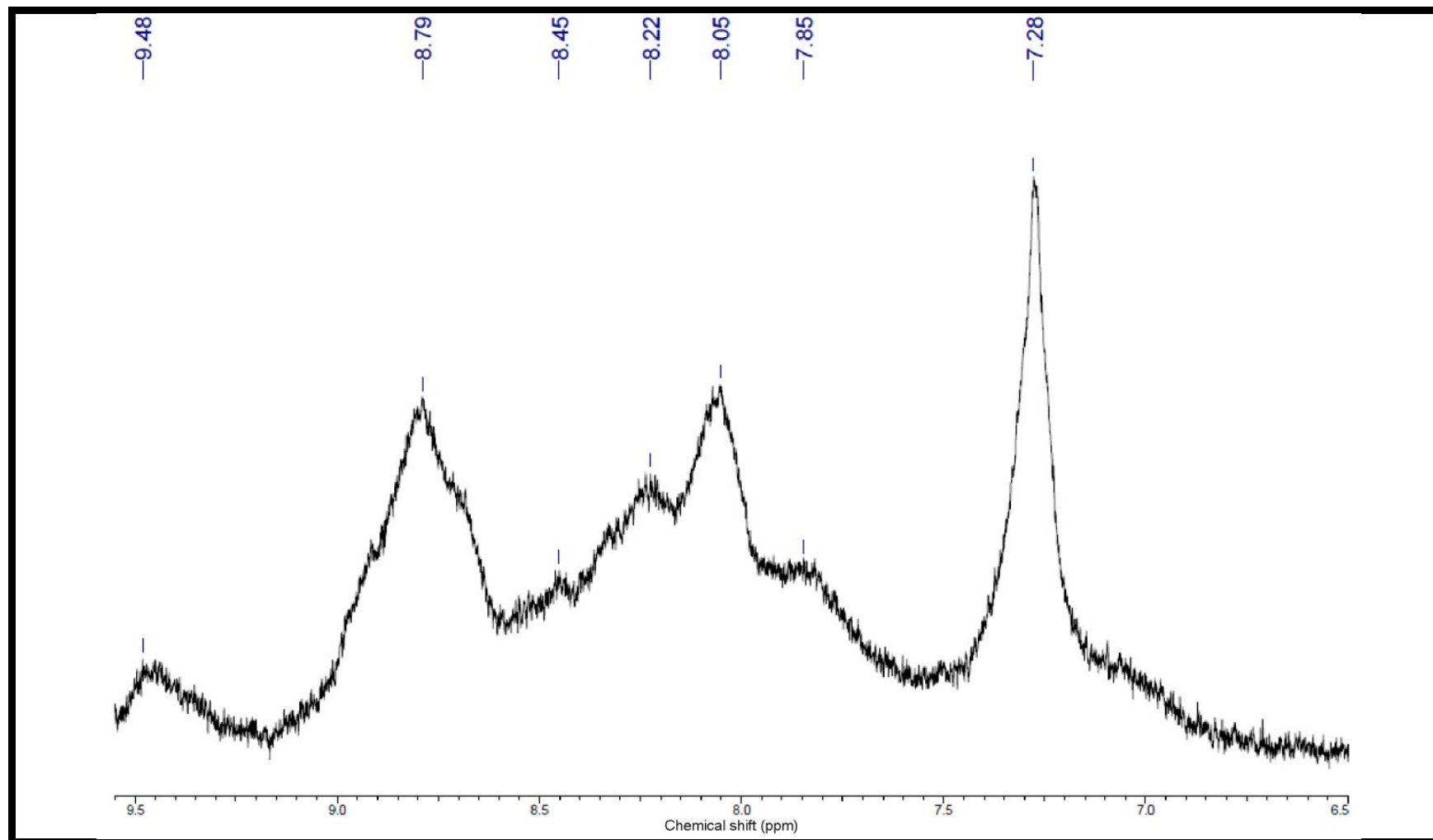
Figure 4.27: ^{1}H NMR Spectrum of CH-PNI in CDCl$_3$+CF$_3$COOD (1:1 by volume) (400 MHz)
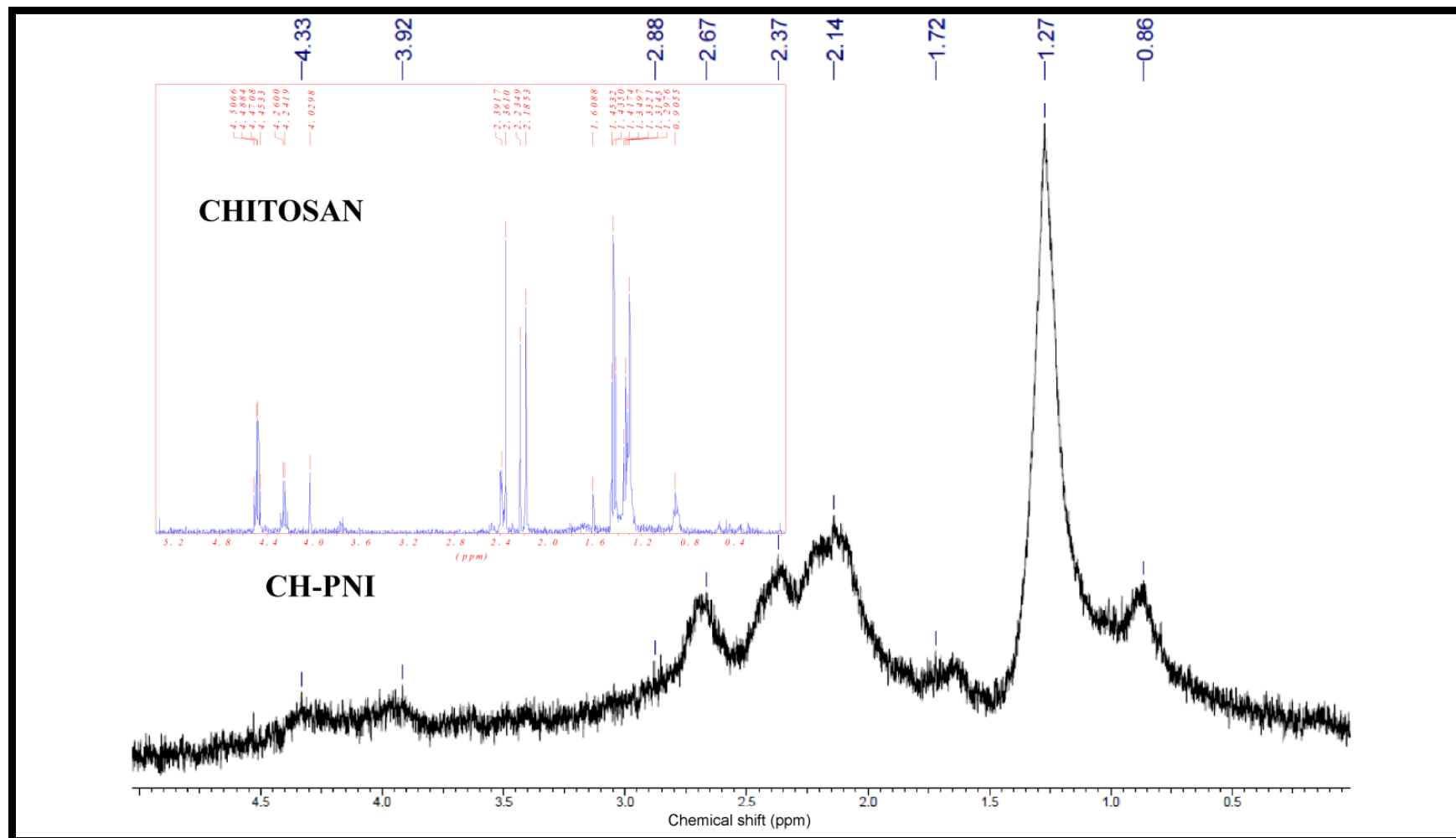
Figure 4.28: Comparison of ^{1}H NMR Spectra of CH and CH-PPI
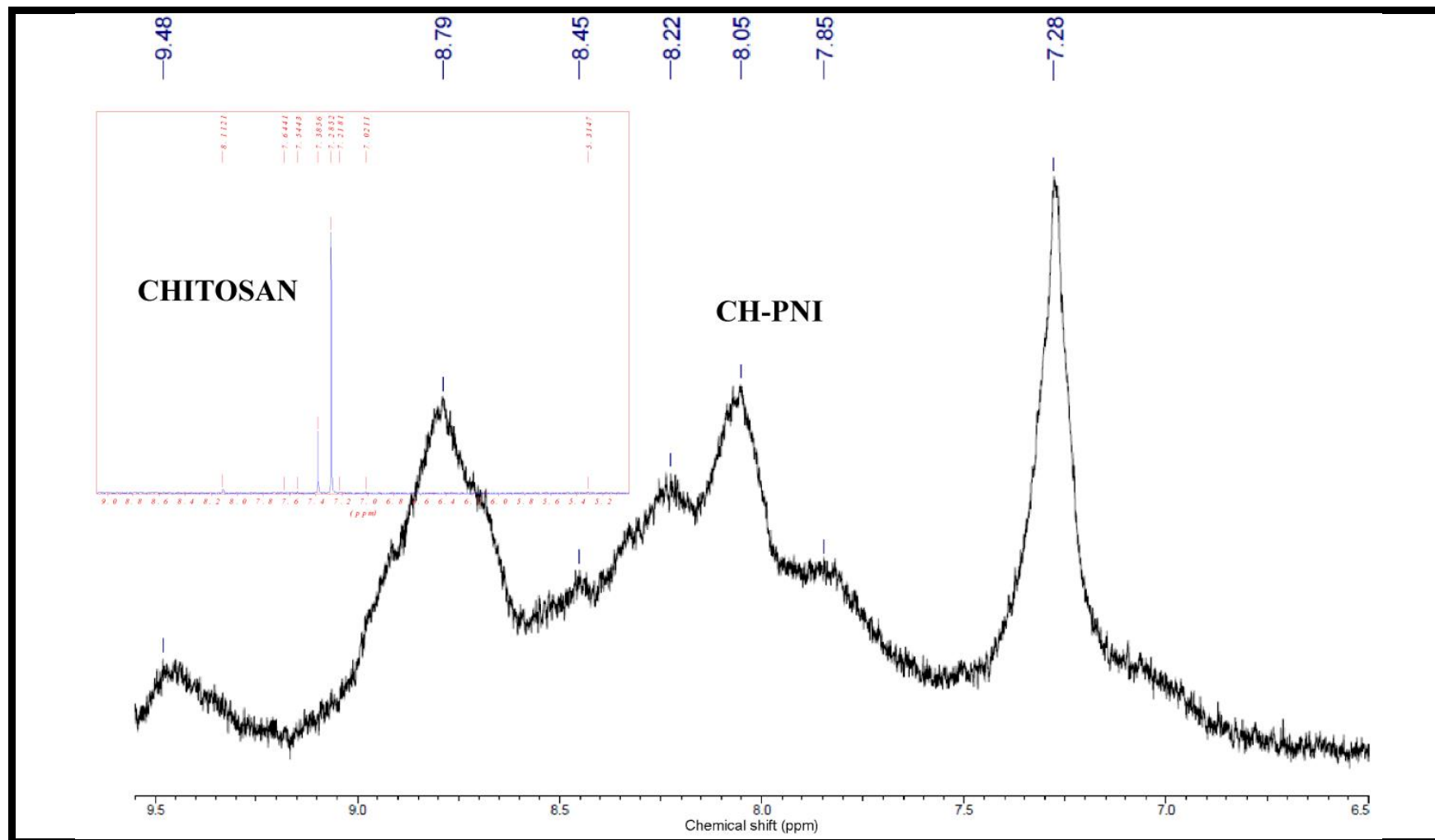
Figure 4.29: Comparison of ^{1}H NMR Spectra of CH and CH-PNI
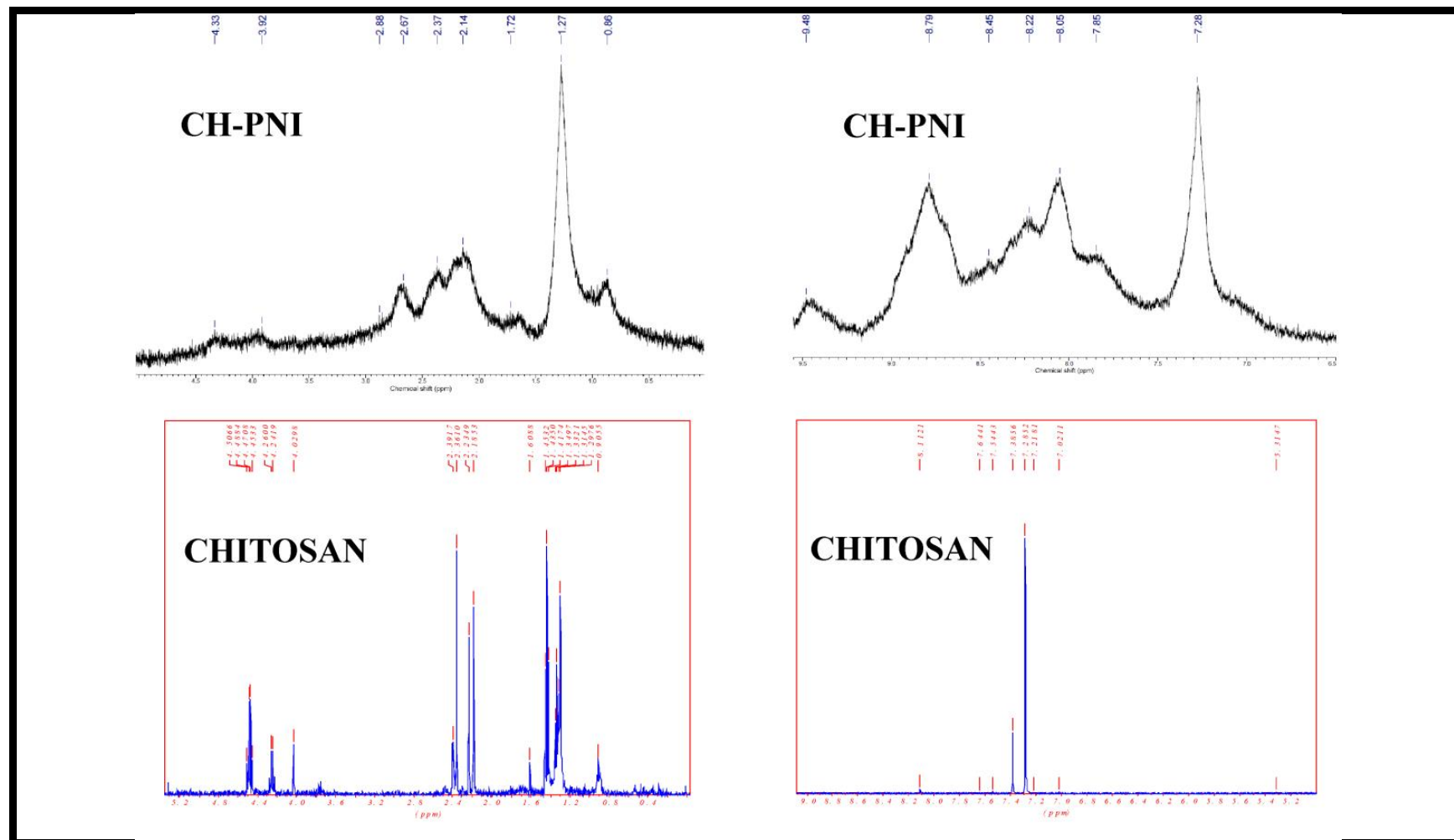
Figure 4.30: Comparison of ^{1}H NMR Spectra of CH and CH-PNI
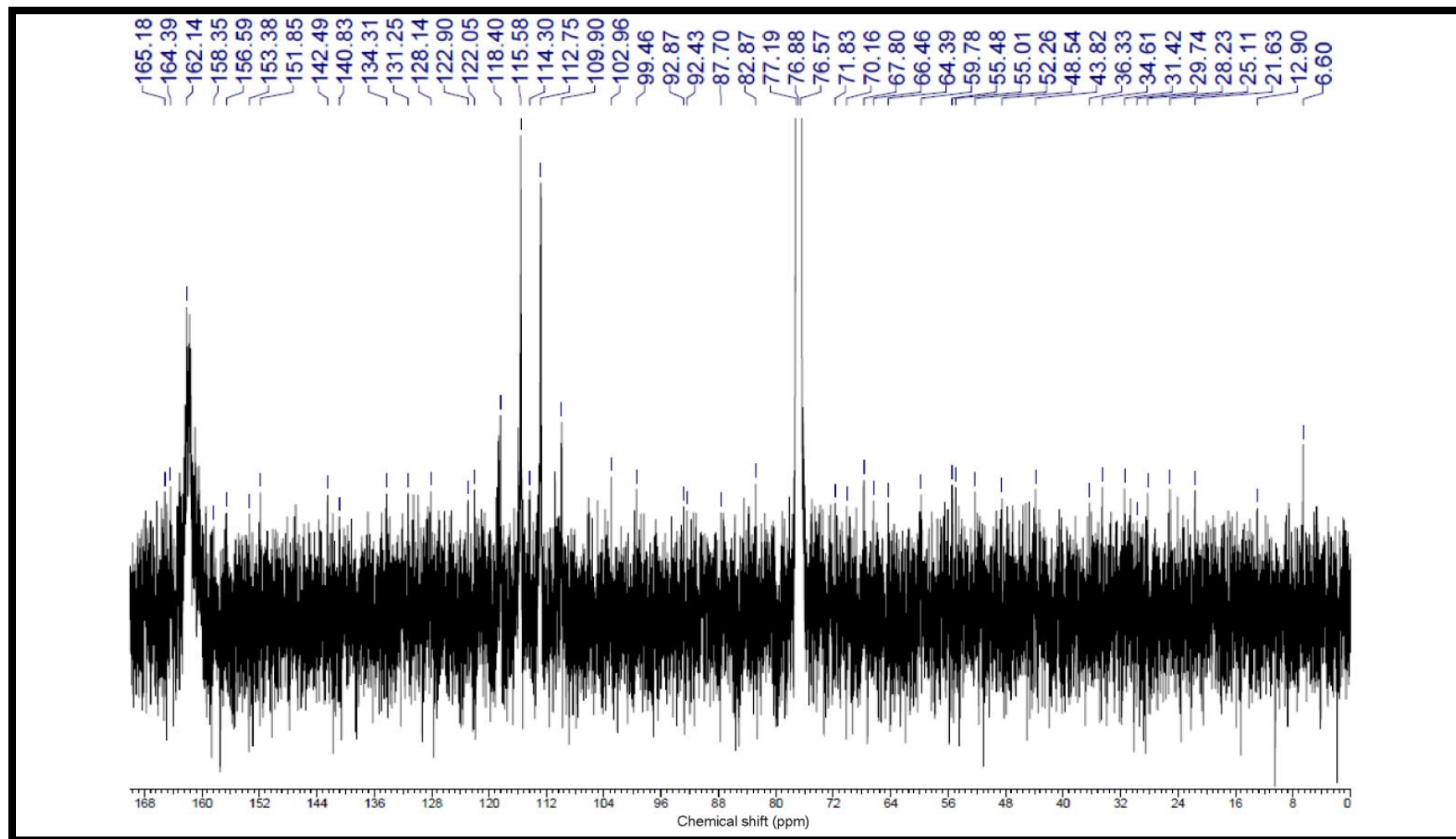
Figure 4.31: ^{13}C NMR Spectrum of CH-PNI in CDCl$_3$+CF$_3$COOD (1:1 by volume) (400 MHz)
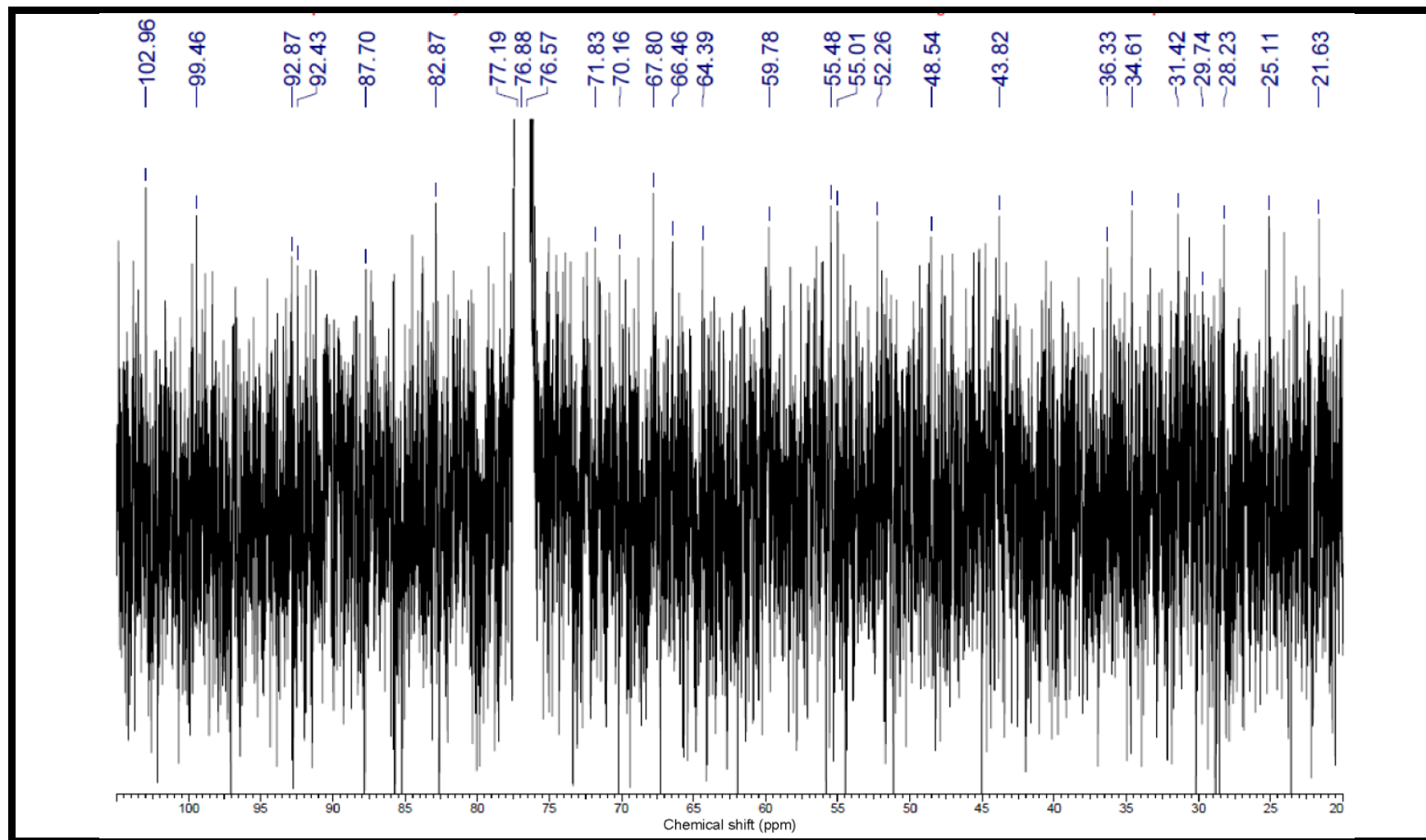
Figure 4.32: ^{13}C NMR Spectrum of CH-PNI in CDCl$_3$+CF$_3$COOD (1:1 by volume) (400 MHz)
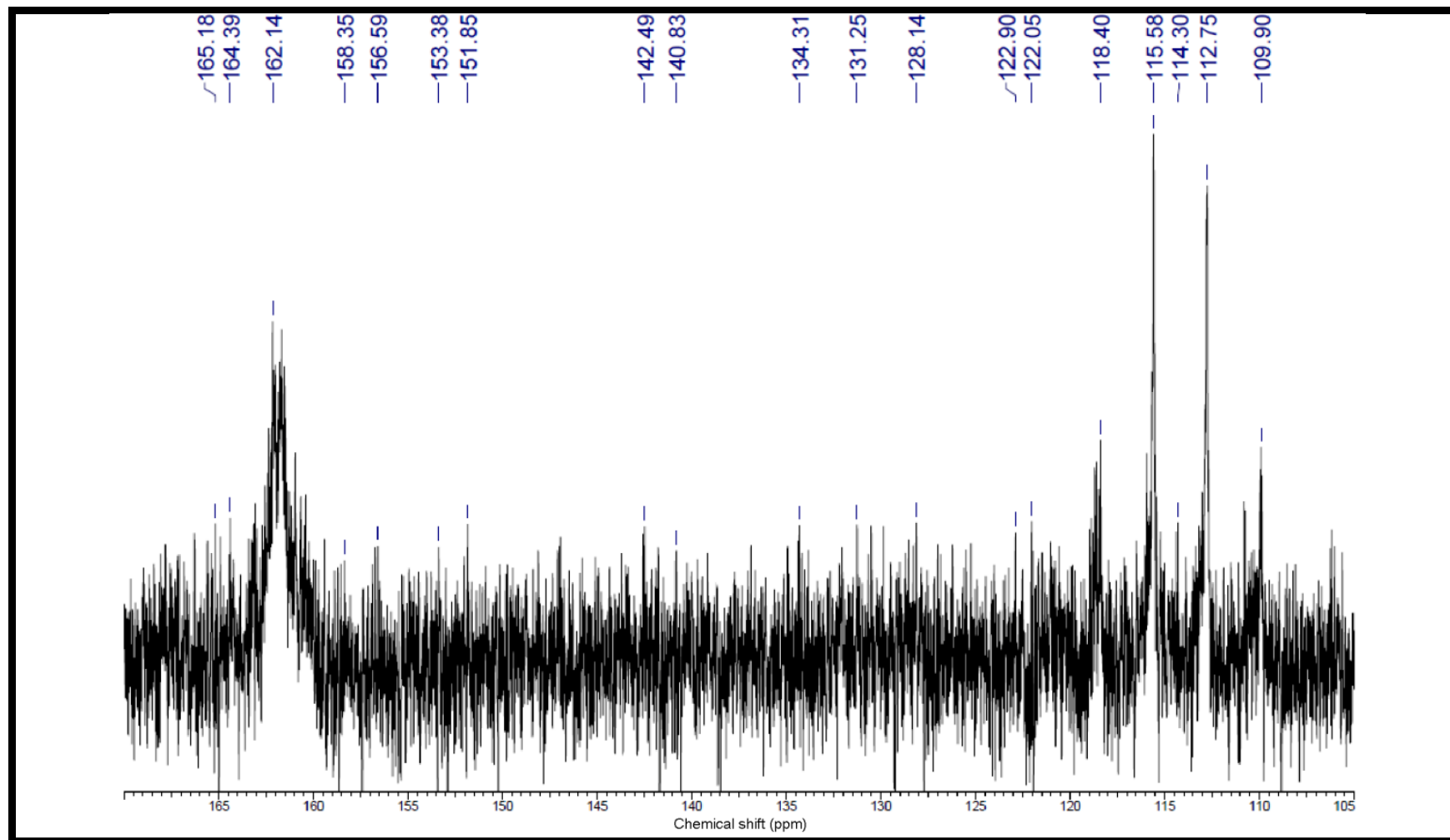
Figure 4.33: ^{13}C NMR Spectrum of CH-PNI in CDCl$_3$+CF$_3$COOD (1:1 by volume) (400 MHz)
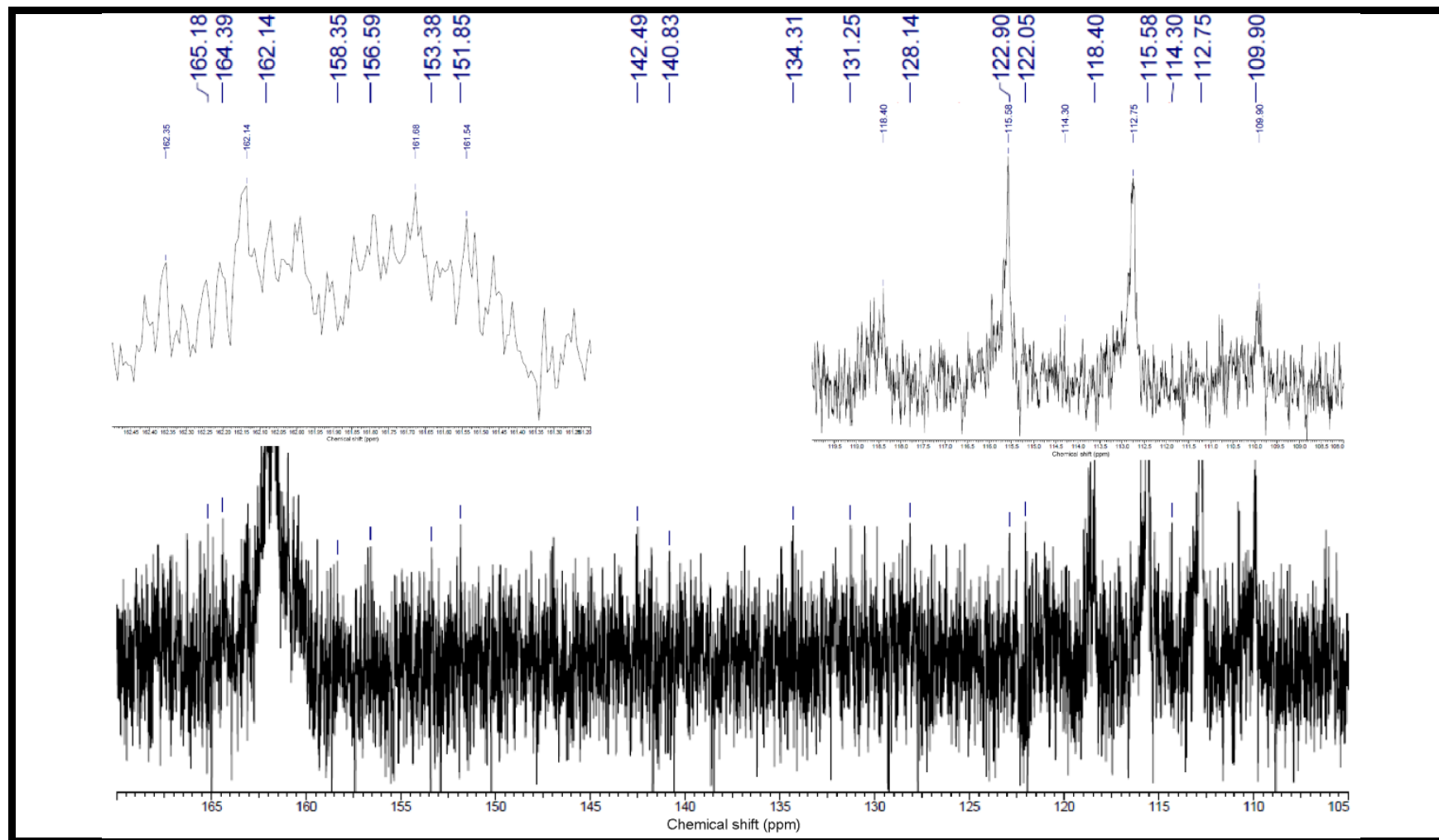
Figure 4.34: ^{13}C NMR Spectrum of CH-PNI in CDCl$_3$+CF$_3$COOD (1:1 by volume) (400 MHz)
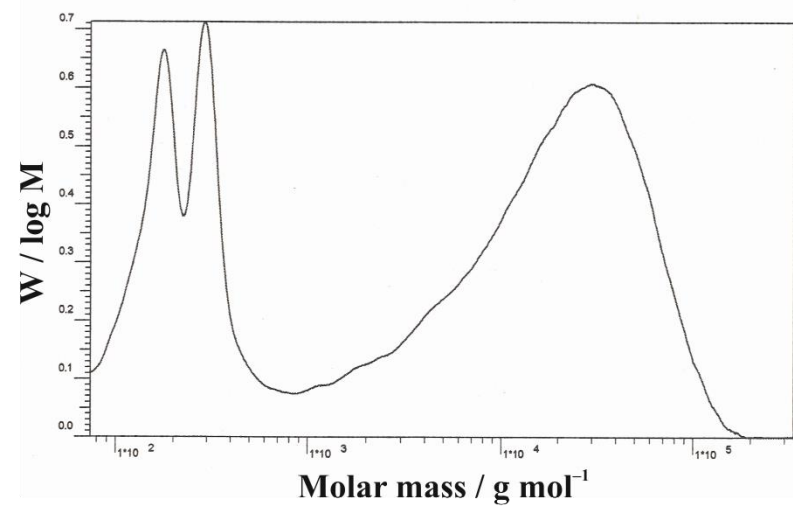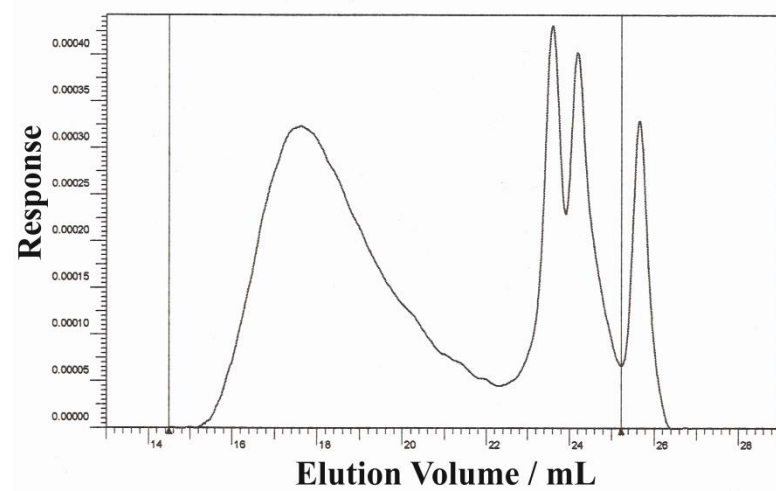
Figure 4.35: GPC Chromatograms of CH
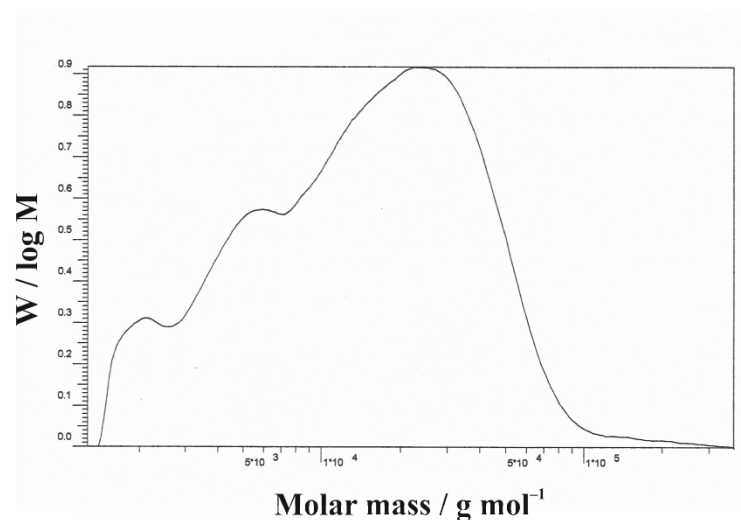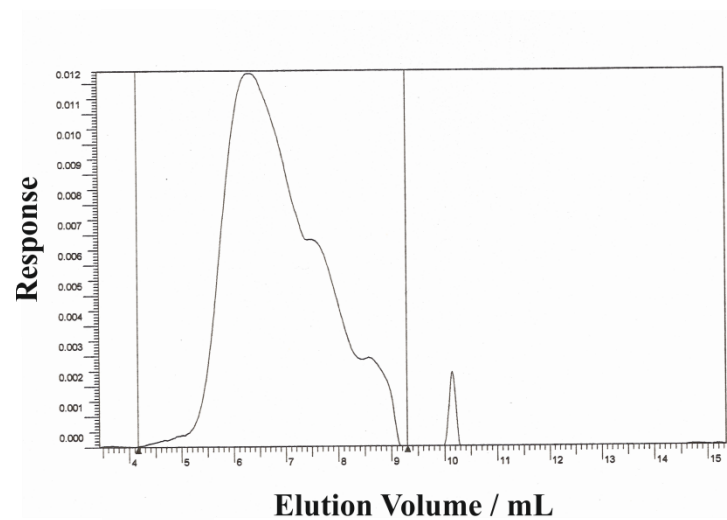
Figure 4.36: GPC Chromatograms of CH-PPI
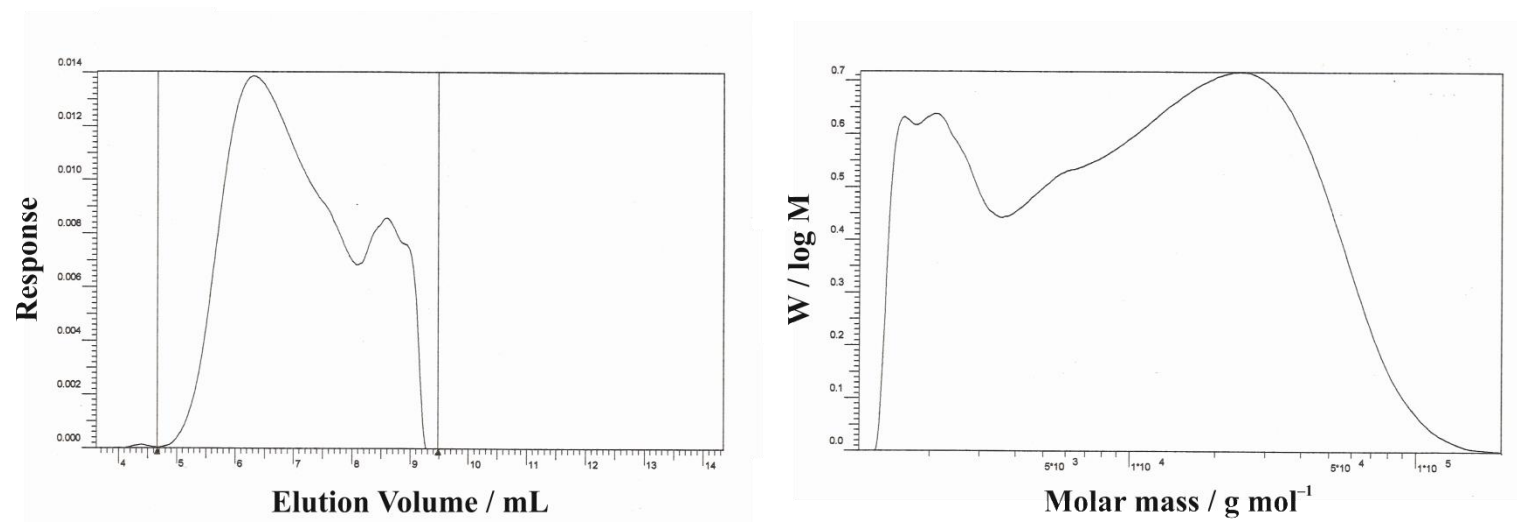
Figure 4.37: GPC Chromatograms of CH-PNI

Figure 4.38: Normalized Absorption, Emission and Excitation Spectra of CH-PPI in Acetone

Figure 4.39: Normalized Absorption, Emission and Excitation Spectra of CH-PPI in Dichloromethane

Figure 4.40: Normalized Absorption, Emission and Excitation Spectra of CH-PPI in Acetonitrile

Figure 4.41: Normalized Absorption, Emission and Excitation Spectra of CH-PPI in Chloroform
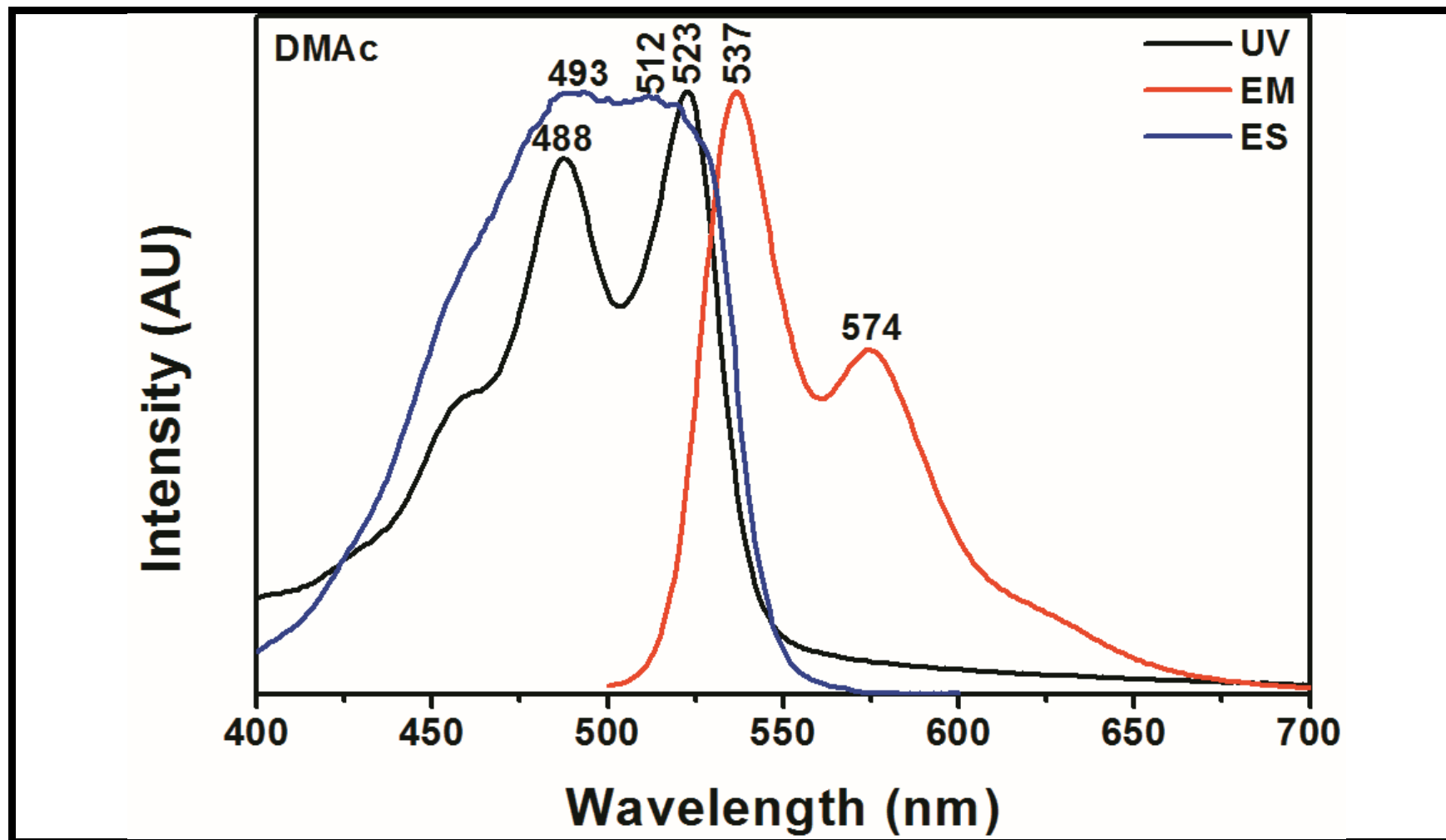
Figure 4.42: Normalized Absorption, Emission and Excitation Spectra of CH-PPI in Dimethylacetamide
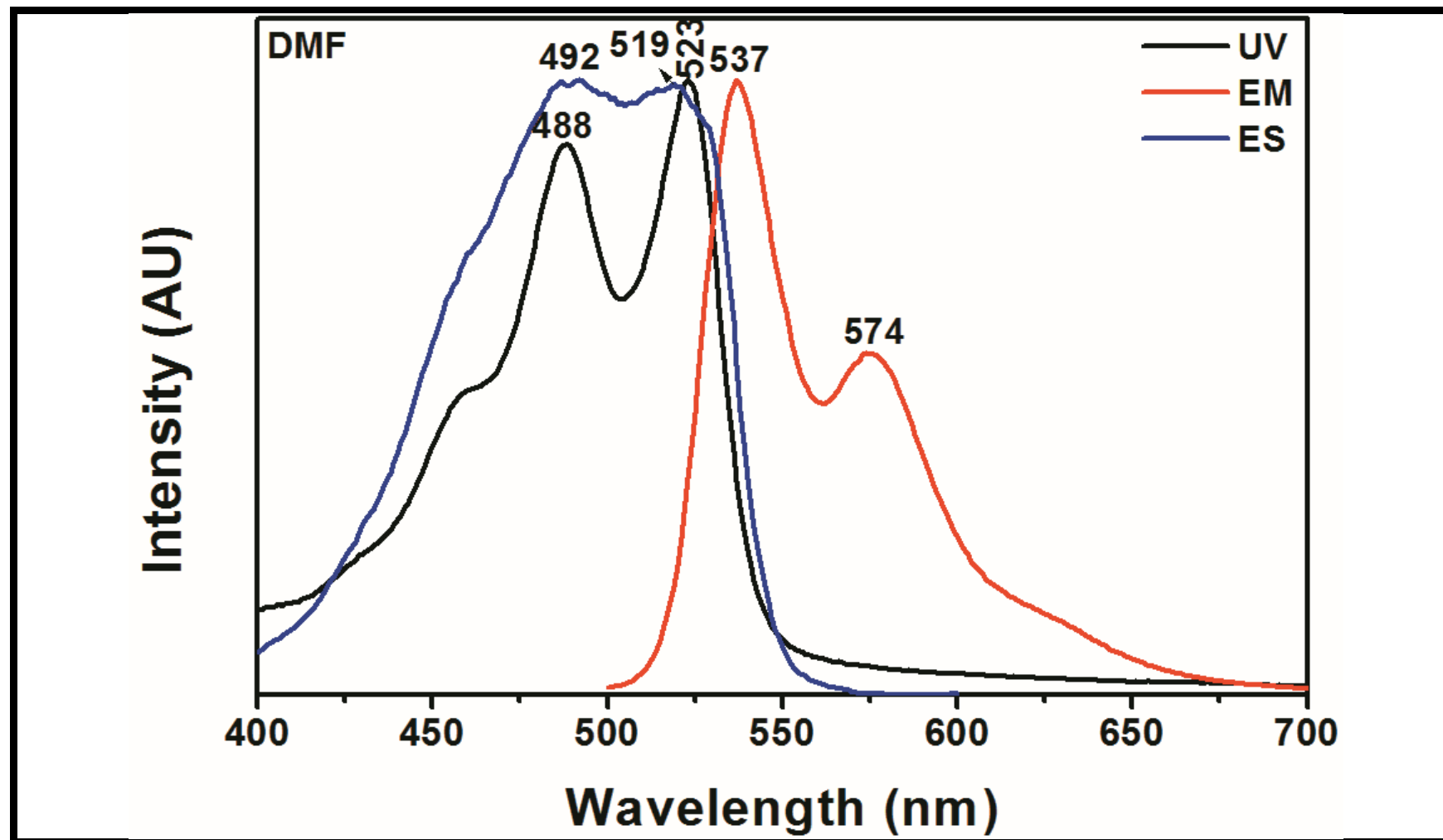
Figure 4.43: Normalized Absorption, Emission and Excitation Spectra of CH-PPI in Dimethylformamide
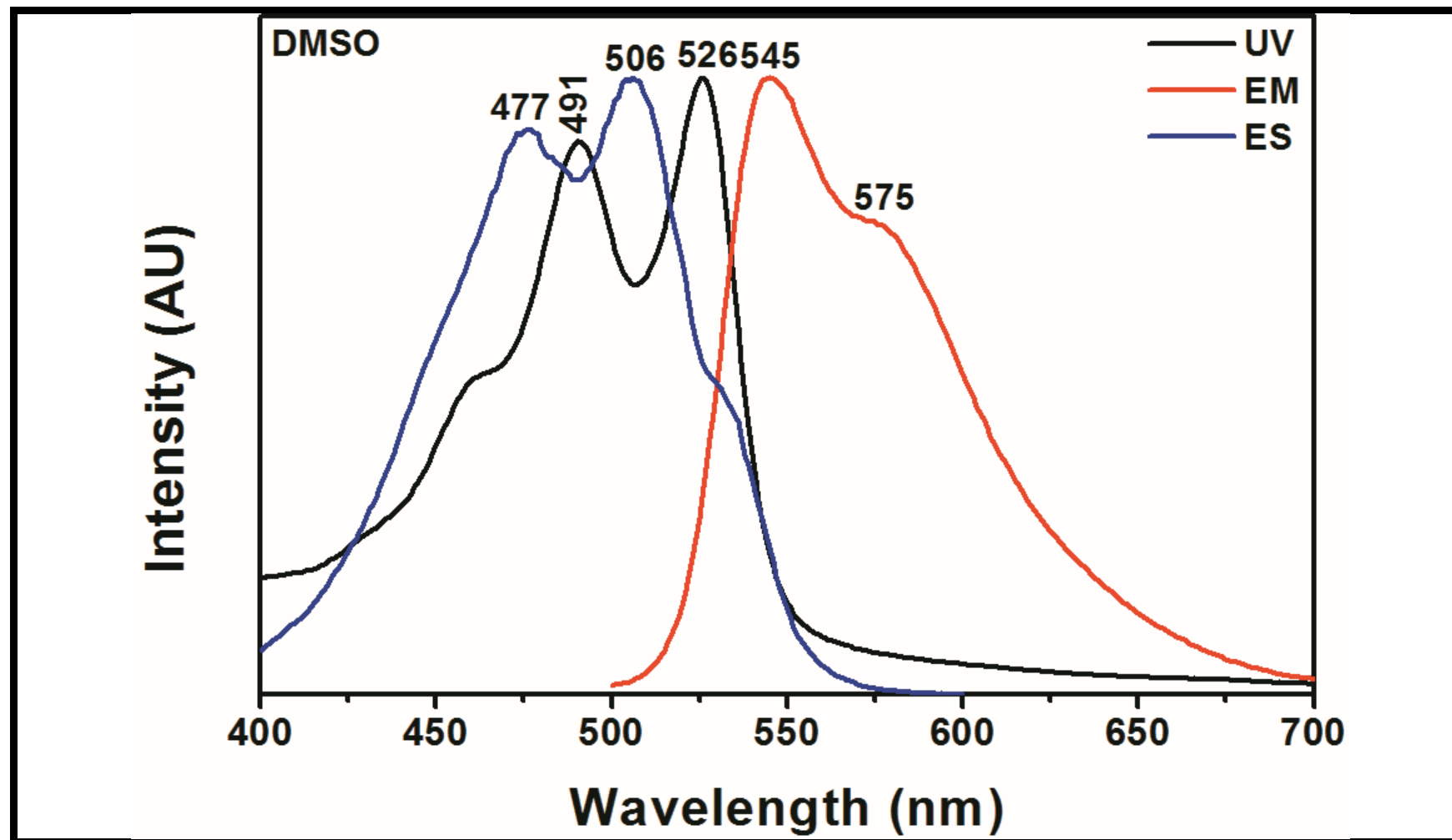
Figure 4.44: Normalized Absorption, Emission and Excitation Spectra of CH-PPI in Dimethyl sulfoxide
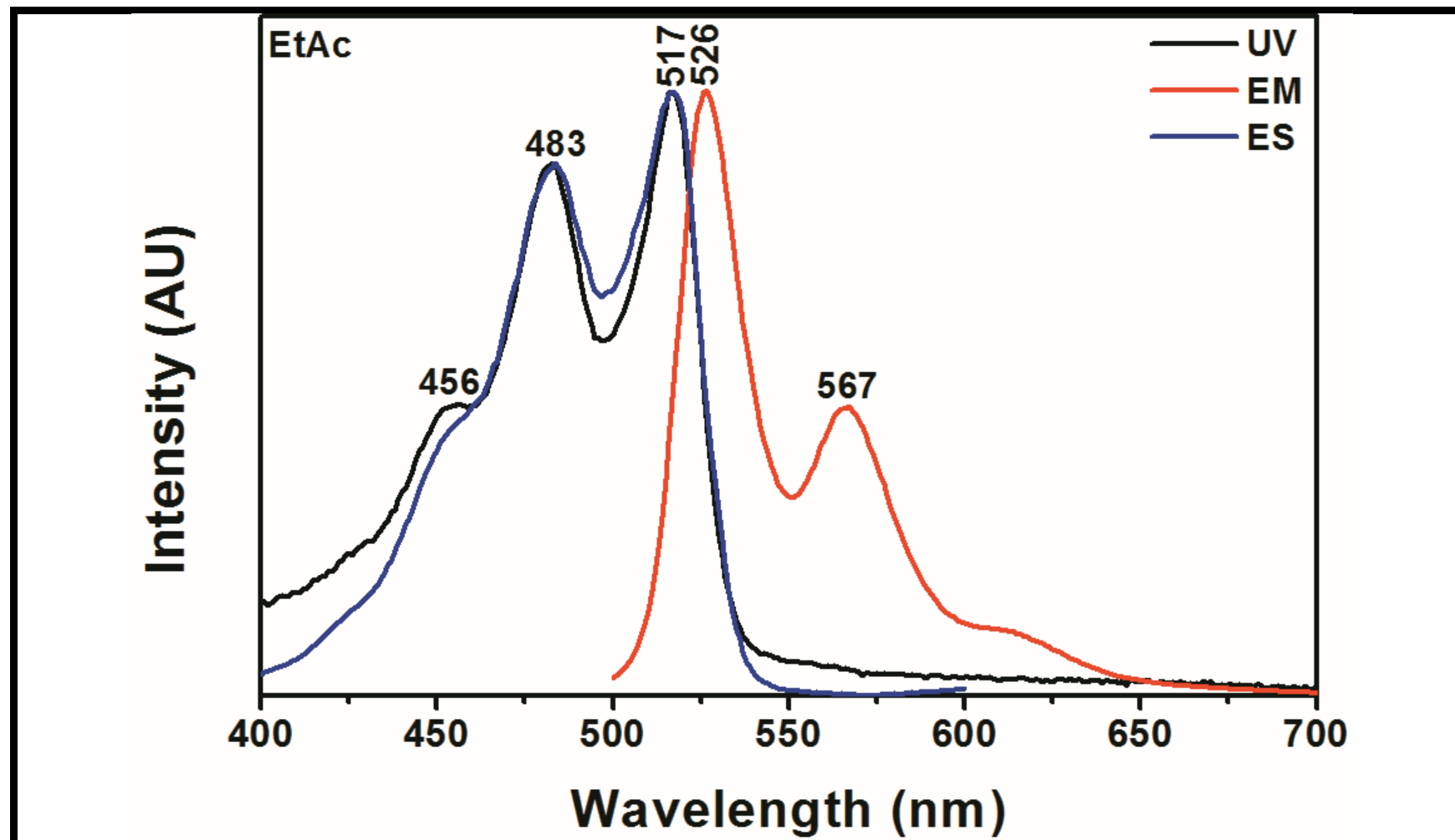
Figure 4.45: Normalized Absorption, Emission and Excitation Spectra of CH-PPI in Ethyl acetate
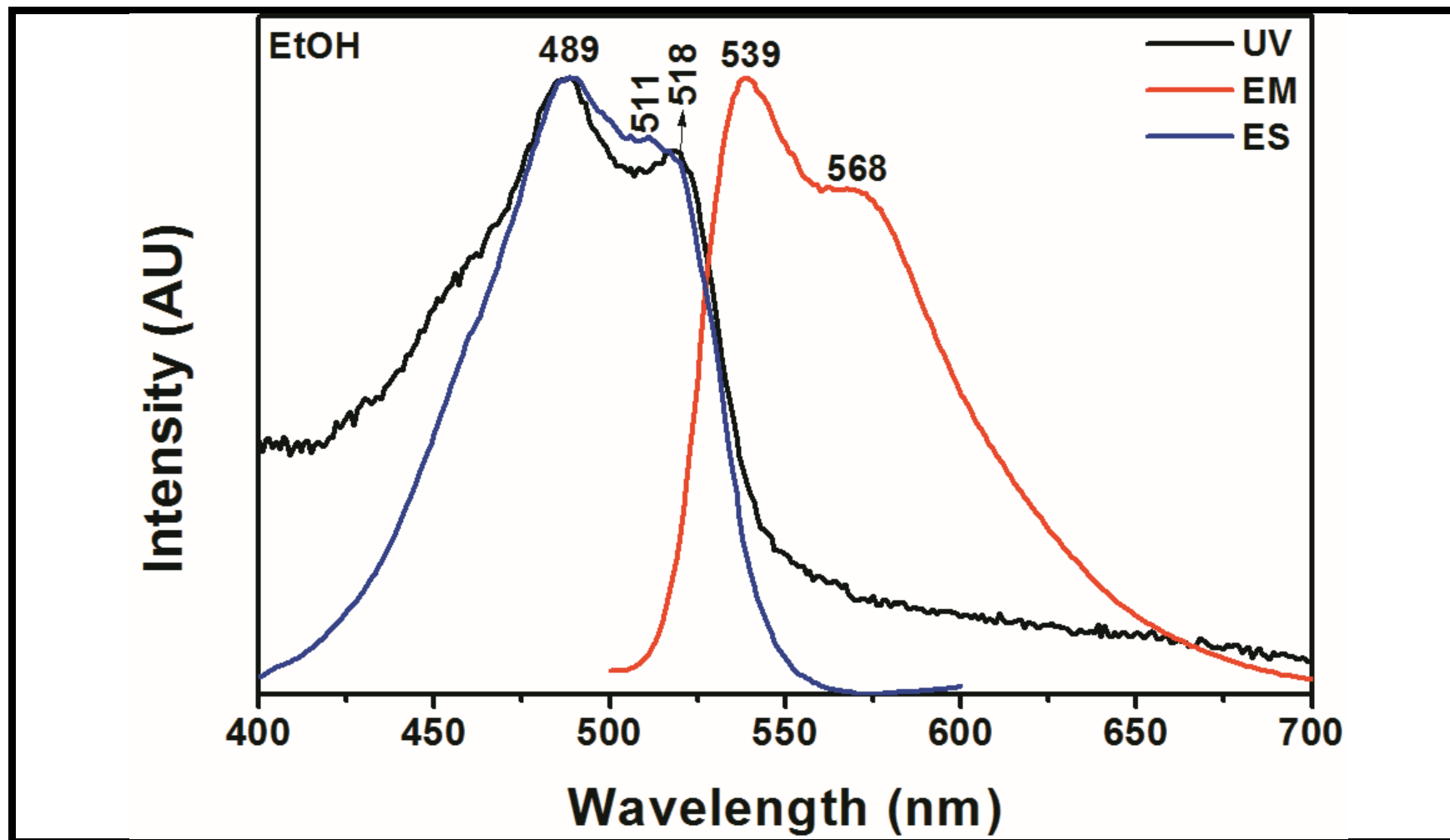
Figure 4.46: Normalized Absorption, Emission and Excitation Spectra of CH-PPI in Ethanol
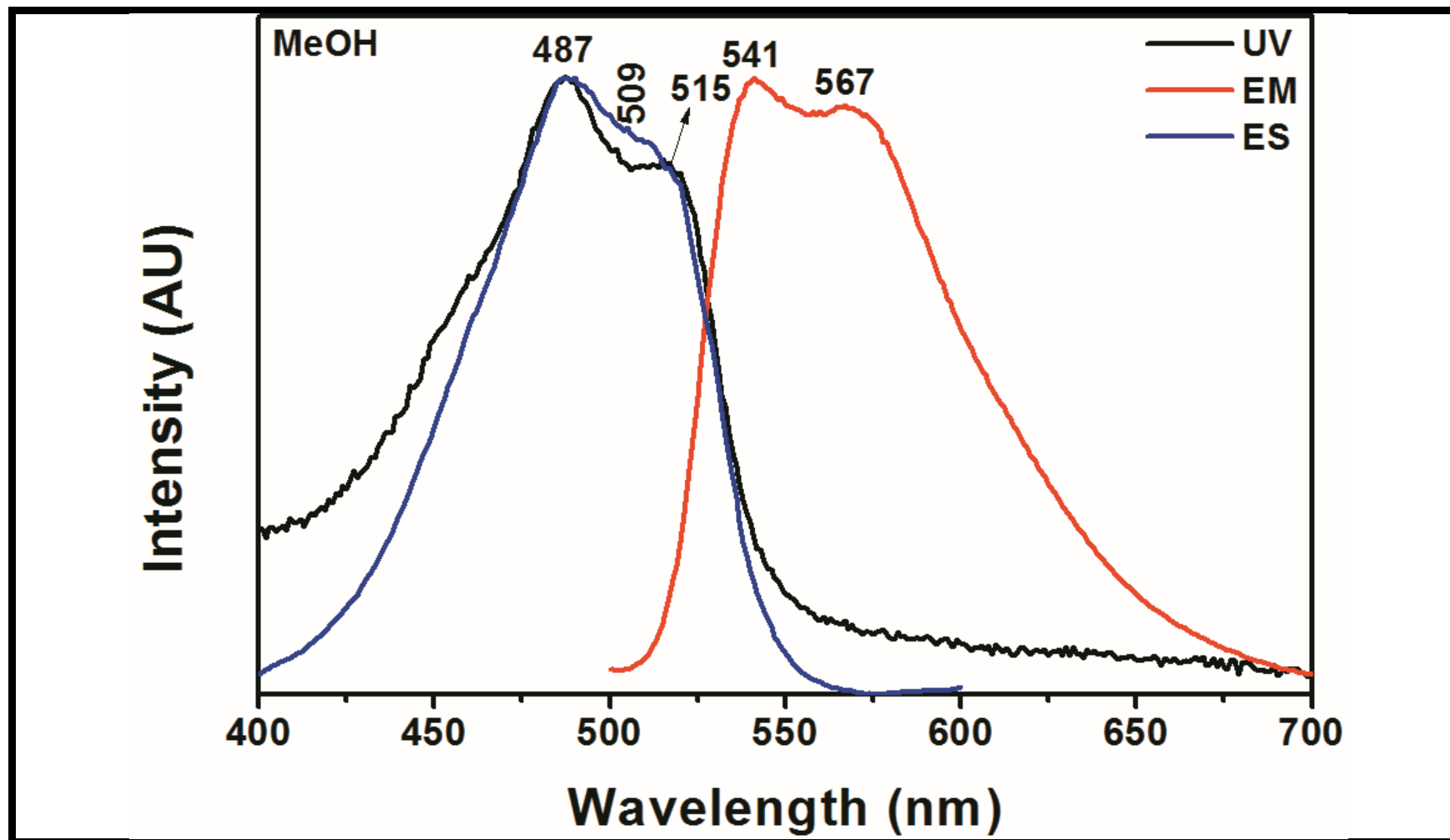
Figure 4.47: Normalized Absorption, Emission and Excitation Spectra of CH-PPI in Methanol
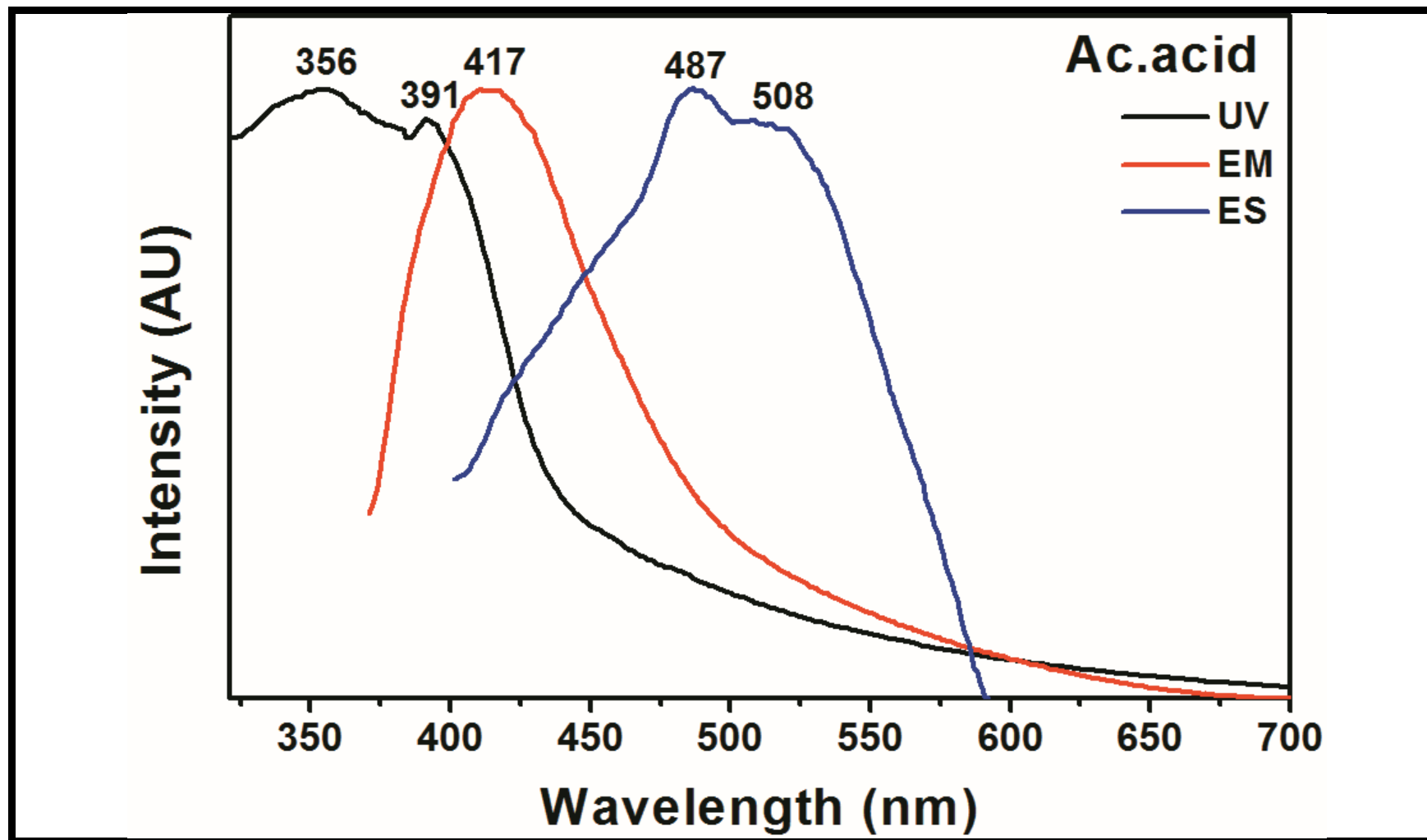
Figure 4.48: Normalized Absorption, Emission and Excitation Spectra of CH-PNI in Acetic acid
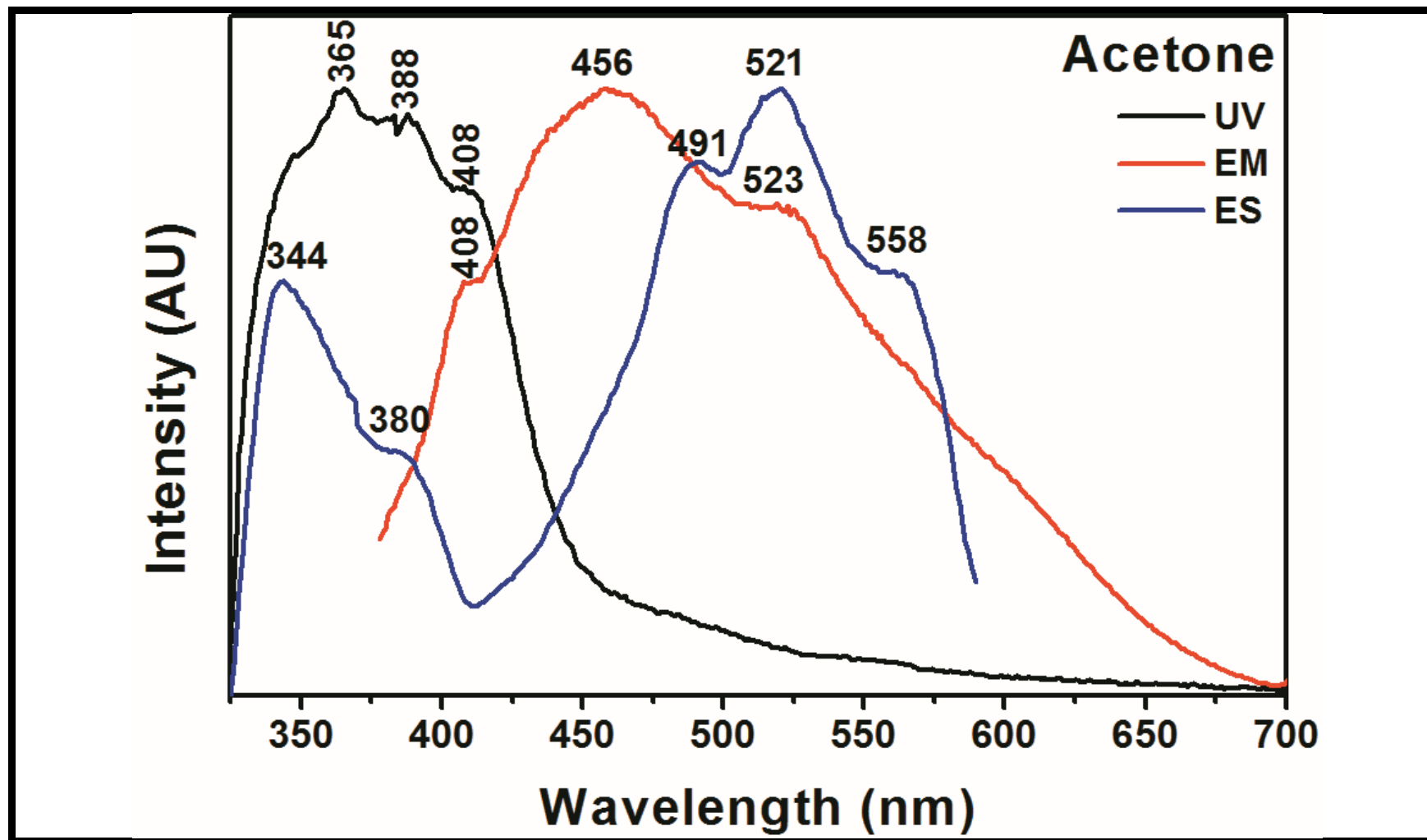
Figure 4.49: Normalized Absorption, Emission and Excitation Spectra of CH-PNI in Acetone
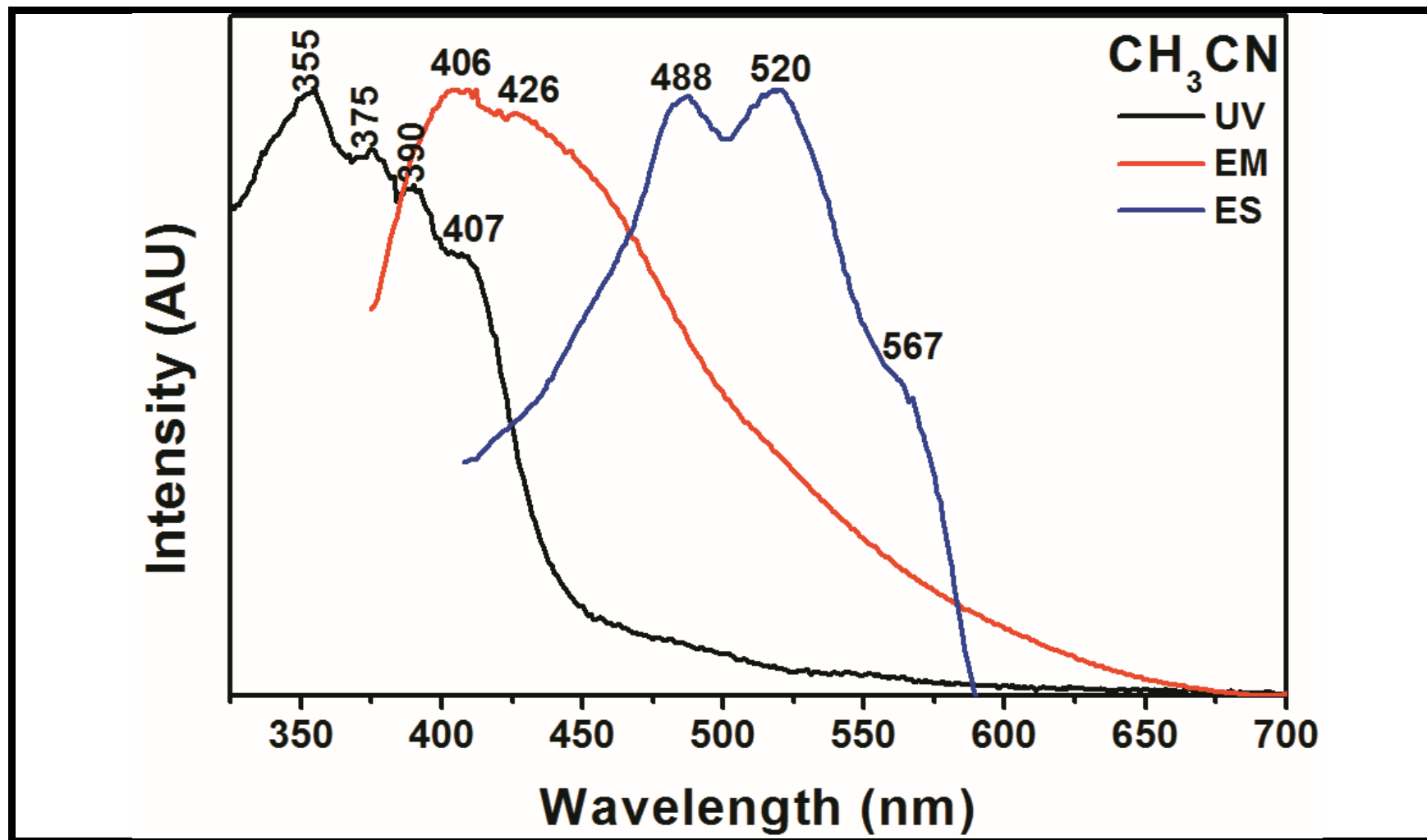
Figure 4.50: Normalized Absorption, Emission and Excitation Spectra of CH-PNI in Acetonitrile
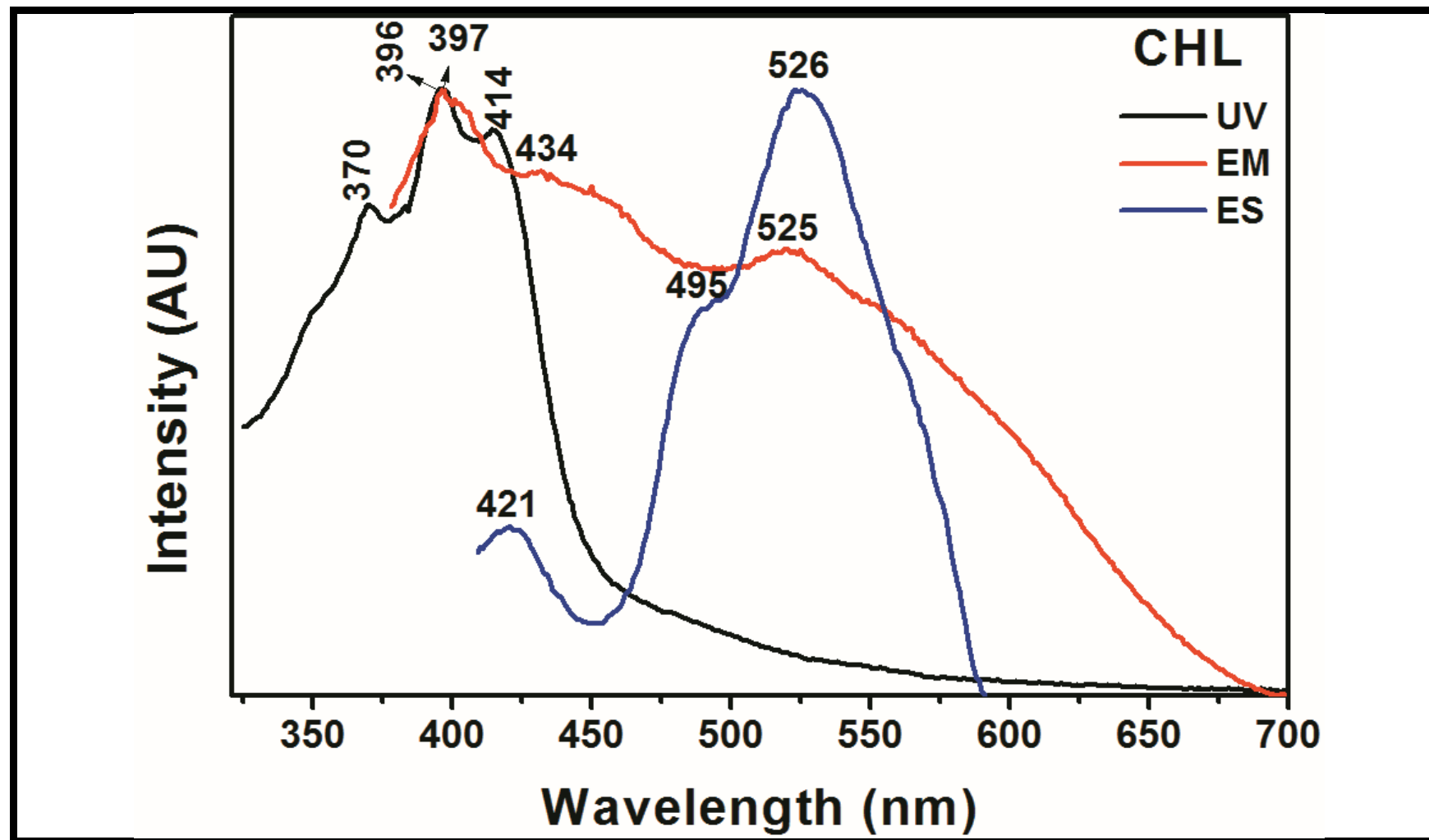
Figure 4.51: Normalized Absorption, Emission and Excitation Spectra of CH-PNI in Chloroform
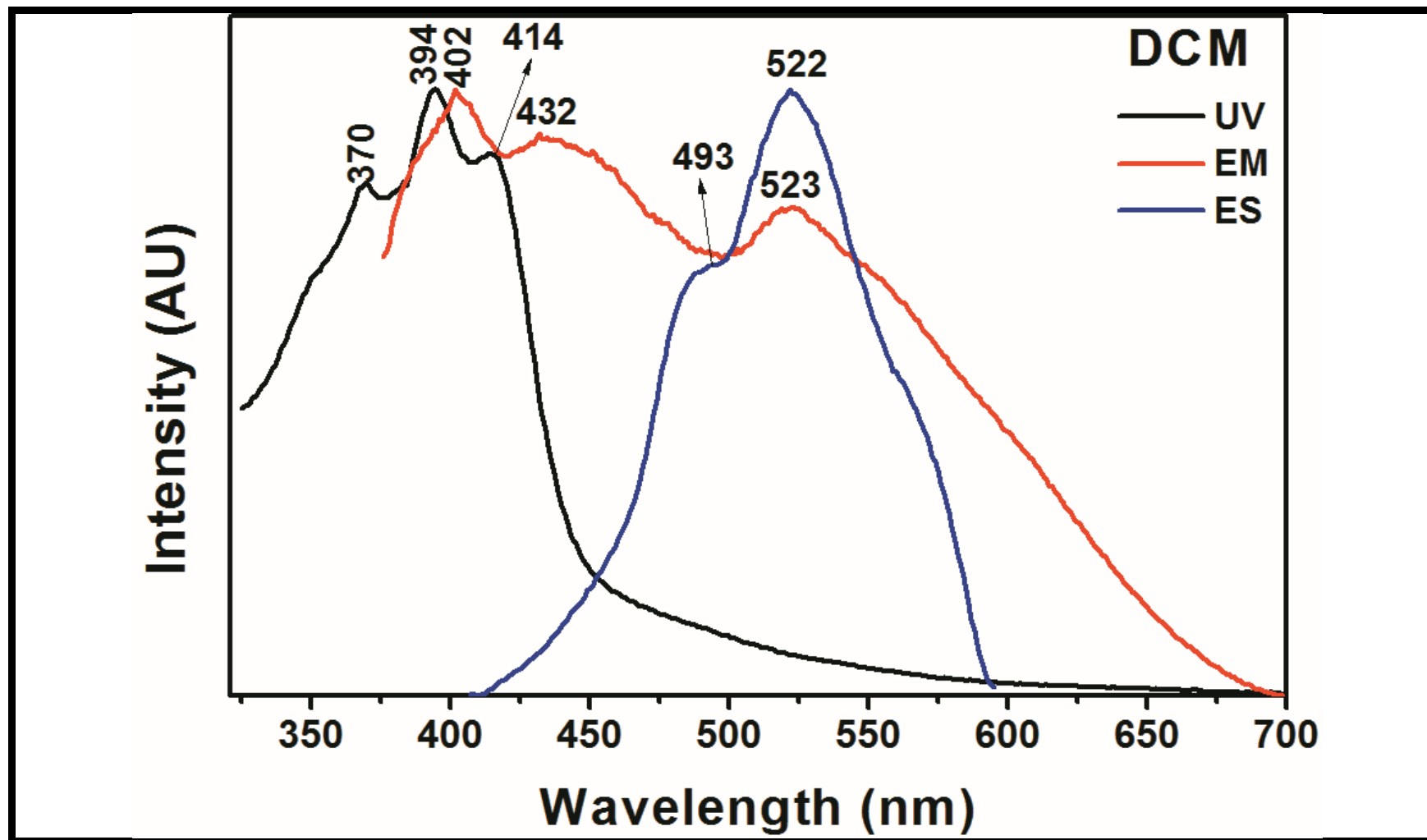
Figure 4.52: Normalized Absorption, Emission and Excitation Spectra of CH-PNI in Dicholoromethane
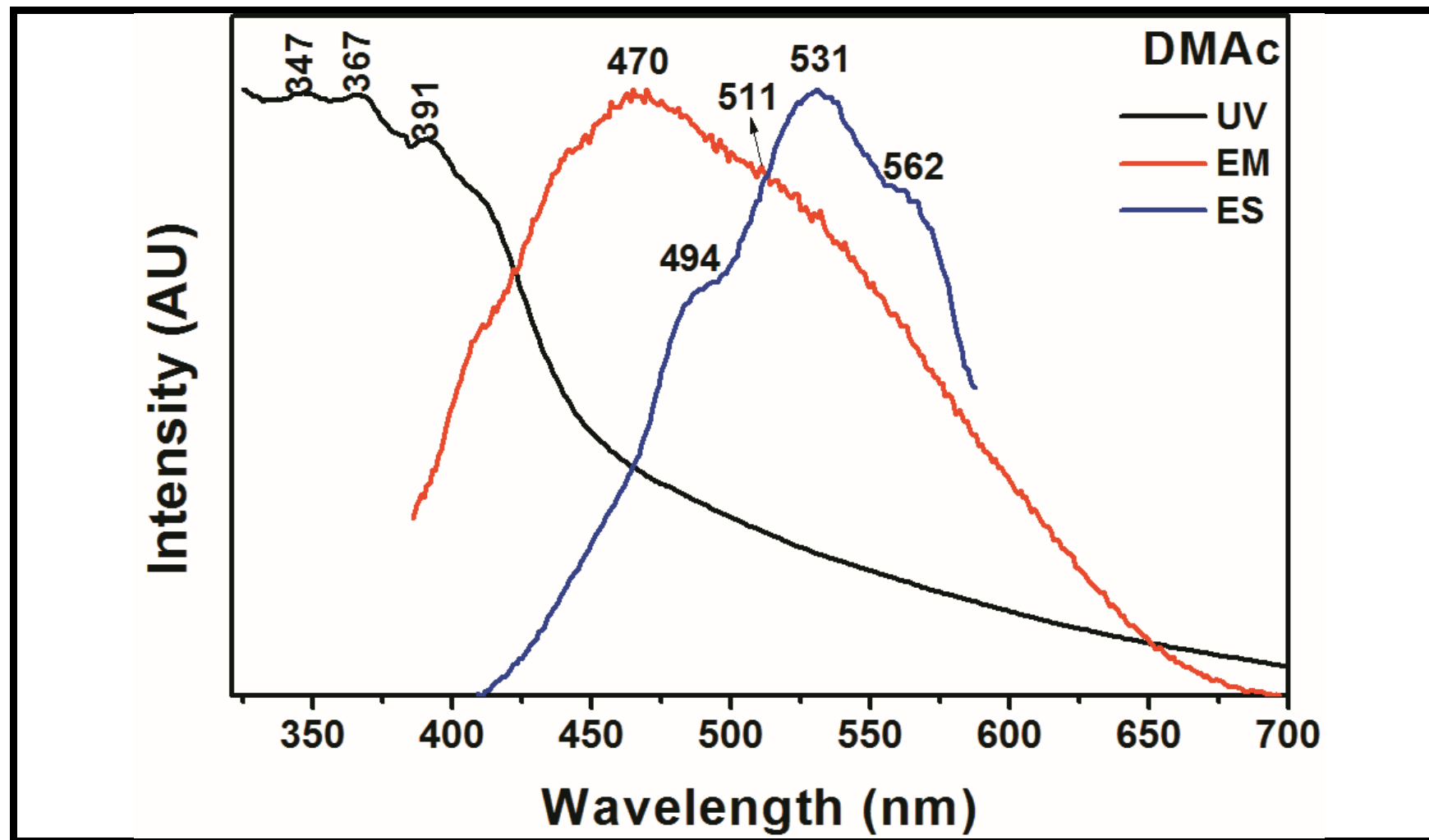
Figure 4.53: Normalized Absorption, Emission and Excitation Spectra of CH-PNI in Dimethylacetamide
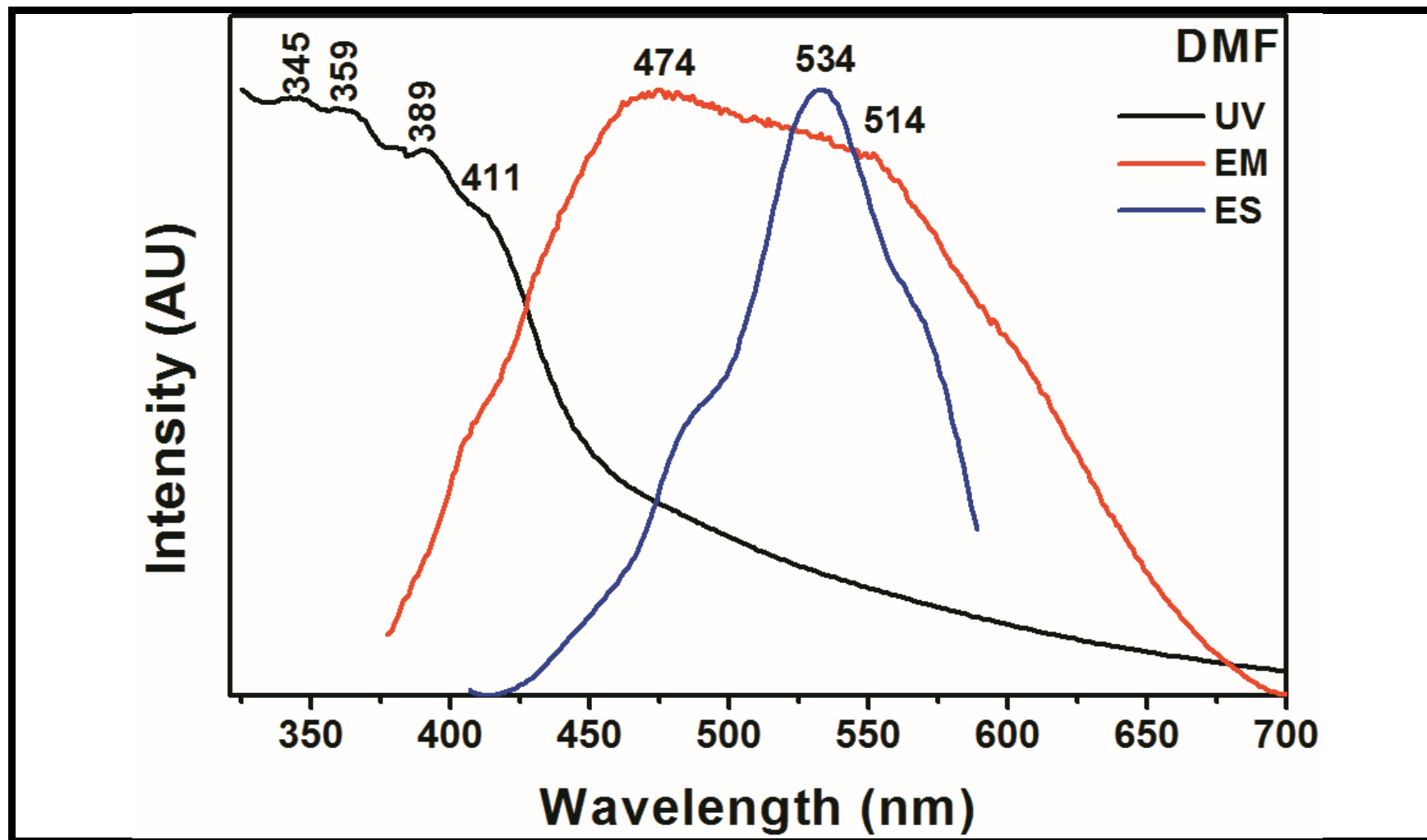
Figure 4.54: Normalized Absorption, Emission and Excitation Spectra of CH-PNI in Dimethylformamide
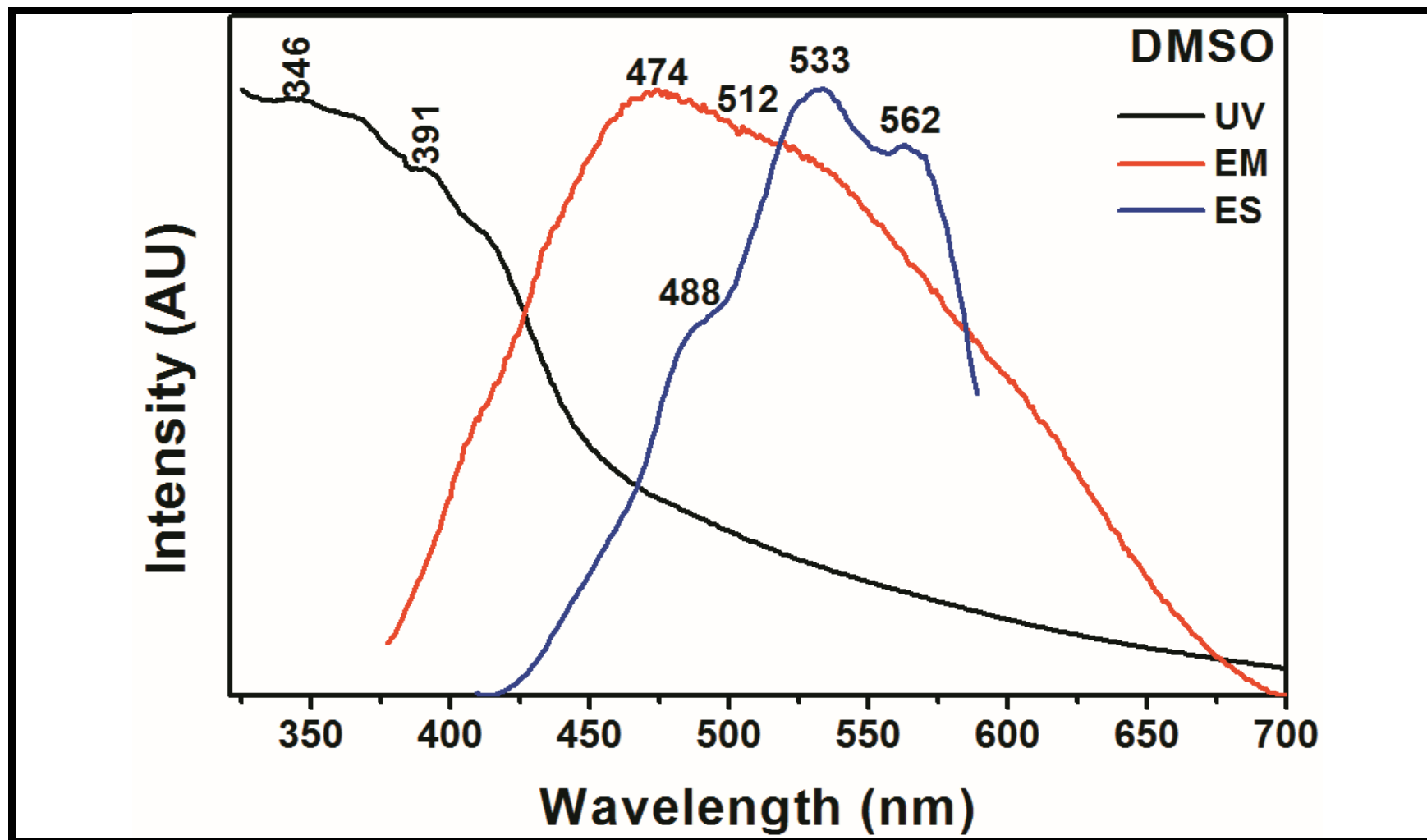
Figure 4.55: Normalized Absorption, Emission and Excitation Spectra of CH-PNI in Dimethyl sulfoxide
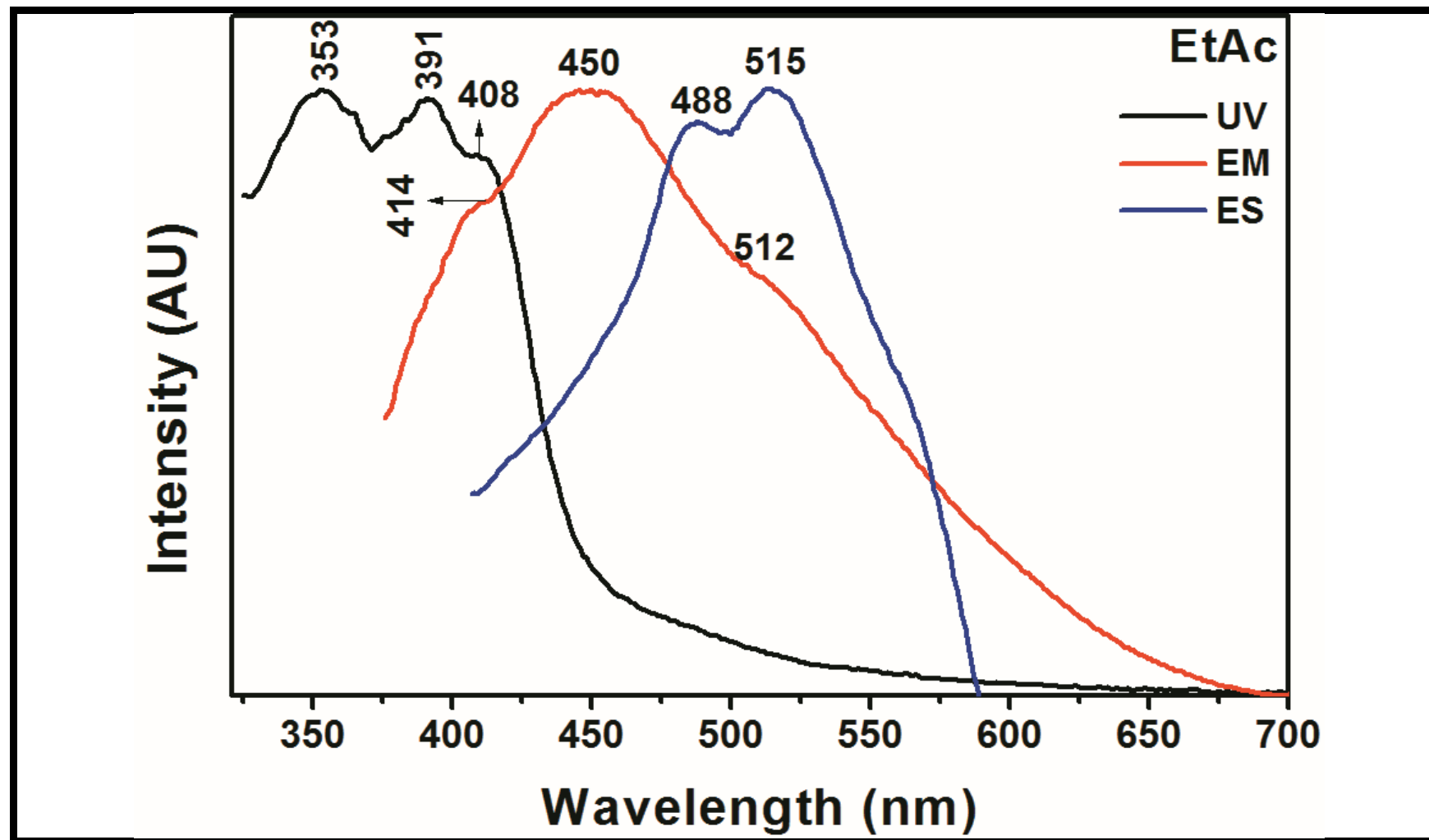
Figure 4.56: Normalized Absorption, Emission and Excitation Spectra of CH-PNI in Ethyl acetate
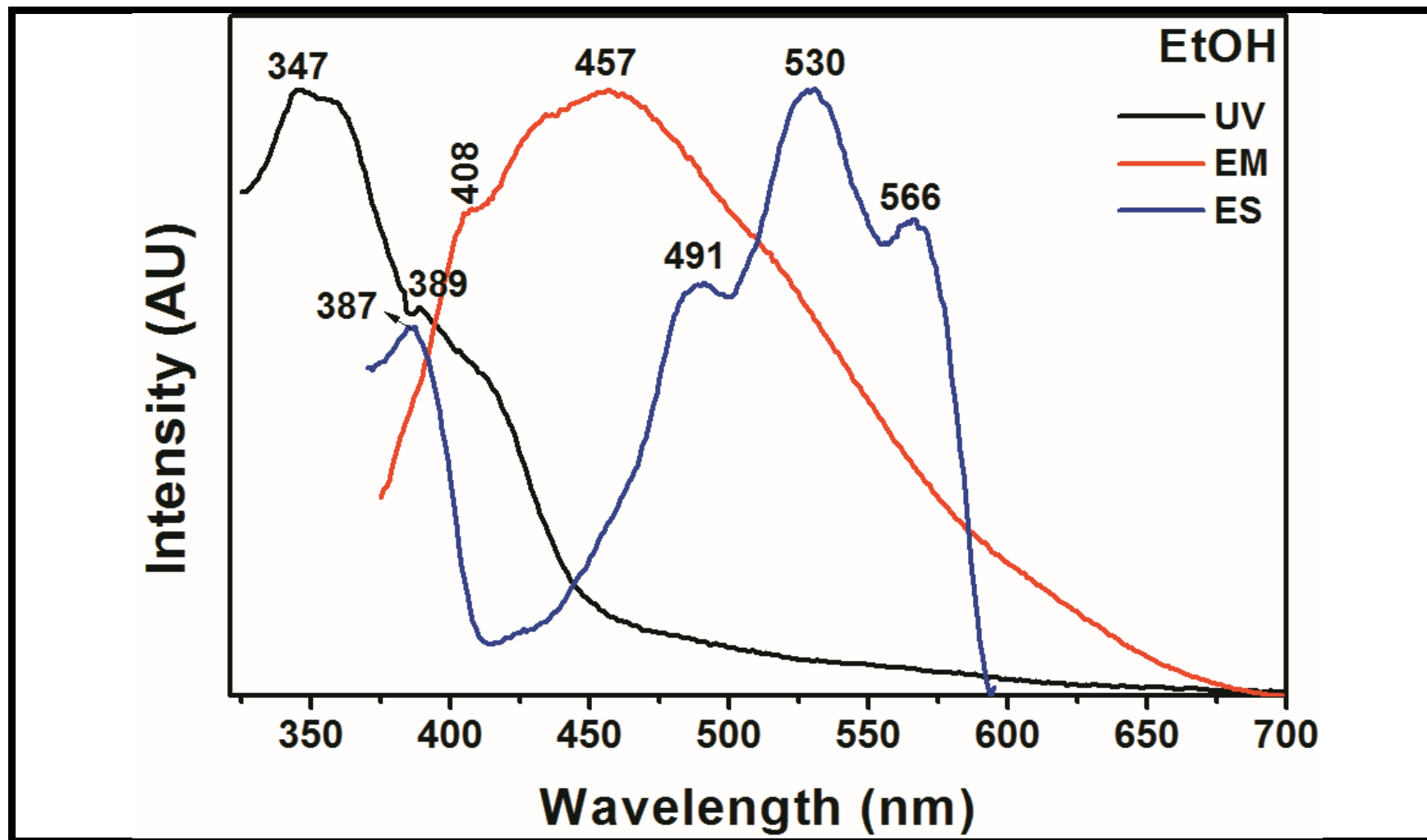
Figure 4.57: Normalized Absorption, Emission and Excitation Spectra of CH-PNI in Ethanol
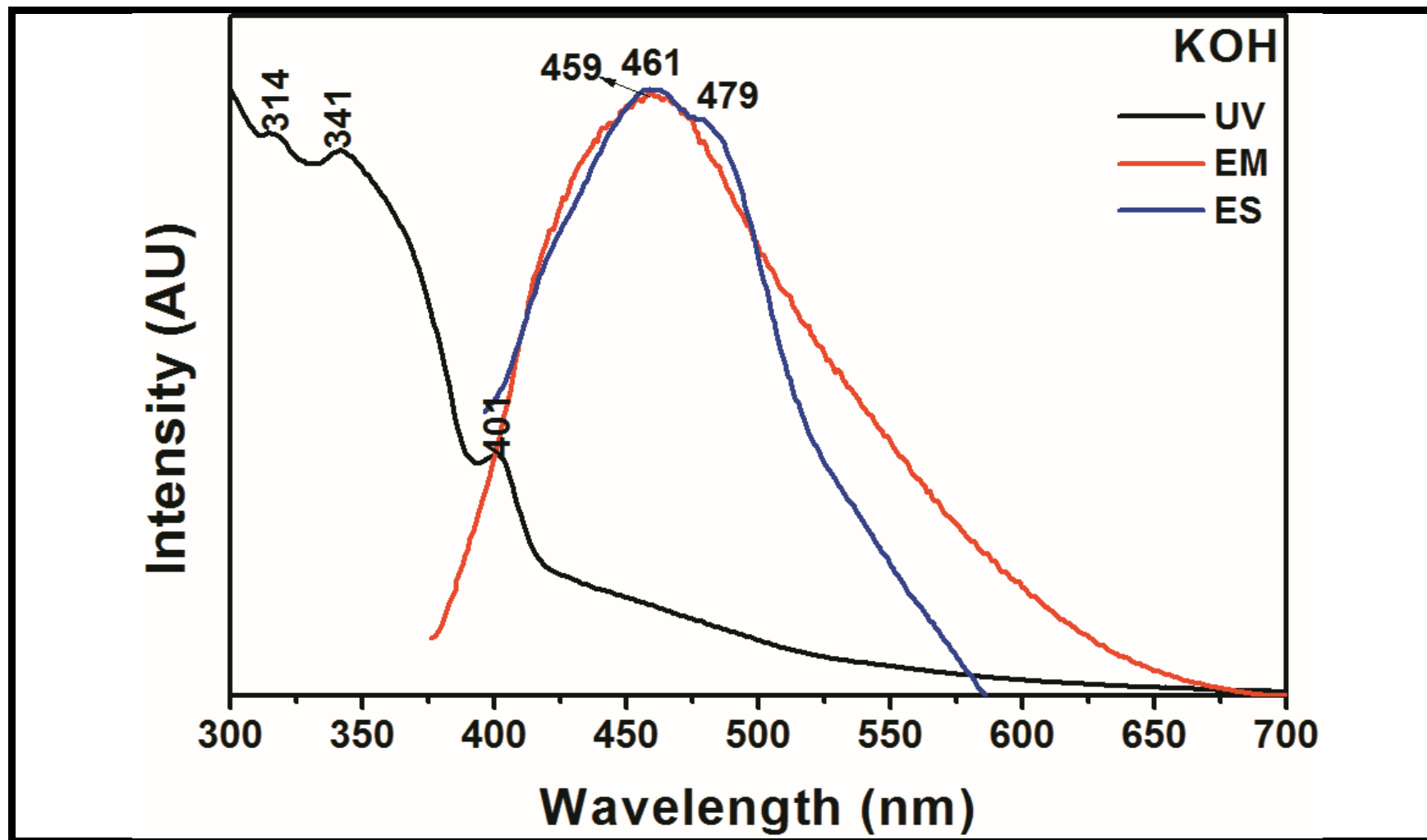
Figure 4.58: Normalized Absorption, Emission and Excitation Spectra of CH-PNI in Potassium Hydroxide
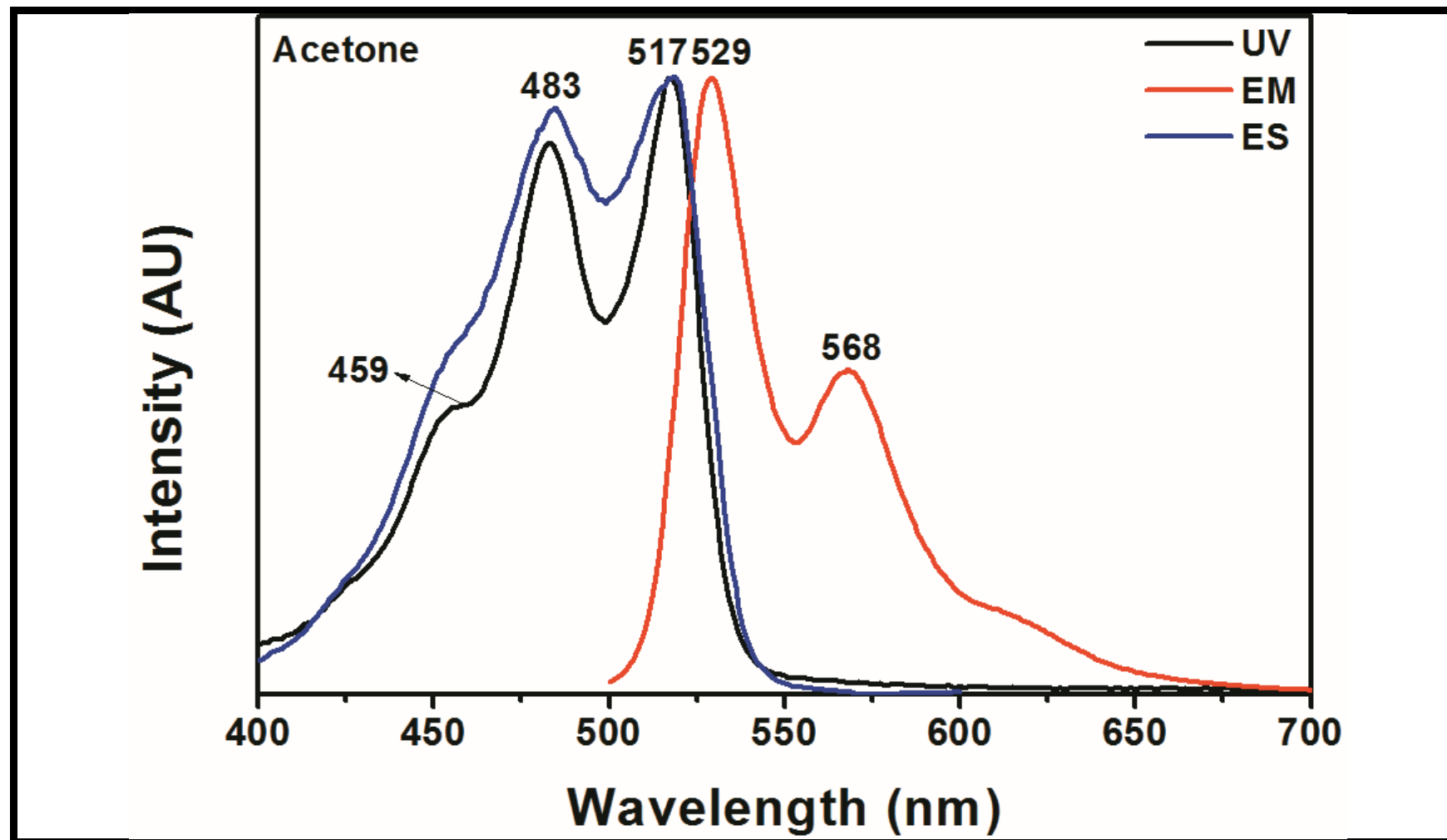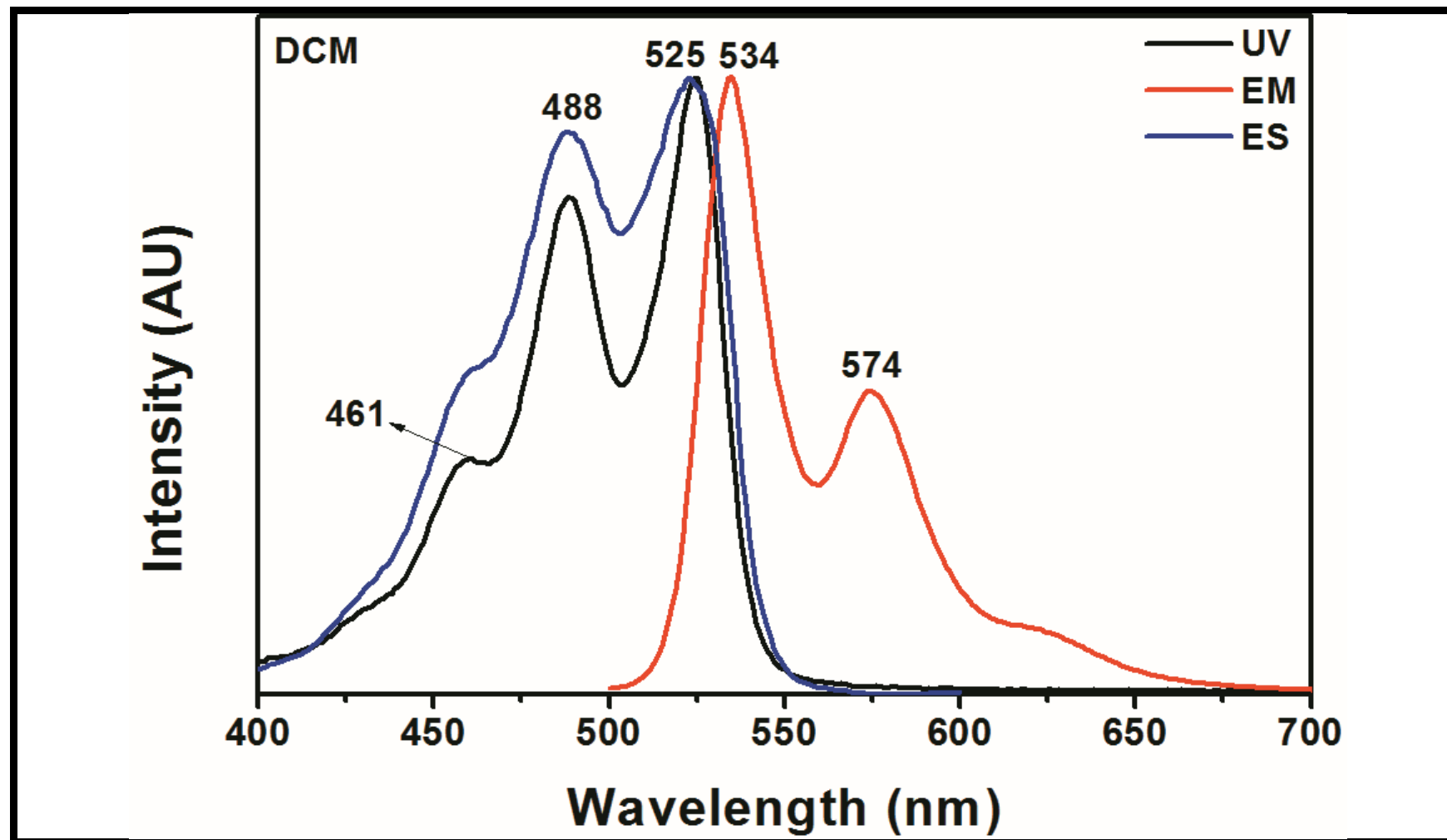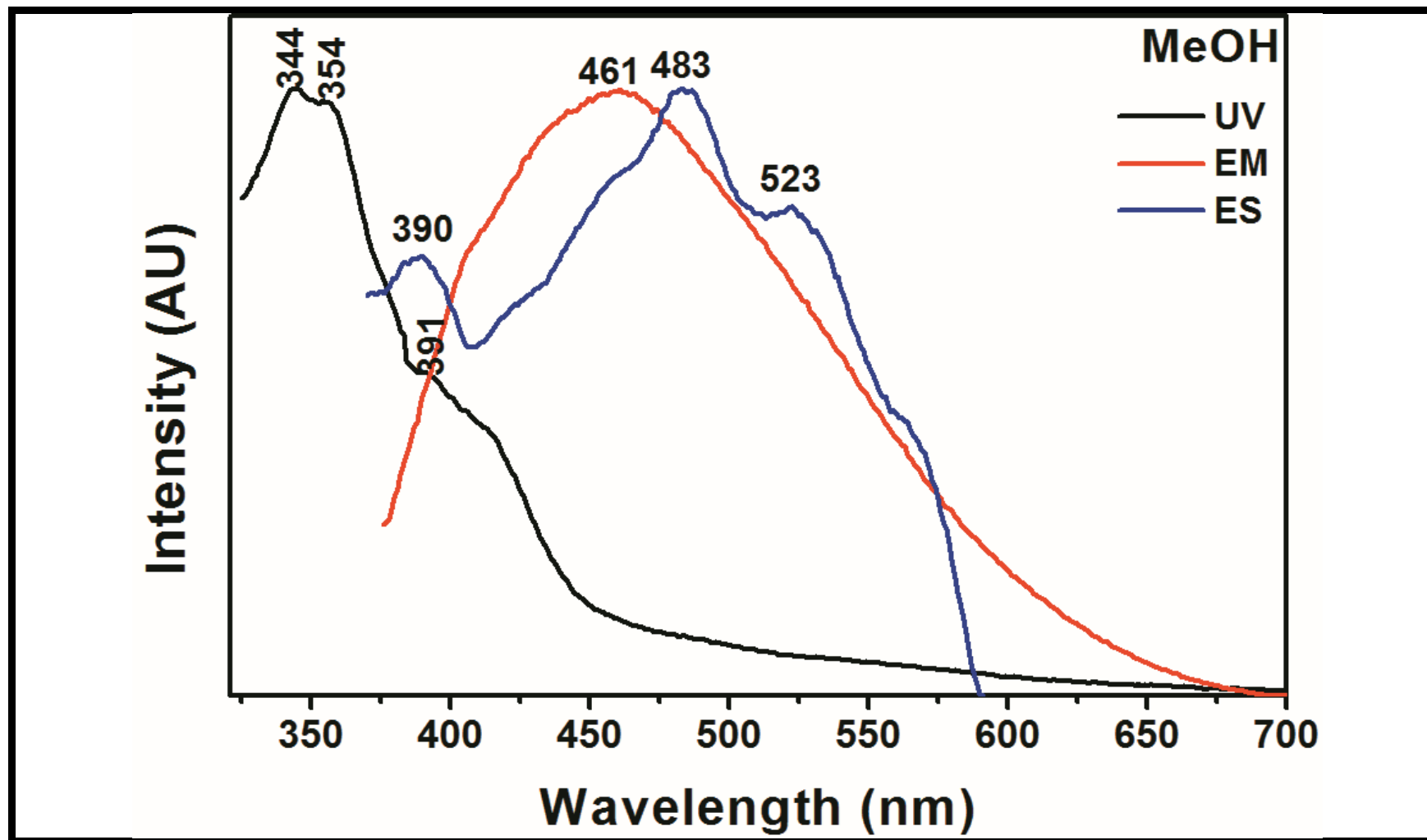
Figure 4.59: Normalized Absorption, Emission and Excitation Spectra of CH-PNI in Methanol
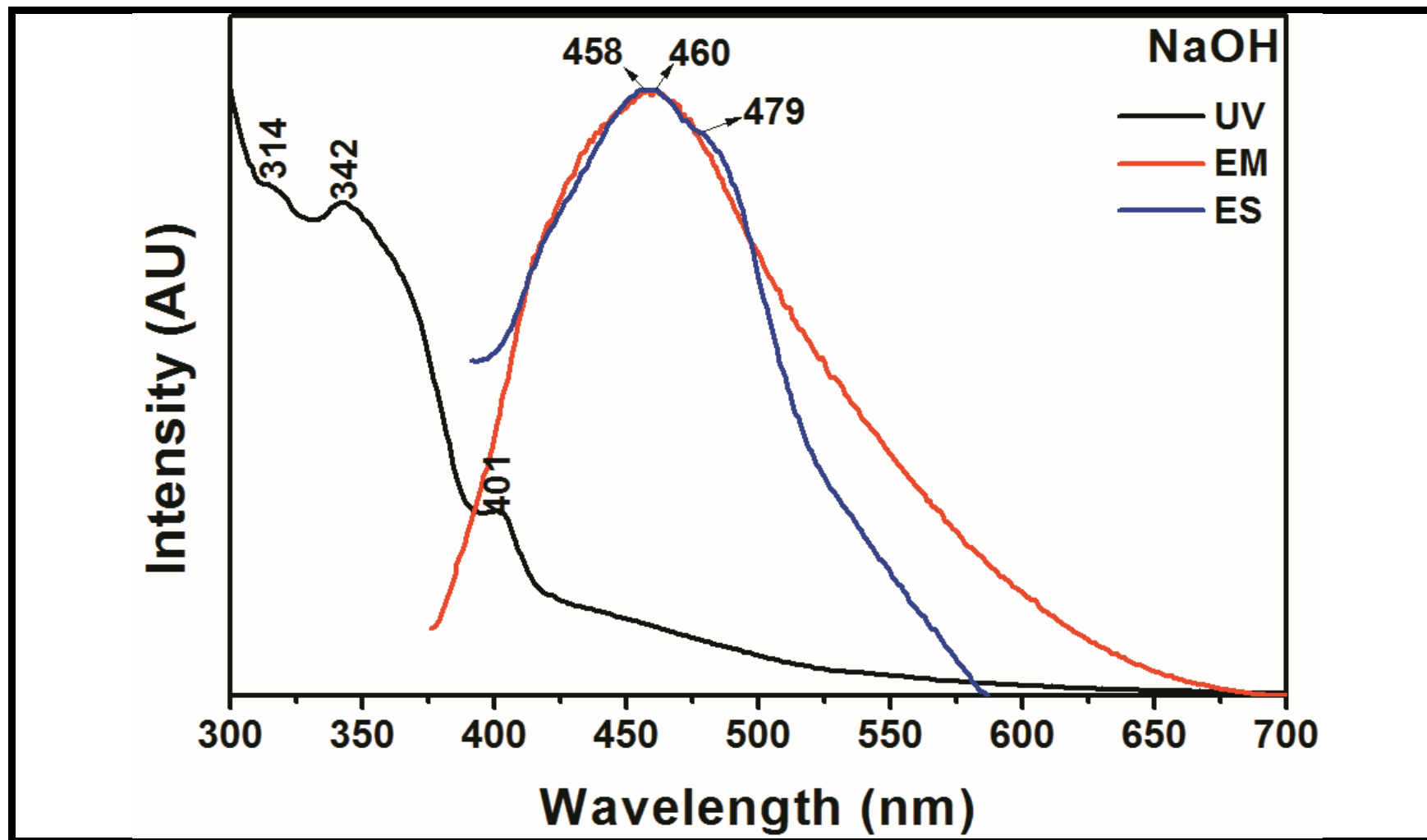
Figure 4.60: Normalized Absorption, Emission and Excitation Spectra of CH-PNI in Sodium Hydroxide
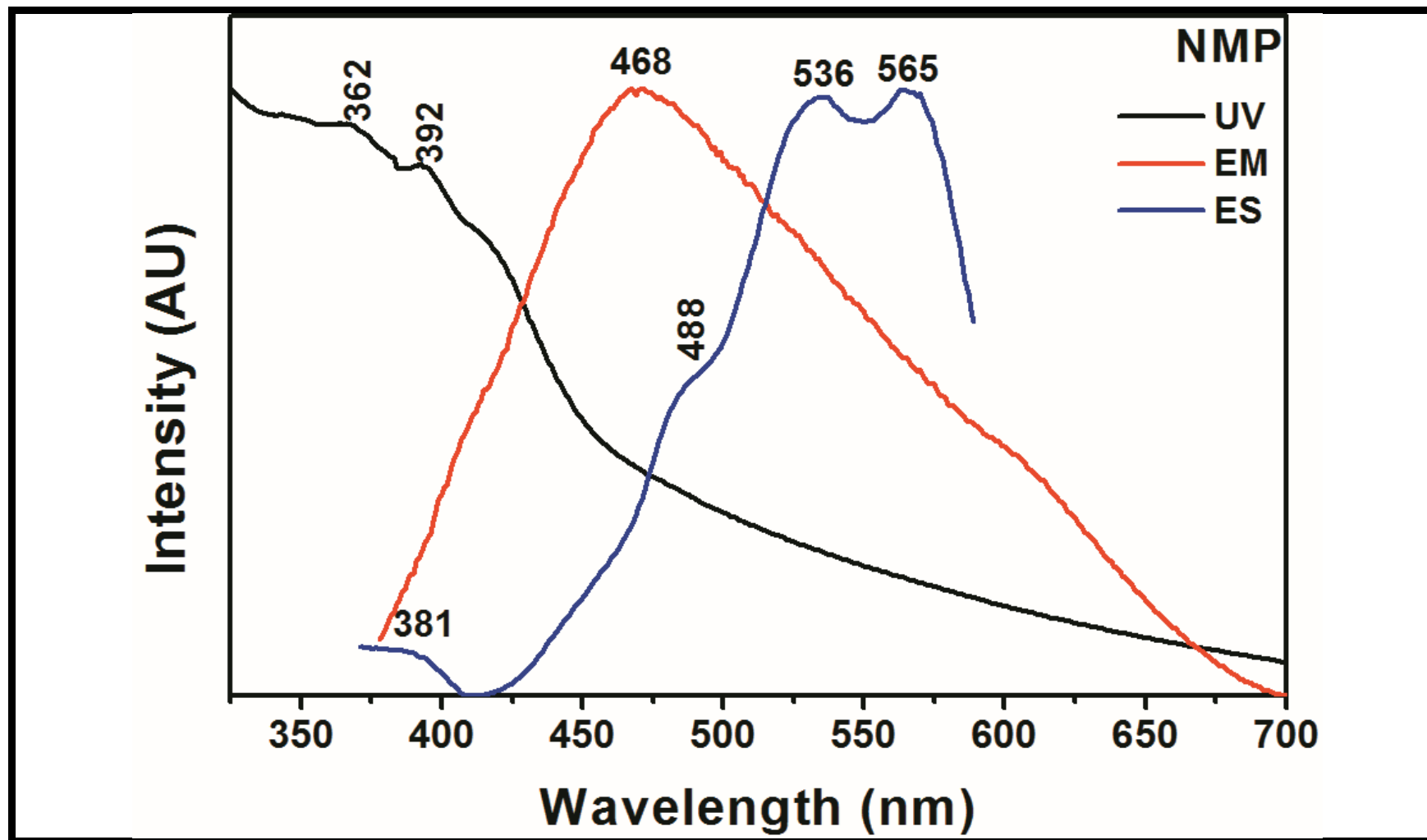
Figure 4.61: Normalized Absorption, Emission and Excitation Spectra of CH-PNI in N-methylpyrrolidone

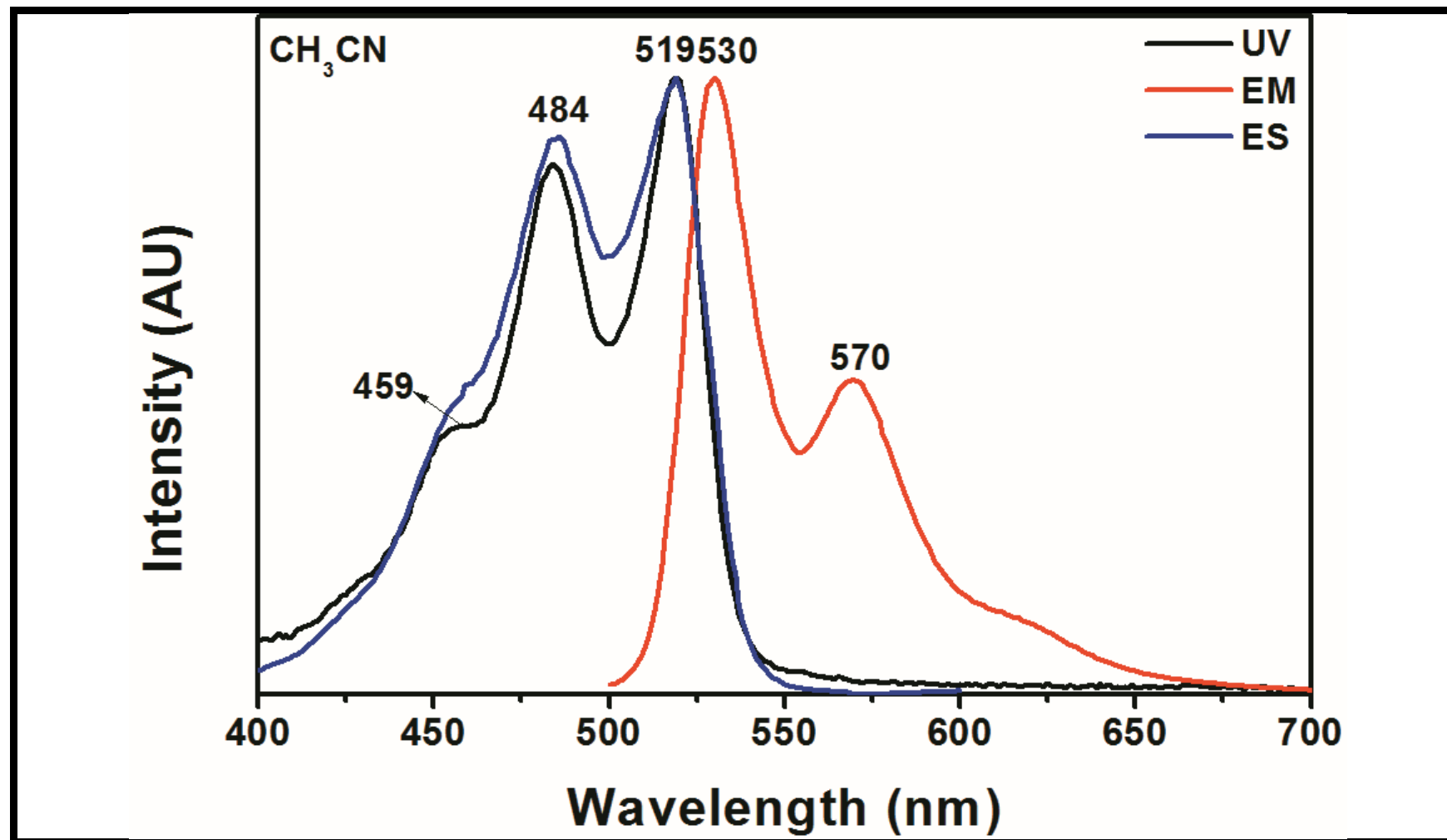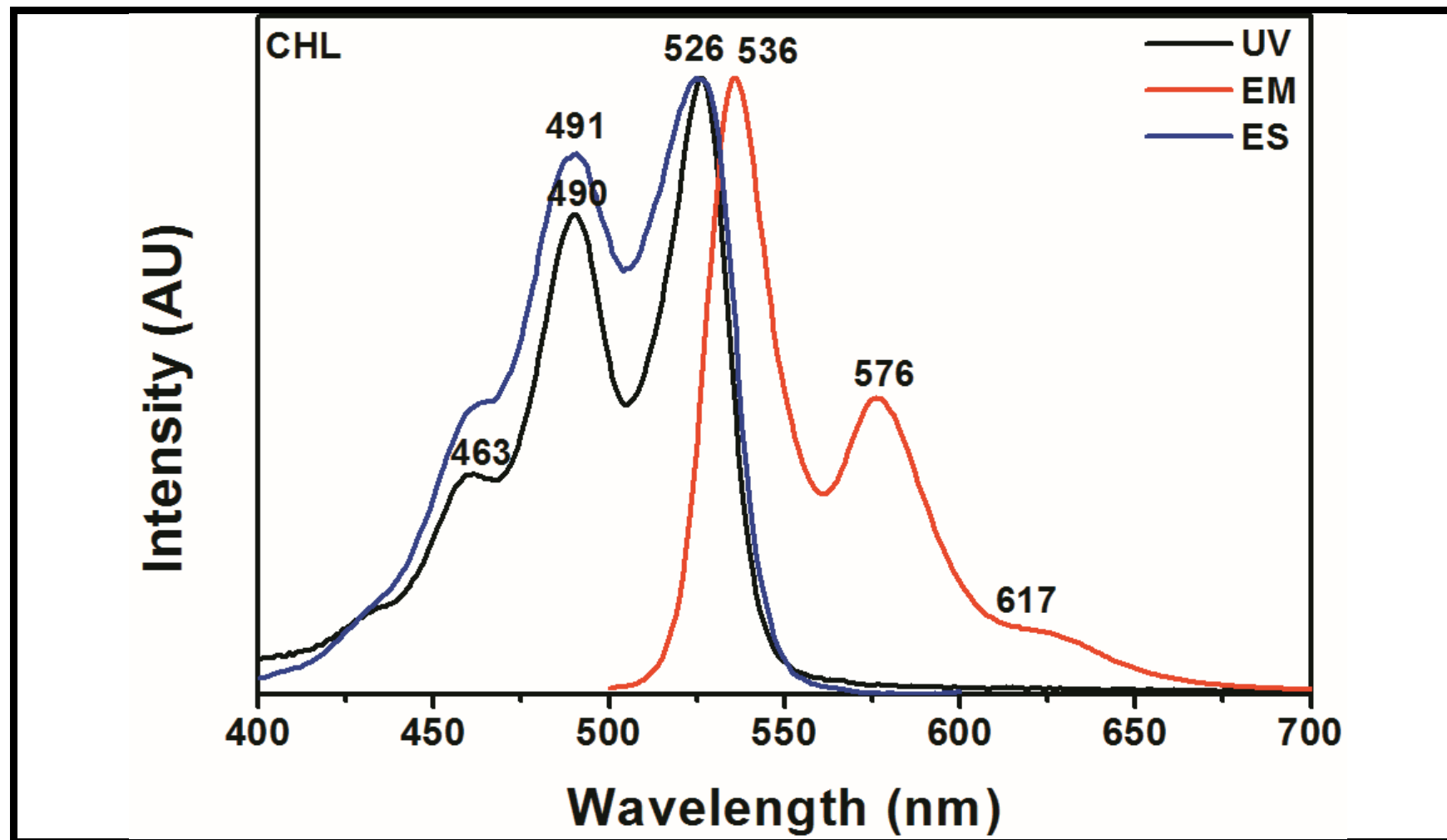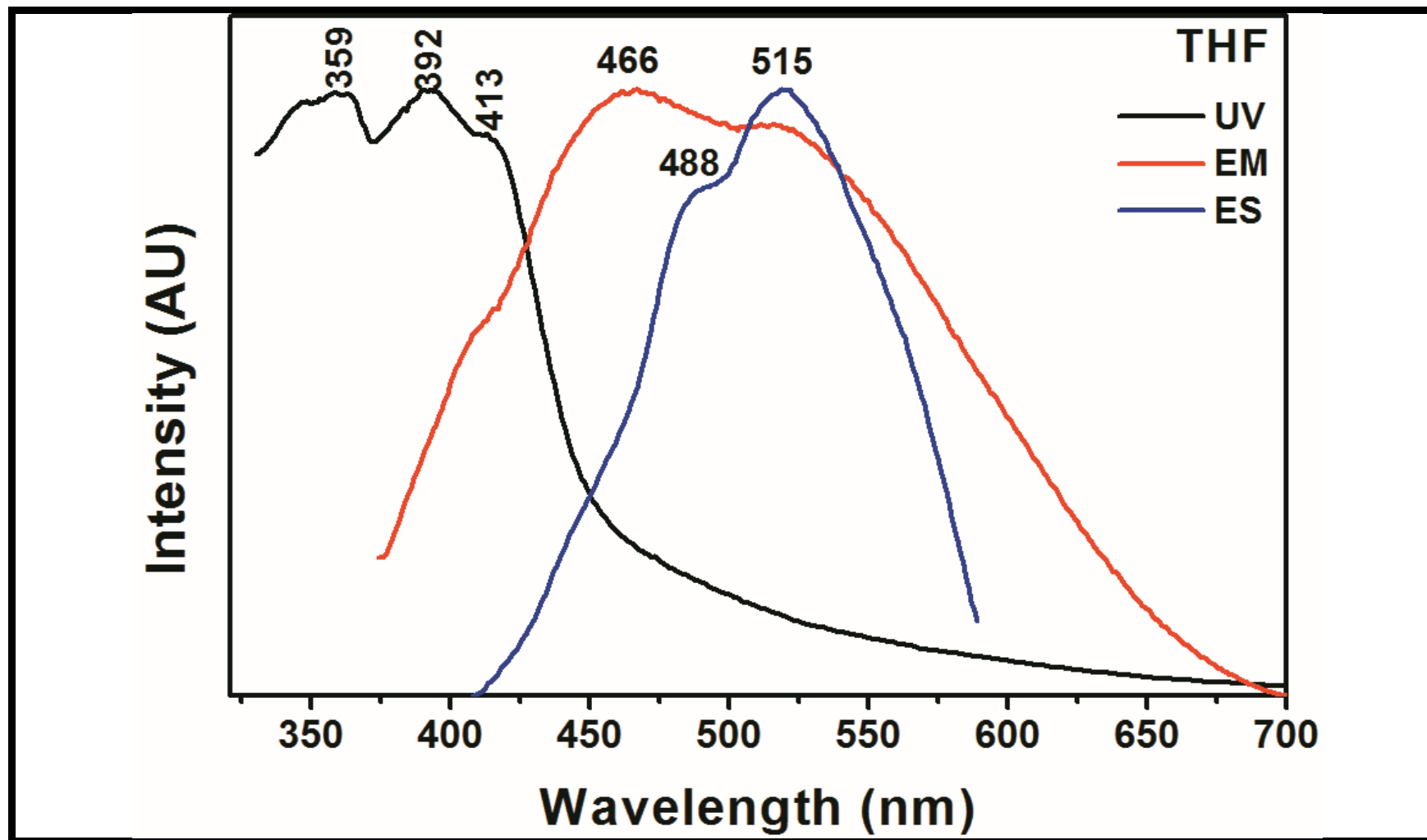Figure 4.62: Normalized Absorption, Emission and Excitation Spectra of CH-PNI in Tetrahydrofuran
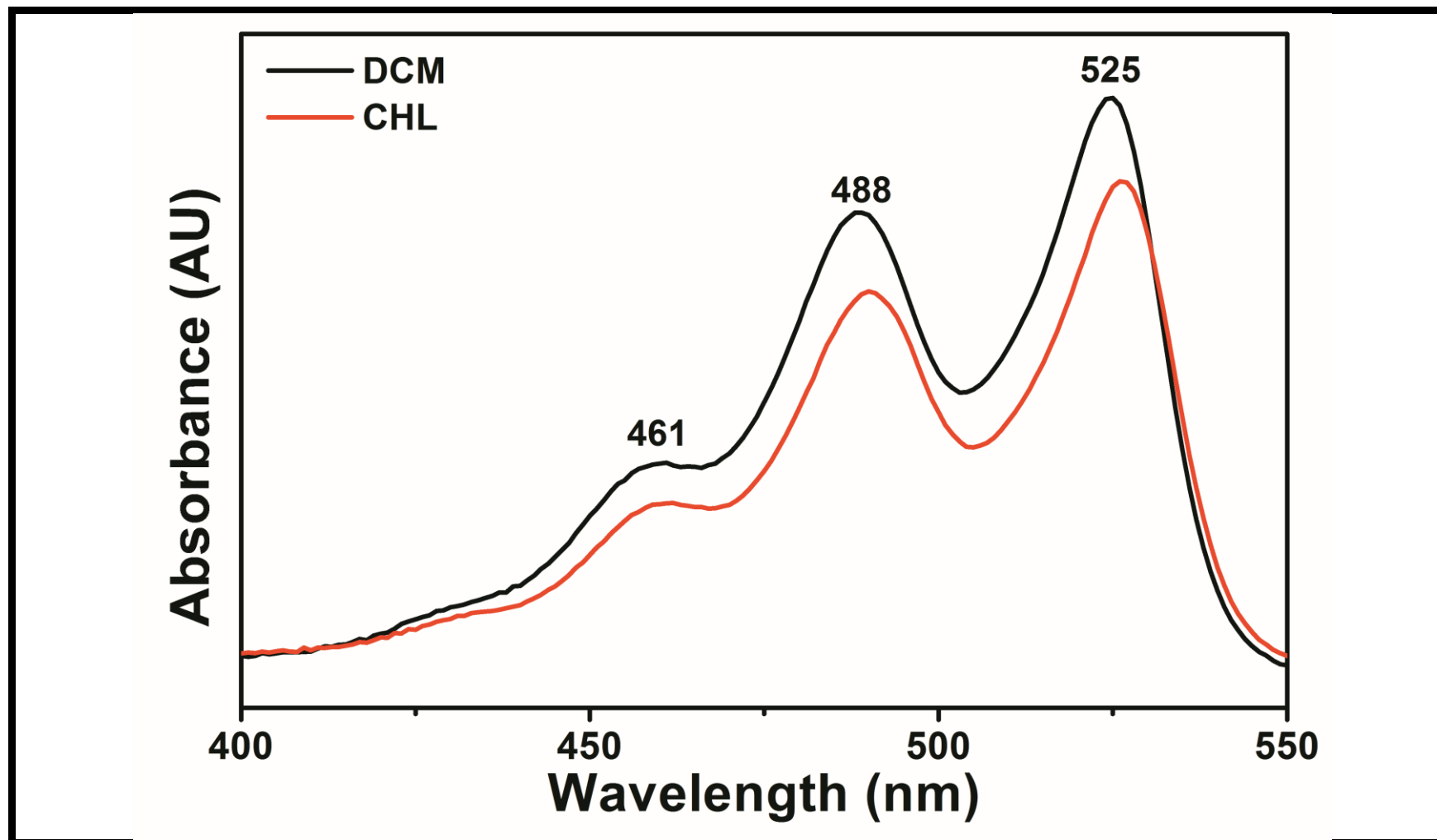
Figure 4.63: Overlap UV-vis Absorption Spectra of CH-PPI in Apolar Solvents
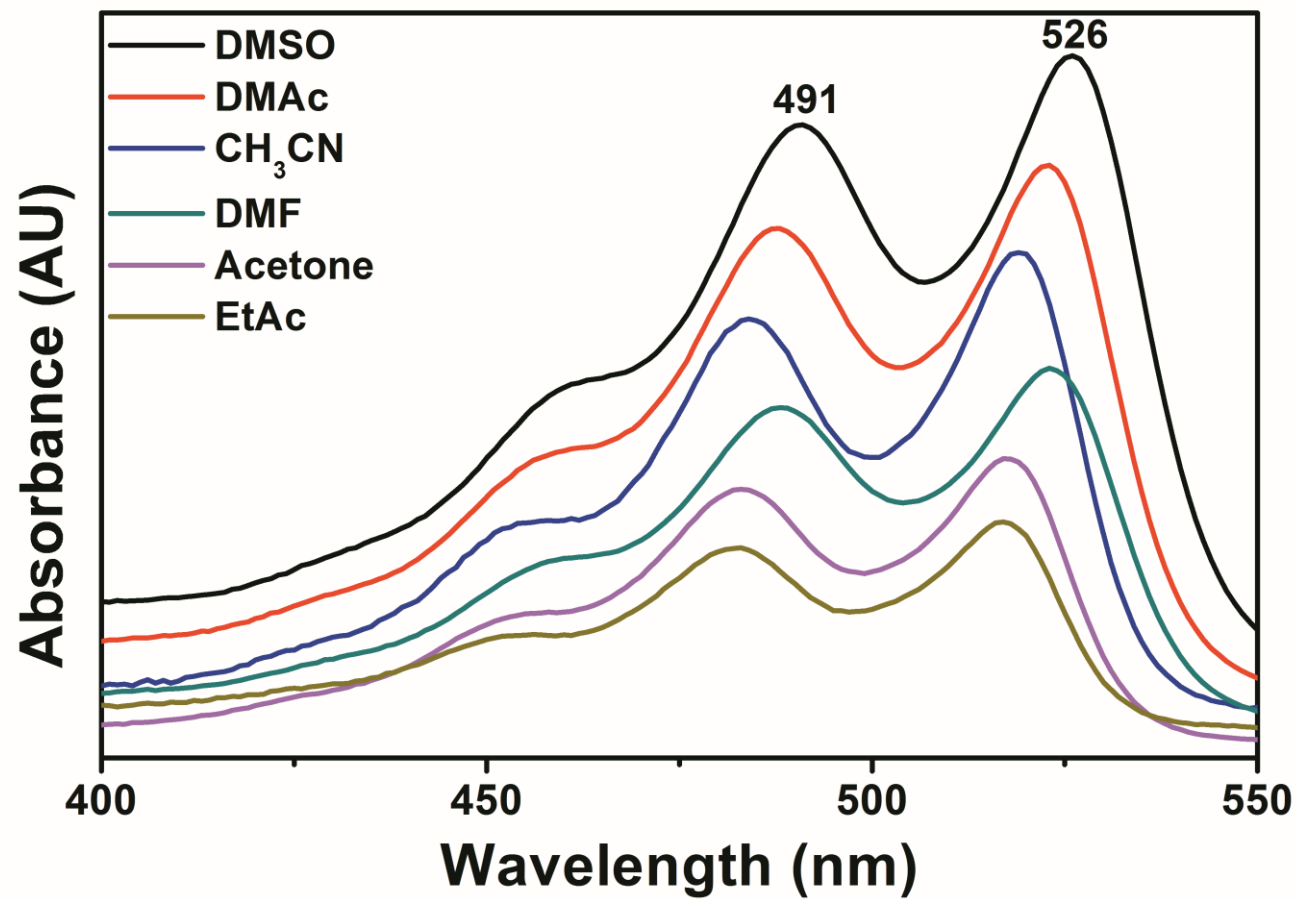
Figure 4.64: Overlap UV-vis Absorption Spectra of CH-PPI in Aprotic Solvents
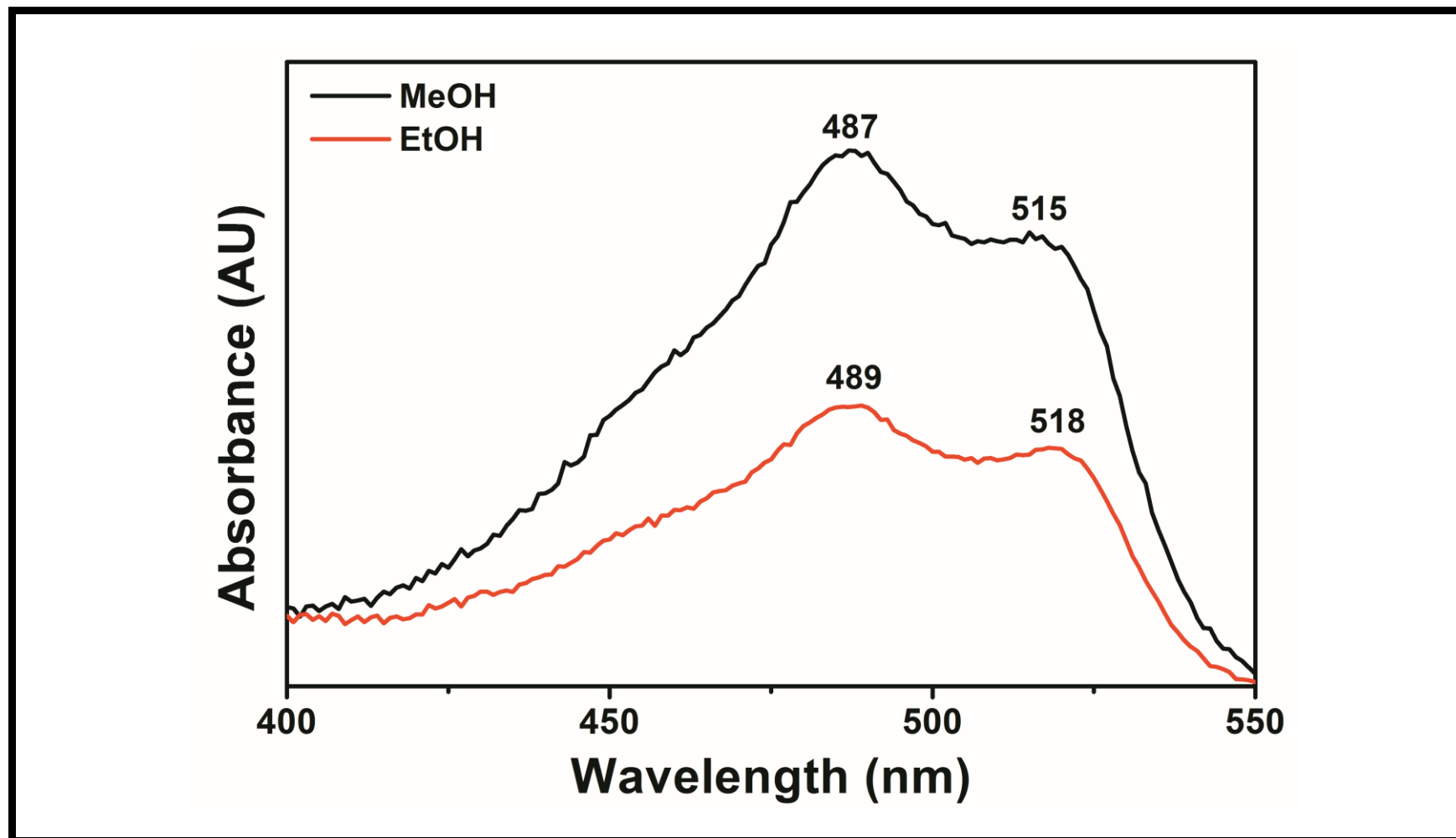
Figure 4.65: Overlap UV-vis Absorption Spectra of CH-PPI in Protic Solvents
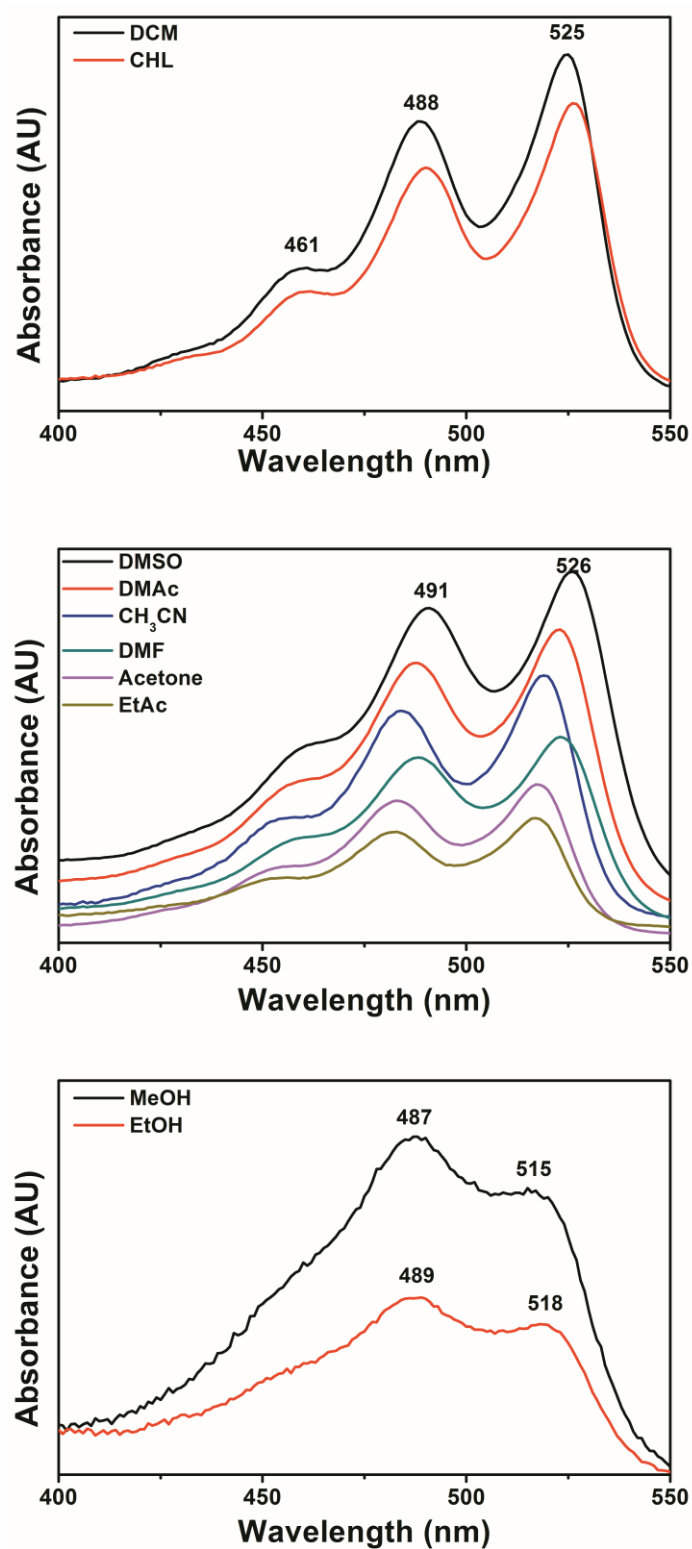
Figure 4.66: Comparison of UV-vis Absorption Spectra of CH-PPI in Various Solvents
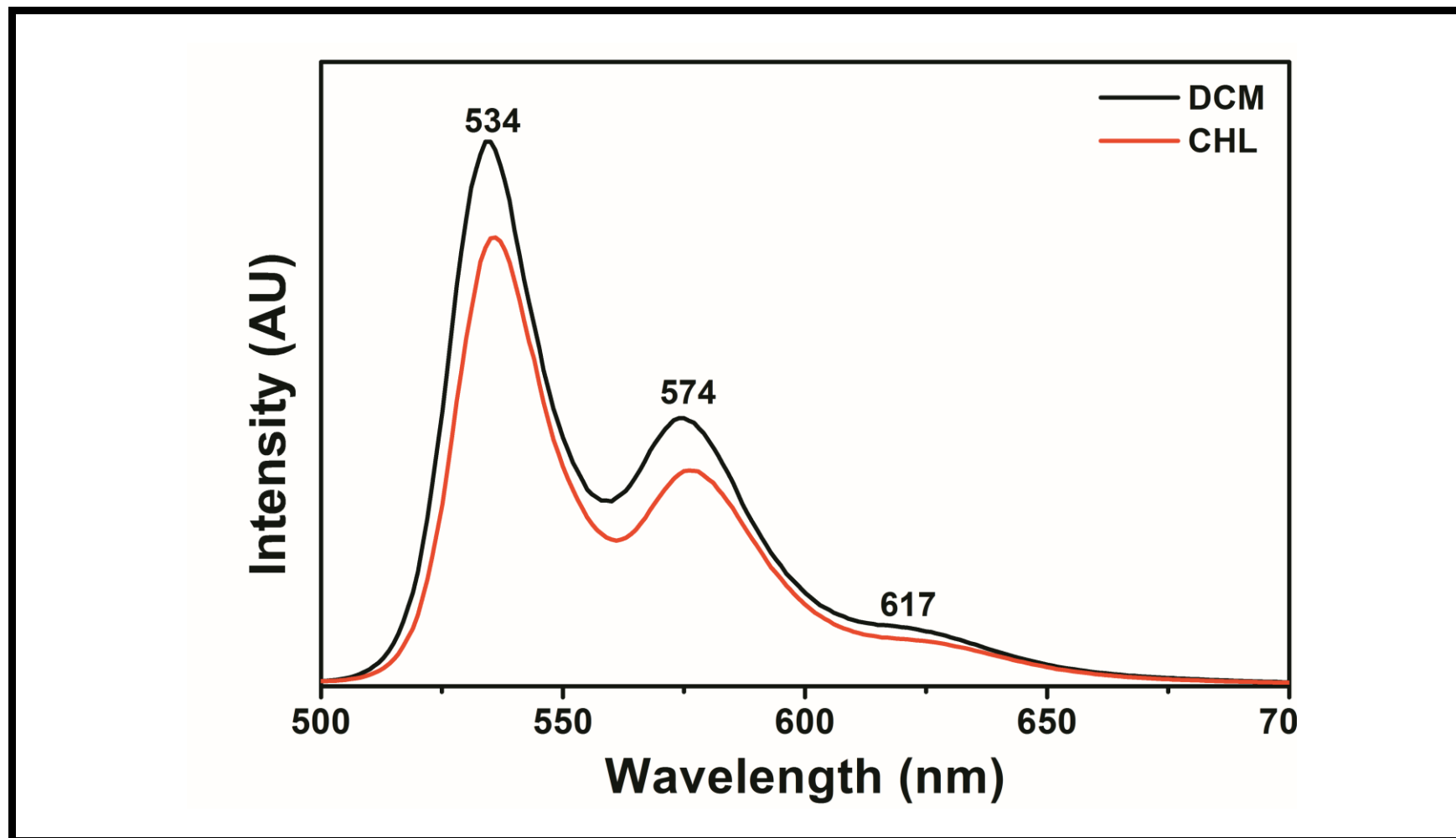
Figure 4.67: Overlap Emission Spectra of CH-PPI in Apolar Solvents
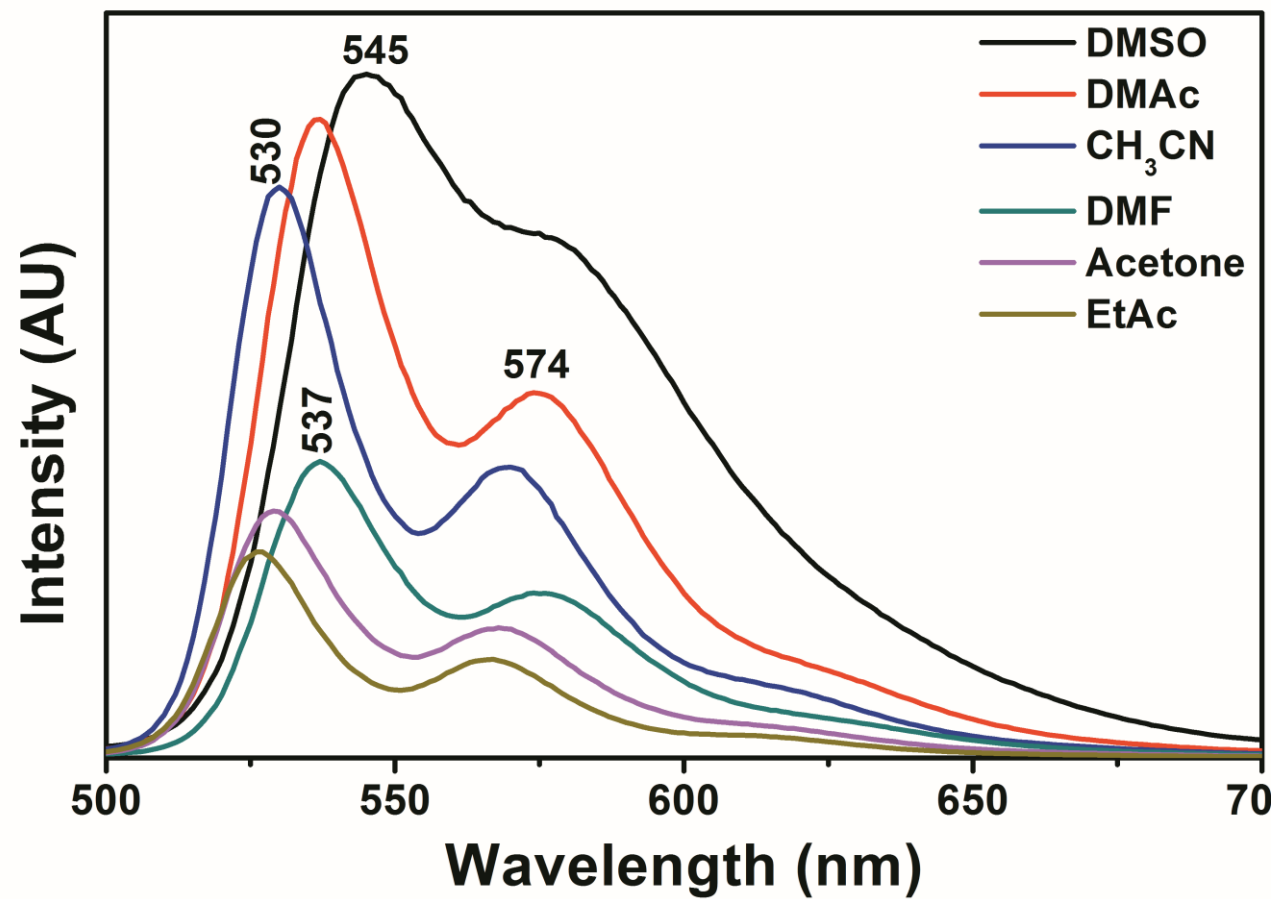
Figure 4.68: Overlap Emission Spectra of CH-PPI in Aprotic Solvents
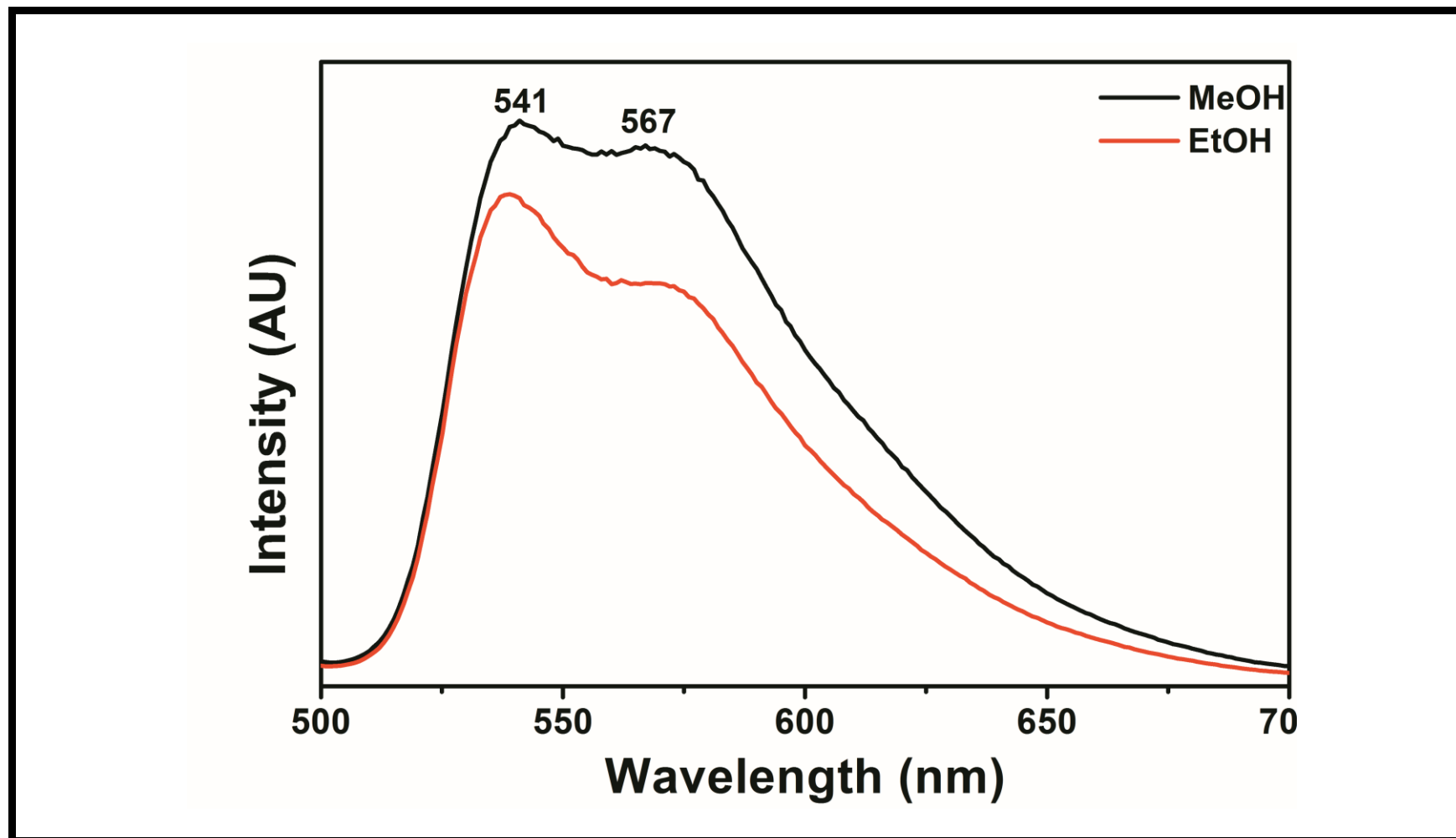
Figure 4.69: Overlap Emission Spectra of CH-PPI in Protic Solvents
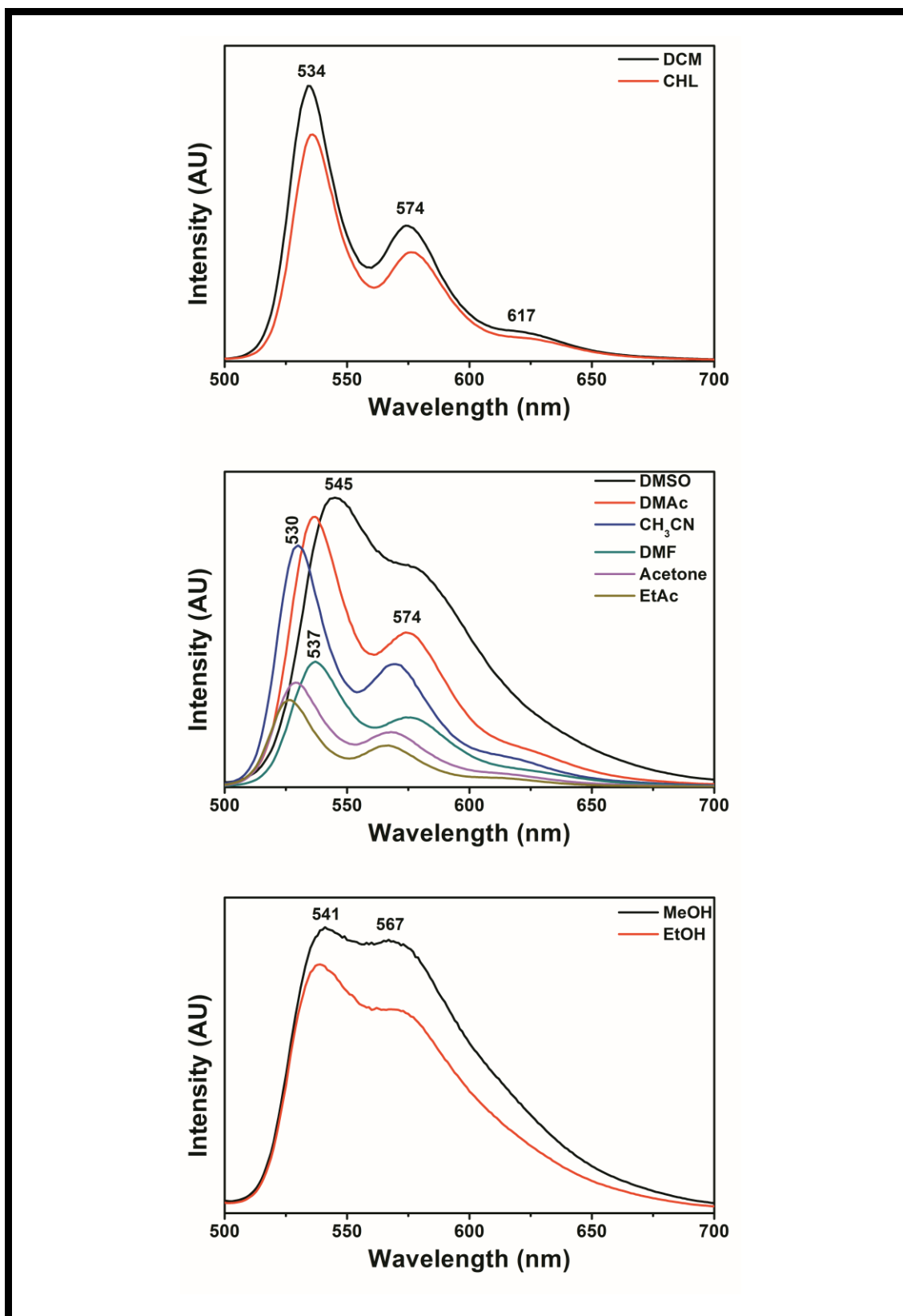
Figure 4.70: Comparison of Emission Spectra of CH-PPI in Various Solvents
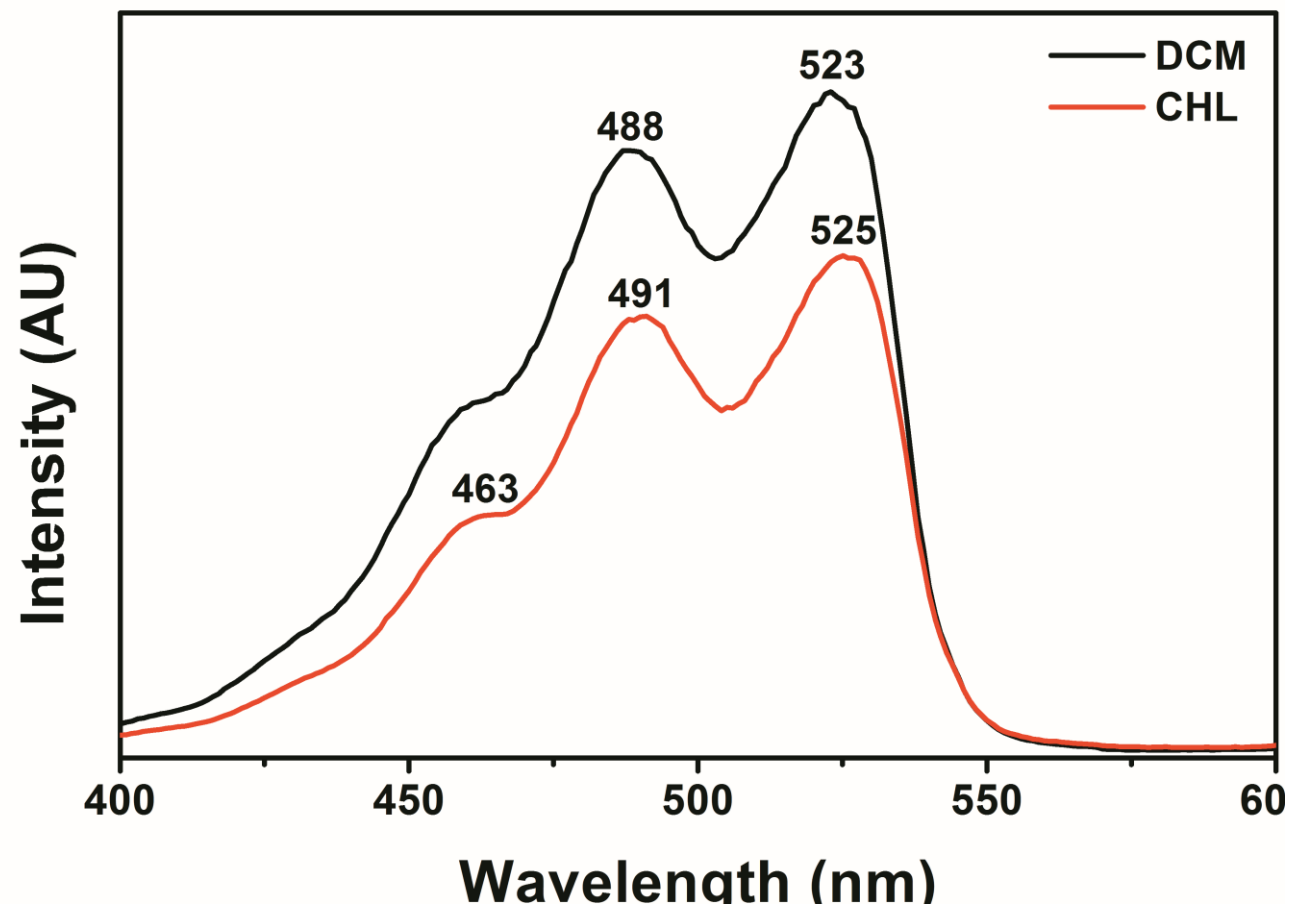
Figure 4.71: Overlap Excitation Spectra of CH-PPI in Apolar Solvents
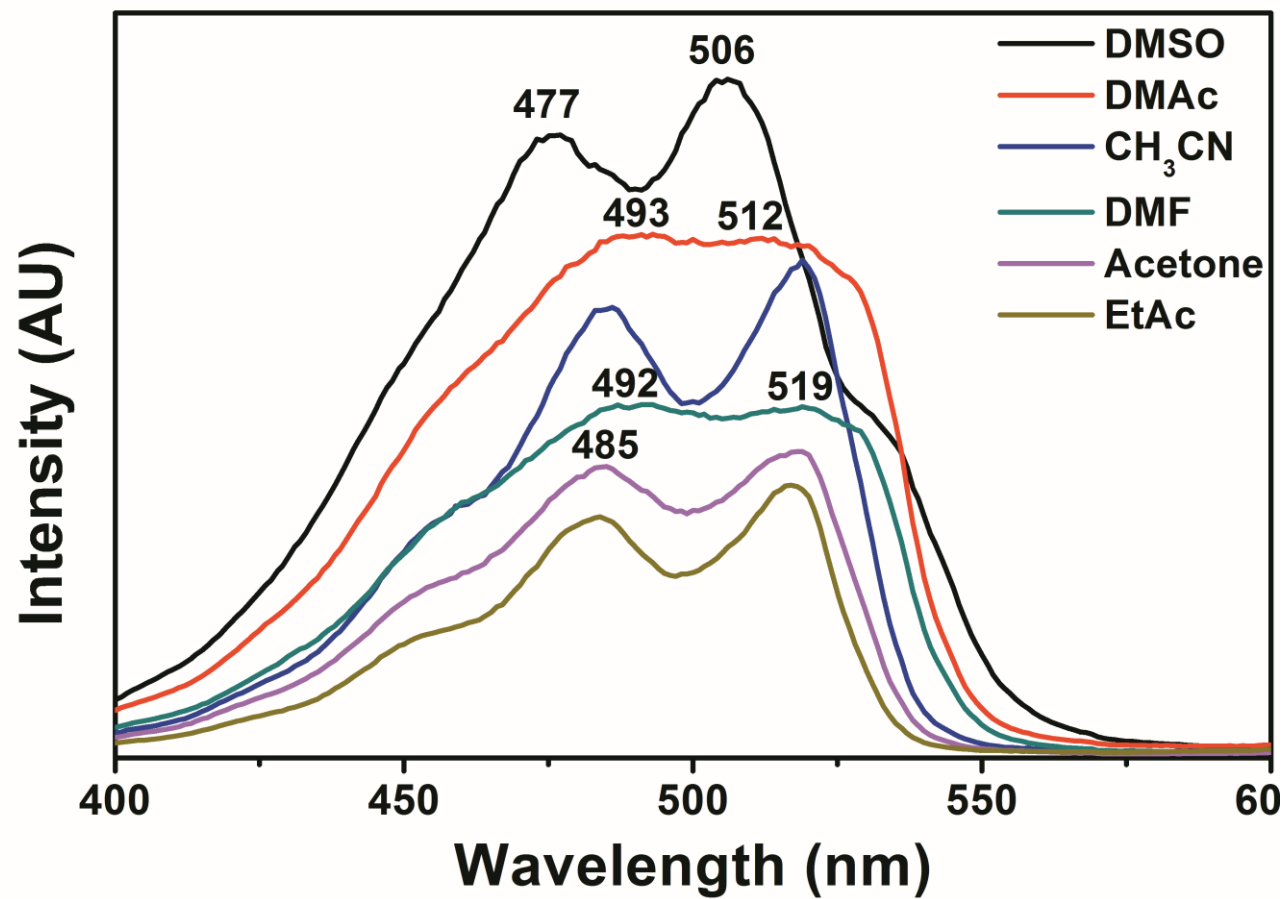
Figure 4.72: Overlap Excitation Spectra of CH-PPI in Aprotic Solvents
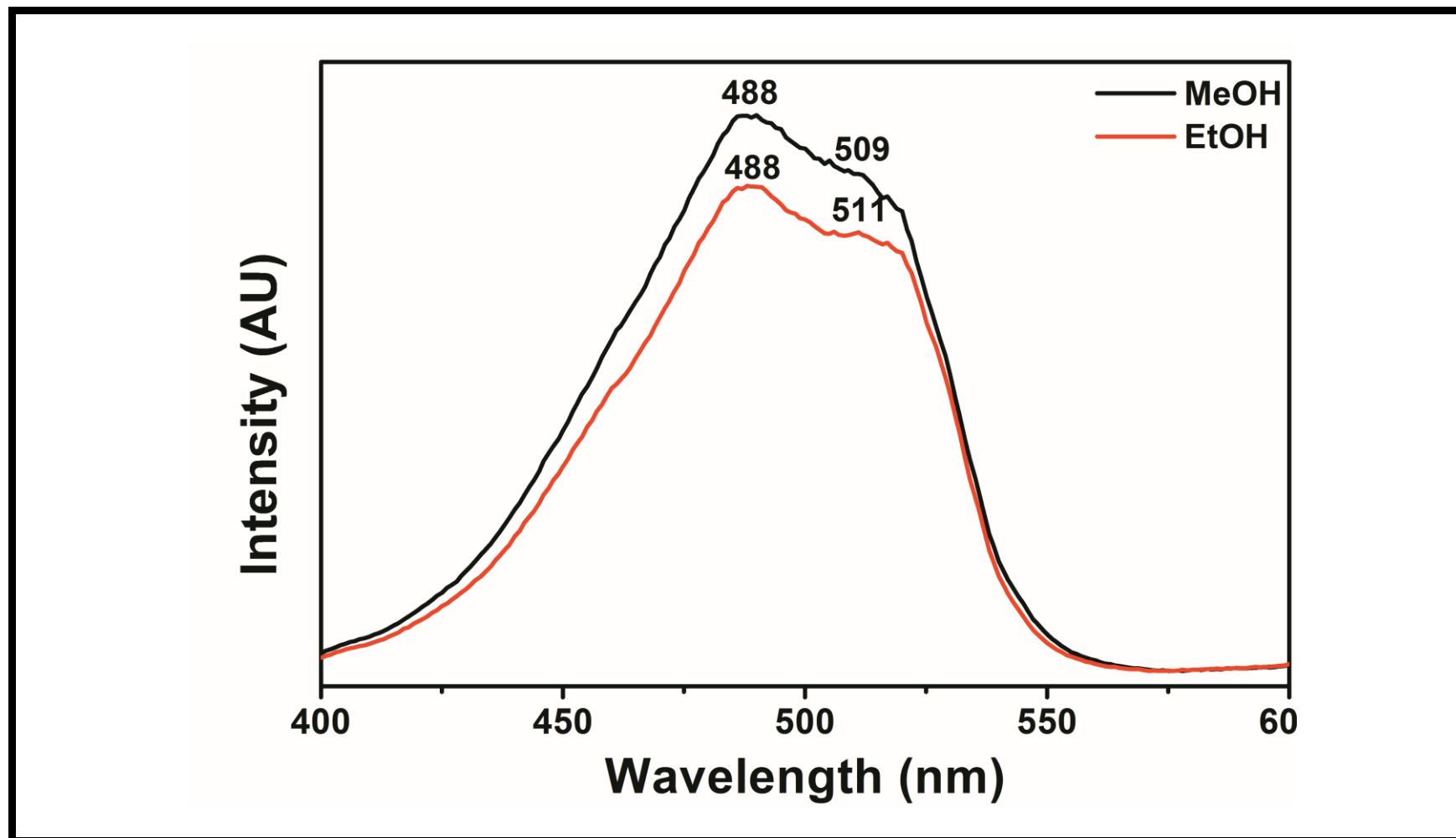
Figure 4.73: Overlap Excitation Spectra of CH-PPI in Protic Solvents
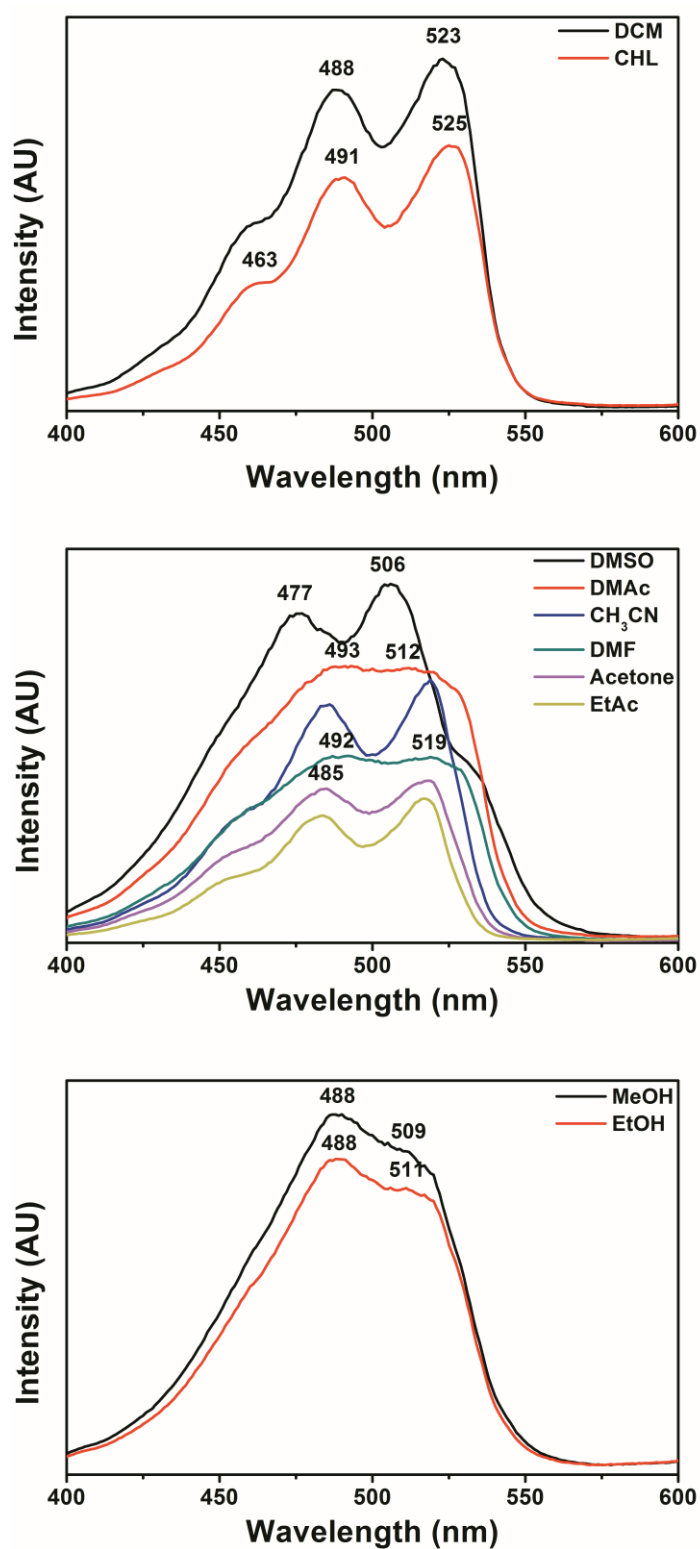
Figure 4.74: Comparison of Excitation Spectra of CH-PPI in Various Solvents
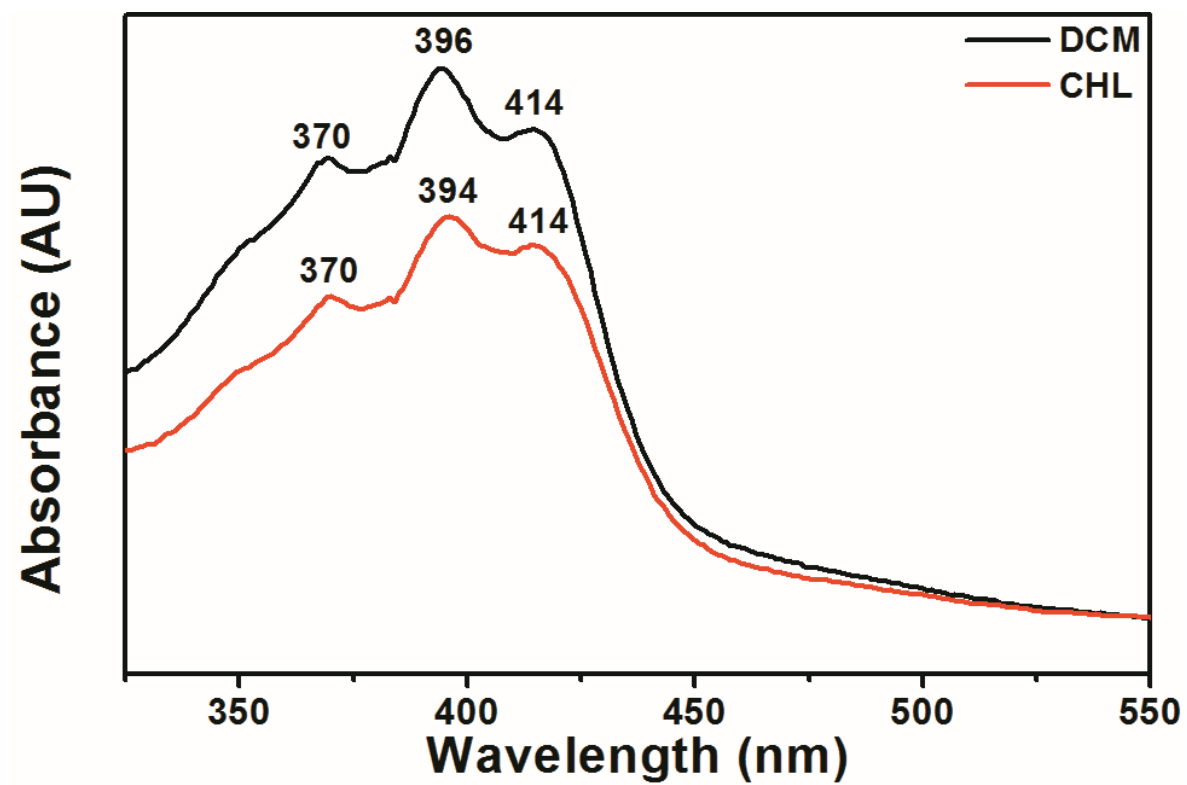
Figure 4.75: Overlap UV-vis Absorption Spectra of CH-PNI in Apolar Solvents
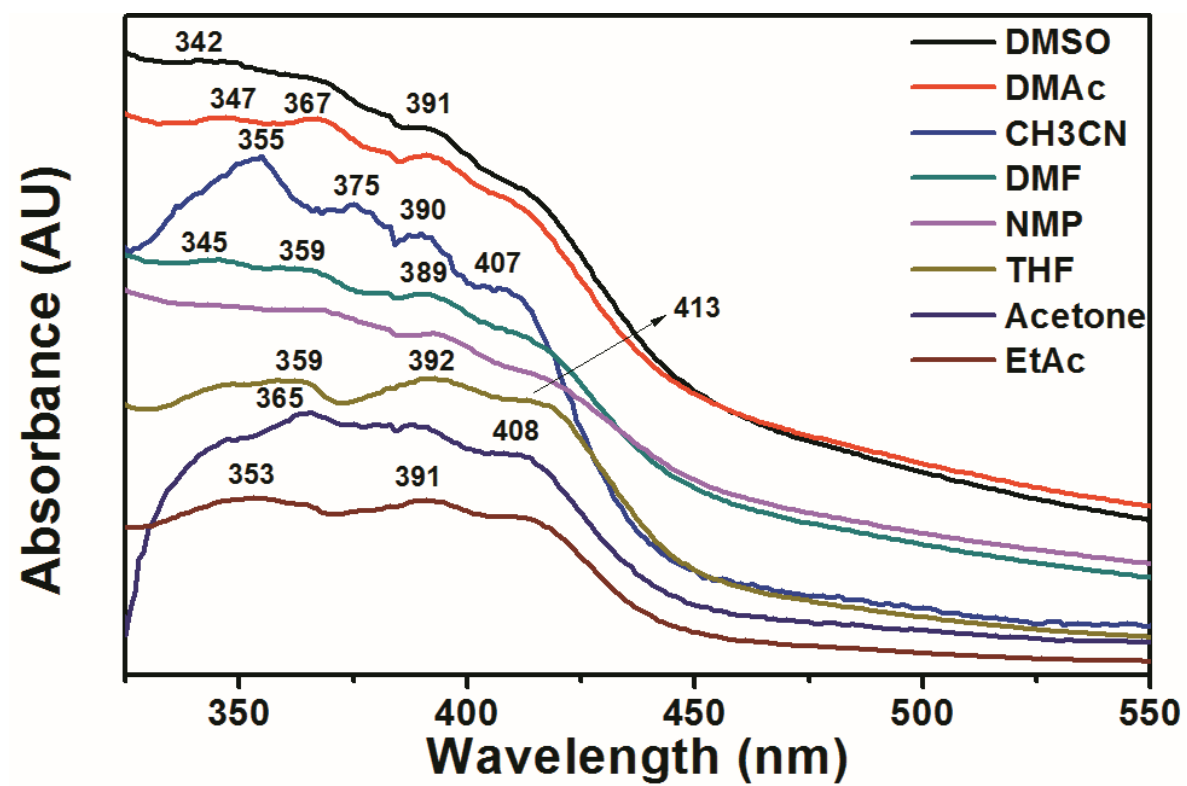
Figure 4.76: Overlap UV-vis Absorption Spectra of CH-PNI in Aprotic Solvents
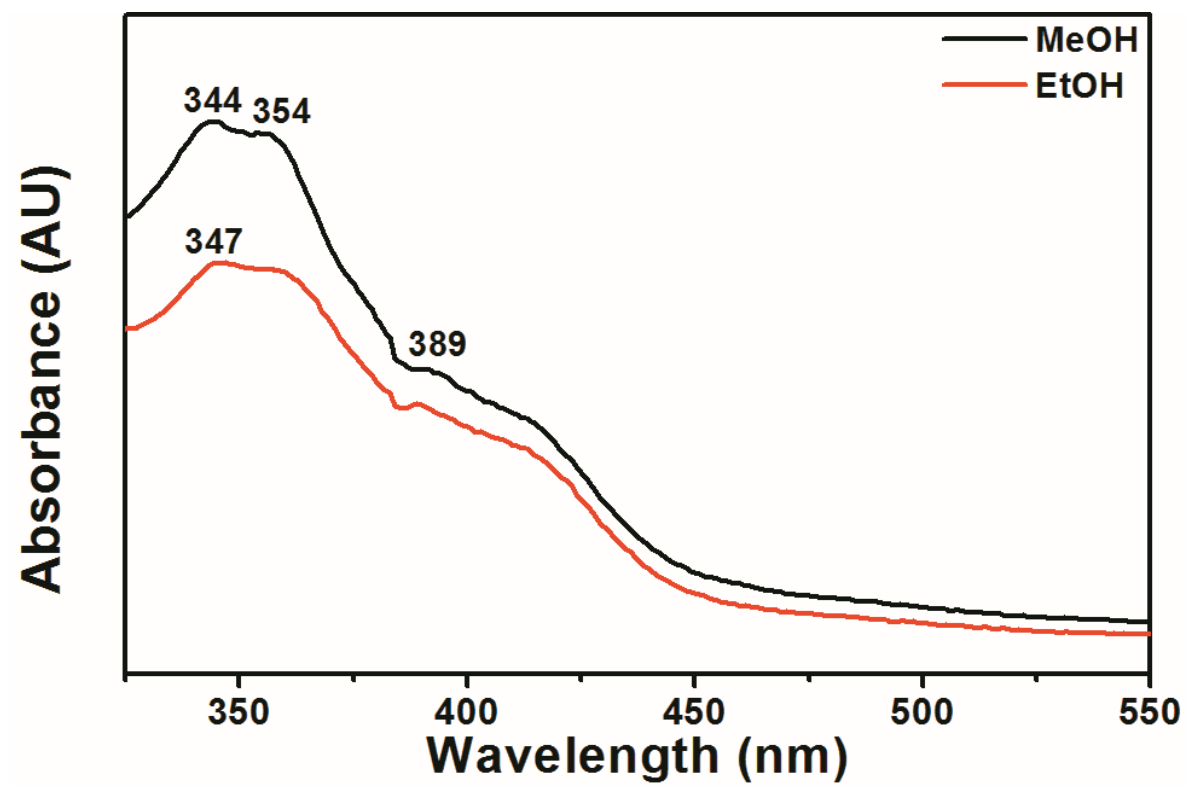
Figure 4.77: Overlap UV-vis Absorption Spectra of CH-PNI in Protic Solvents
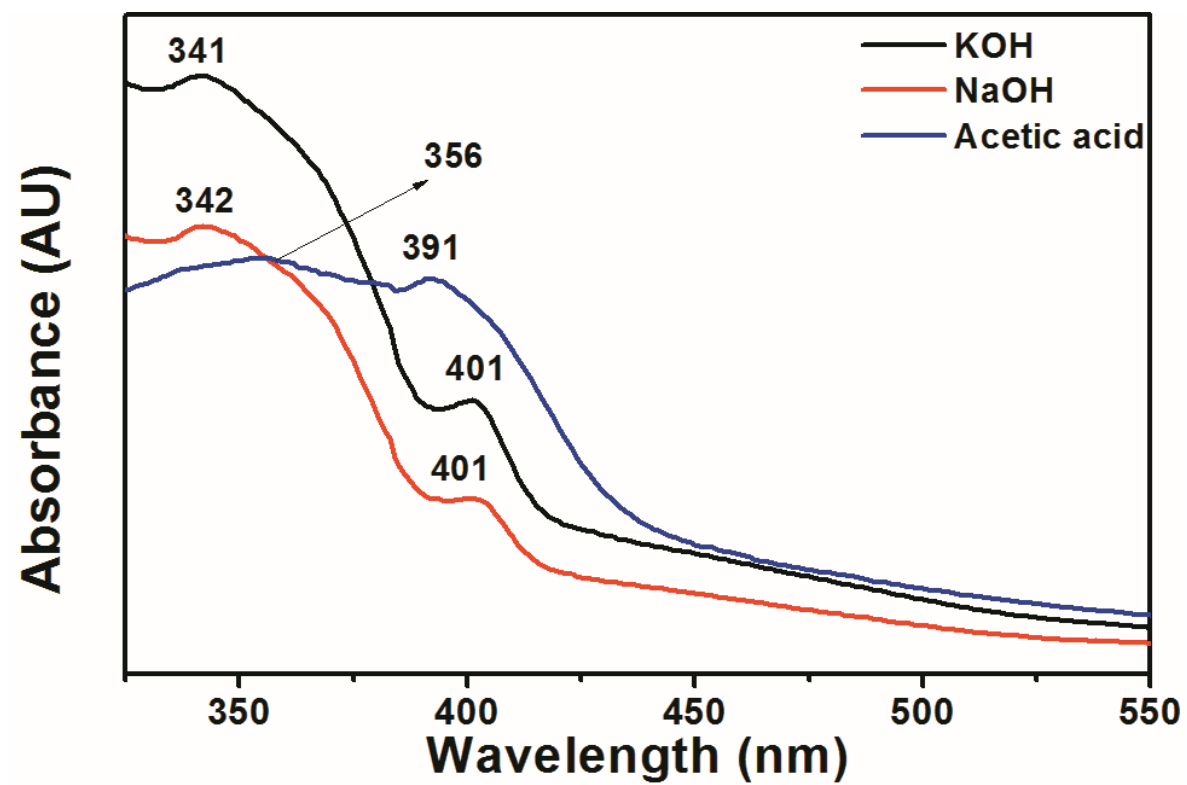
Figure 4.78: Overlap UV-vis Absorption Spectra of CH-PNI in Other Solvents
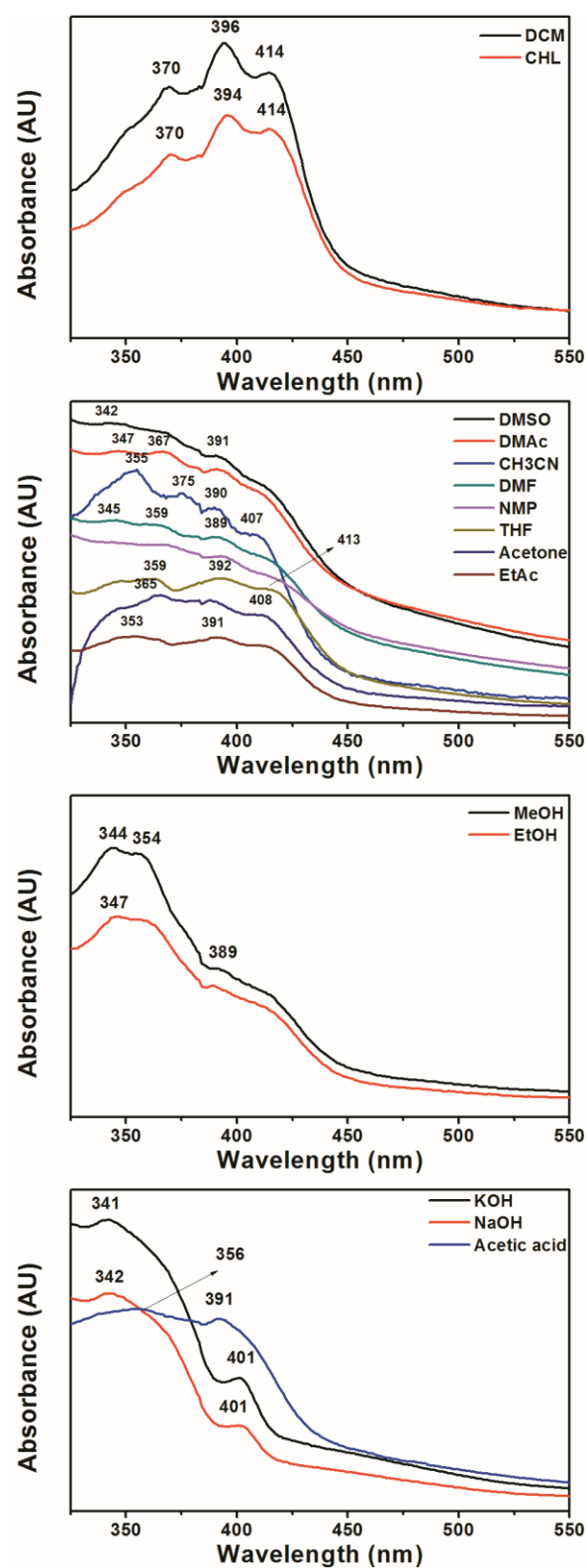
Figure 4.79: Comparison of UV-vis Absorption Spectra of CH-PNI in Various Solvents
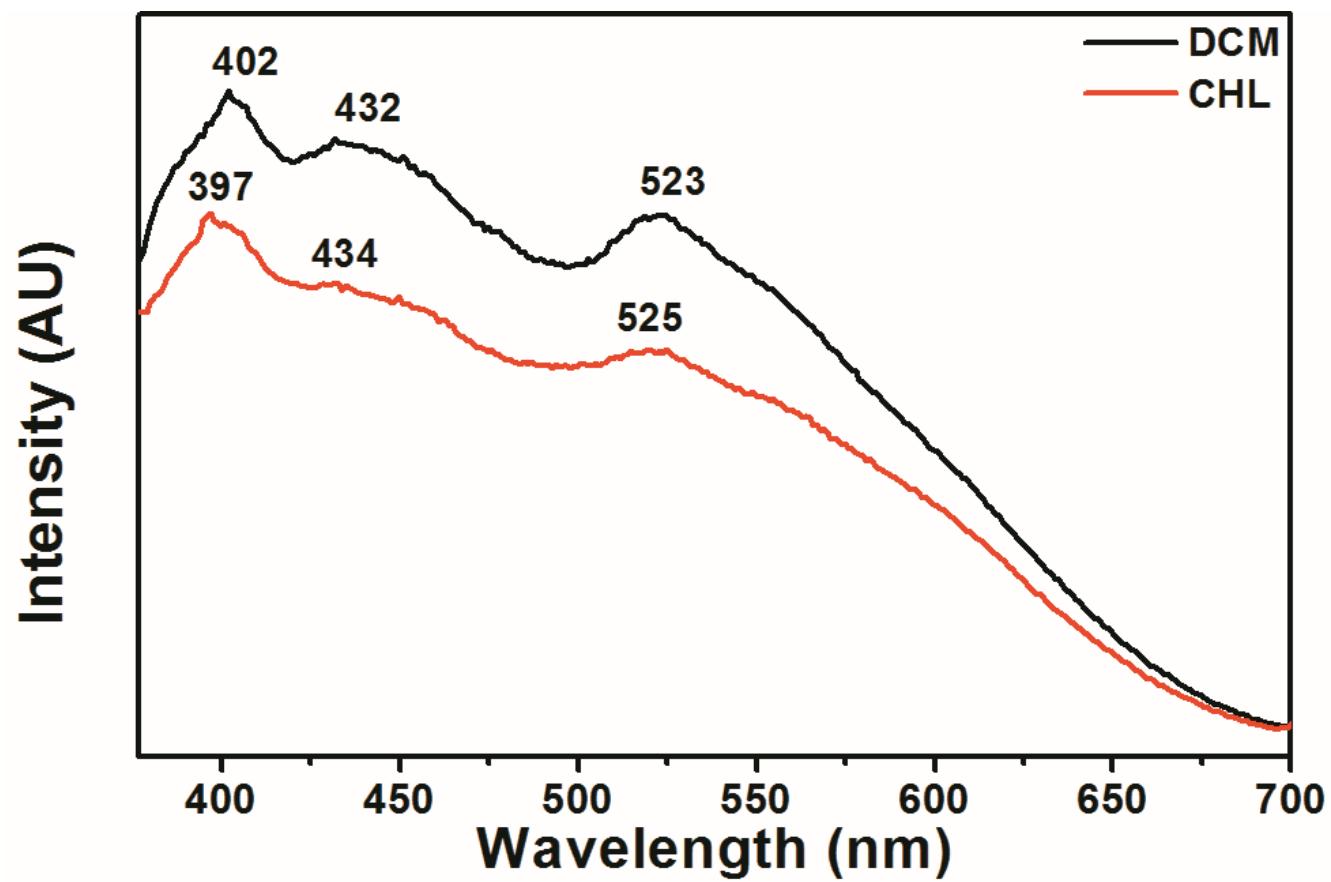
Figure 4.80: Overlap Emission Spectra of CH-PNI in Apolar Solvents
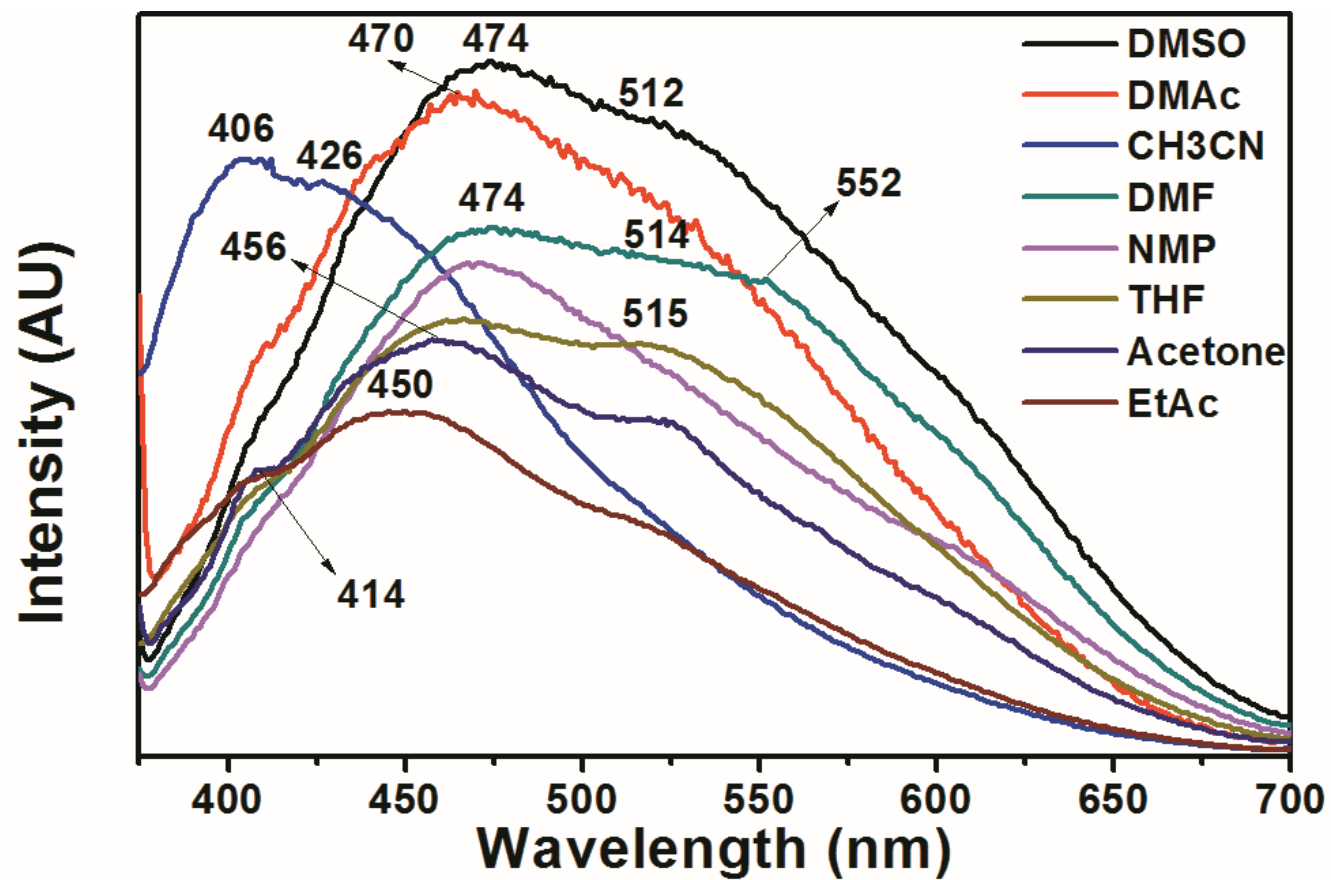
Figure 4.81: Overlap Emission Spectra of CH-PNI in Aprotic Solvents
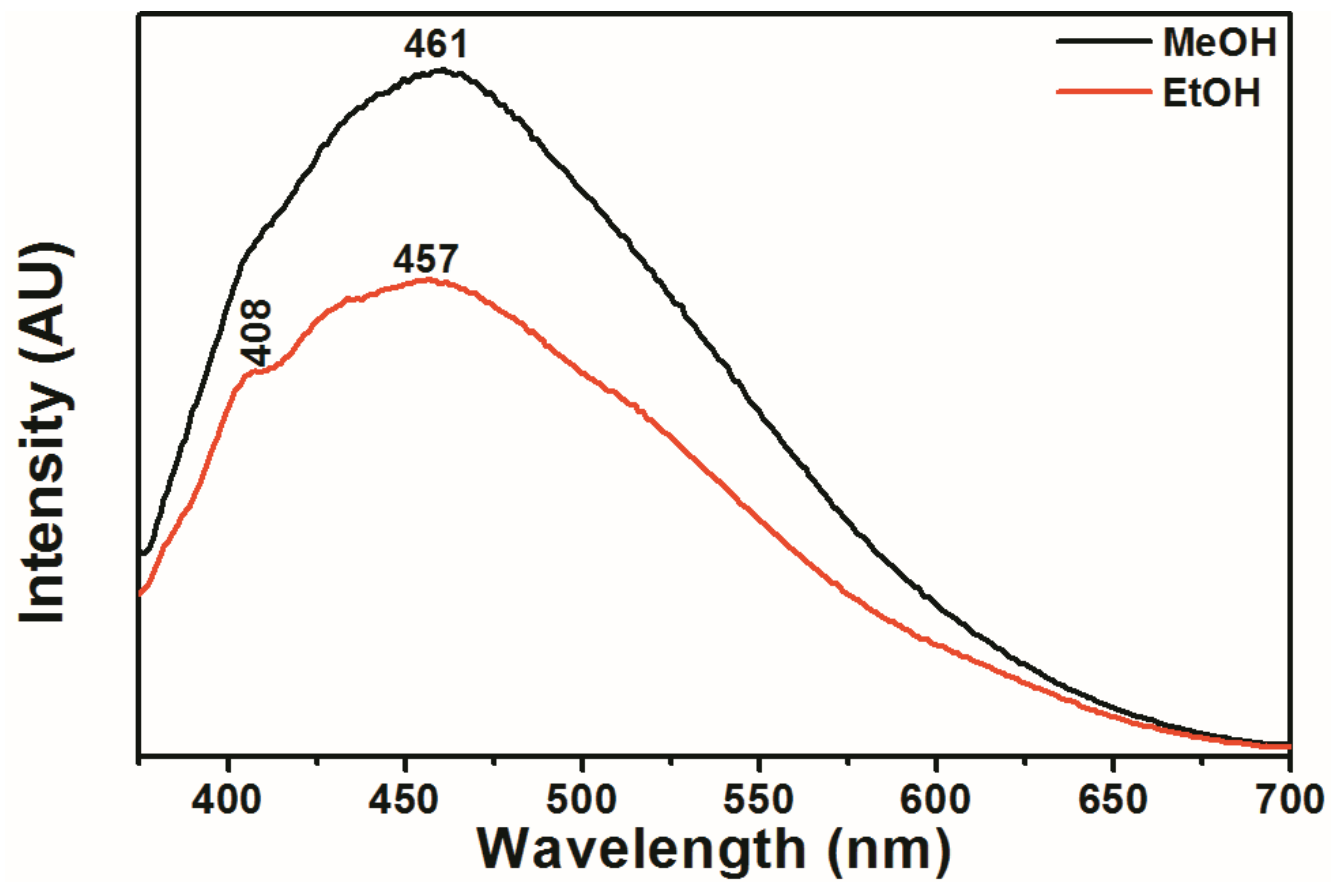
Figure 4.82: Overlap Emission Spectra of CH-PNI in Protic Solvents
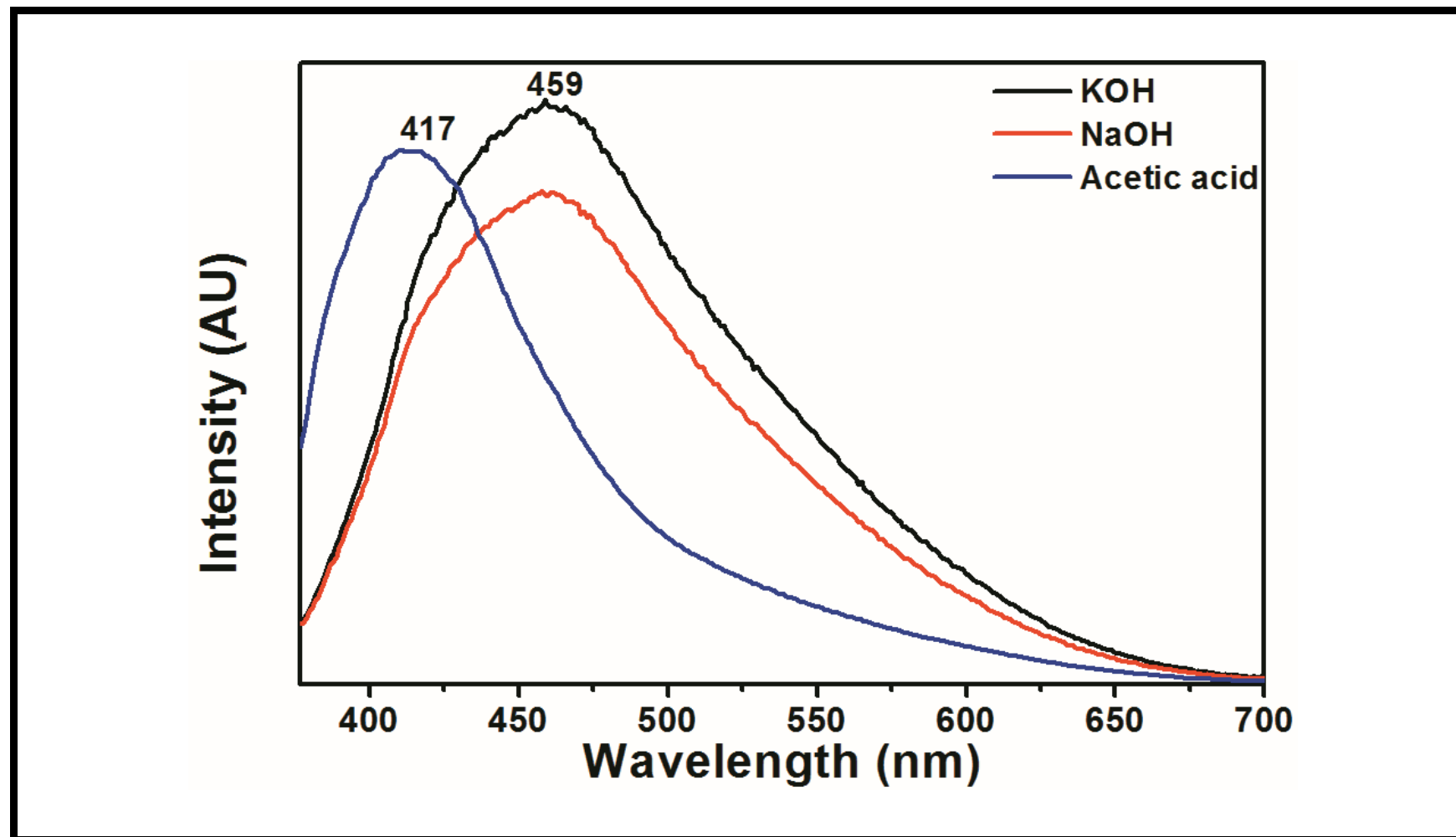
Figure 4.83: Overlap Emission Spectra of CH-PNI in Other Solvents
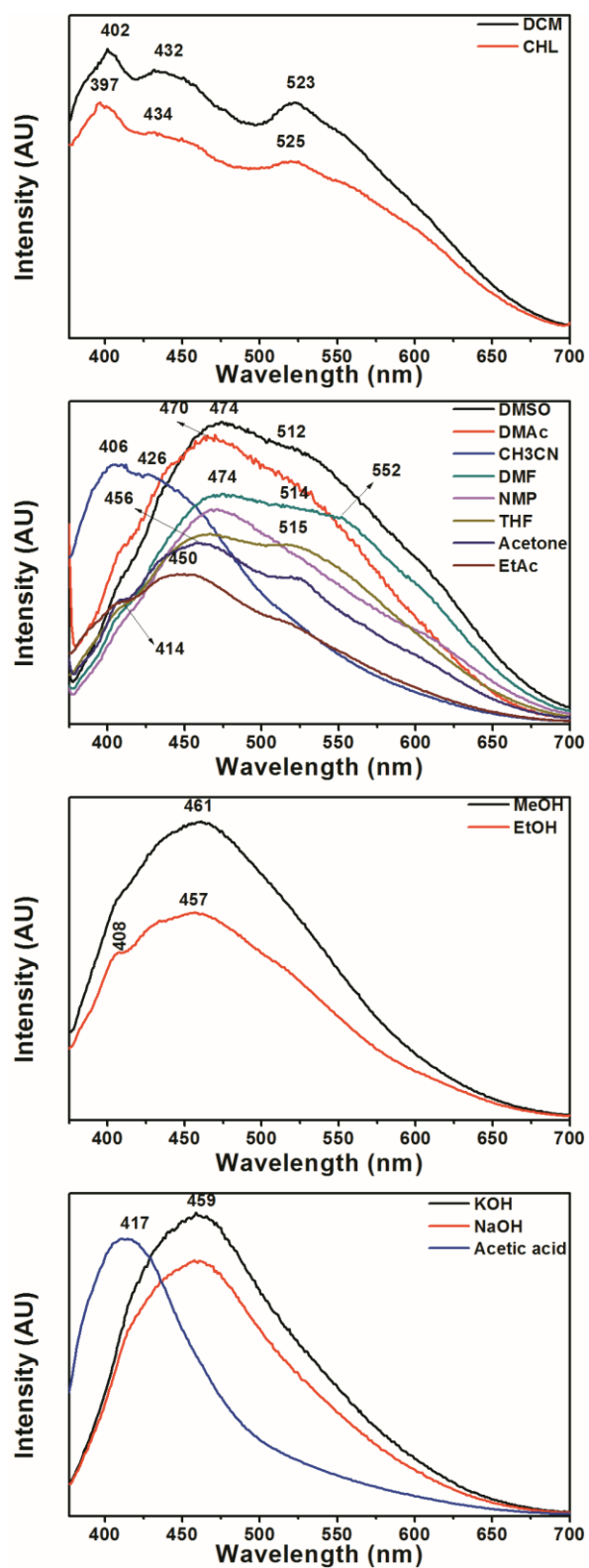
Figure 4.84: Comparison of Emission Spectra of CH-PNI in Various Solvents
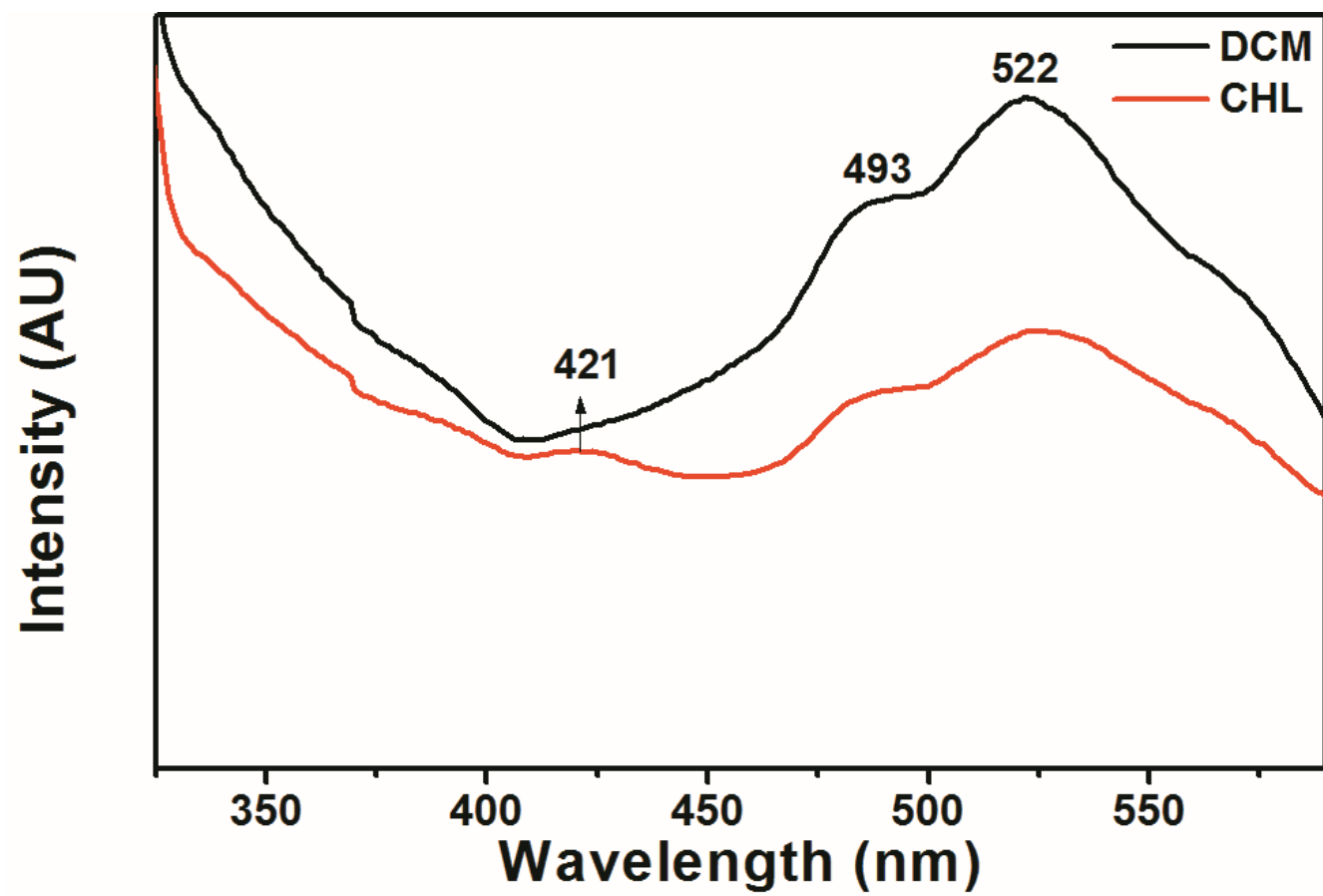
Figure 4.85: Overlap Excitation Spectra of CH-PNI in Apolar Solvents
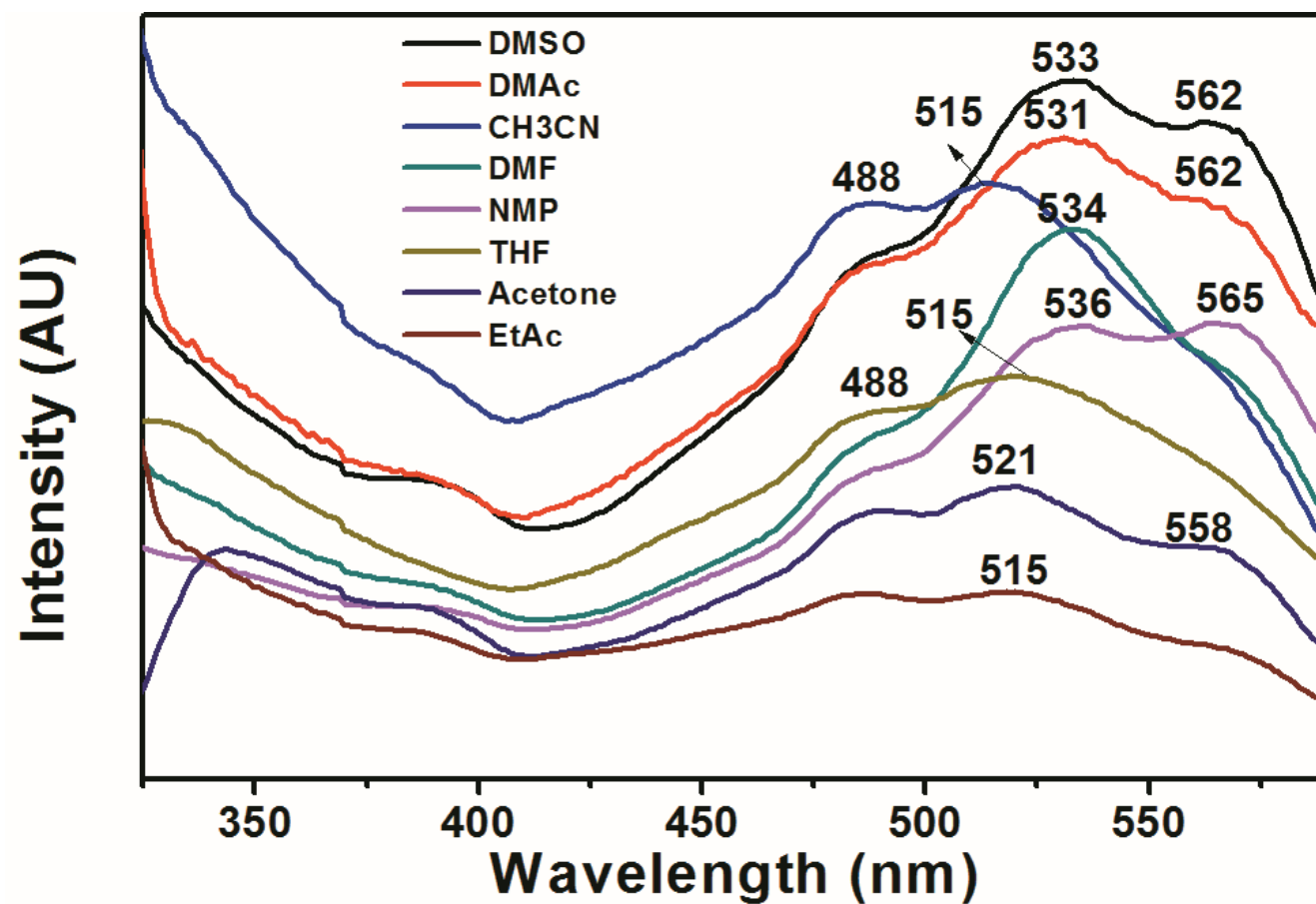
Figure 4.86: Overlap Excitation Spectra of CH-PNI in Aprotic Solvents
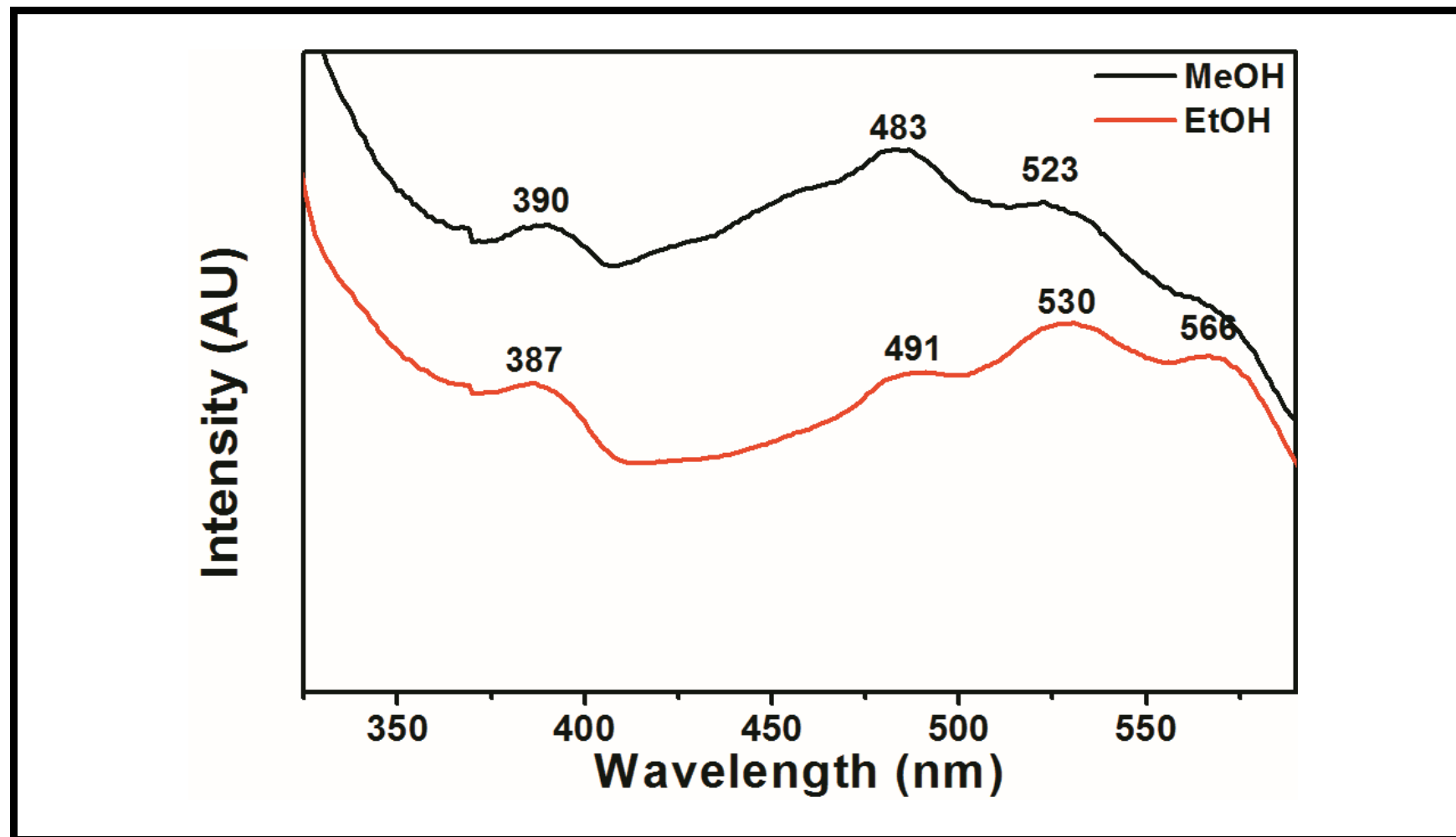
Figure 4.87: Overlap Excitation Spectra of CH-PNI in Protic Solvents
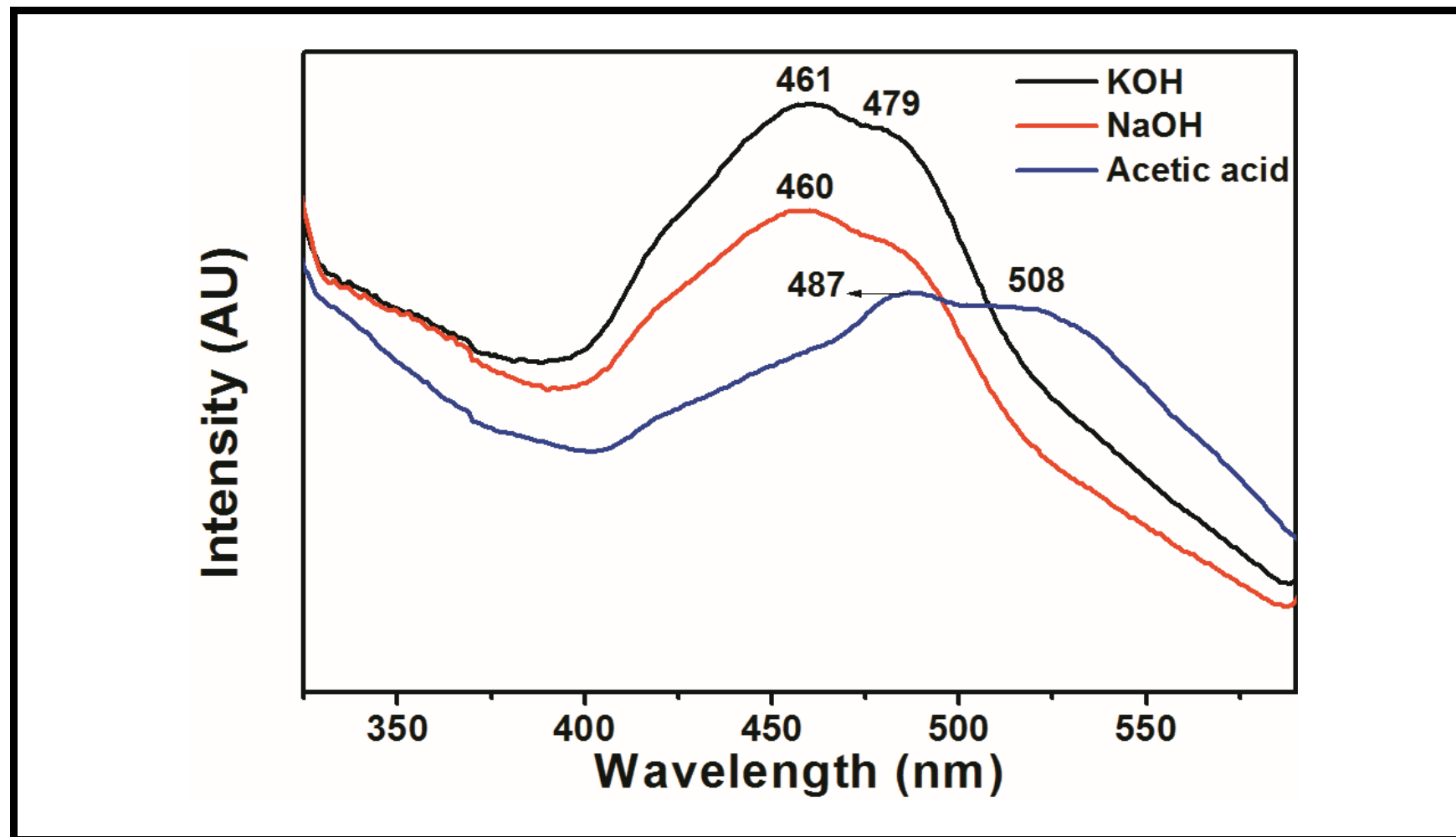
Figure 4.88: Overlap Excitation Spectra of CH-PNI in Other Solvents
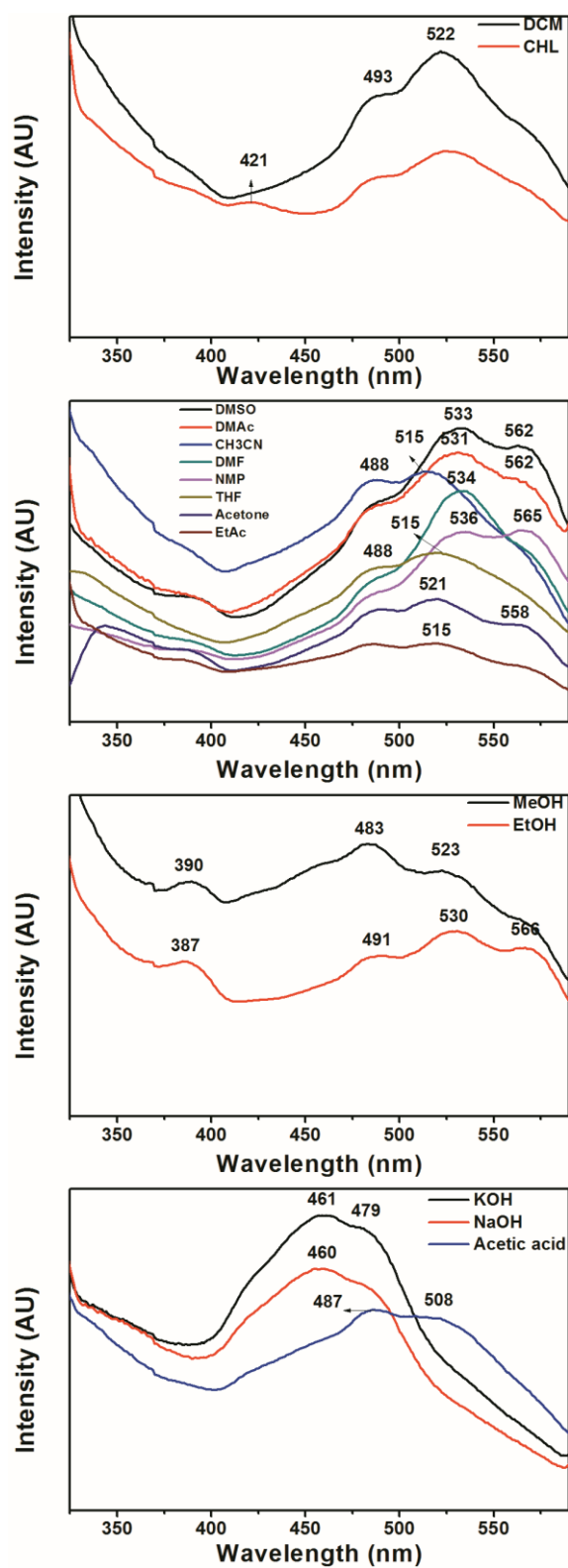
Figure 4.89: Comparison of Excitation Spectra of CH-PNI in Various Solvents
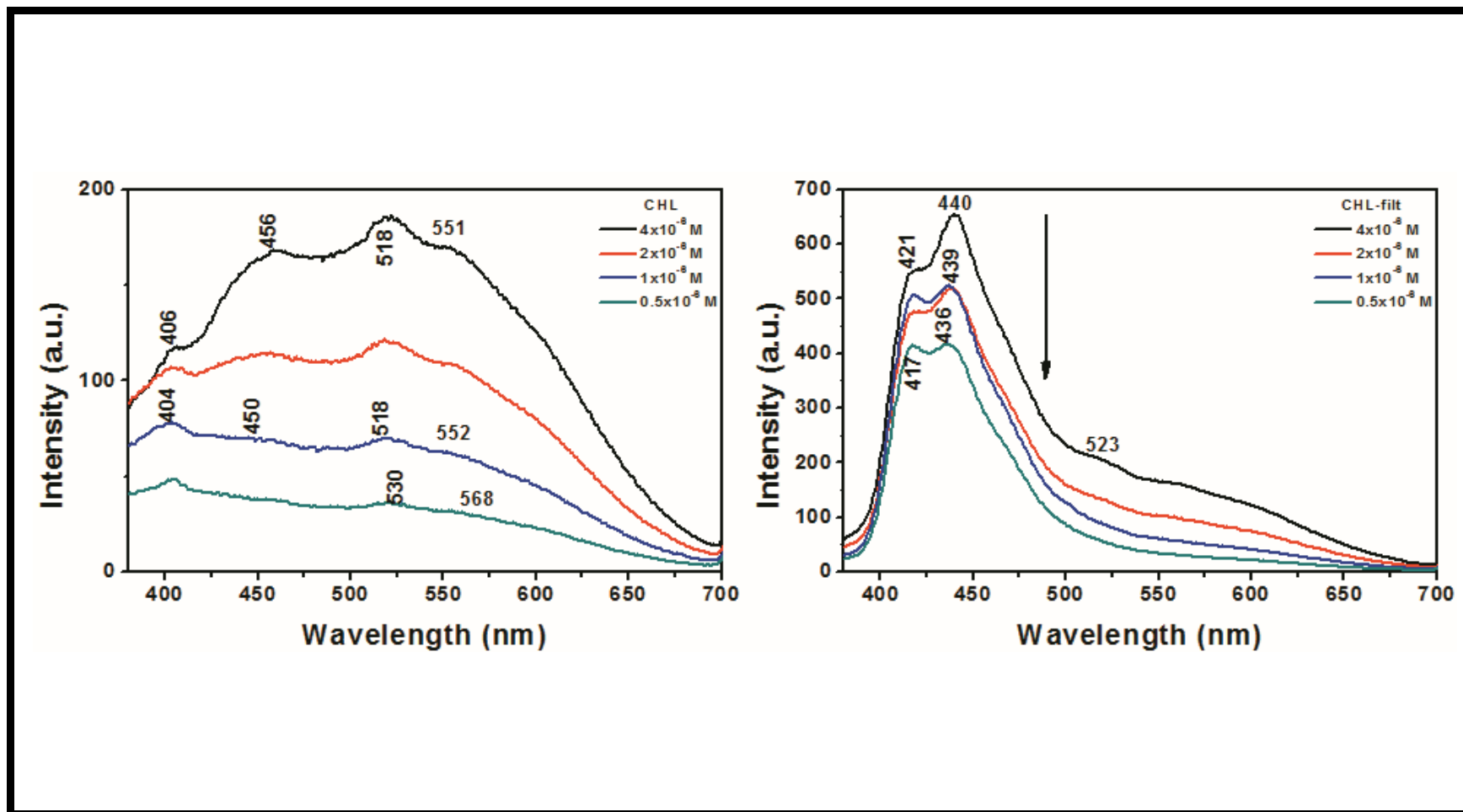
Figure 4.90: Effect of Concentration and Filtration (with 0.2 μm microfilter) on Emission Spectra of CH-PNI in CHCl$_3$ at Different Concentrations
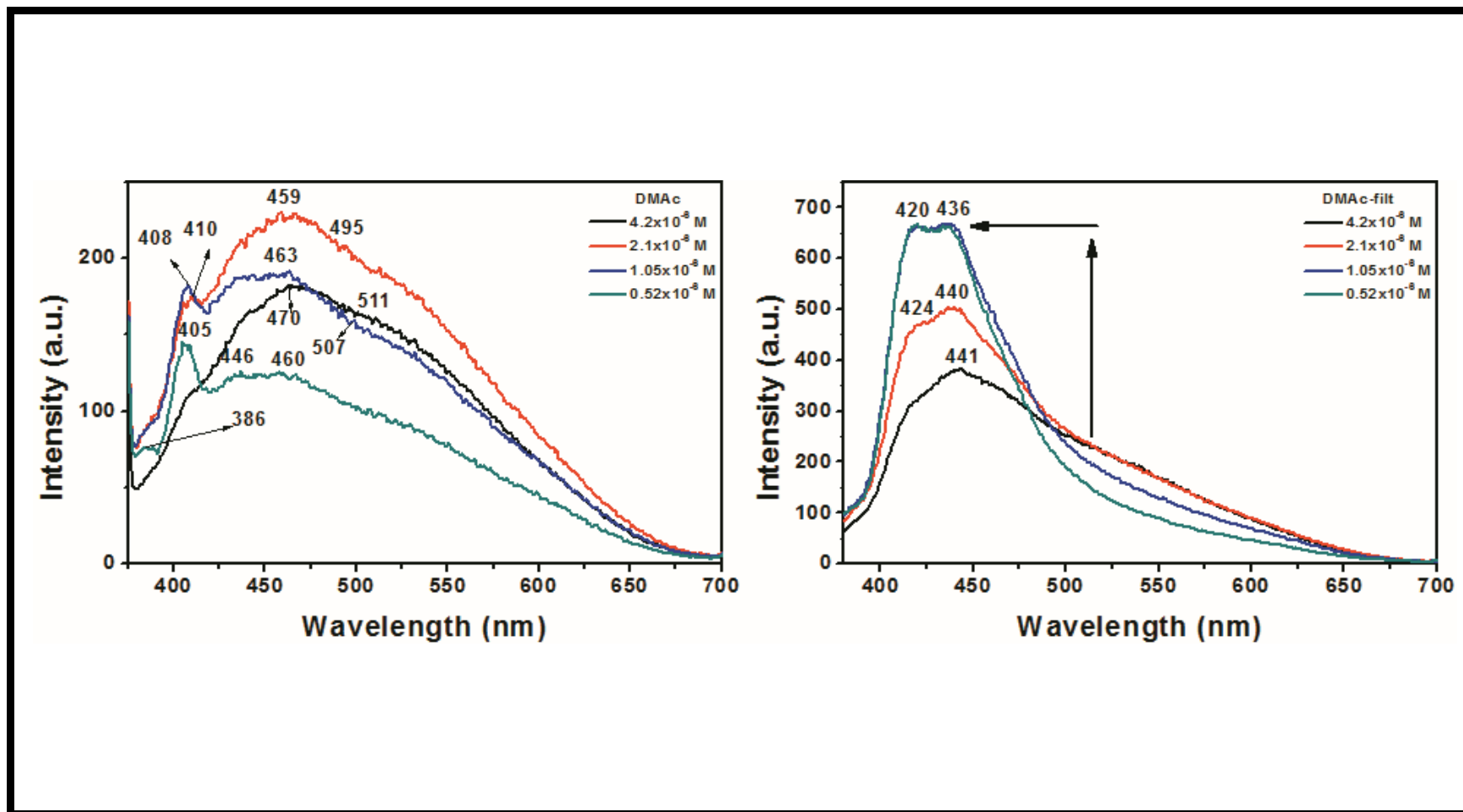
Figure 4.91: Effect of Concentration and Filtration (with 0.2 μm microfilter) on Emission Spectra of CH-PNI in DMAc at Different Concentrations
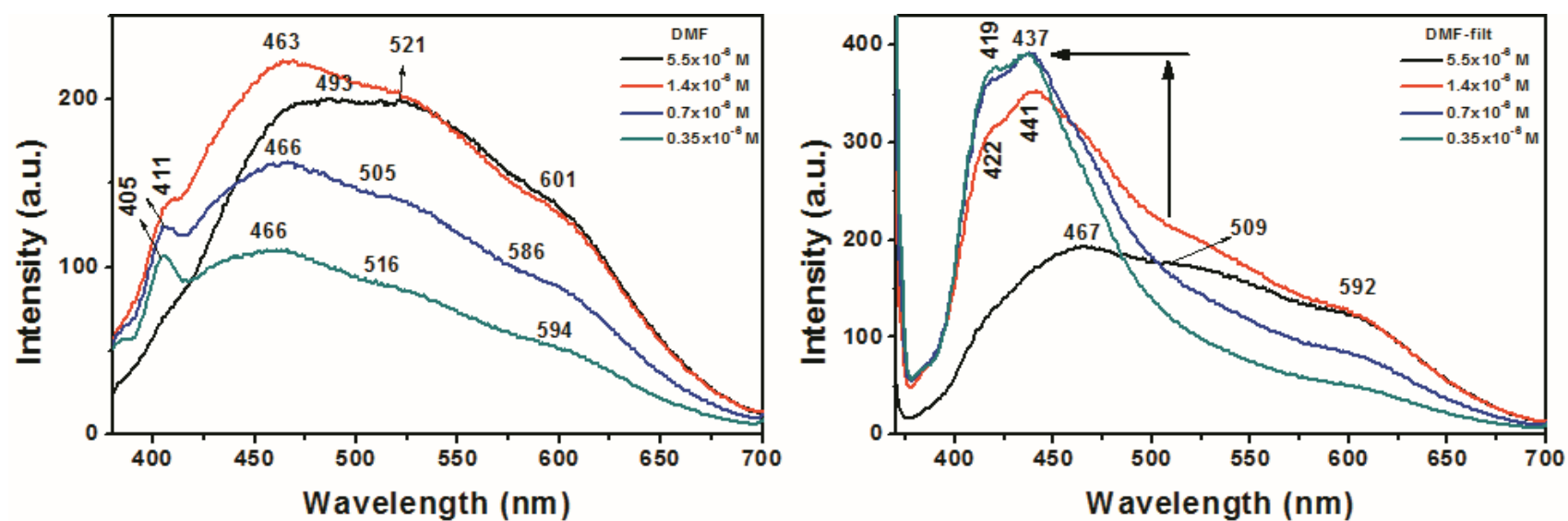
Figure 4.92: Effect of Concentration and Filtration (with 0.2 μm microfilter) on Emission Spectra of CH-PNI in DMF at Different Concentrations
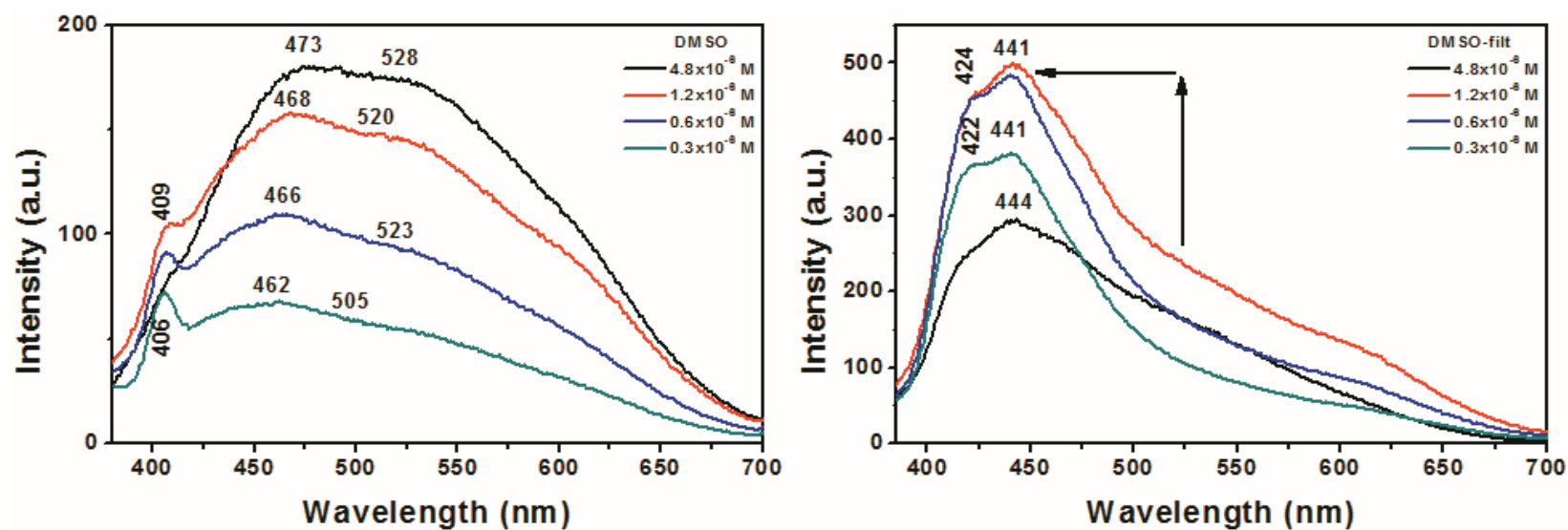
Figure 4.93: Effect of Concentration and Filtration (with 0.2 μm microfilter) on Emission Spectra of CH-PNI in DMSO at Different Concentrations
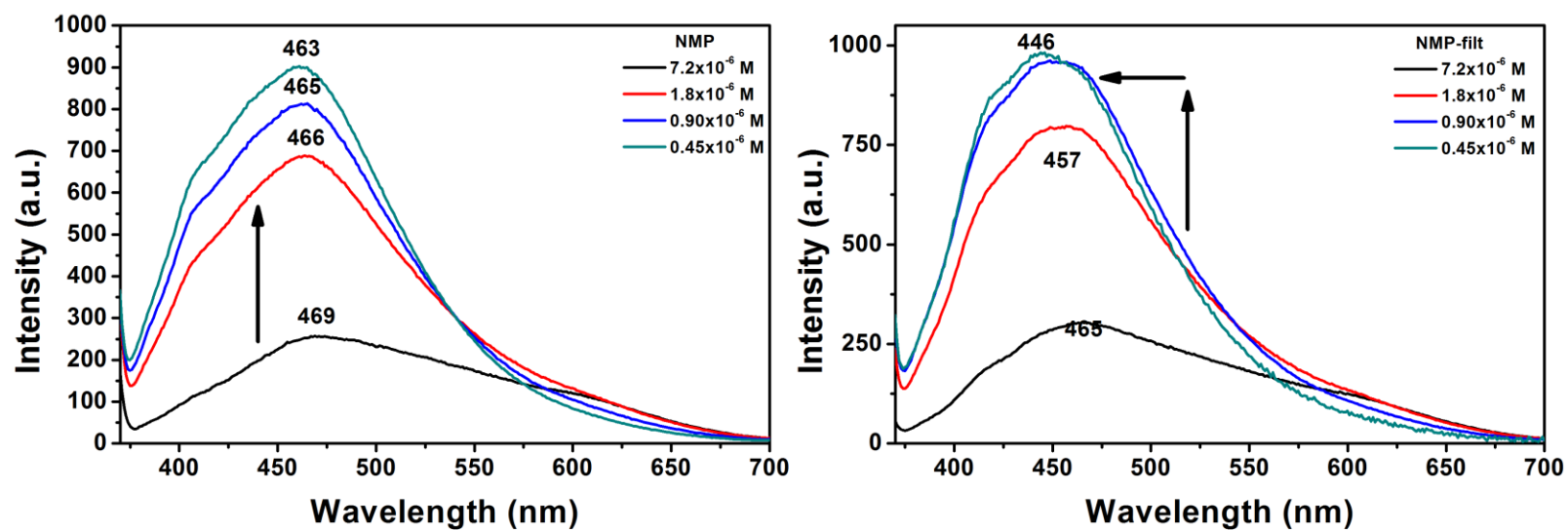
Figure 4.94: Effect of Concentration and Filtration (with 0.2 μm microfilter) on Emission Spectra of CH-PNI in NMP at Different Concentrations
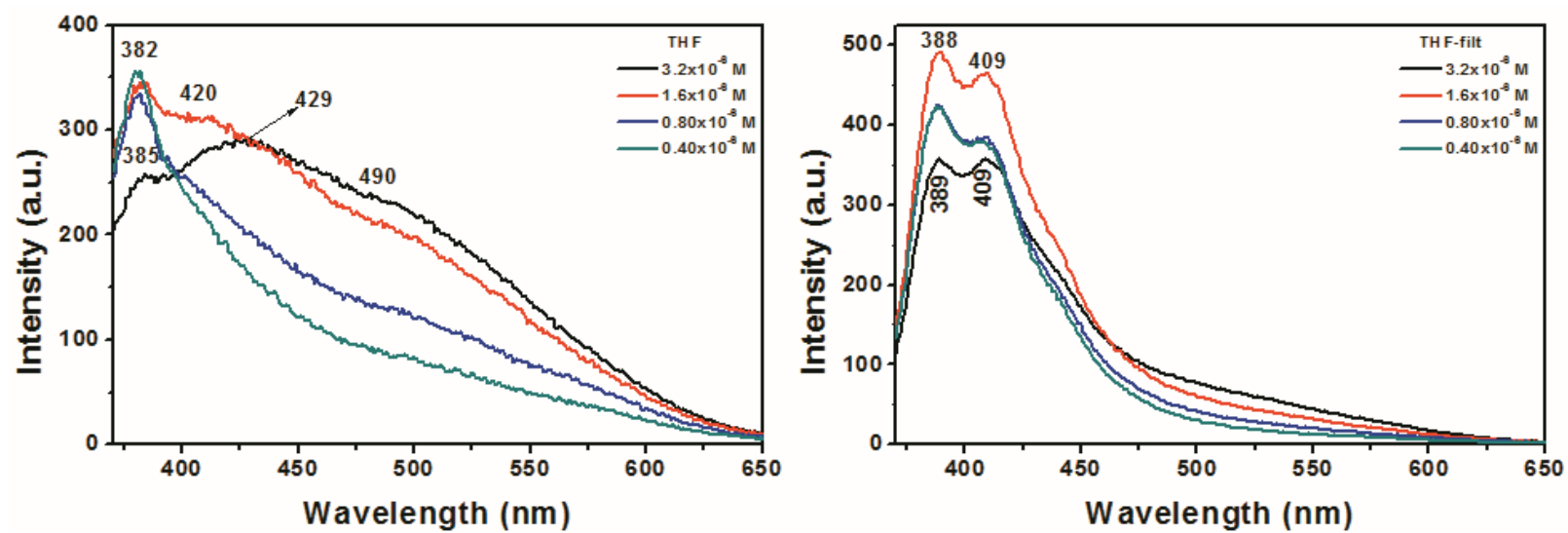
Figure 4.95: Effect of Concentration and Filtration (with 0.2 μm microfilter) on Emission Spectra of CH-PNI in THF at Different Concentrations
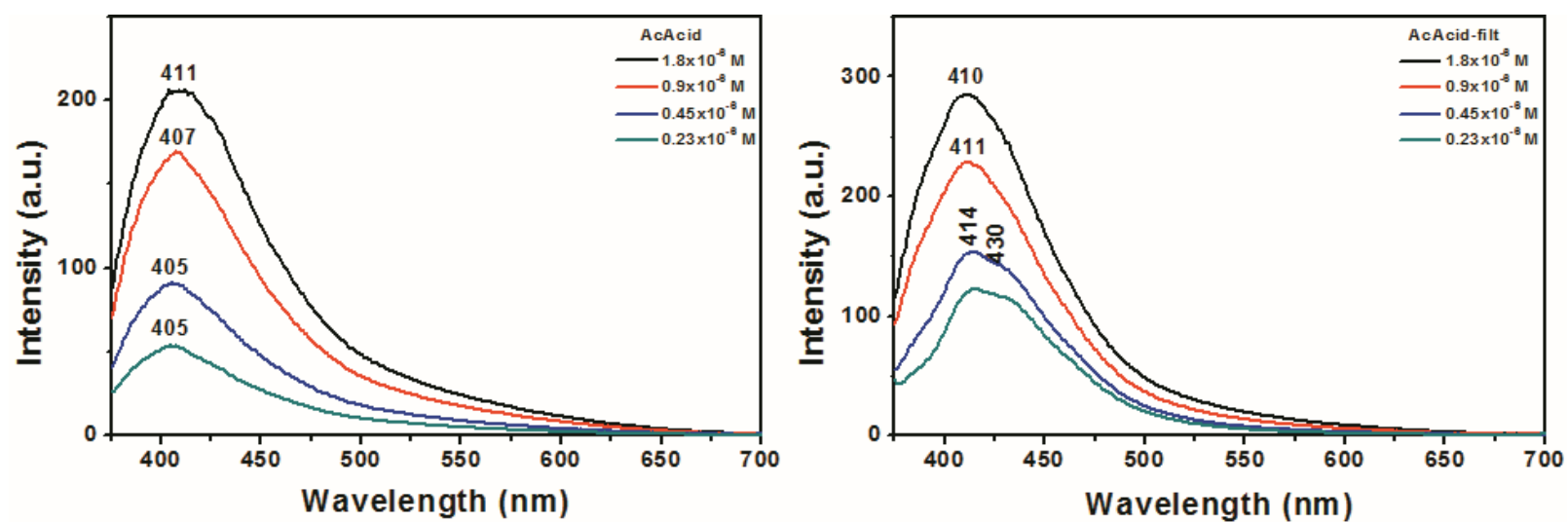
Figure 4.96: Effect of Concentration and Filtration (with 0.2 μm microfilter) on Emission Spectra of CH-PNI in Acetic Acid at Different Concentrations
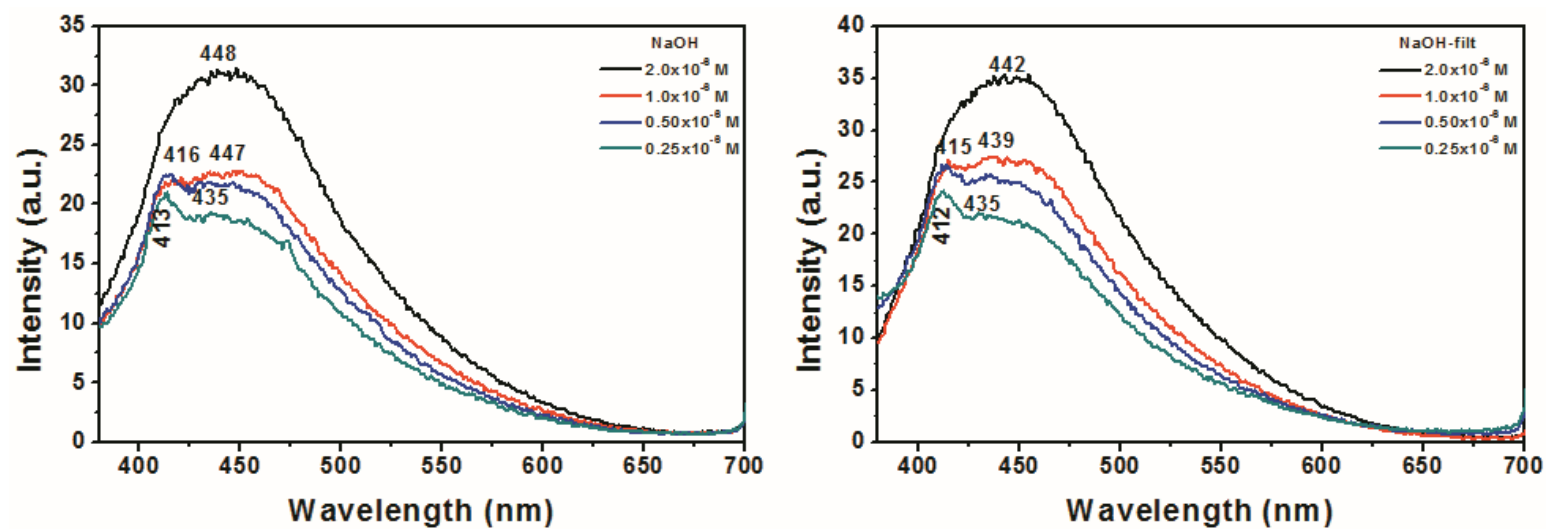
Figure 4.97: Effect of Concentration and Filtration (with 0.2 μm microfilter) on Emission Spectra of CH-PNI in Sodium Hydroxide at Different Concentrations
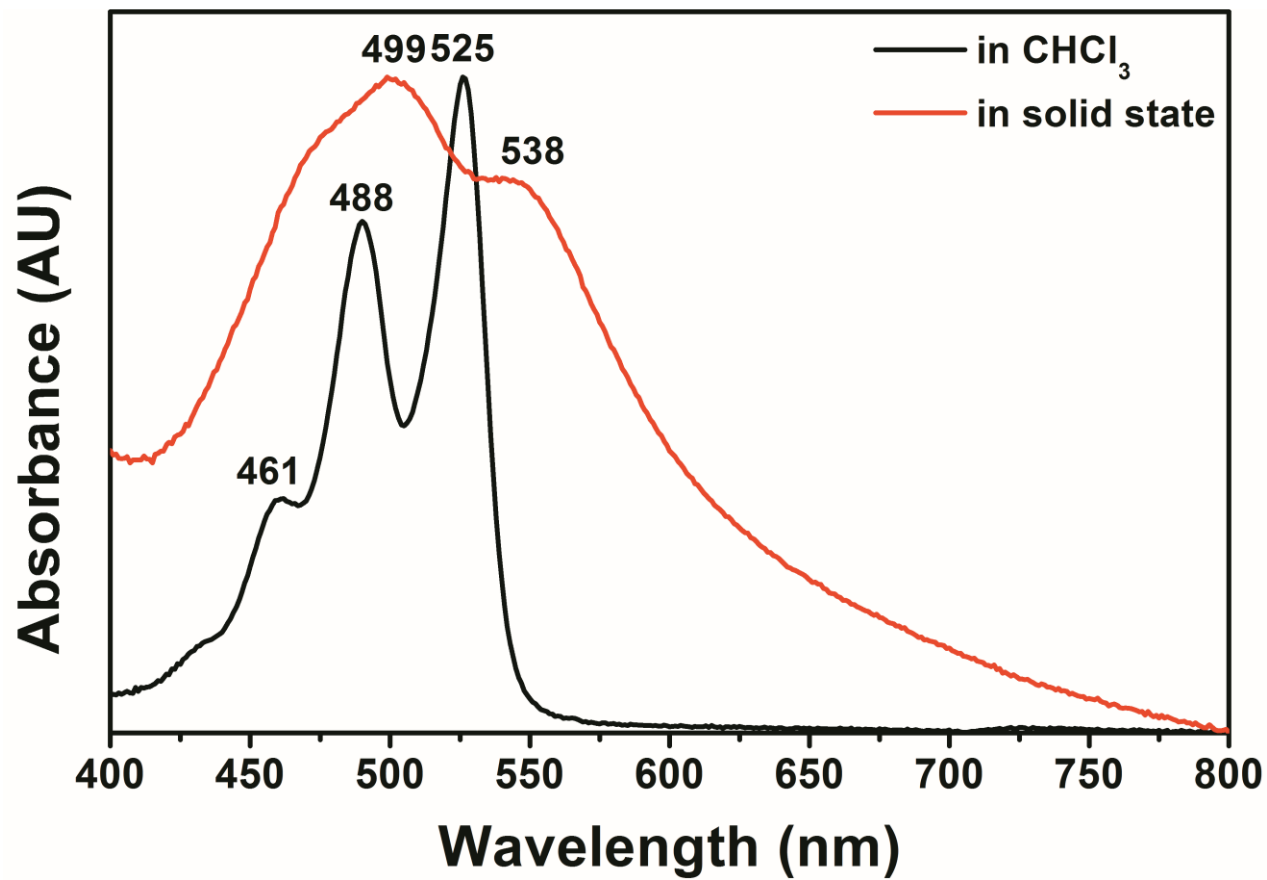
Figure 4.98: Comparison of UV-vis Absorption Spectra of CH-PPI in Solution and Solid-state
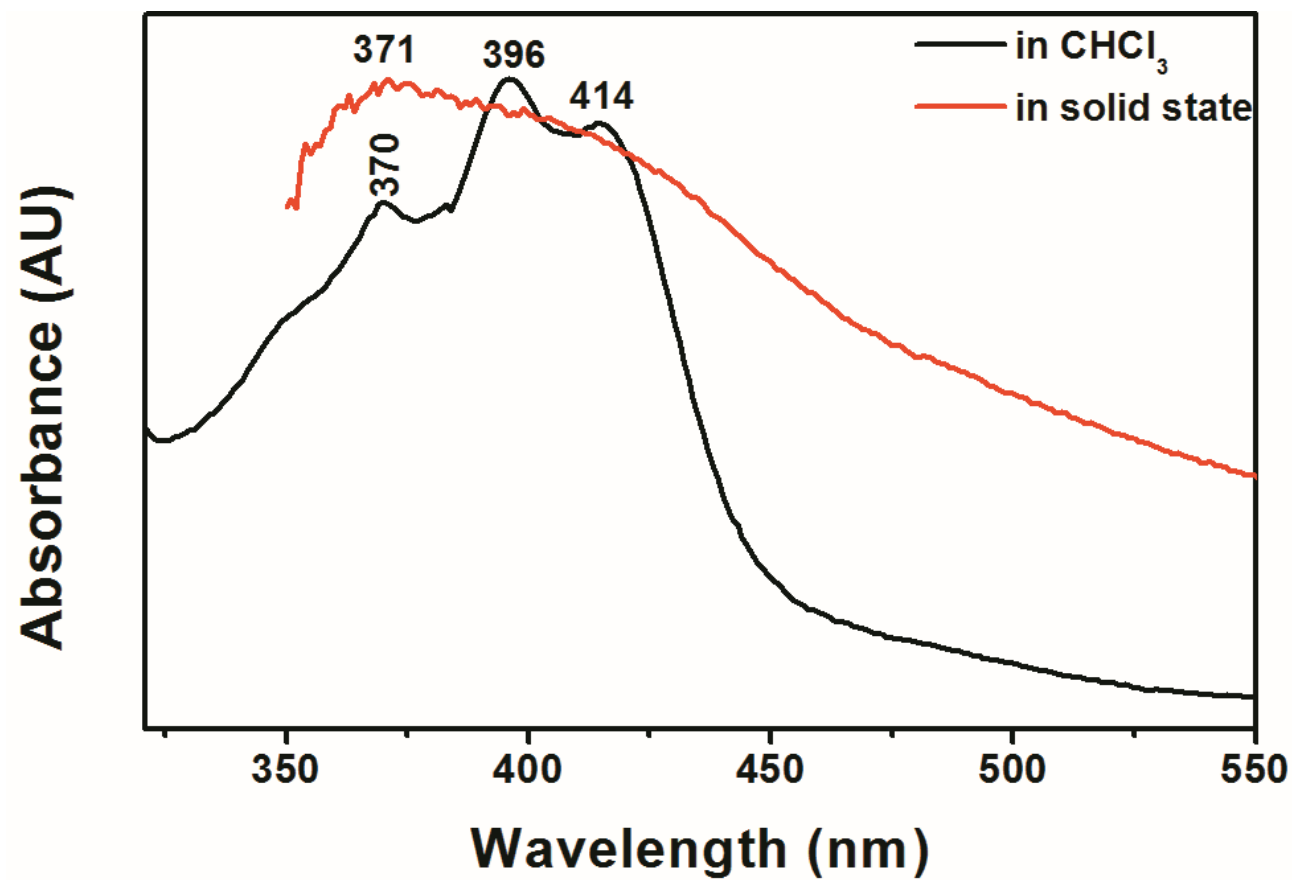
Figure 4.99: Comparison of UV-vis Absorption Spectra of CH-PNI in Solution and Solid-state
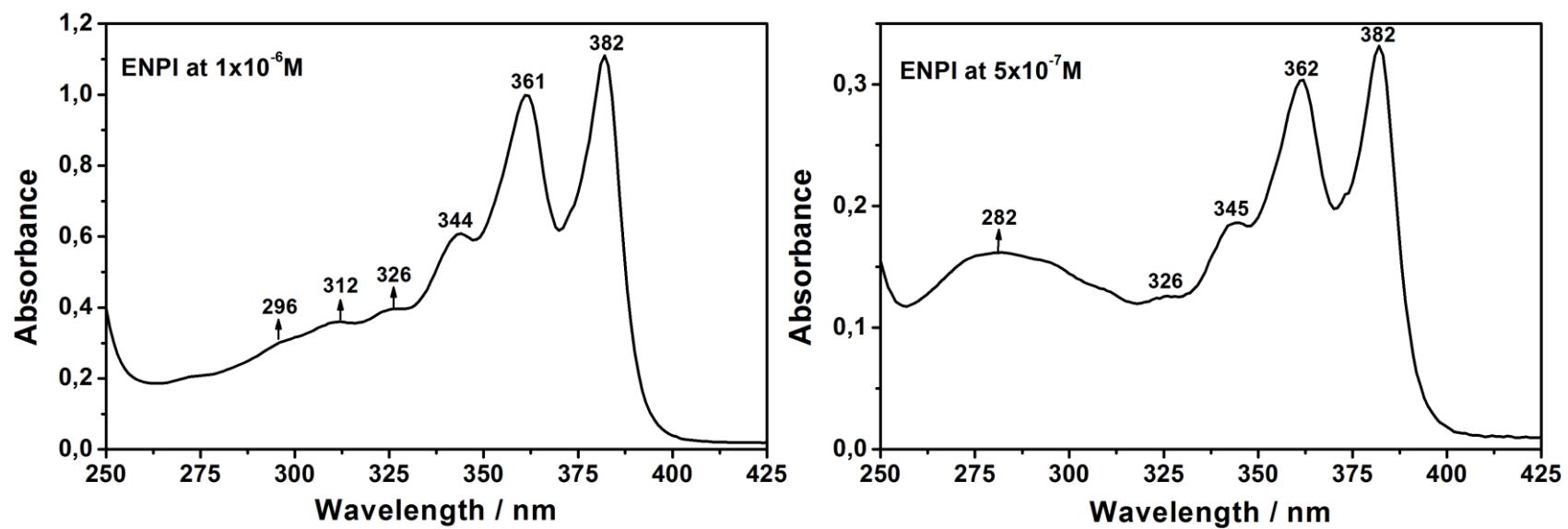
Figure 4.100: Absorption Spectra of ENPI in TCE at 1×10^{-6} M and 5×10^{-7} M.
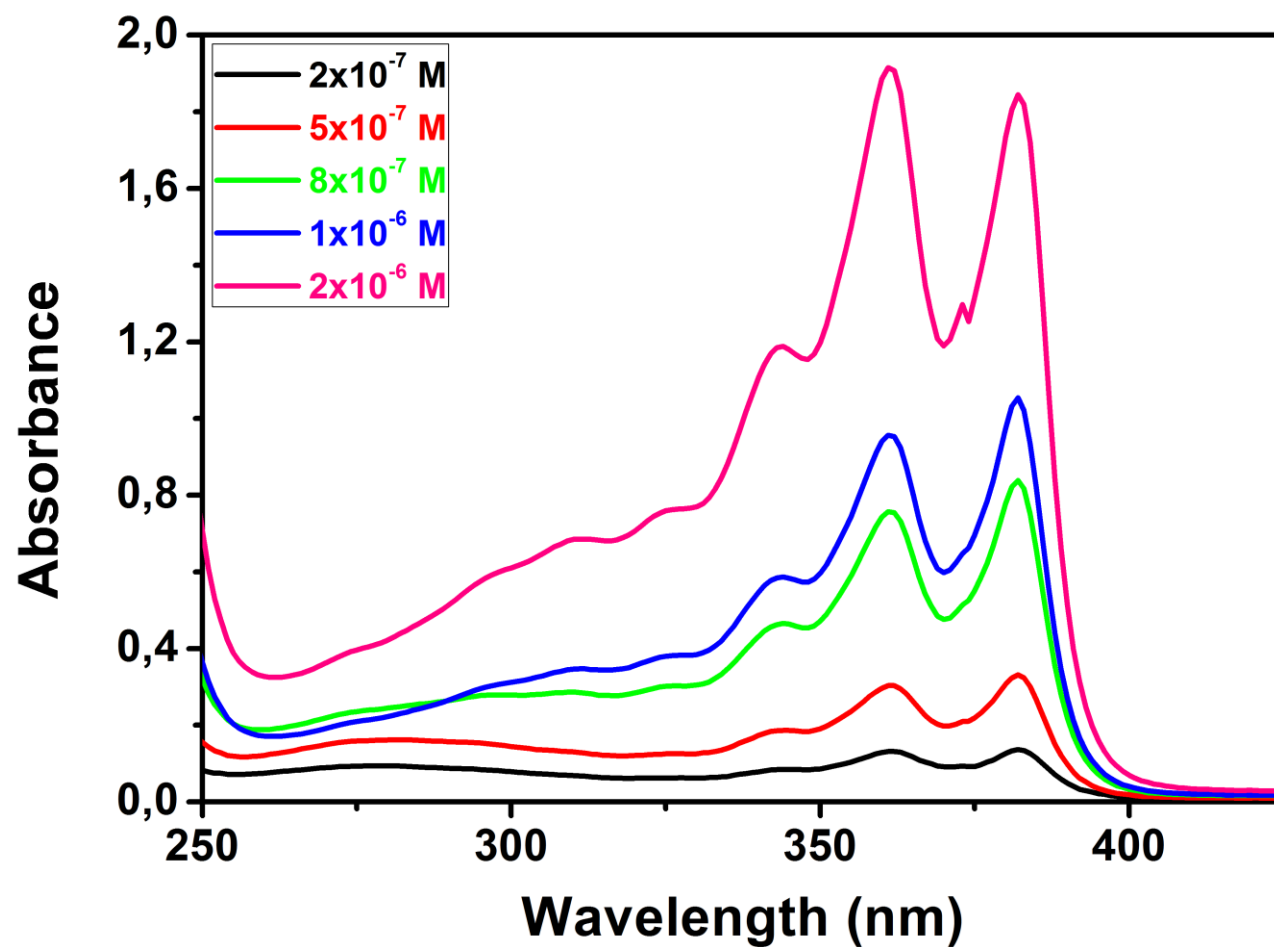
Figure 4.101: Effect of Concentration on Absorption Spectra of ENPI in TCE at Different Concentrations
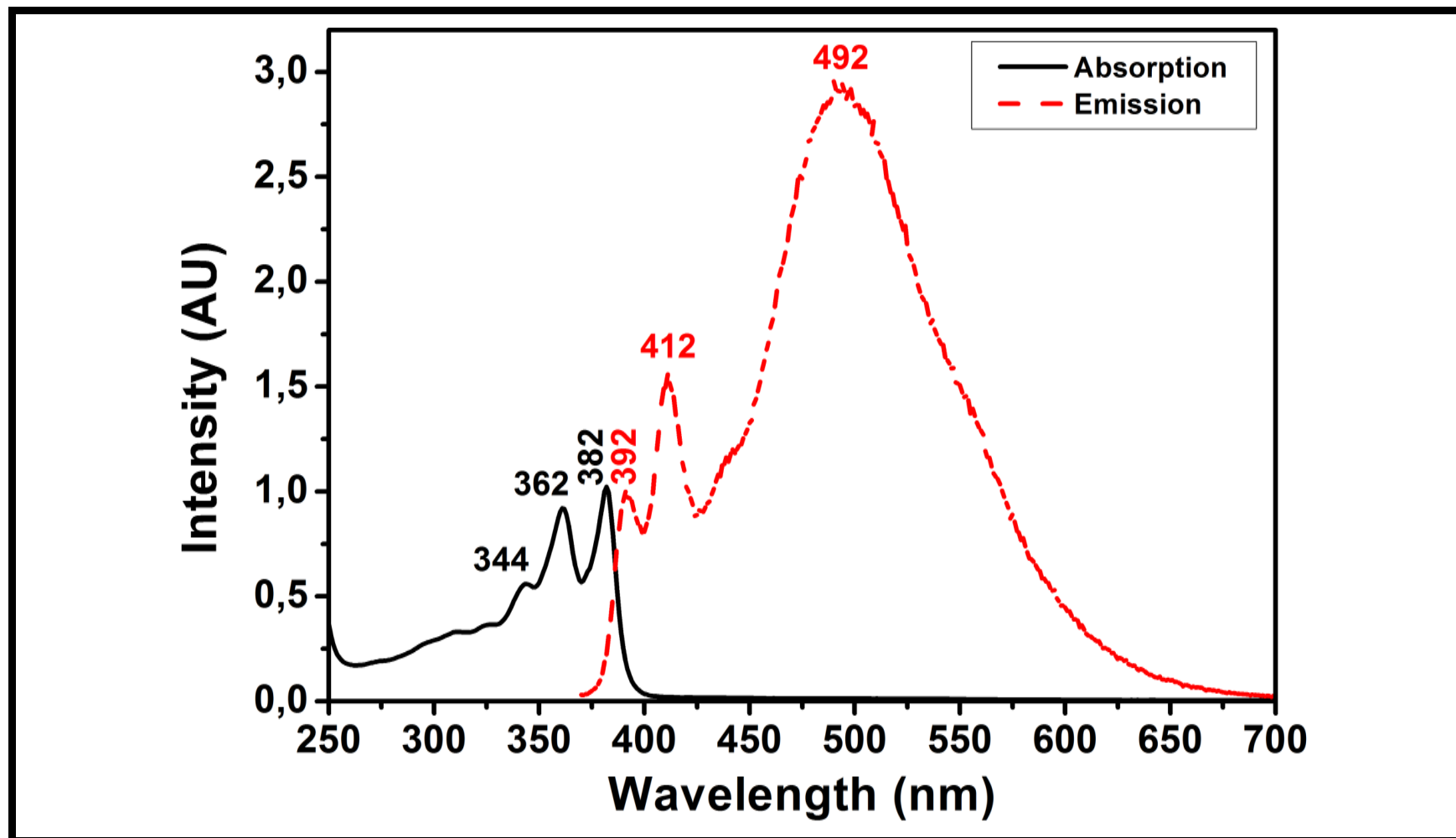
Figure 4.102: Normalized Absorption, and Emission Spectra of ENPI in TCE
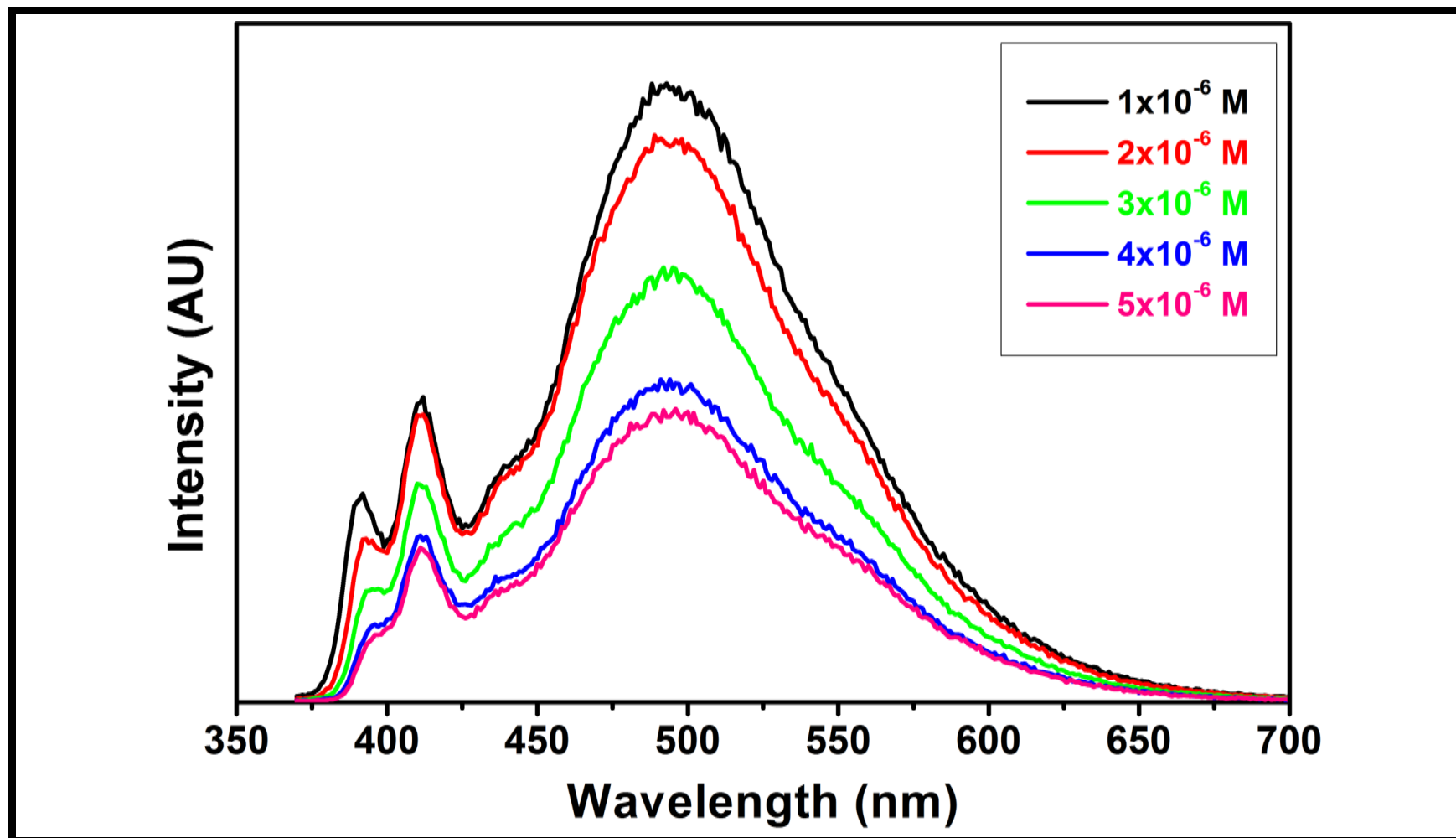
Figure 4.103: Effect of Concentration on Emission Spectra of ENPI in TCE at Different Concentrations
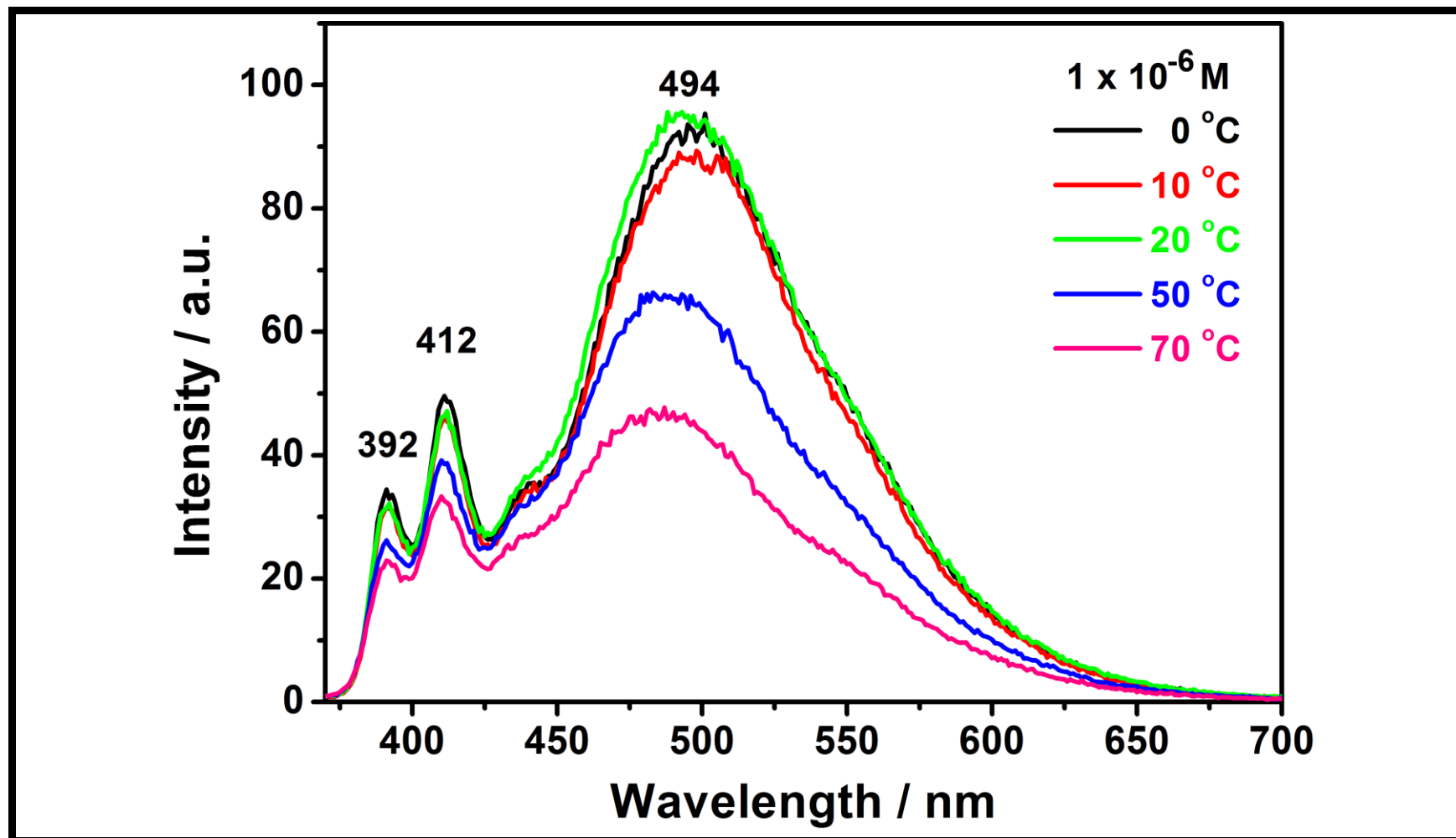
Figure 4.104: Effect of Temperature on Emission Spectra of ENPI in TCE at 1×10^{-6} M
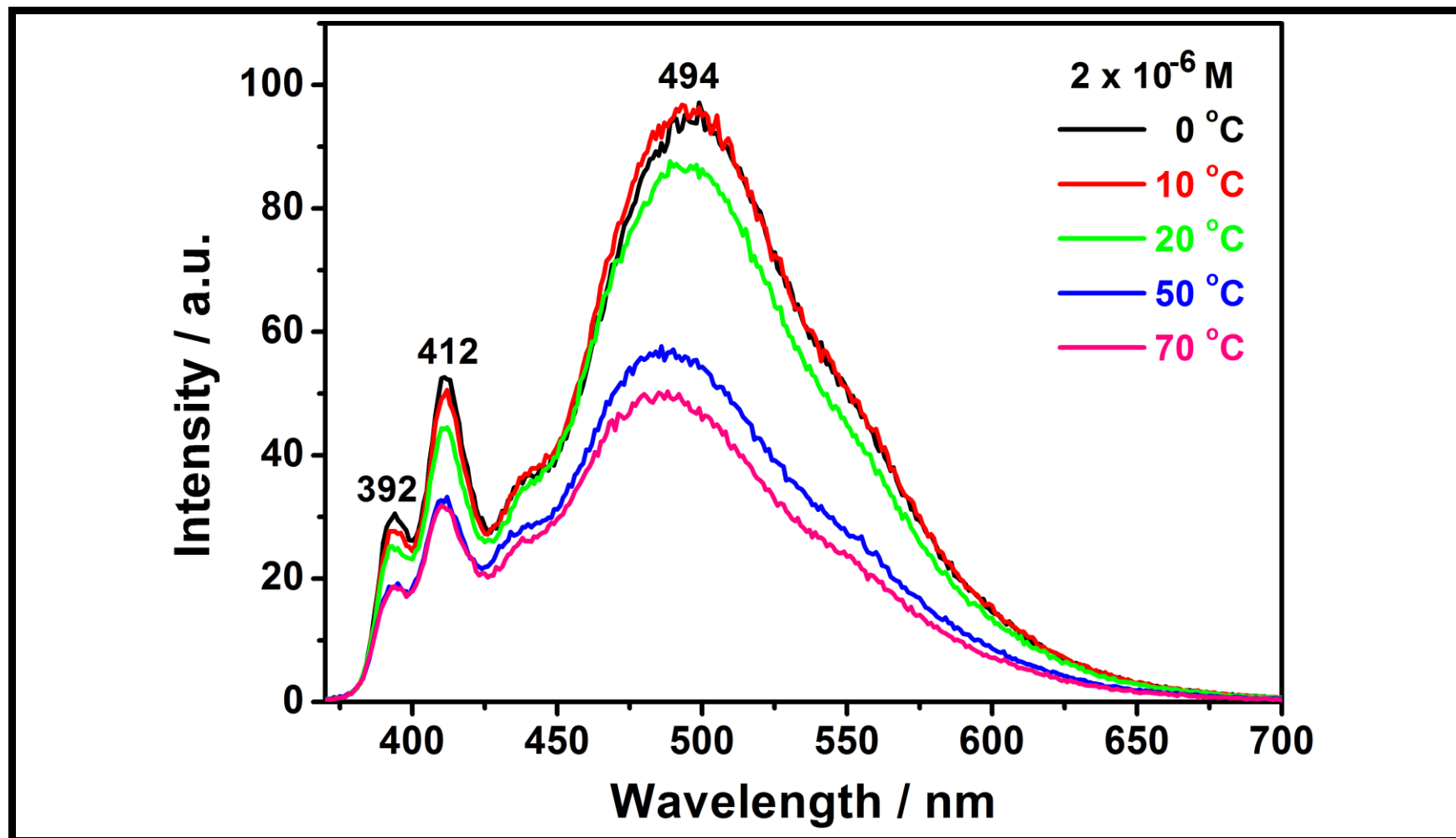
Figure 4.105: Effect of Temperature on Emission Spectra of ENPI in TCE at 2×10^{-6} M
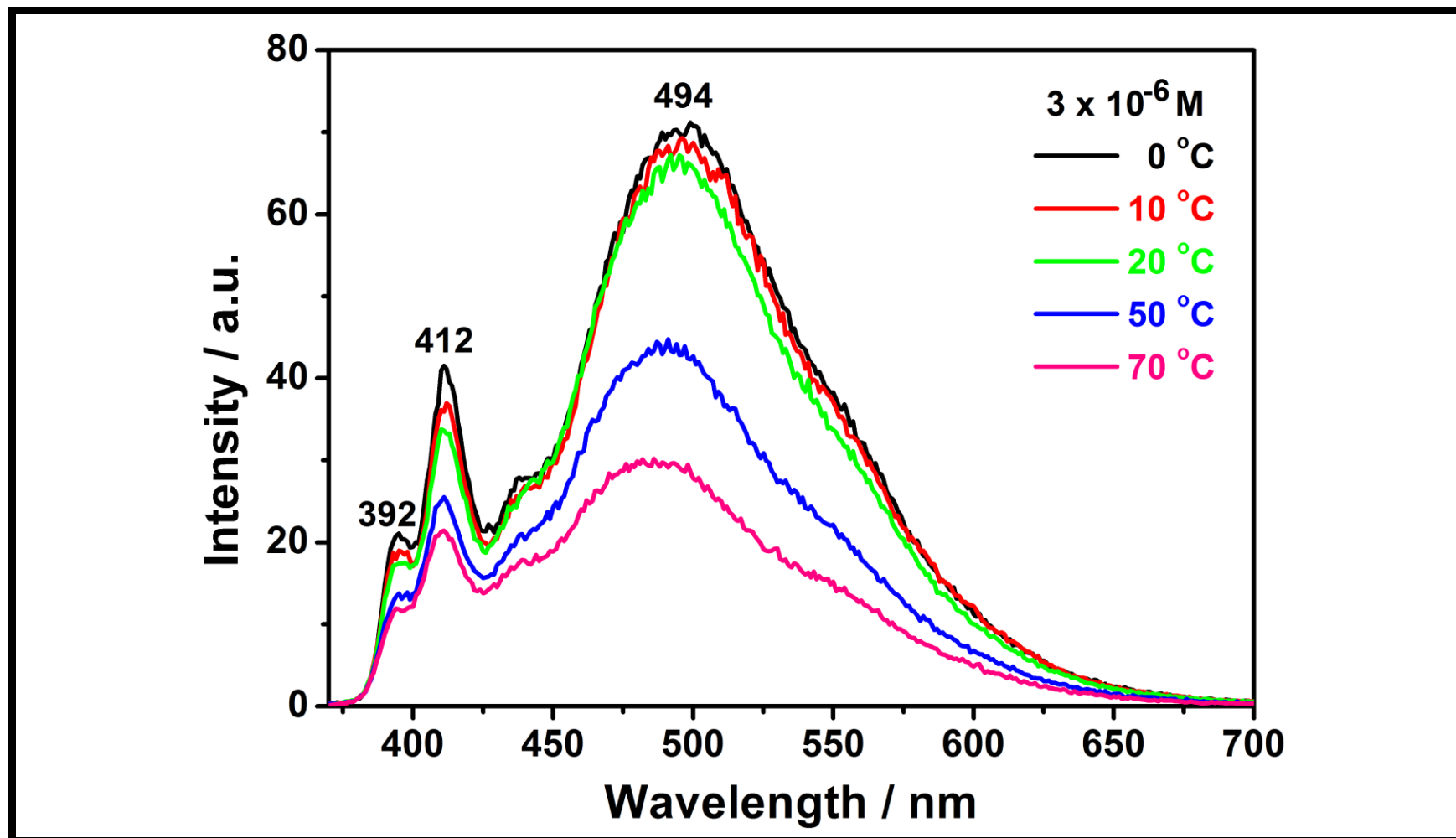
Figure 4.106: Effect of Temperature on Emission Spectra of ENPI in TCE at 3×10^{-6} M
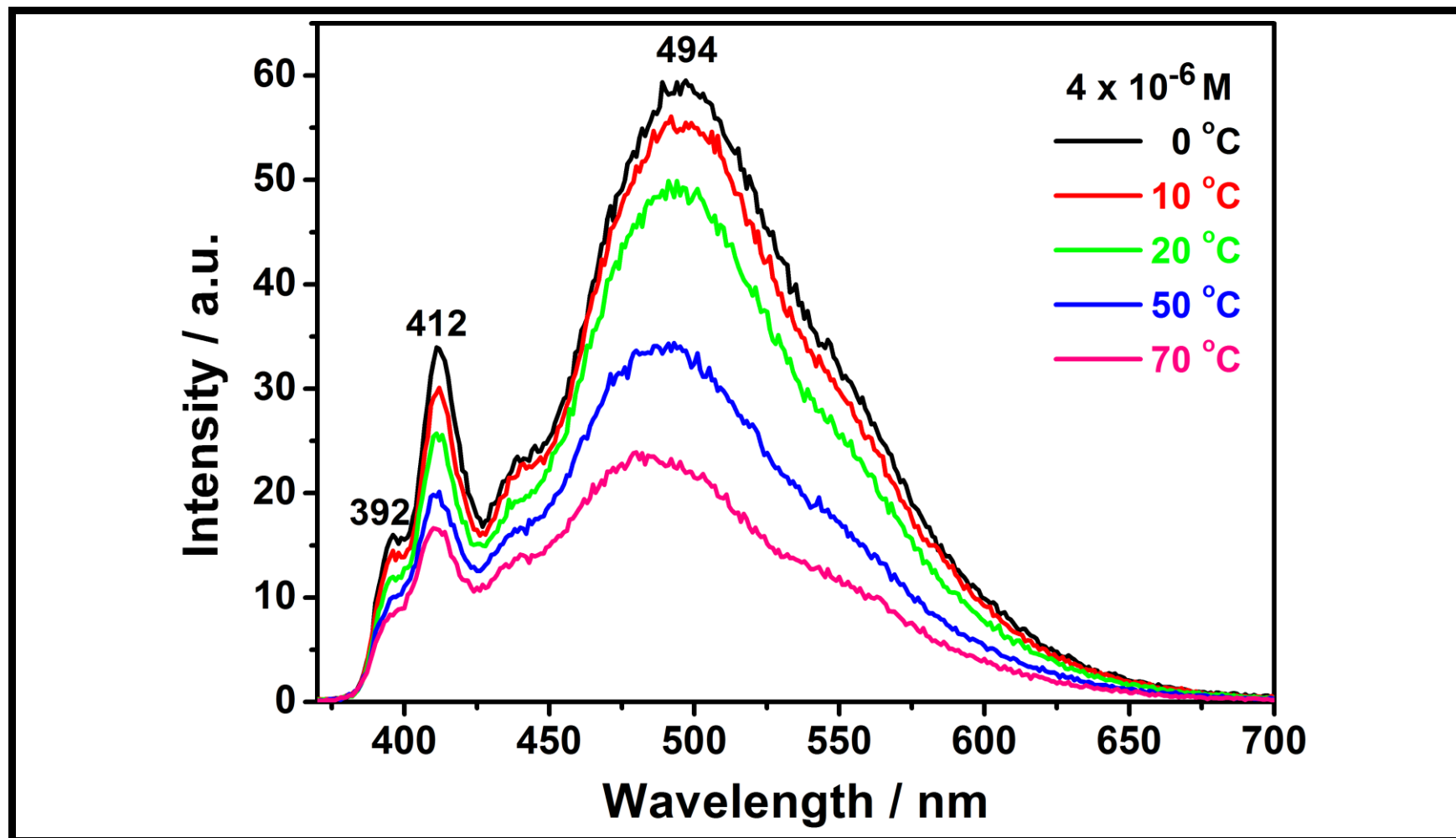
Figure 4.107: Effect of Temperature on Emission Spectra of ENPI in TCE at 4×10^{-6} M
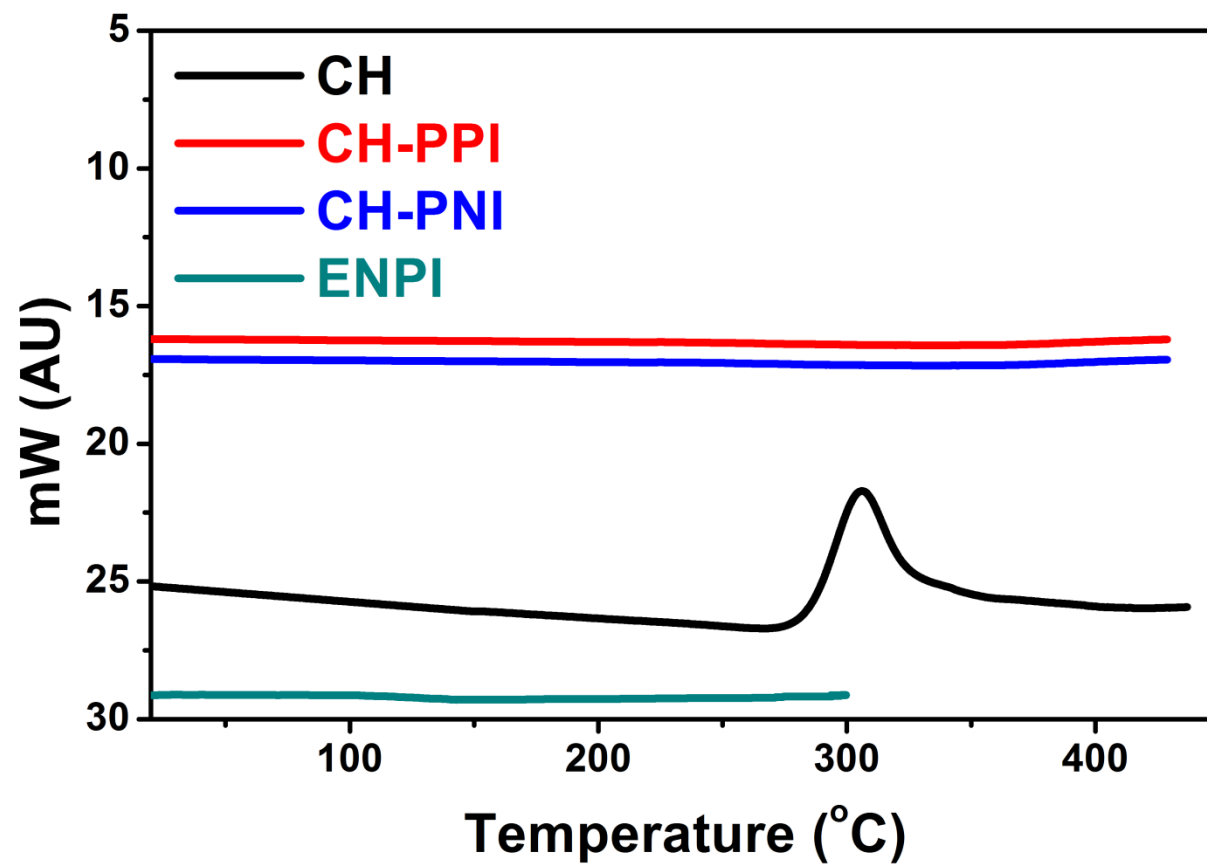
Figure 4.108: DSC thermograms of CH, CH-PPI, CH-PNI and ENPI
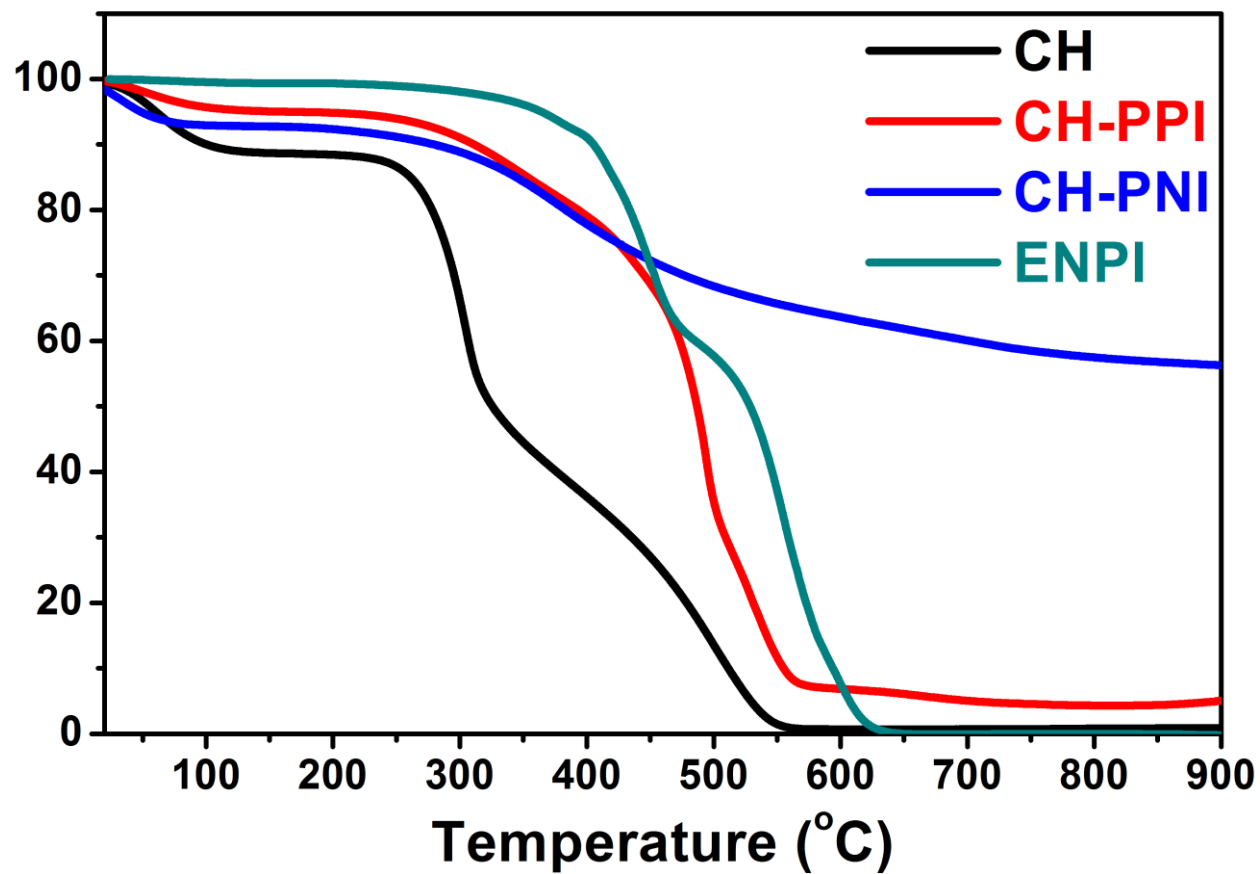
Figure 4.109: TGA Curves of CH, CH-PPI, CH-PNI and ENPI
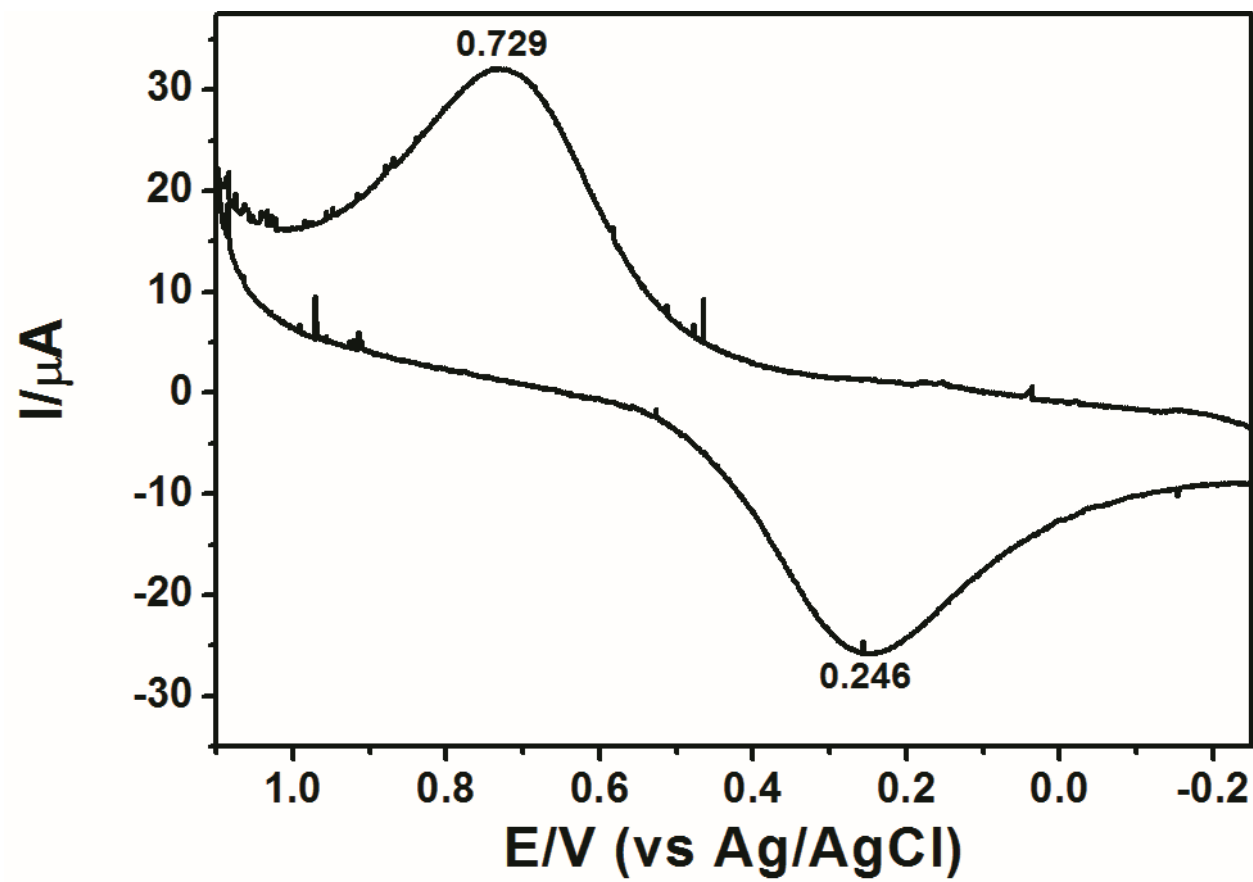
Figure 4.110: Solid-state cyclic voltammogram of CH at a scan rate of 100 mVs^{-1}
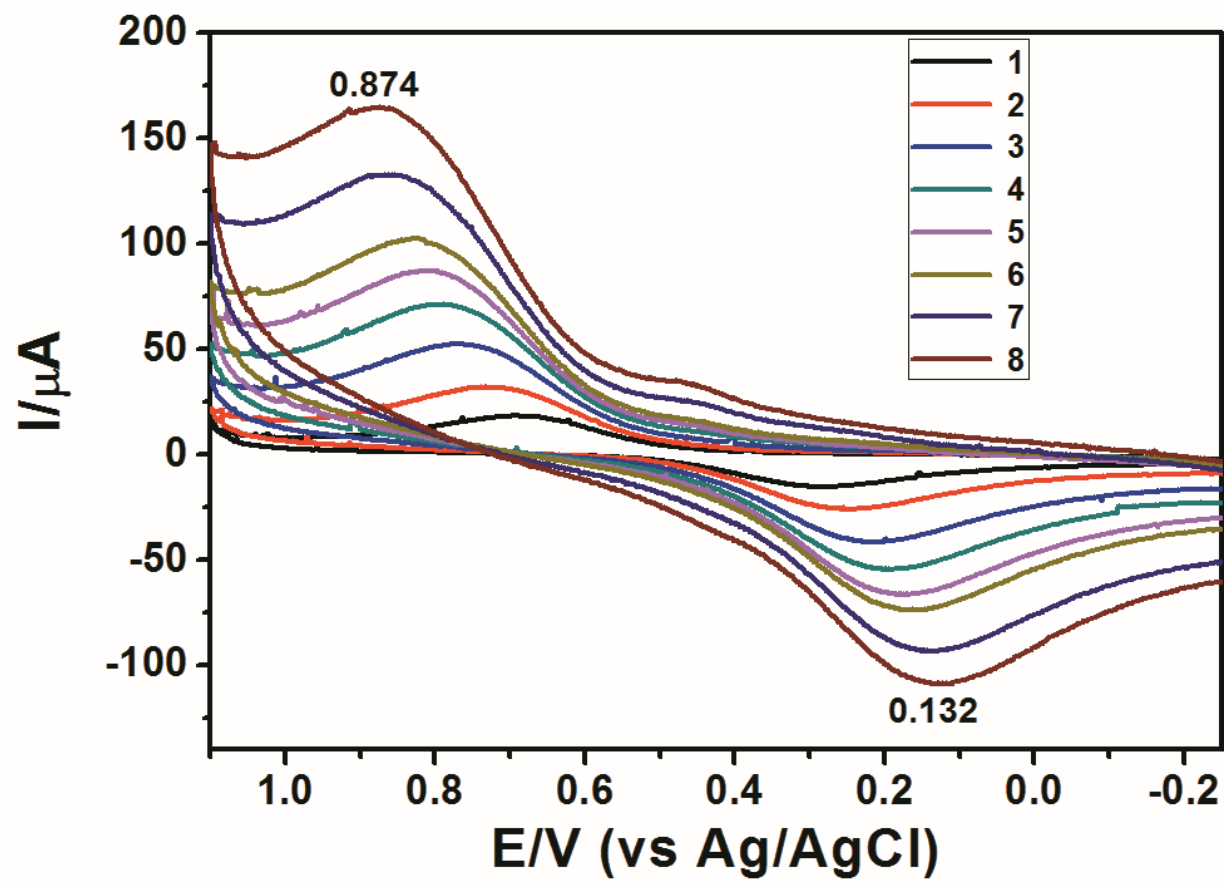
Figure 4.111: Solid-state cyclic voltammogram of CH at different scan rates (mVs^{-1}): 1 (50), 2 (100), 3 (200), 4 (300), 5 (400), 6 (500), 7 (750), 8 (1000) at 25°C
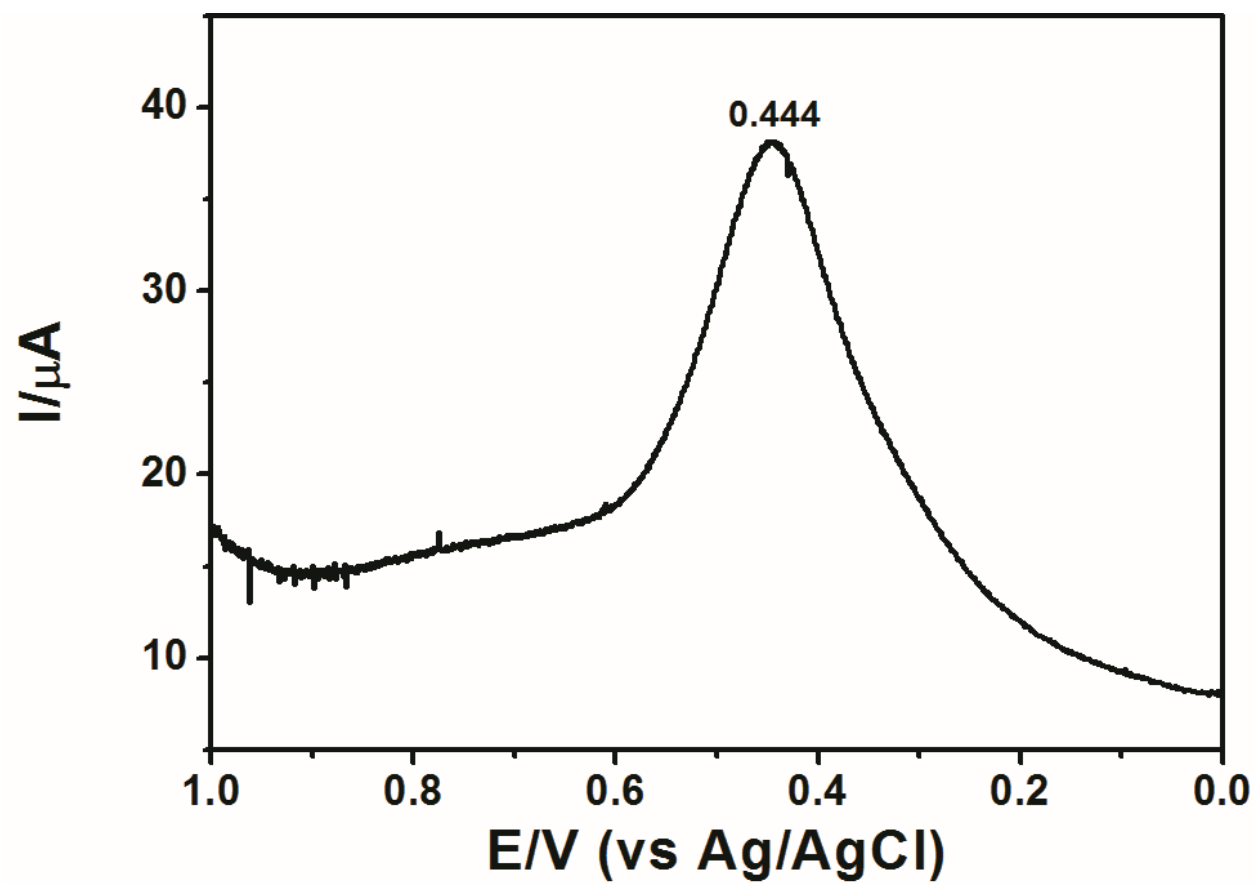
Figure 4.112: Solid-state Squarewave Voltammograms of CH at a Frequency of 100 Hz
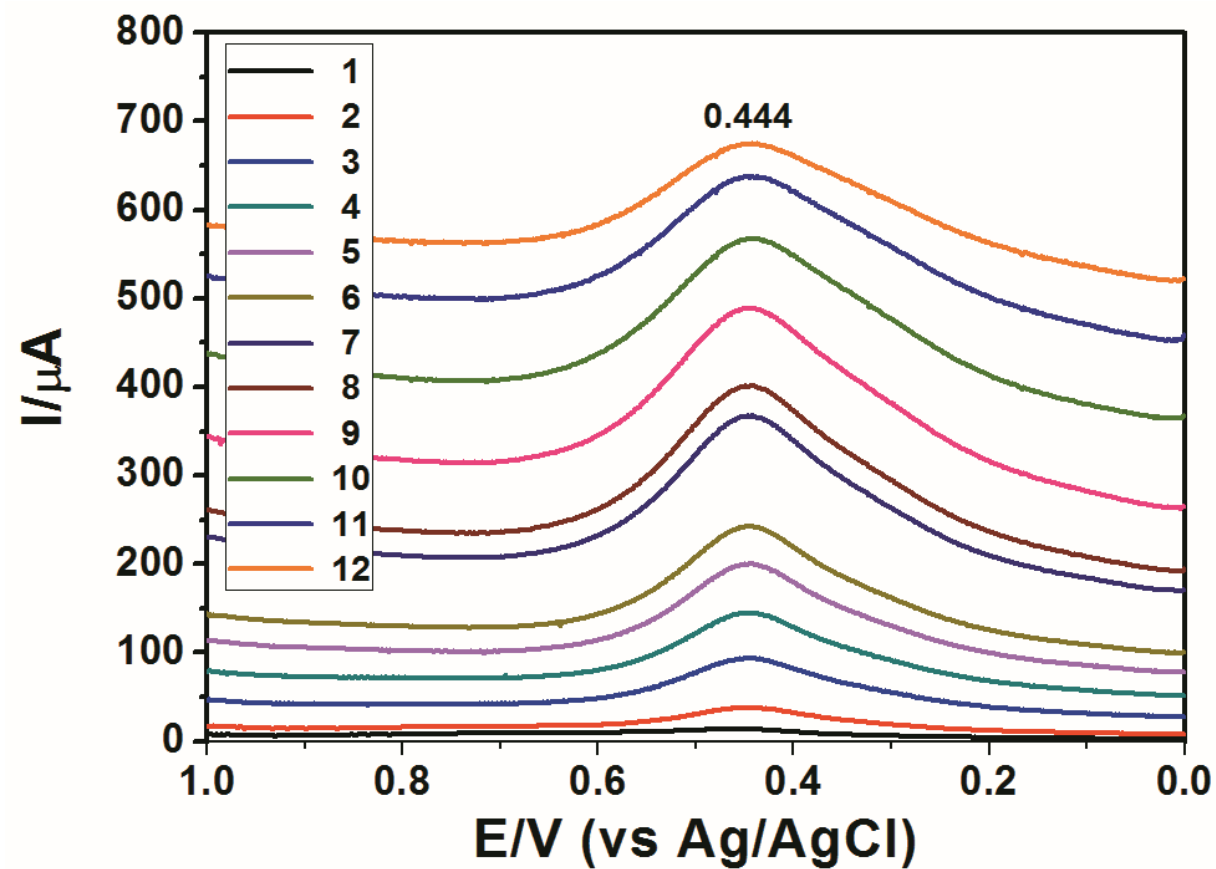
Figure 4.113: Solid-state Squarewave Voltammograms of CH-PPI at Different frequencies (Hz): 1 (50), 2 (100), 3 (200), 4 (300), 5 (400), 6 (500), 7 (750), 8 (1000), 9 (1250), 10 (1500), 11 (1750), 12 (2000), at 25 °C
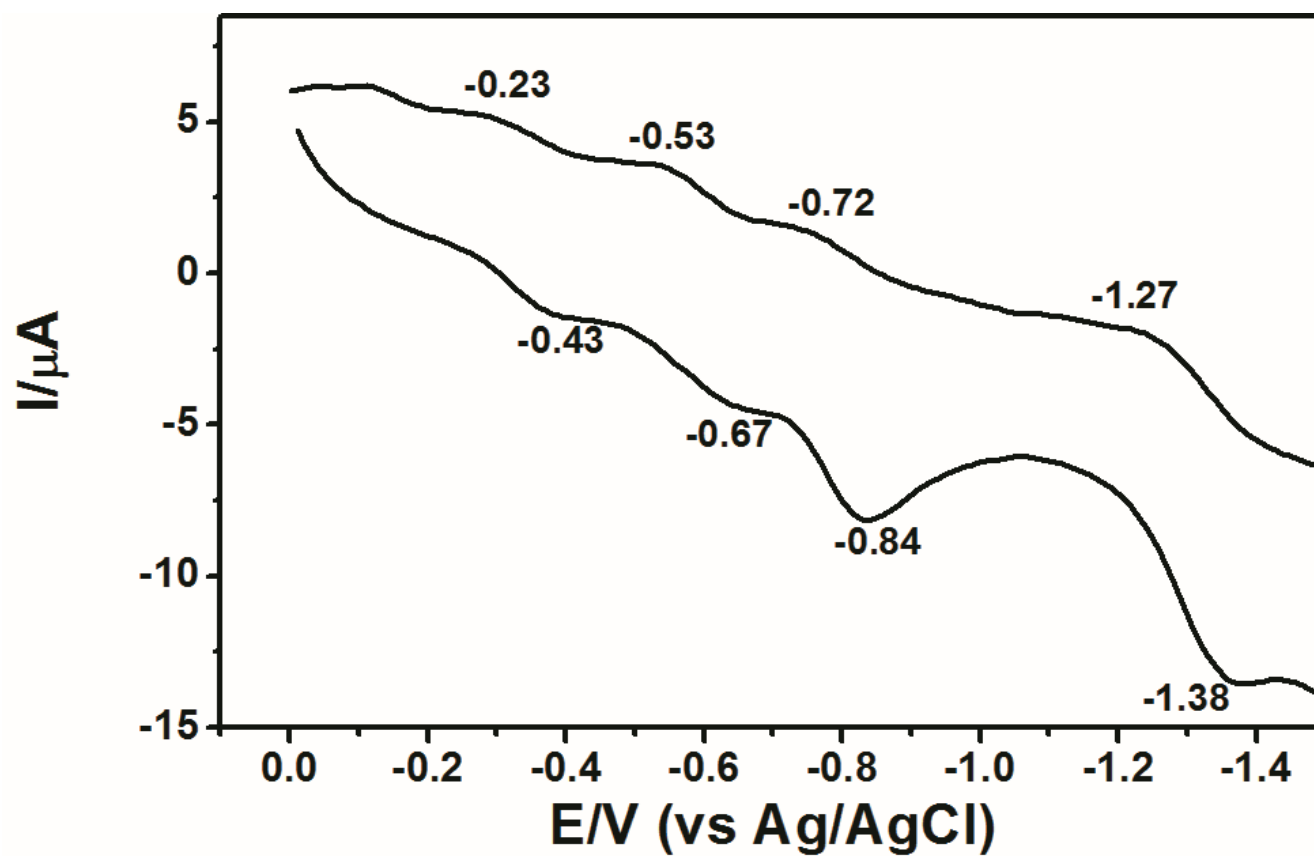
Figure 4.114: Cyclic Voltammogram of CH-PPI in DMAc; supporting electrolyte: $NaBF_4$, scan rates (mVs^{-1}): 100 at 25 °C
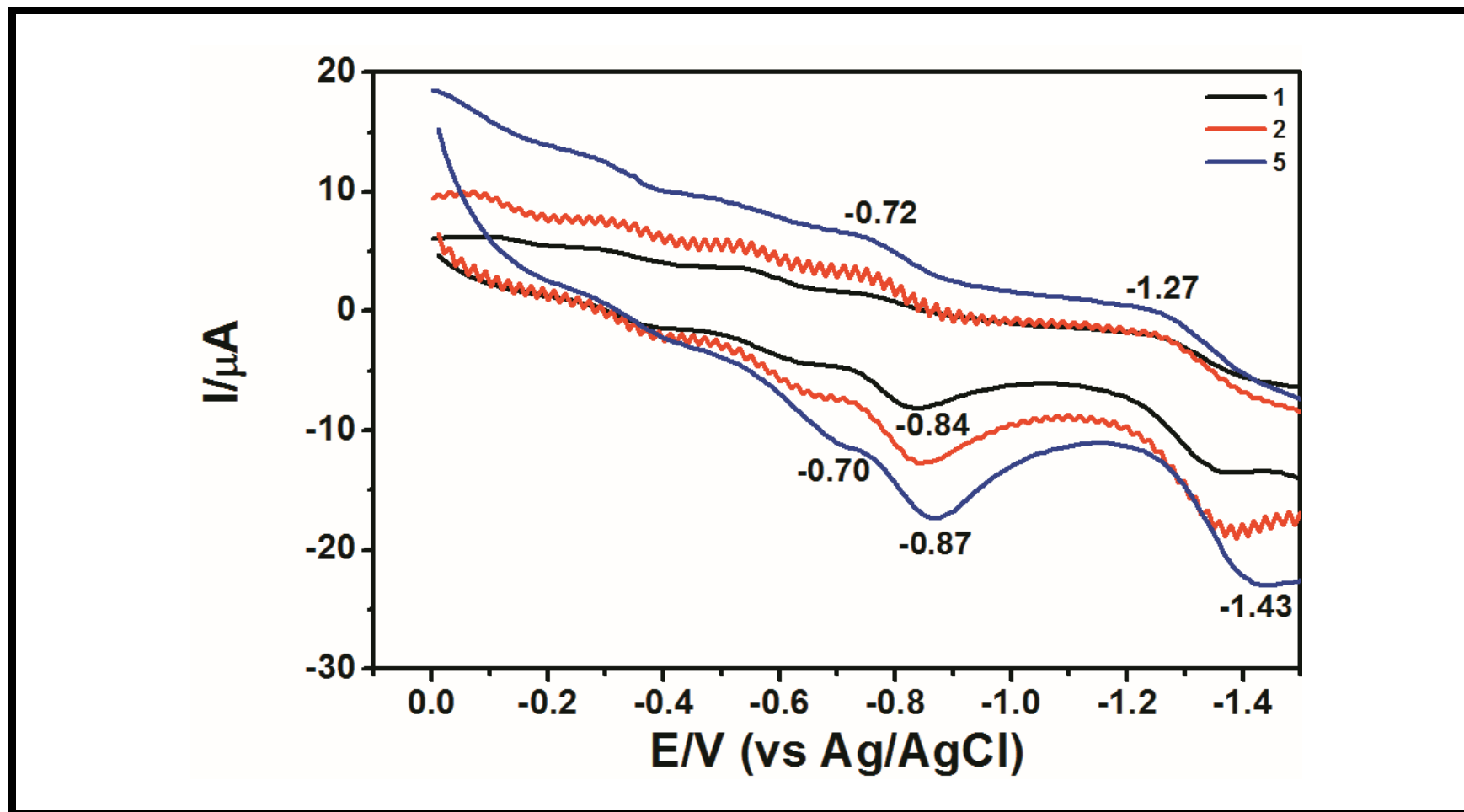
Figure 4.115: Cyclic Voltammograms of CH-PPI at Different Scan Rates in DMAc; supporting electrolyte: $NaBF_4$, scan rates (mVs^{-1}): 1 (100), 2 (200), 3 (500) at 25 °C
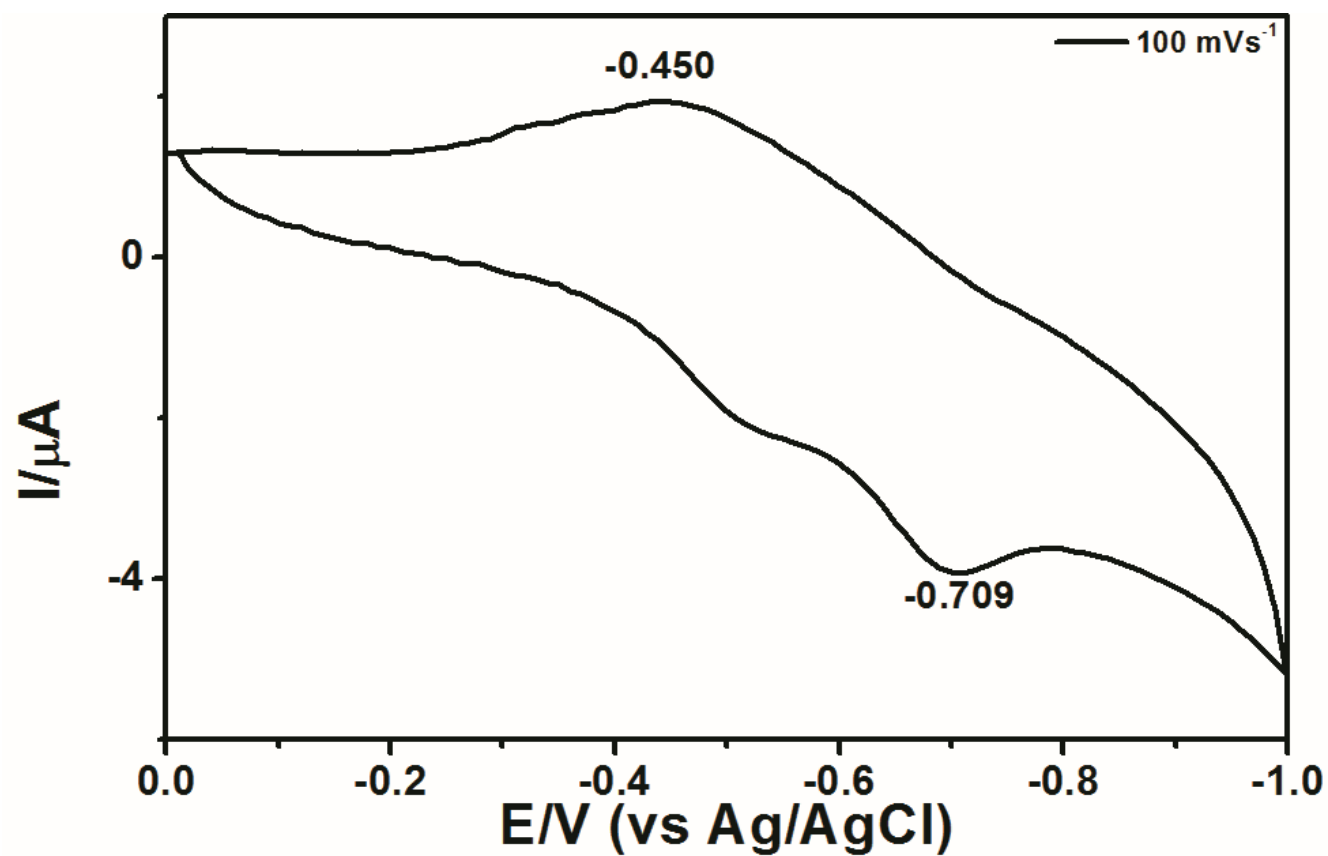
Figure 4.116: Cyclic Voltammogram of CH-PNI in NMP; supporting electrolyte: $NaBF_4$, scan rates (mVs^{-1}): 100 at 25 °C
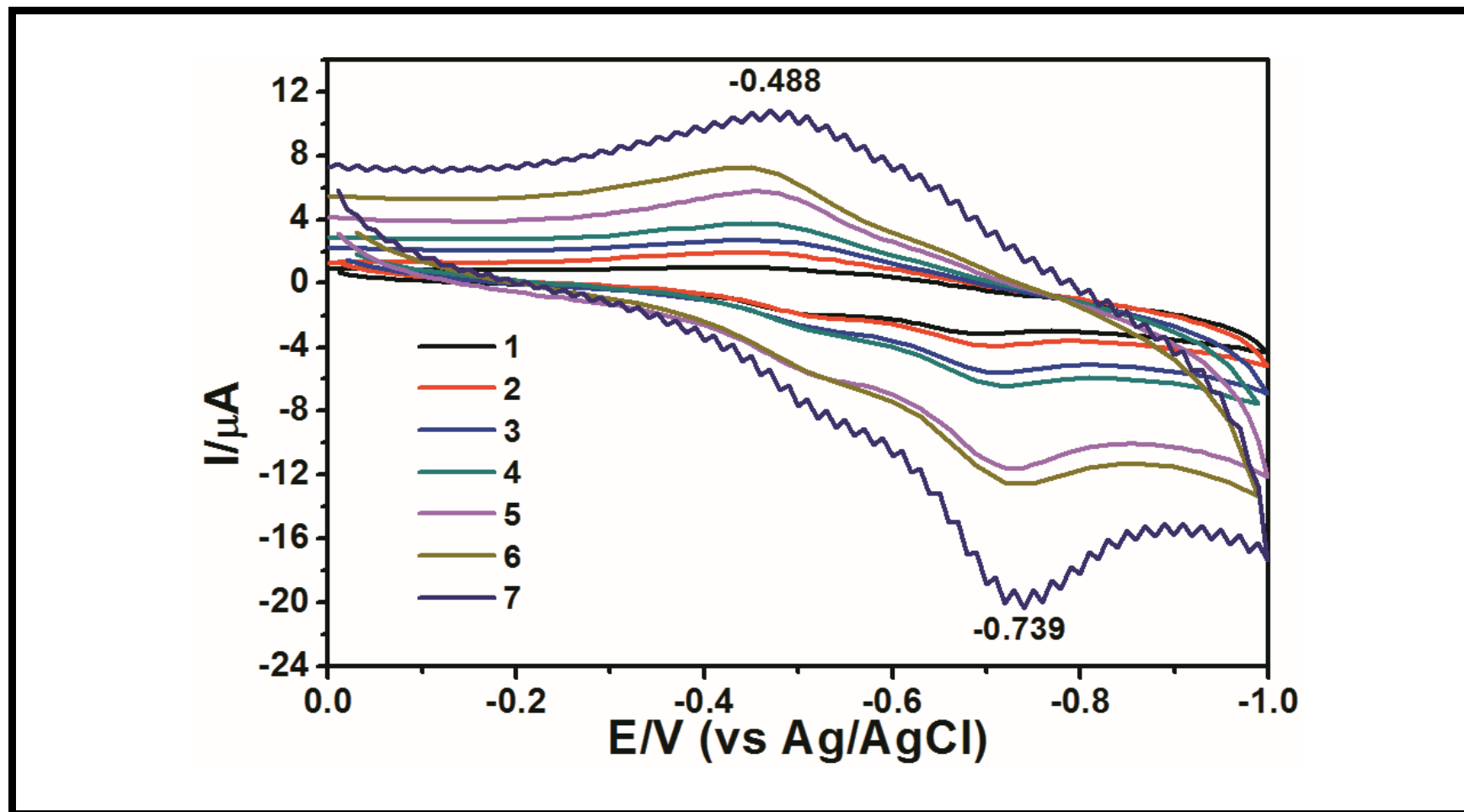
Figure 4.117: Cyclic Voltammograms of CH-PNI at Different Scan Rates in NMP; supporting electrolyte: NaBF$_4$, scan rates (mVs^{-1}): 1 (50), 2 (100), 3 (200) 4 (300), 5 (500), 6 (750), 8 (1000) at 25 °C
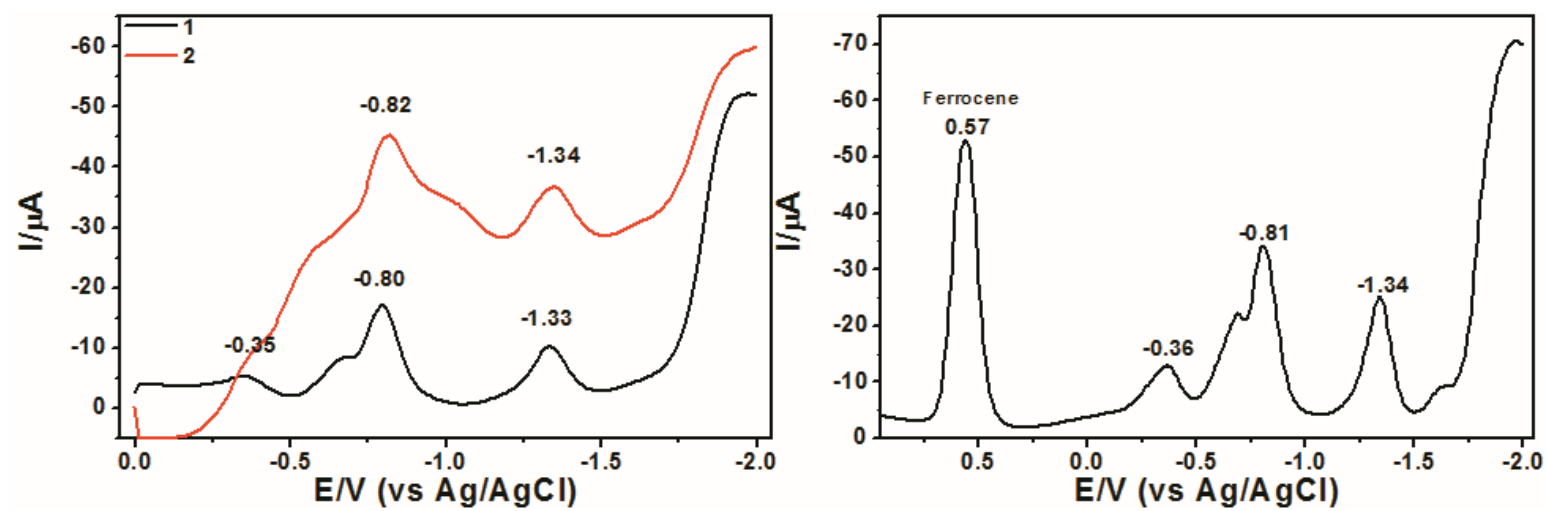
Figure 4.118: Square-wave voltammograms of CH-PPI in DMAc; supporting electrolyte: NaBF$_4$, frequencies (Hz): 1 (25), 2 (50), at 25 °C
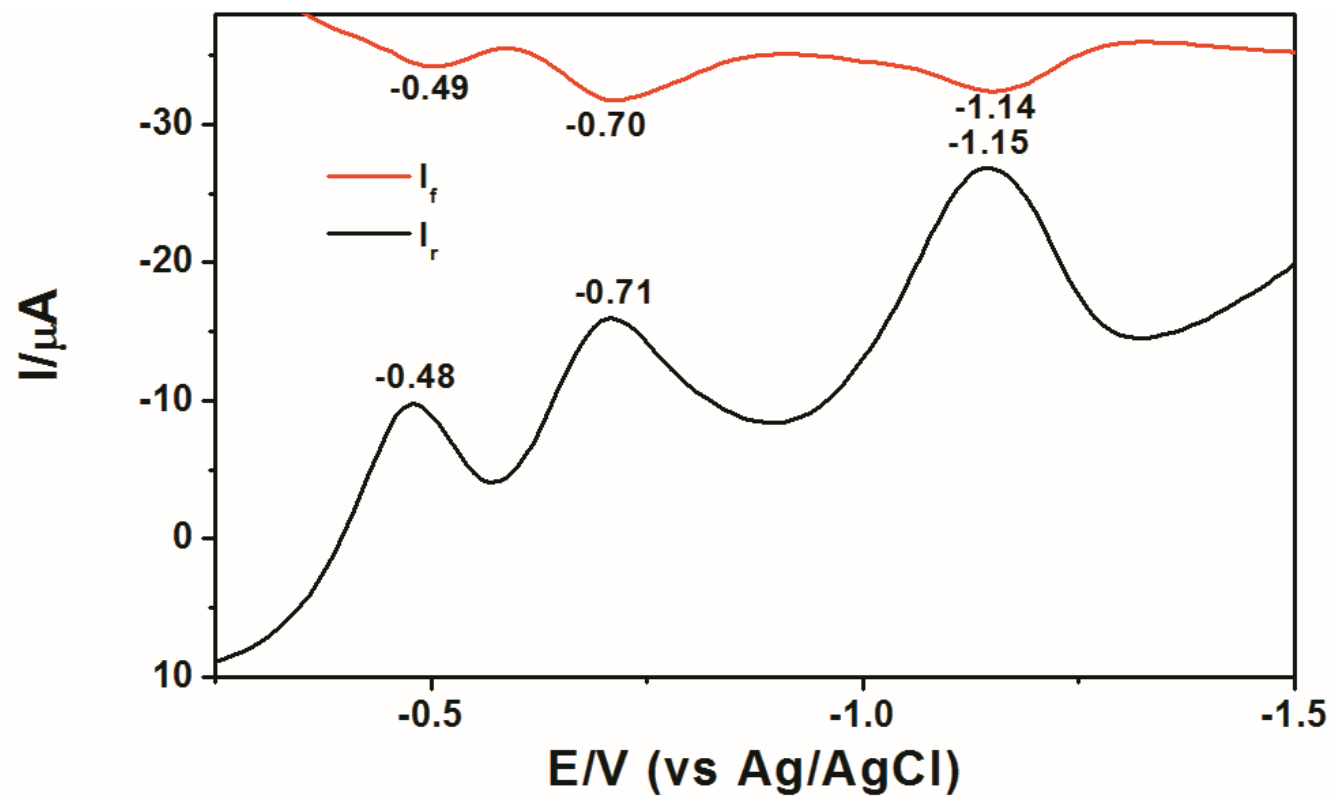
Figure 4.119: Solid-state Squarewave Voltammograms of CH-PNI in NMP at different Frequencies (Black:25 Hz, red:50Hz)
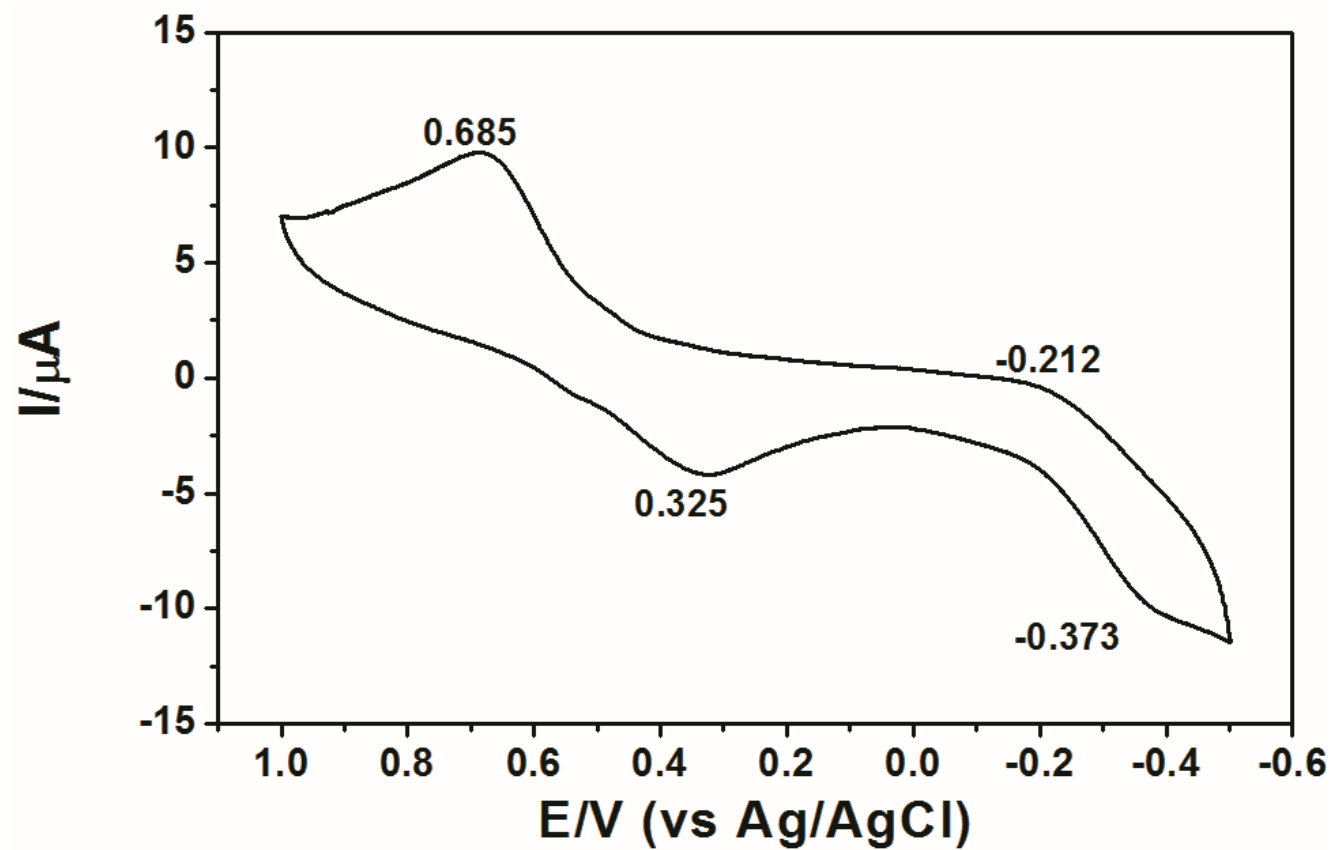
Figure 4.120: Solid-state cyclic voltammogram of CH-PPI at a scan rate of 100 mVs^{-1}
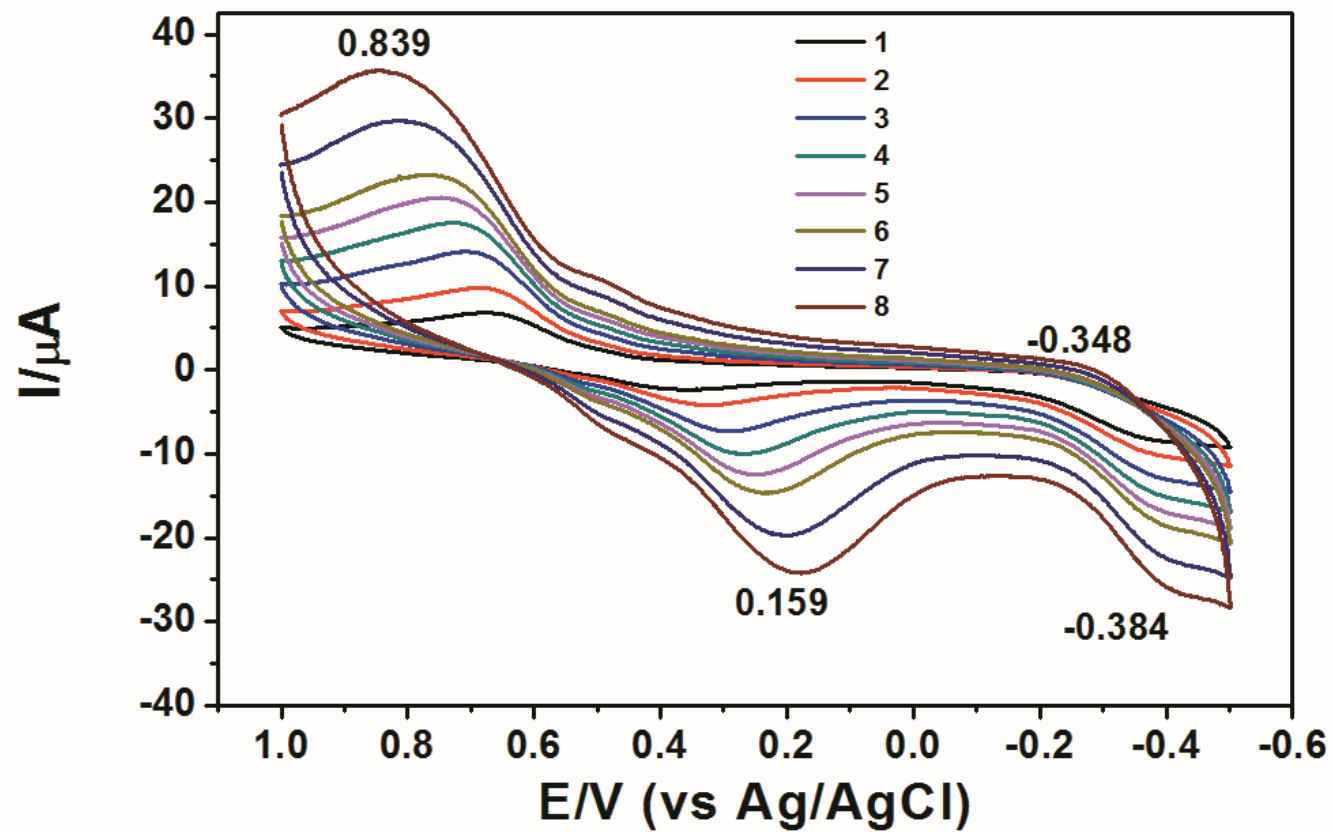
Figure 4.121: Solid-state cyclic voltammograms of CH-PPI at different scan rates (mVs^{-1}): 1 (50), 2 (100), 3 (200), 4 (300), 5 (400), 6 (500), 7 (750), 8 (1000) at 25°C
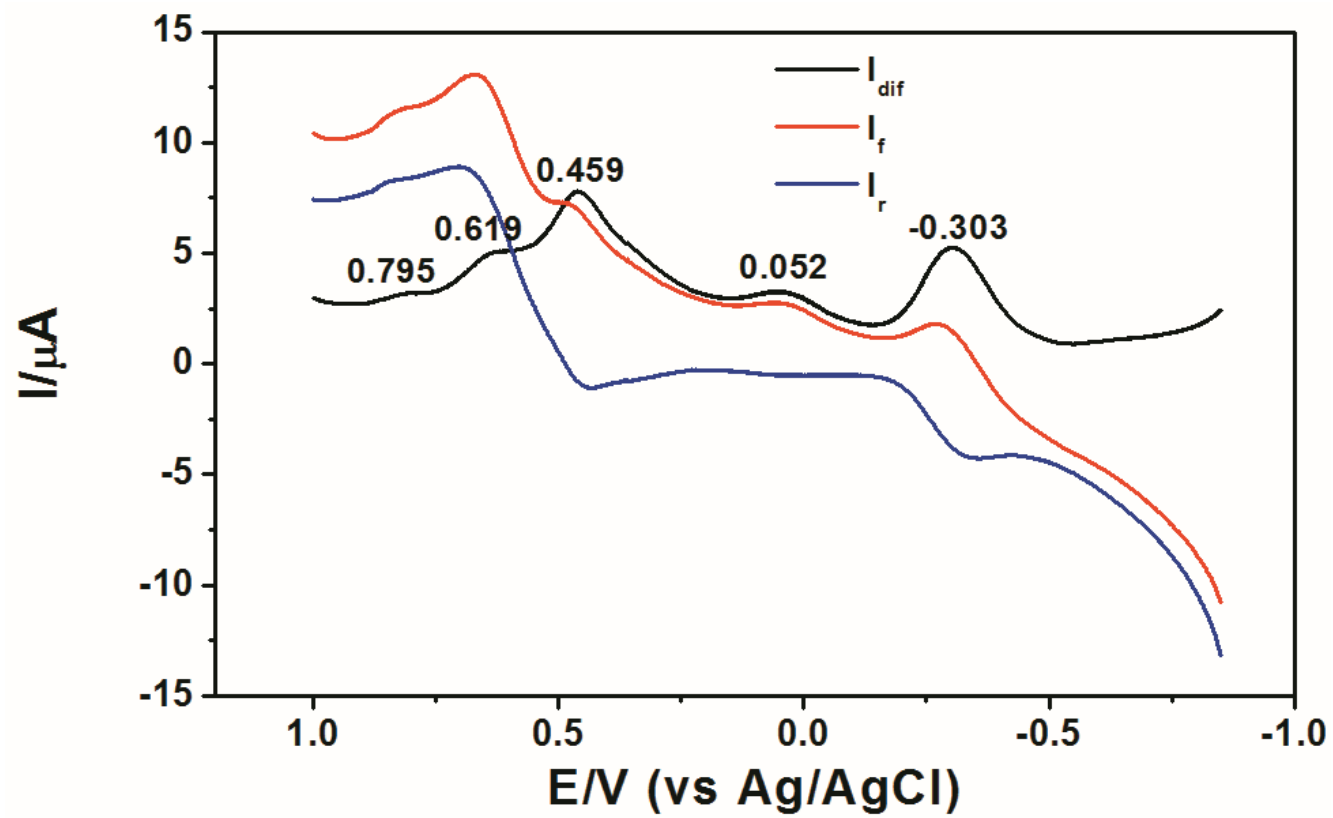
Figure 4.122: Solid-state Squarewave Voltammograms of CH-PPI at a Frequency of 100 Hz
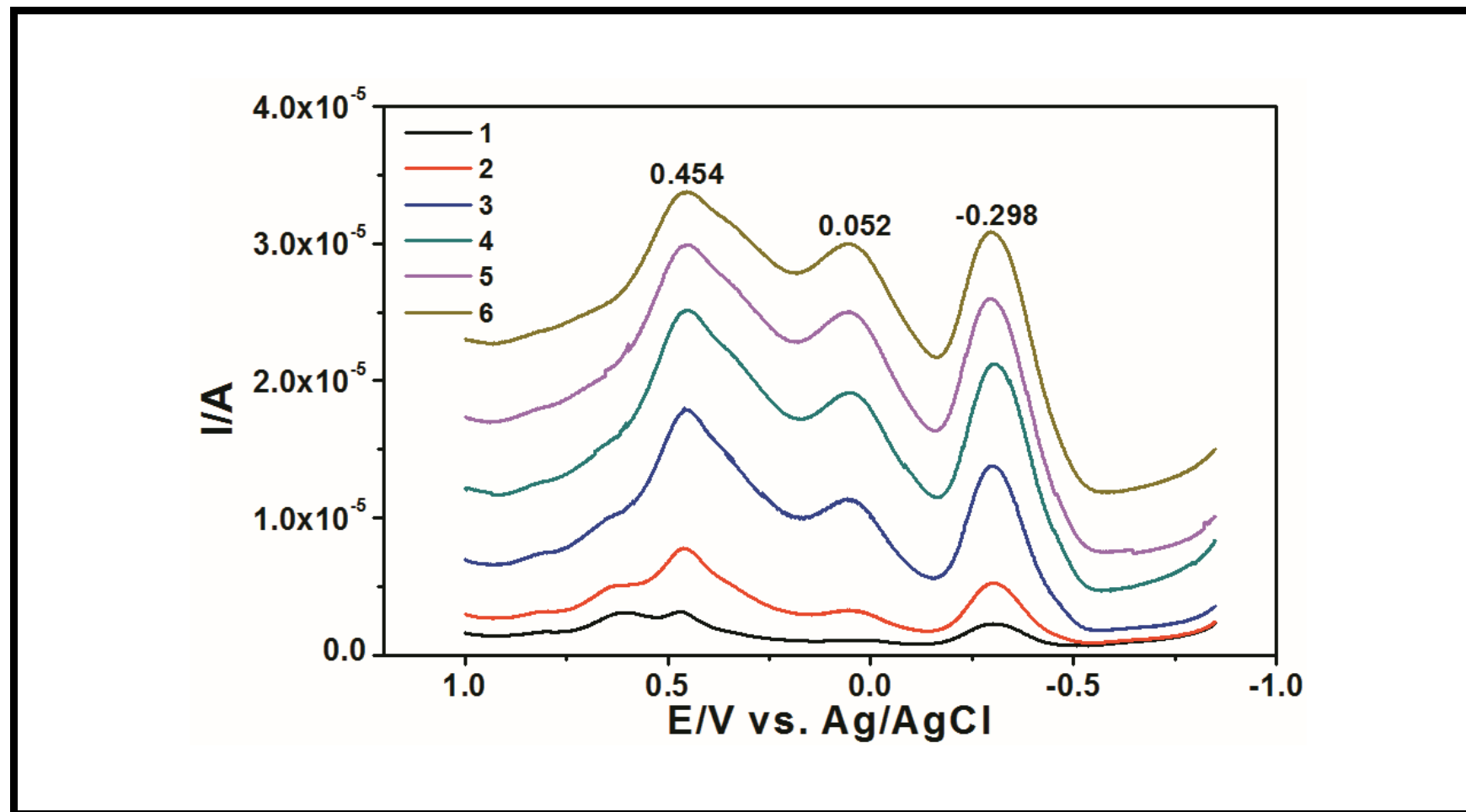
Figure 4.123: Solid-state Squarewave Voltammograms of CH-PPI at Different frequencies (Hz): 1 (50), 2 (100), 3 (200), 4 (300), 5 (400), 6 (500), at 25 °C
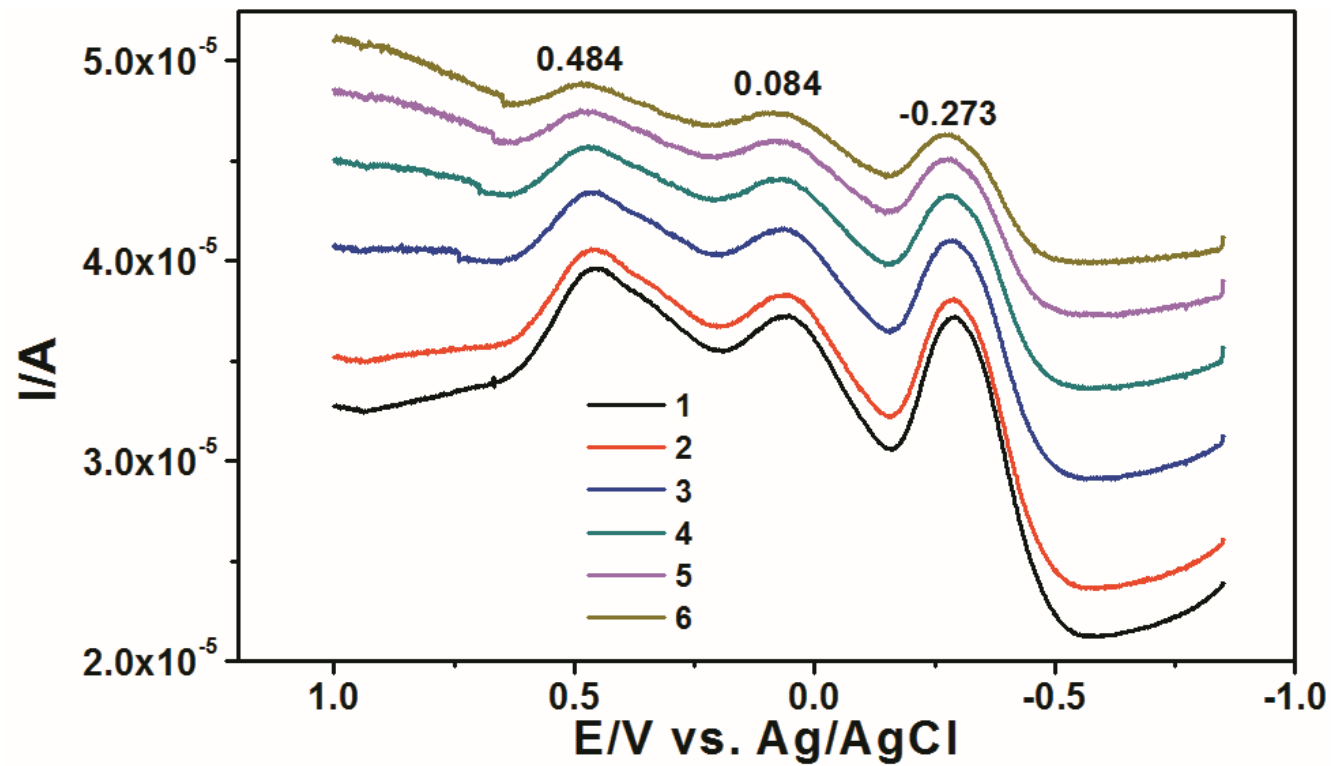
Figure 4.124: Solid-state Squarewave Voltammograms of CH-PPI at Different frequencies (Hz): 1 (750), 2 (1000), 3 (1250), 4 (1500), 5 (1750), 6 (2000), at 25 °C
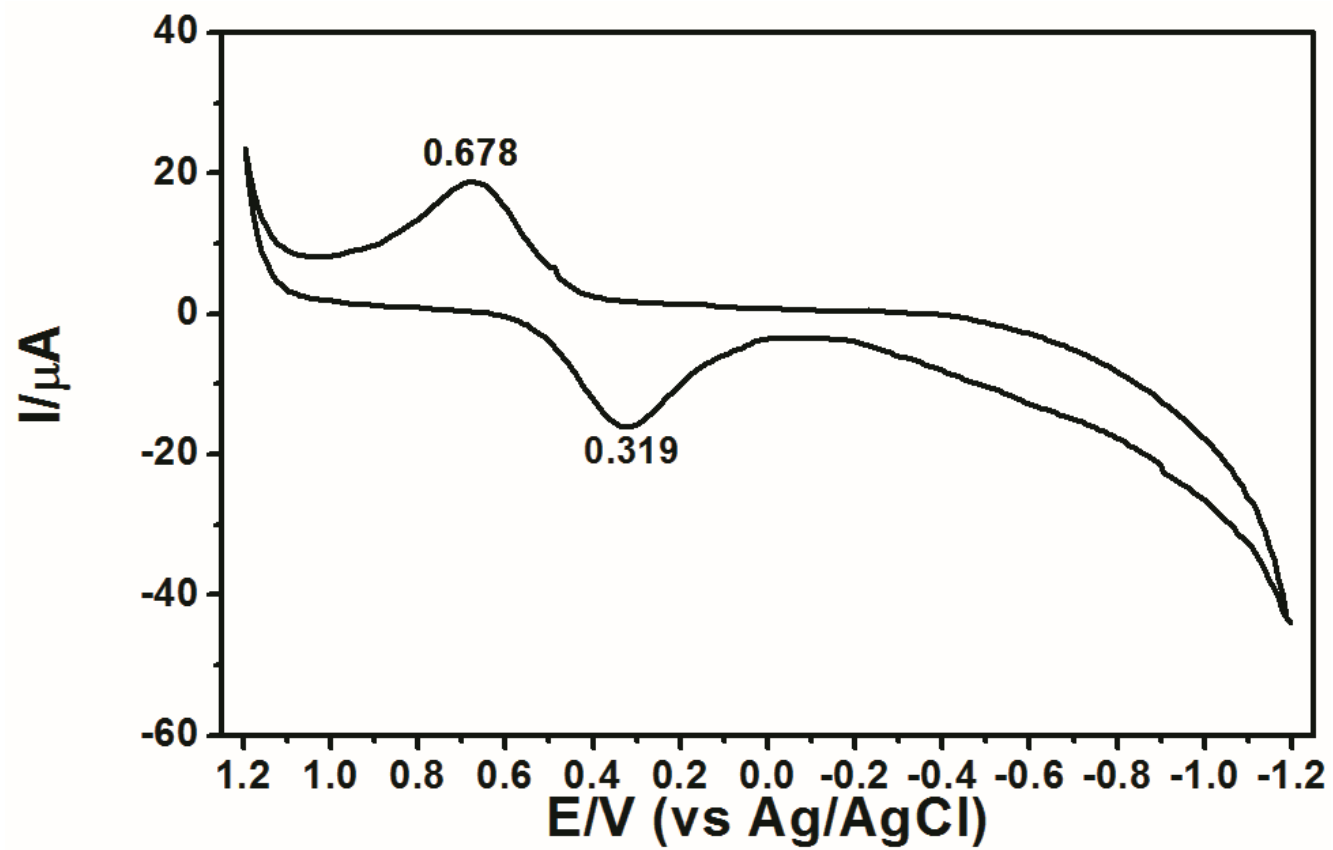
Figure 4.125: Solid-state cyclic voltammogram of CH-PNI at a scan rate of 100 mVs^{-1}
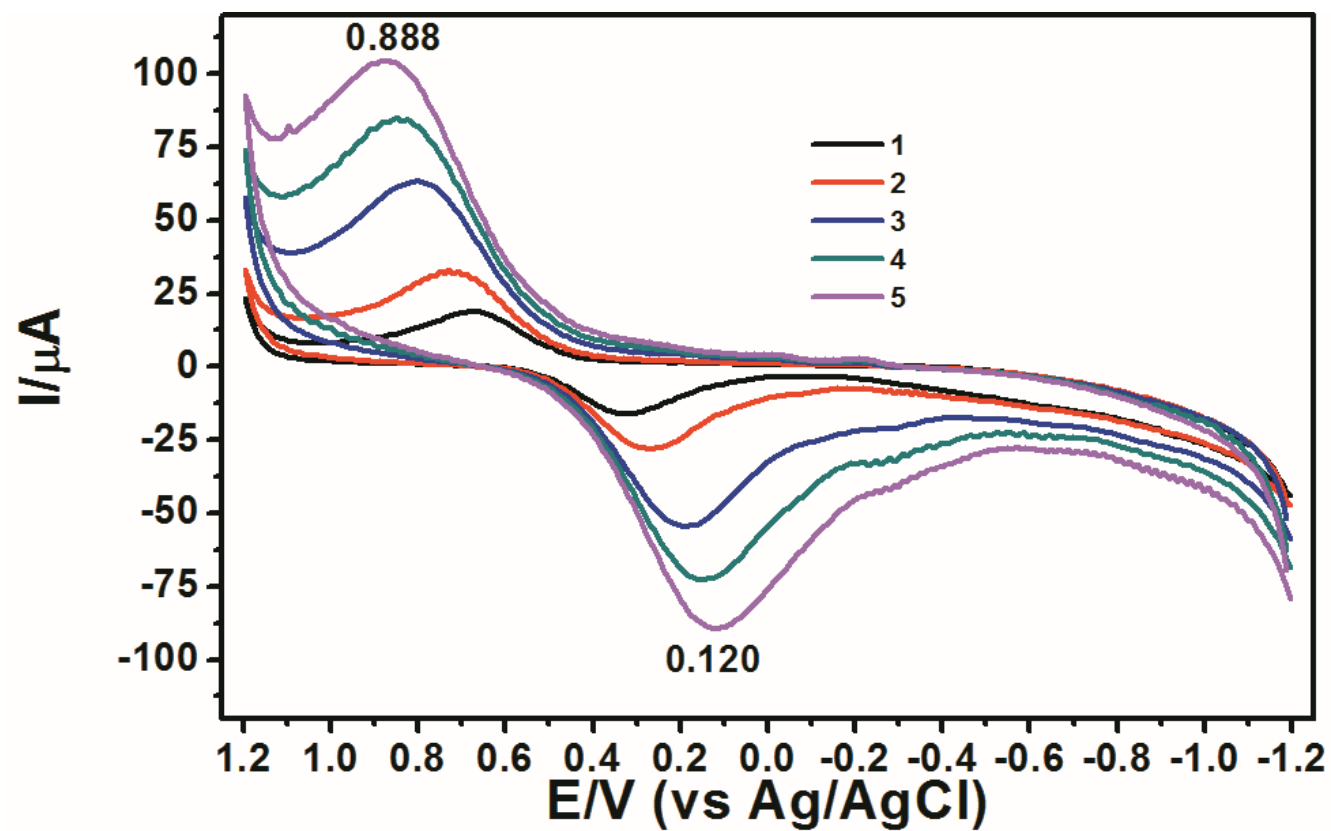
Figure 4.126: Solid-state cyclic voltammograms of CH-PNI at different scan rates (mVs^{-1}): 1 (100), 2 (200), 3 (500), 4 (750), 5 (1000), at 25°C
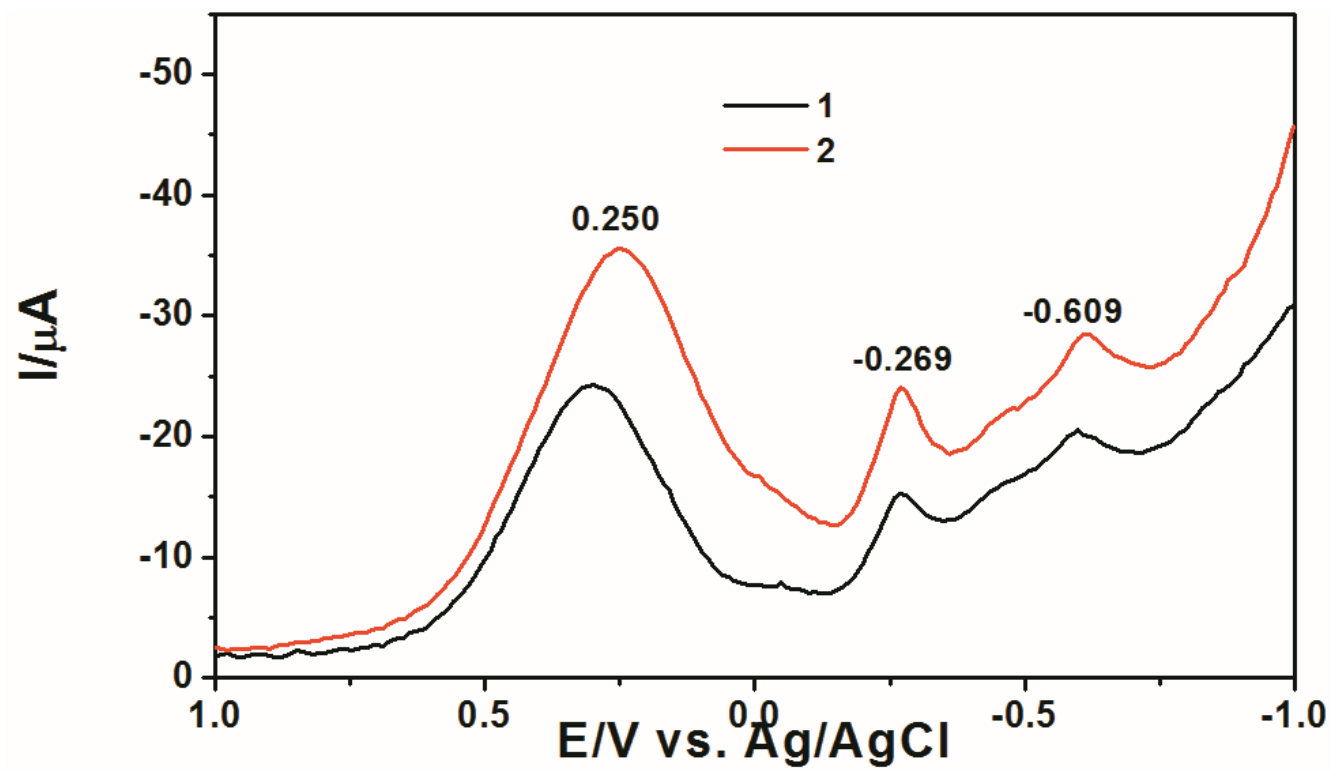
Figure 4.127: Solid-state Squarewave Voltammograms of CH-PNI at Different frequencies (Hz): 1 (25), 2 (50) at 25 °C
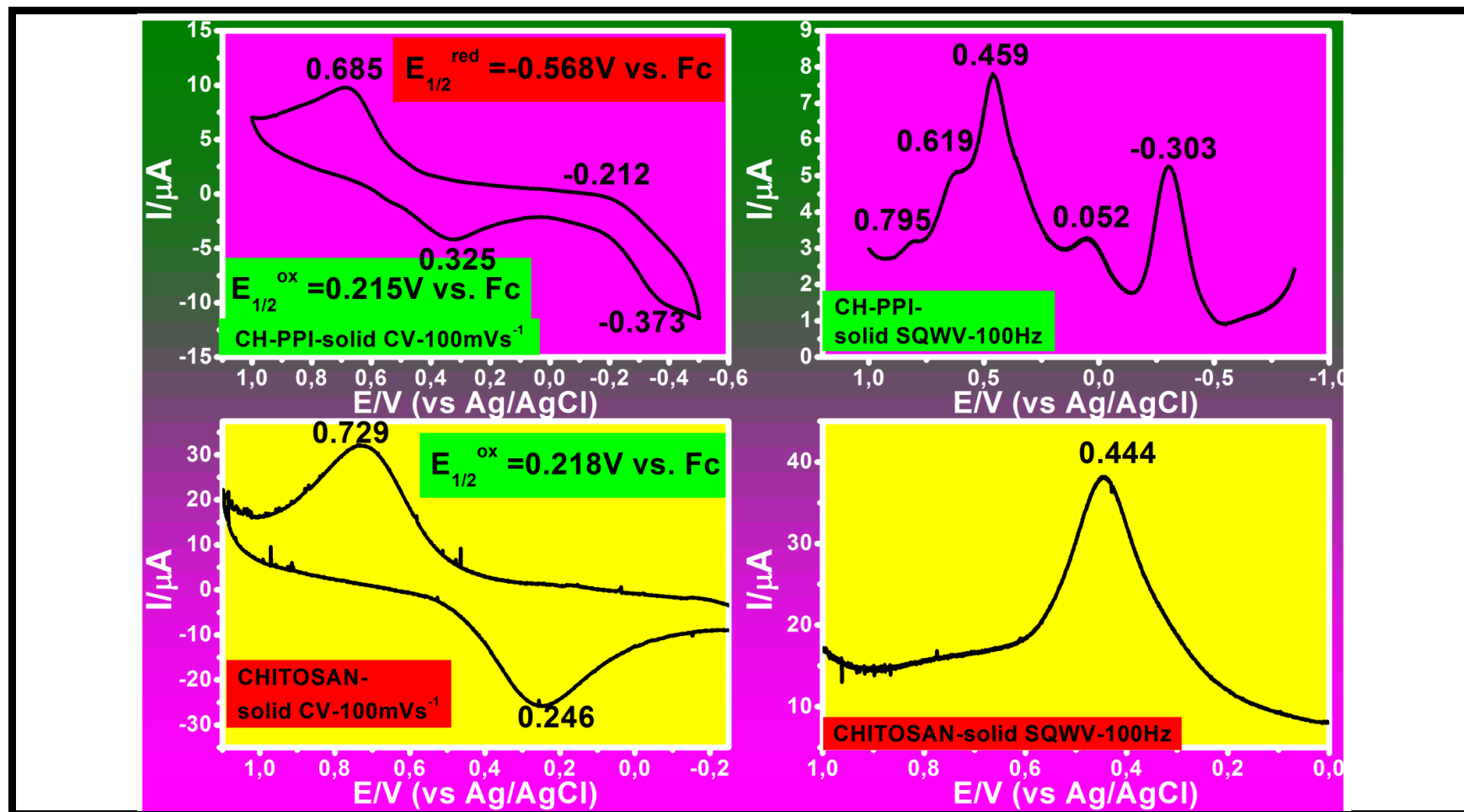
Figure 4.128: Comparison of Solid-state Cylic and Squarewave Voltammograms of CH-PPI and CH at 100 mVs^{-1} scan rate and 100Hz freqeuncy, respectively.
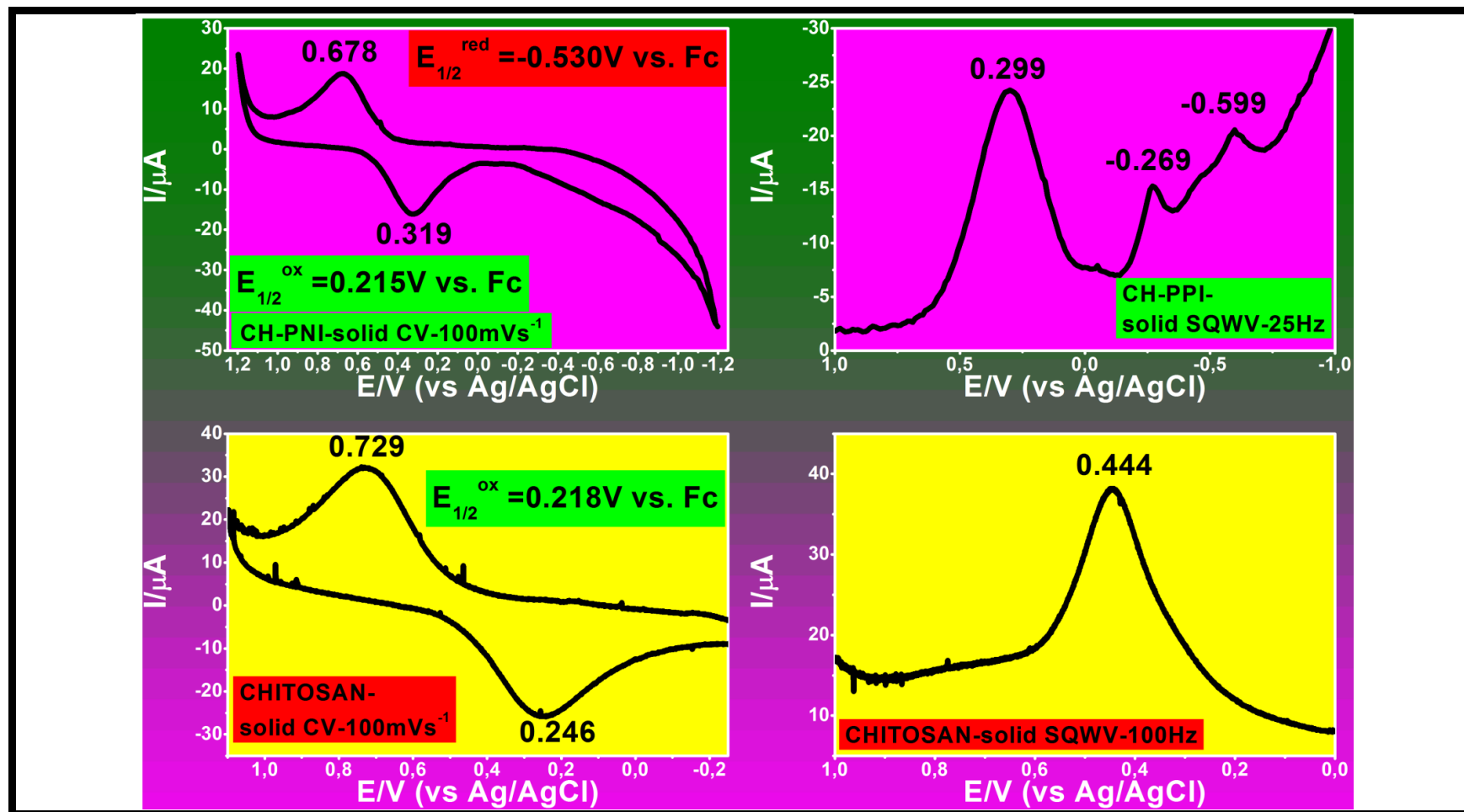
Figure 4.129: Comparison of Solid-state Cylic and Squarewave Voltammograms of CH-PNI and CH at 100 mVs^{-1} scan rate and 100Hz freqeuncy, respectively.
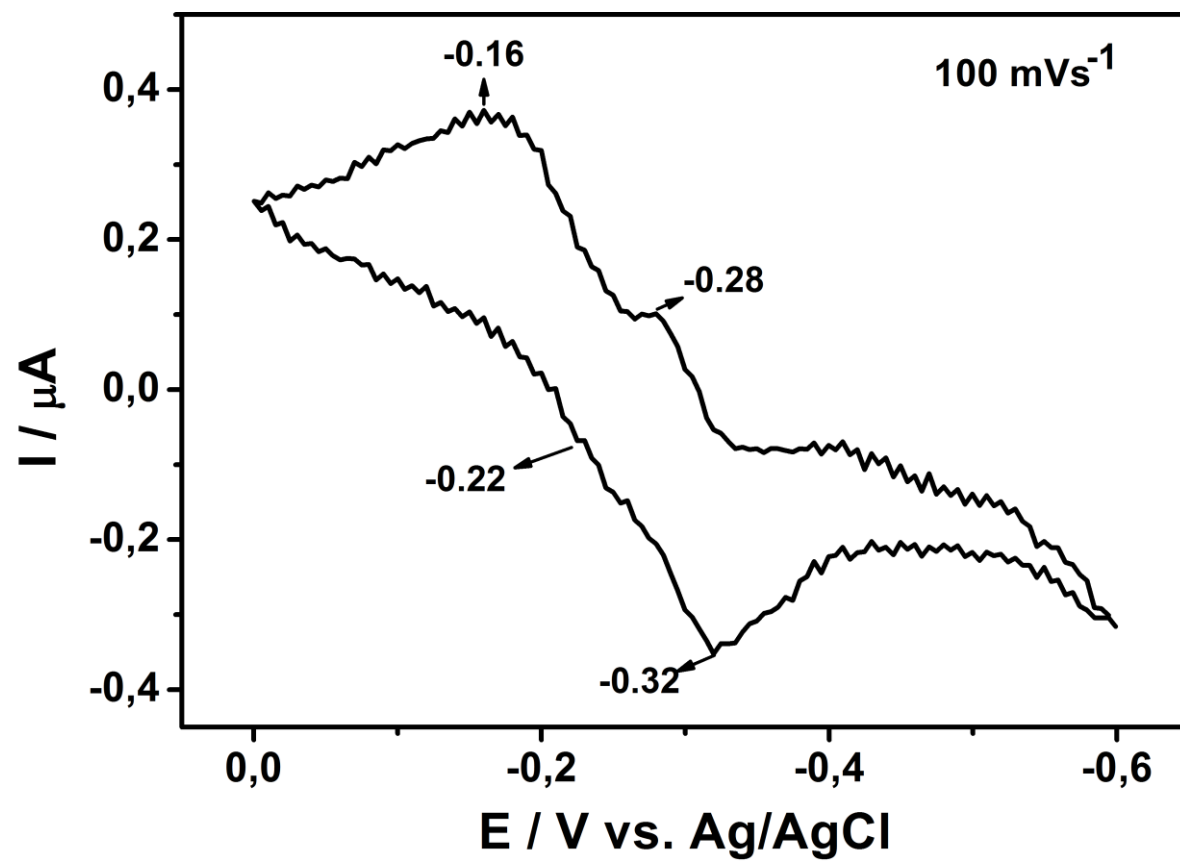
Figure 4.130: Solid-state cyclic voltammogram of ENPI at a scan rate of 100 mVs^{-1}
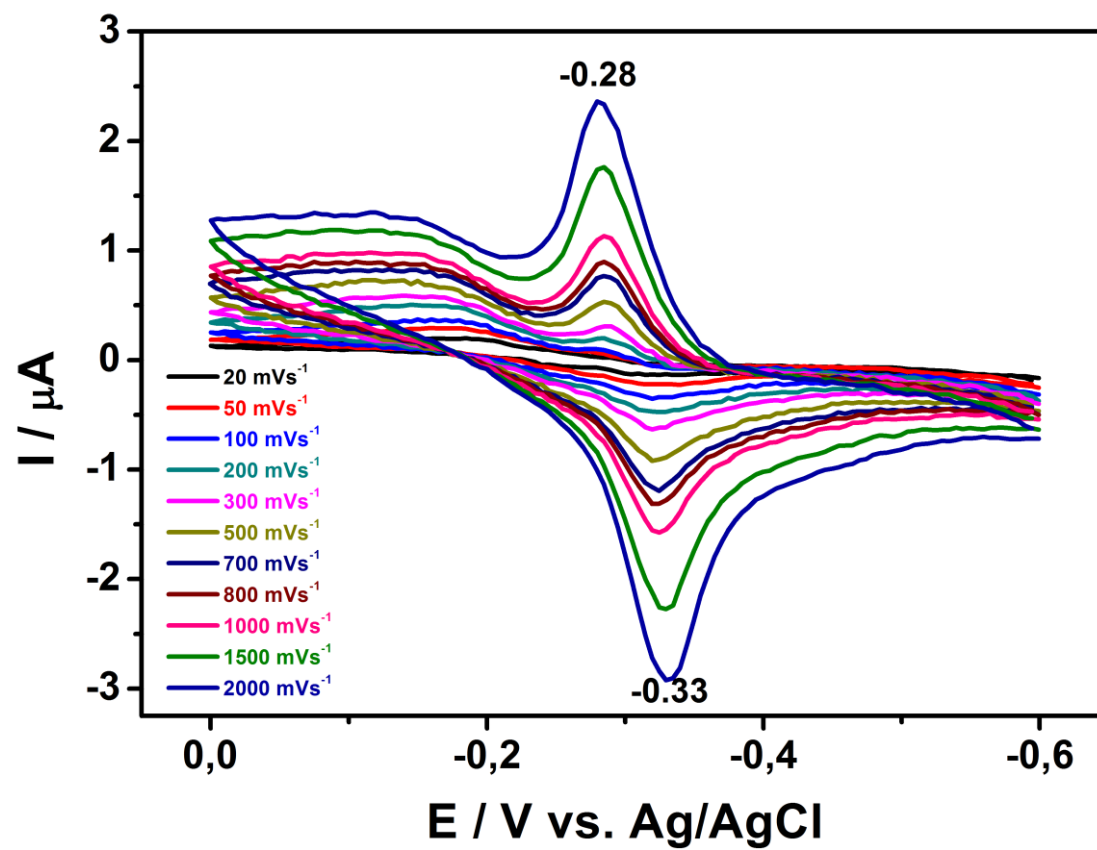
Figure 4.131: Solid-state cyclic voltammograms of ENPI at different scan rates
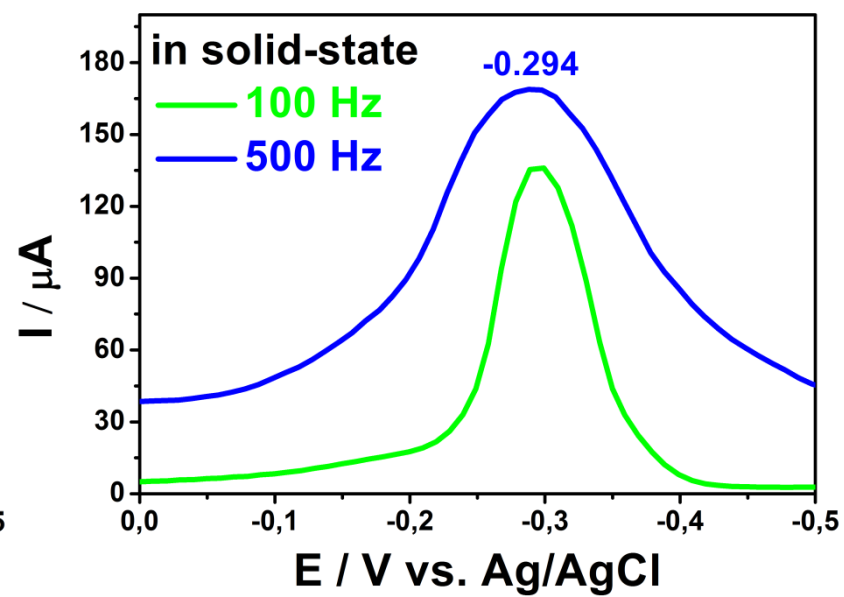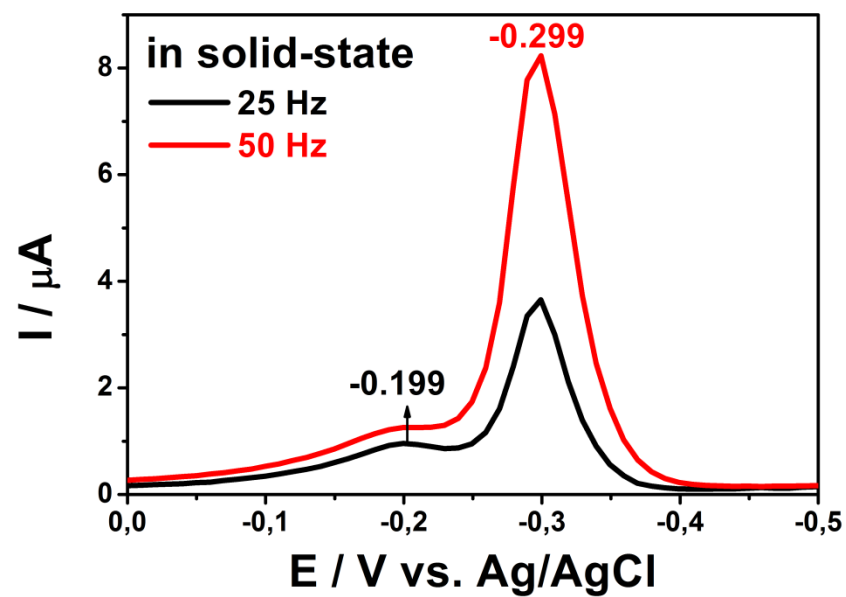
Figure 4.132: Solid-state square-wave voltammogram of ENPI at different scan rates
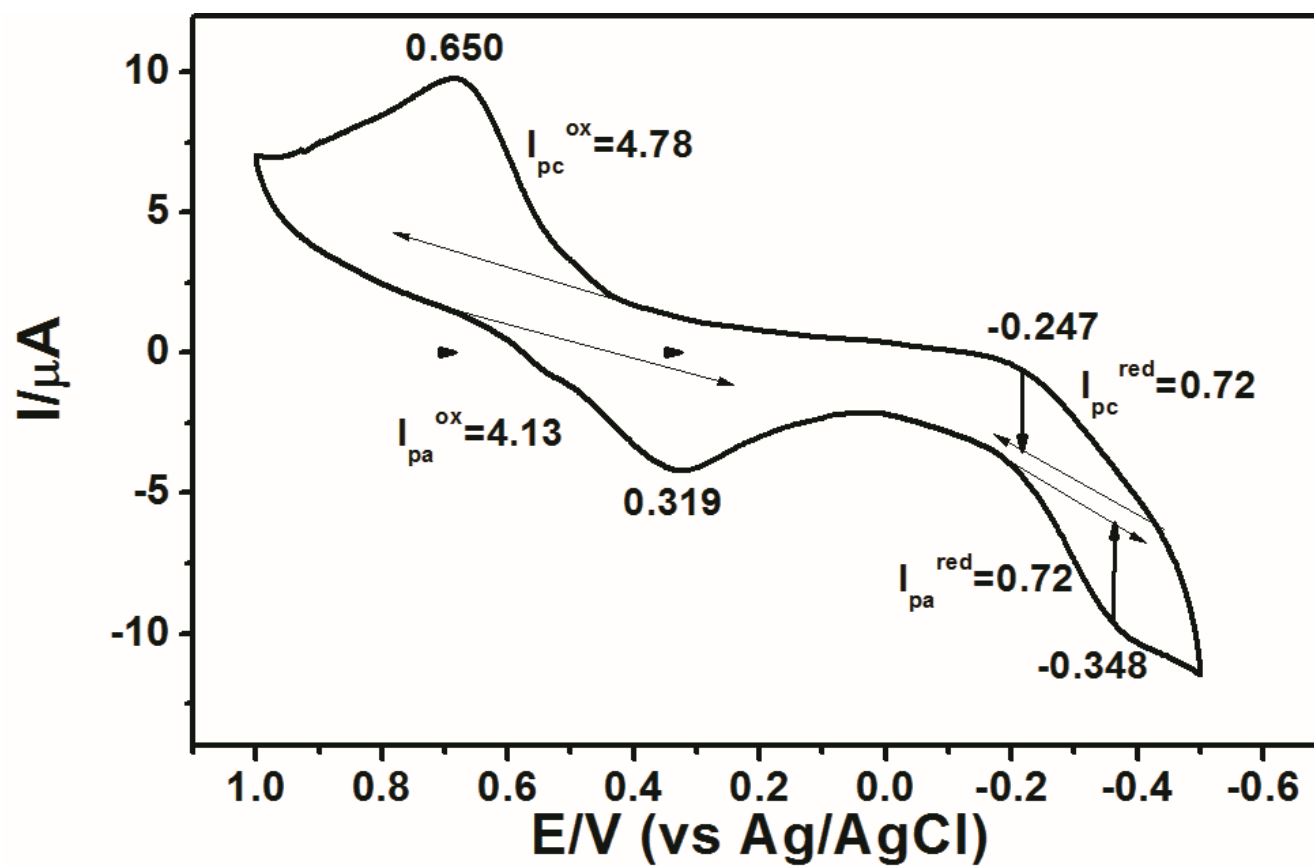
Figure 4.133: Calculation of Peak Currents (i_{pc} and i_{pa}) of CH-PPI
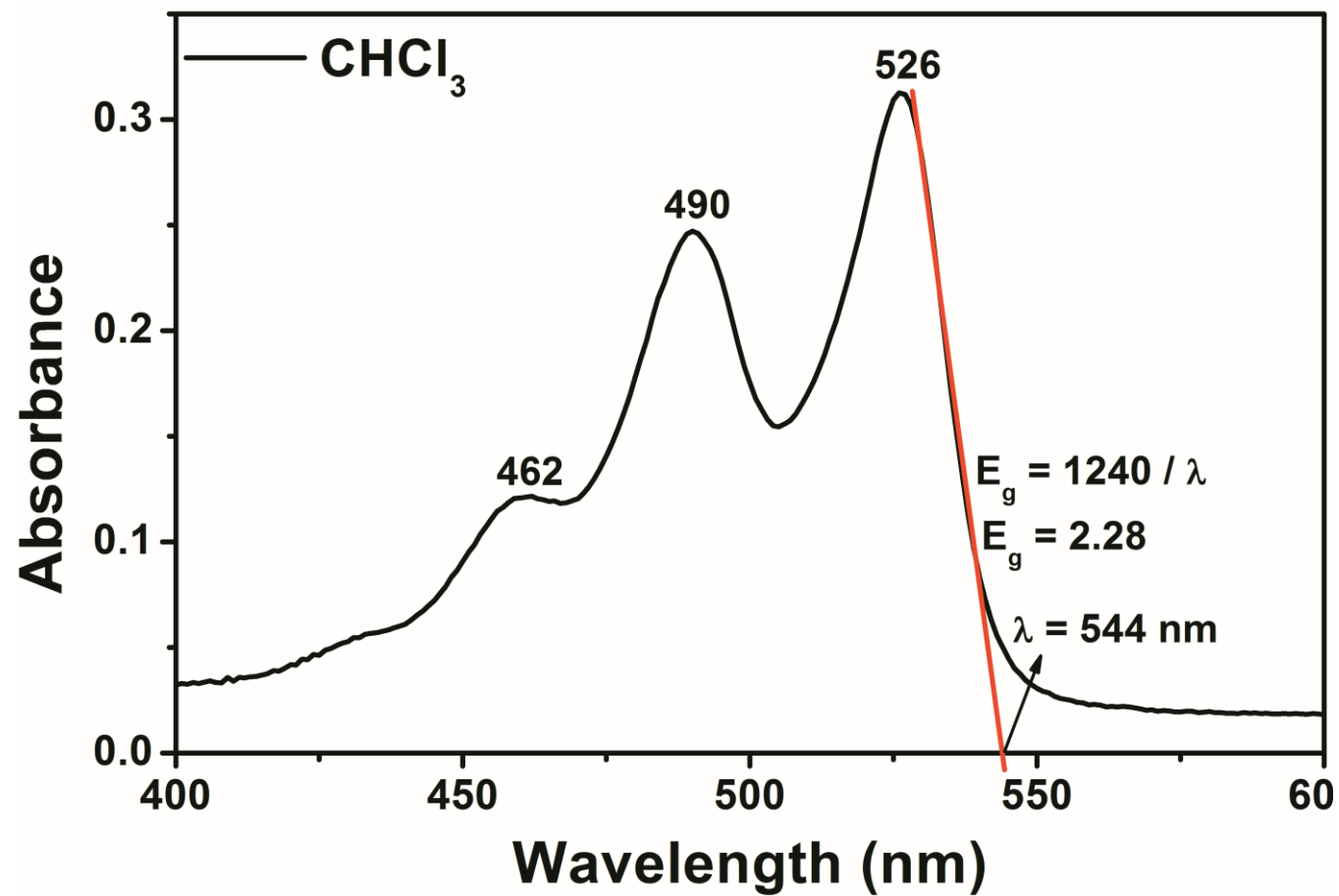
Figure 4.134: Optical Band Gap of CH-PPI in CHCl₃.
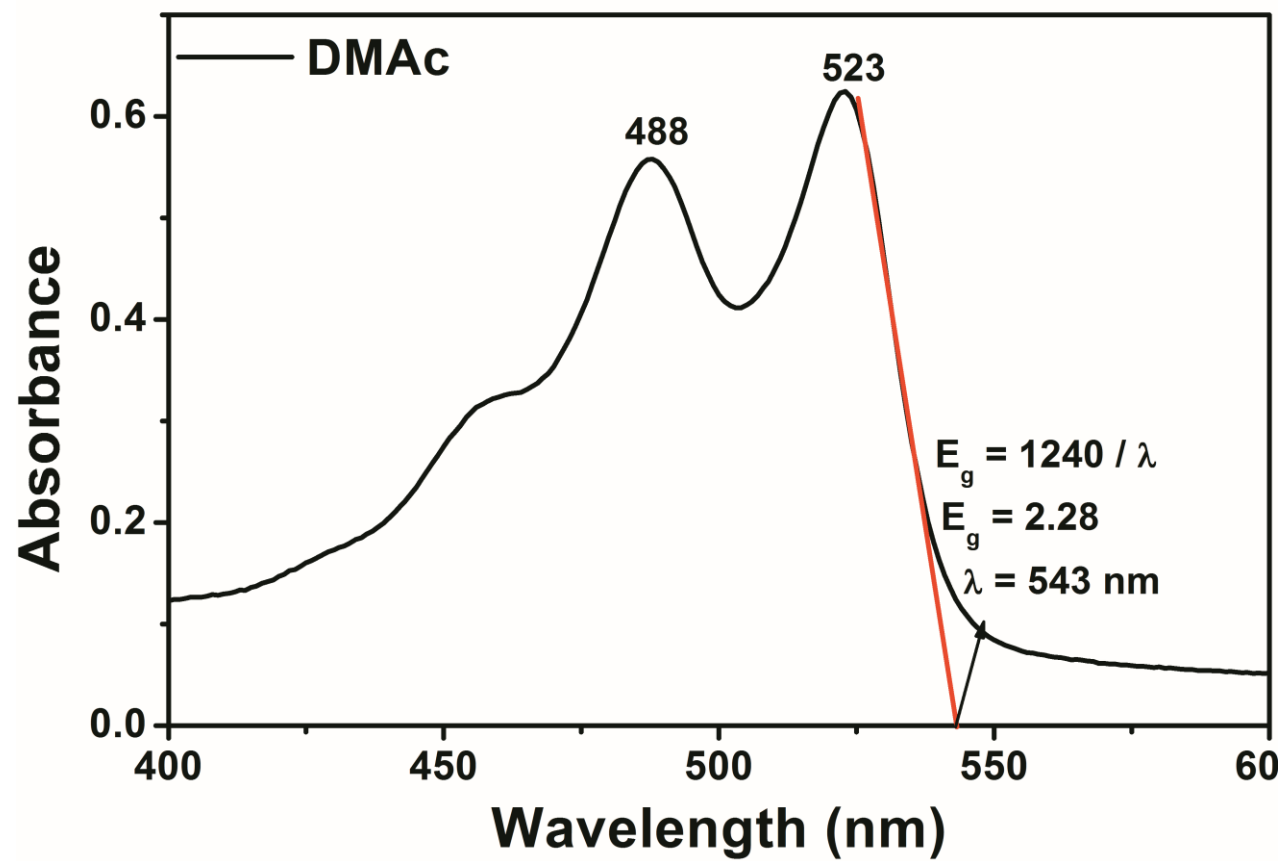
Figure 4.135: Optical Band Gap of CH-PPI in DMAc.
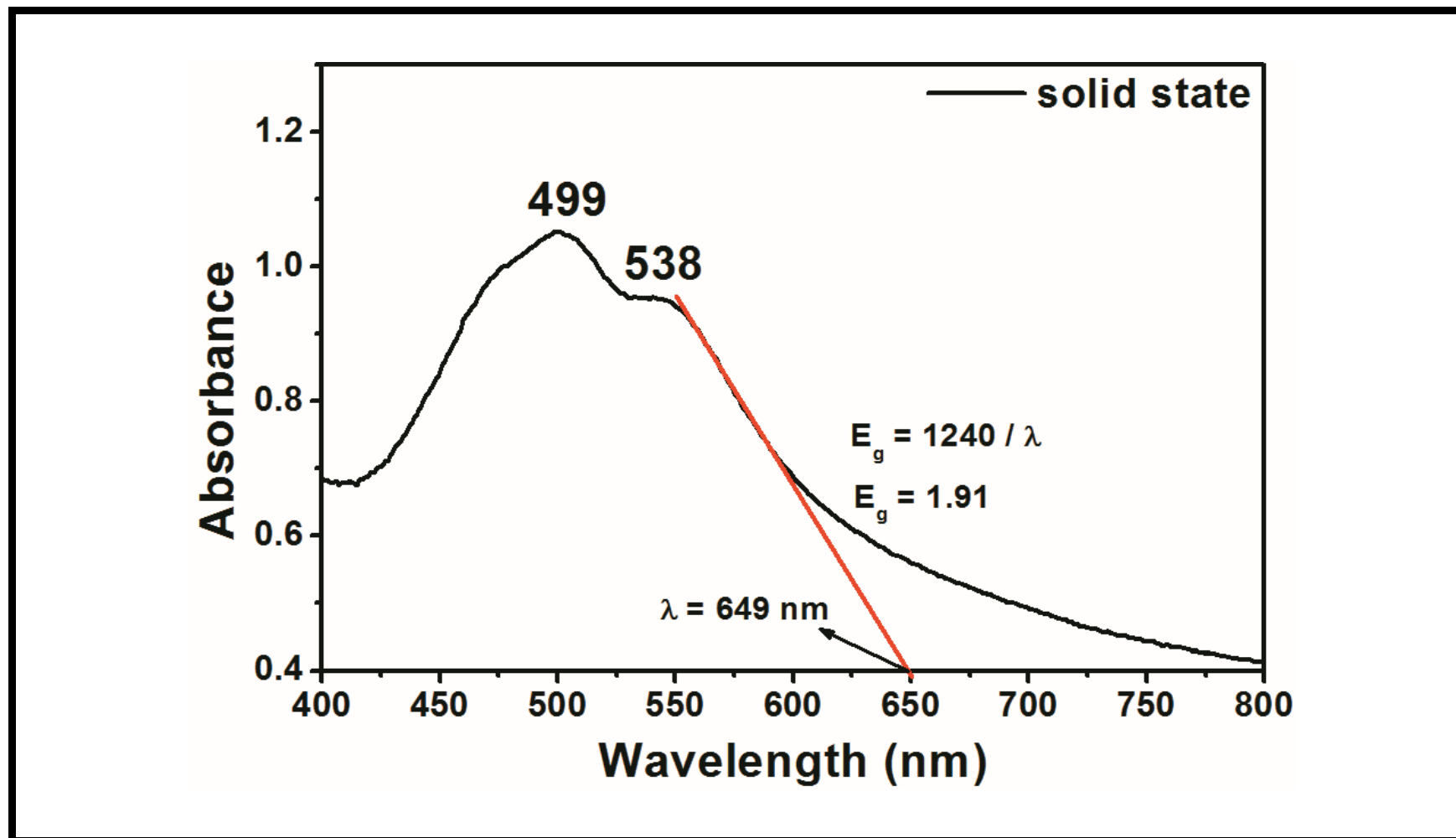
Figure 4.136: Optical Band Gap of CH-PPI in solid state
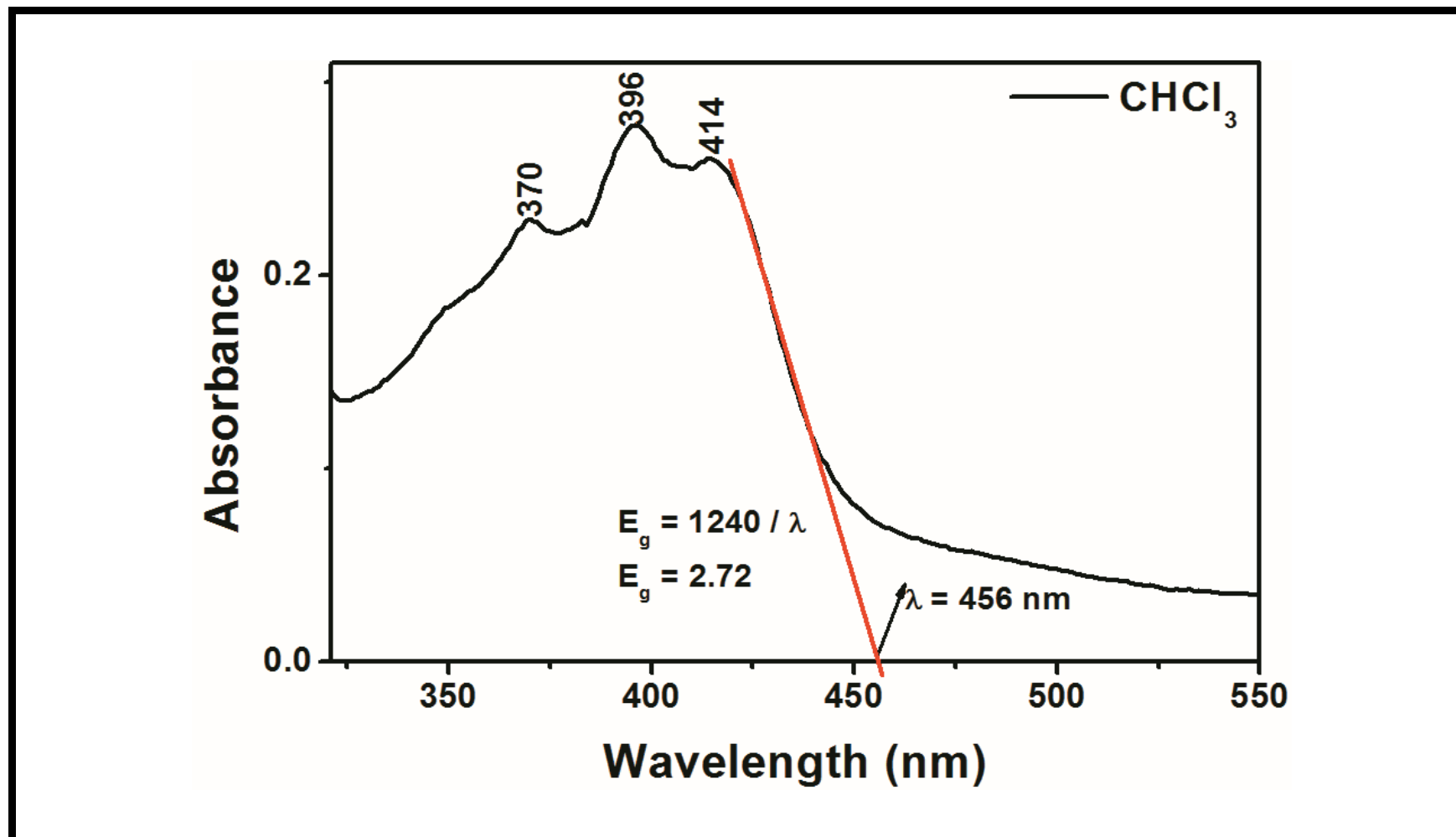
Figure 4.137: Optical Band Gap of CH-PNI in CHCl$_3$.
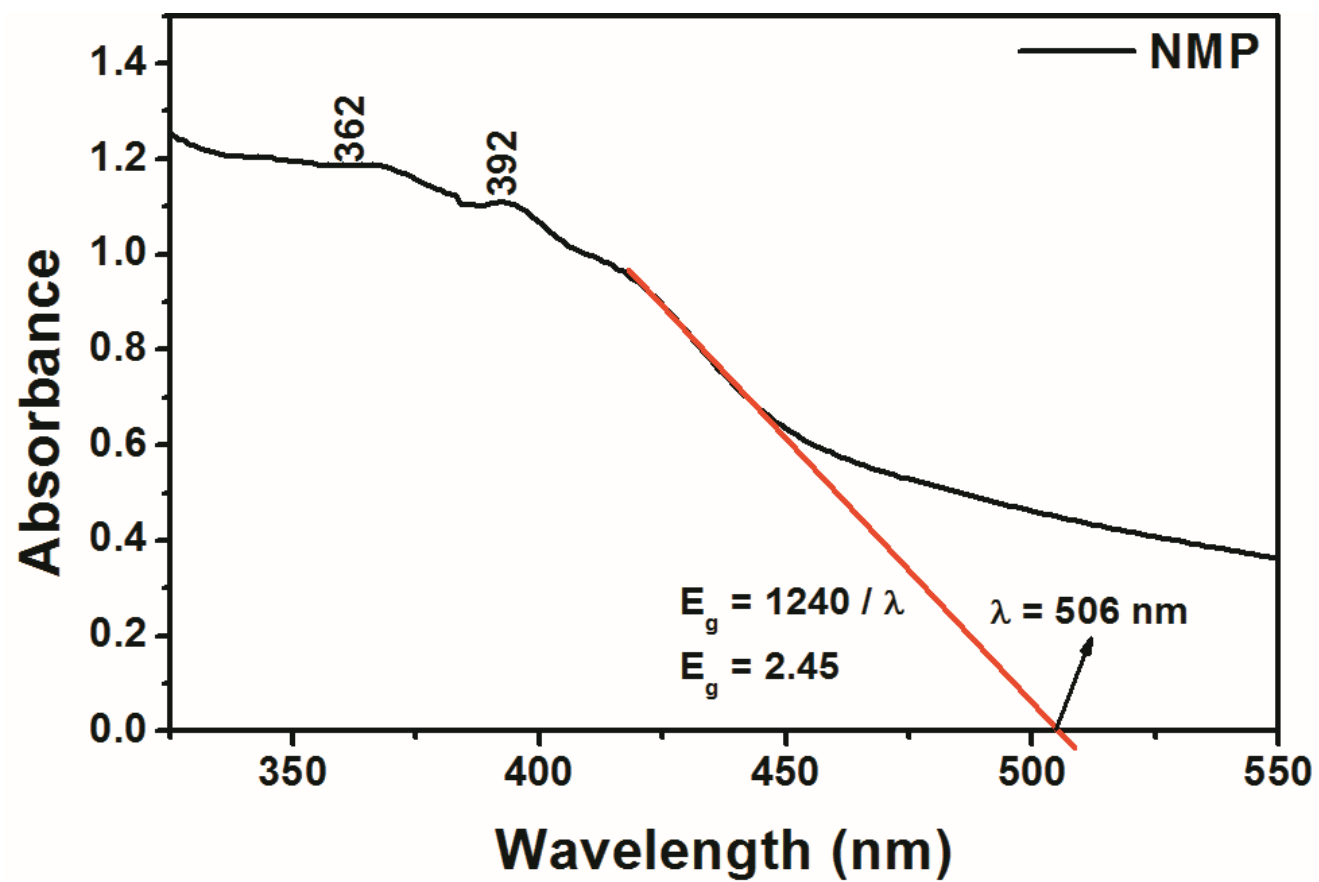
Figure 4.138: Optical Band Gap of CH-PNI in NMP.
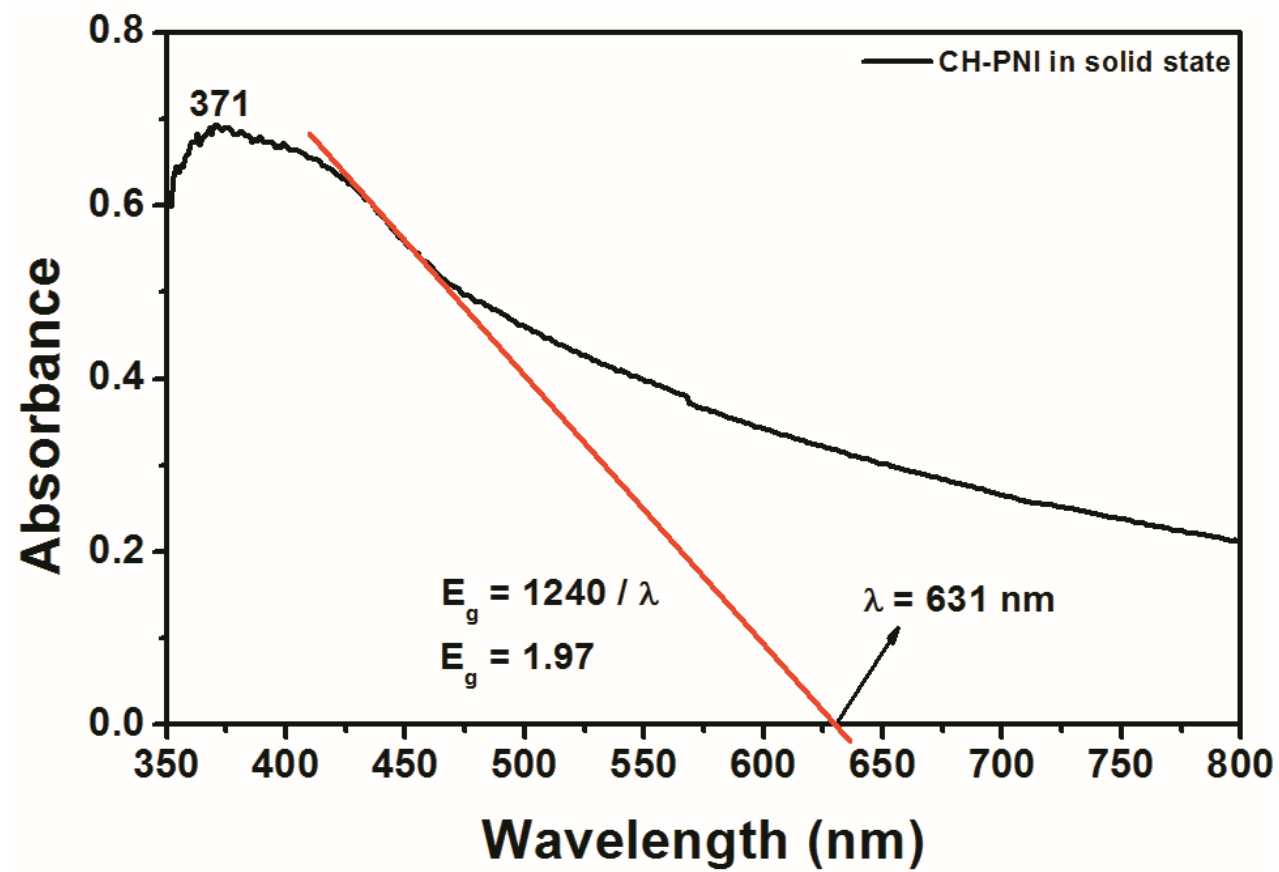
Figure 4.139: Optical Band Gap of CH-PNI in solid state.

Chapter 5

RESULTS and DISCUSSION

5.1 Synthesis and Characterization

The synthetic routes, which are illustrated in Scheme 3.1 and Scheme 3.2, is used for the synthesis of new low band gap polyimides. The syntheses of CH-PPI and CH-PNI were accomplished by substitution reaction between amine groups of commercially available chitosan (CH) and amide groups of industrial dyes, perylene dianhydride (PDA) and naphthalene dianhydride (NDA) in the presence of Zn as catalyst. All polymers were synthesized in significant yield. To prove the success of the synthesis, reactants and products were fully characterized by Fourier transform infrared spectra (FTIR) and, hydrogen- and carbon-nuclear magnetic resonance (^{1}H and ^{13}C NMR) as well as via elemental analysis. The synthesis details and characterization of the aromatic polyimides were gathered together in the Chapter 4.

FTIR spectroscopy confirmed the covalent attachment of the chromophore dyes to the chitosan polymer chains as shown in Figures 4.7 – 4.11. The infrared spectra of CH-PPI retained most of the bands of PDA; some of them lost and show new bands (Figure 4.10). There are two features to attention; the characteristic band of the perylene anhydride carbonyl strecthing band at 1773 cm^{-1} had disappeared and was replaced by N-imide carbonyl strecthing band (1690 cm^{-1}). Similarly, the characteristic band of the C-O-C strecthing (1025 cm^{-1}) had disappeared and was replaced by C-N-C strecthing band (1362 cm^{-1}). Similarly, the infrared spectrum of CH-PNI was very similar to those of CH-PPI. In the FTIR spectrum of CH-PNI (Figure 4.11), the characteristic band of the naphthalene anhydride carbonyl

strecthing band at 1782 cm^{-1} had lost and was altered by N-imide carbonyl strecthing band (1707 cm^{-1}). In the similar manner, the characteristic band of the C-O-C strecthing (1043 cm^{-1}) had lost and was altered by C-N-C stretching band (1365 cm^{-1}). After substitution of the perylene and naphthalene cores into the chitosan polymer, the bands which indicate aromacity are not altered in the all spectra of PDA, NDA, CH-PPI and CH-PNI. The IR spectrum of chitosan has shown characteristic O-H stretchings at 3430 cm^{-1}. Similarly, in the IR spectra of CH-PPI and CH-PNI, O-H strecthings appeared at 3450 cm^{-1} and 3436 cm^{-1}, respectively. Additionally, -C-O-C- glycosidic linkage (1160 cm^{-1} in CH, 1180 cm^{-1} in CH-PPI, 1155 cm^{-1} in CH-PNI) and C-O strecthings coming from aliphatic ring appeared almost same position in all spectra.

Completion of the synthesis has also been verified by ^{1}H and ^{13}C NMR which are illustrated from Figure 4.12 – to Figure 4.34. The ^{1}H NMR spectrum of CH-PPI and CH-PNI showed characteristics chemical shifts from the aromatic core moiety (seen as a broad signal from 8.91 to 7.37 ppm for the perylene aromatic protons (Figure 4.17) and from 9.48 to 7.85 ppm for the naphthalene aromatic protons (Figure 4.26)) as well as the chitosan polymer moiety demonstrated distinct proton signals in the aliphatic region that conflict with each other in the range between 4.48 to 1.43 ppm correspond to the aliphatic protons of natural chitosan polymer (Figure 4. 18 and 4.28). In general, monomeric form of perylene and naphthalene diimides showed sharp signals for the aromatic protons, in contrast with the polymeric ones the resonance of the aromatic protons are differently shielded because of aggregation behaviour [59]. The signals of aromatic protons in CH-PPI and CH-PNI were significantly different from the monomeric ones and observed in a wide area. At this point, it should be noted that the aromatic protons of CH-PPI and CH-PNI could be shielded or de-shielded by the π-system of the neighbouring dye molecules that are tightly packed in network structure. A new set of broad signals in the ^{13}C NMR

spectrum of CH-PPI (from 147.01 to 120.07 ppm) in Figure 4.23 and CH-PNI (from 142.49 to 102.96 ppm) in Figure 4.33 were attributed to aromatic carbons associated with the perylene and naphthalene chromophore part, respectively. Furthermore, carbonyl peaks of new fluorescent polyimides are observed at 165.66 ppm for CH-PPI in Figure 4.24 and 162.14 ppm for CH-PNI in Figure 4.34. The signals of the aliphatic carbons located in a reasonable chemical shift region from 96.98 to 51.19 ppm for CH-PPI in Figure 4.22 and from 102.96 to 43.82 ppm for CH-PNI in Figure 4.32. As a conclusion, both FTIR and NMR datas prove the structure of the new polyimides.

5.2 Solubility of Low Band Gap Polyimides

The solubility properties of the PDA, NDA, CH, CH-PPI and CH-PNI are also listed in Table 5.1. It was clearly noticed that incorporation of the aliphatic chitosan biopolymer in the backbone caused striking solubility of polyimides. It is well known that CH is poorly soluble except only in acidic solvents such as 1 % acetic acid and 1 M HCl as well as PDA and NDA is usually insoluble in most organic solvents. Although most of the polyimides in the literature have pour solubility, new chitosan substituted perylene and naphthalene polyimides have remarkable solubility in common organic solvents including dimethylacetamide, dimethylsulfoxide, and dimethylformamide at room temperature. By imidization aromatic core of dyes at imide position can interrupt the steric hindrance of dye molecules by losing the rigid planarity thus improving solubility. However, the solubility of new polyimides in aqueous medium was not as touchy as organic medium. When viewed in terms of application the restricted solubility of CH and industrial dyes limits their feasibility, but CH-PPI and CH-PNI with improved solubility in a wide range of common organic solvents are strong candidates for solution processable polymer based organic solar cells.

Table 5.1: Solubility of PDA, NDA, CH, CH-PPI and CH-PNI.

Solvent	Solubility/Color									
	PDA		**NDA**		**CH**		**CH-PPI**		**CH-PNI**	
CHCl$_3$	$--$	Colorless	$--$	Colorless	$--$	Colorless	$+-$	Orange	$+-$	Yellow
EtAc	$--$	Colorless	$--$	Colorless	$--$	Colorless	$+-$	Green	$+-$	Pale Green
CH$_2$Cl$_2$	$--$	Colorless	$--$	Colorless	$--$	Colorless	$+-$	Yellow	$+-$	Yellow
Acetone	$--$	Colorless	$--$	Colorless	$--$	Colorless	$+-$	Green	$+-$	Pale Green
EtOH	$--$	Colorless	$--$	Colorless	$--$	Colorless	$+-$	Orange	$+-$	Pale Green
MeOH	$--$	Colorless	$--$	Colorless	$--$	Colorless	$+-$	Orange	$+-$	Pale Green
THF	$--$	Colorless	$--$	Colorless	$--$	Colorless			$+-$	Green
NMP	$--$	Colorless	$+-$	Pale Green	$--$	Colorless			$+-$	Dark Green
DMF	$--$	Colorless	$+-$	Pale Pink	$--$	Colorless	$+-$	Brown	$+-$	Dark Green
CH$_3$CN	$--$	Colorless	$--$	Colorless	$--$	Colorless	$+-$	Orange	$+-$	Pale Green
DMAc	$--$	Colorless	$+-$	Pale Green	$--$	Colorless	$+-$	Brown	$+-$	Green
DMSO	$--$	Colorless	$--$	Colorless	$--$	Colorless	$+-$	Brown	$+-$	Green
H$_2$O	$--$	Colorless	$--$	Colorless	$--$	Colorless	$--$	Colorless	$--$	Colorless
NaOH	$--$	Colorless	$--$	Colorless	$--$	Colorless	$--$	Colorless	$+-$	Green
KOH	$--$	Colorless	$--$	Colorless	$--$	Colorless	$--$	Colorless	$+-$	Green
Acedic Acid (%1)	$--$	Colorless	$--$	Colorless	$++$	Colorless	$--$	Colorless	$+-$	Green

Measured at a concentration of 0.1 mg mL^{-1} in solvents at 25 °C. (+ +): soluble; (+ –): partially soluble; (– –): not soluble. EtAc: ethylacetate; NMP:N-methylpyrrolidinone; DMF: *N,N*-dimethylformamide; DMAc: dimethylacetamide; DMSO: dimethyl sulfoxide.

5.3 Characterization of GPC and Intrinsic Viscosities

The result of GPC measurement of chitosan polymer was obtained by gel permeation chromatography (GPC) in 0.1 M NaCl / 0.1% trifluoroacetic acid solution at 25 °C and showed in Figure 4.35. The weight-average molecular weight (M_w) and number-average molecular weight (M_n) of commercial chitosan biopolymer were measured as about 460000 g/mol and 43315 g/mol with a high polydispersity index (PDI) of 10.62, respectively. Such a polymer with a high polydispersity demonstrated the non-homogeneous appearance in size. The intrinsic viscosity of chitosan biopolymer was estimated also as 4.0 dL g^{-1}.

GPC chromatograms of fluorescent chitosan polymers, showed in Figure 4.36 and Figure 4.37, were achieved from a GPC measurement recorded in DMSO / 0.1 M LiCl solution. The weight-average molecular weights (M_w) of CH-PPI and CH-PNI were found as 21300 g/mol and 18600 g/mol, respectively. The number-average molecular weights (M_n) of the polymers were found also as 8290 g/mol and 5760 g/mol, respectively. The polydispersity index (PDI) of CH-PPI and CH-PNI were found as 2.56 and 3.23, respectively. The PDI values of polyimides were lower than commercial chitosan.

In comparison with GPC datas, viscosity measurements of polymers were carried out to determine intrinsic viscosities. The measured intrinsic viscosities ([η]) of polymers were calculated as 8.71 dL g^{-1} in dimethylacetamide for CH-PPI and as 6.38 dL g^{-1} in N-methylpyrrolidinone for CH-PNI. As expected, it is noteworthy that the intrinsic viscosities of polyimides were higher than CH owing to the polymeric network structure.

5.4 Analyses of NMR Spectra

The NMR spectra of commercial chitosan biopolymer and synthesized new polyimides have been shown below (Fig 4.12 to 4.34). The structure of the polymers and purity of the products were confirmed by the NMR datas.

CHITOSAN:
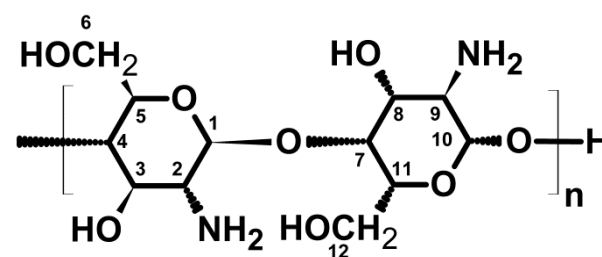
Figure 5.1. NMR Analysis of Chitosan

^{1}HNMR(400 MHz, CF$_3$COOD + CDCl$_3$ (1:1)) δ (ppm):

1.43 (t, J = 7.16 Hz, 2CH, H-C (4), H-C (7)), 2.19 (s, 2CH, H-C (2), H-C (9)), 2.23 (s, 2NH$_2$, H$_2$N-C (2), H$_2$N-C (9)), 2.36 (s, 4OH, HO-C (3), HO-C (6), HO-C (8), HO-C (12), 2.39 (d, J = 3.12 Hz, 2CH, H-C (3), H-C (8)), 4.03 (s, 2CH, H-C (5), H-C (11)), 4.25 (q, J = 7.40 Hz, 2CH$_2$, H$_2$-C (6), H$_2$-C (12)), 4.48 (q, J = 7.16 Hz, 2CH, H-C (1), H-C (10)).

CH-PPI:
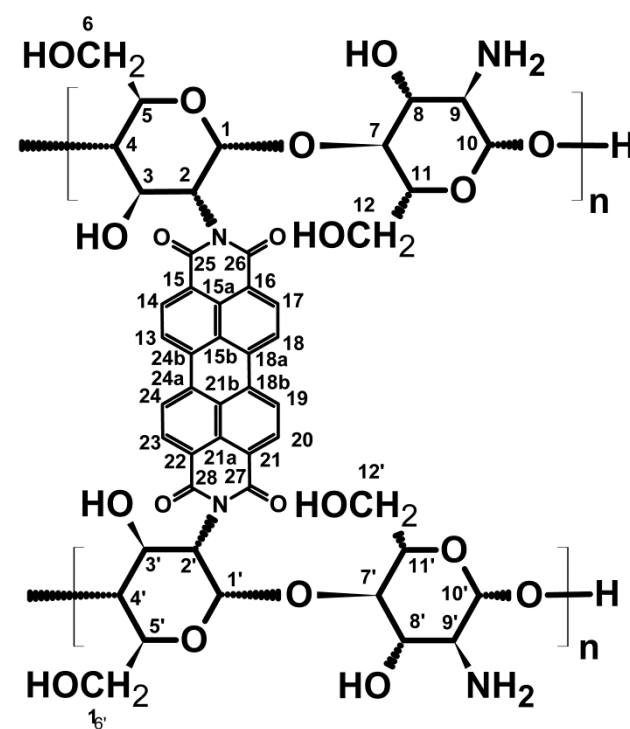
Figure 5.2. NMR Analysis of CH-PPI

^{13}C NMR(400 MHz, $C_2F_3O_2D$ + $CDCl_3$ (2:3), δ): 65.09 (4 CH_2, C (6), C (6'), C (12), C (12')), 104.29 (4 CH, C (1), C (1'), C (7), C (7'), 147.01-120.07 (20 Ar (C), C (13-24)), 165.66 (4 C=O, C (25), C (26), C (27), C (28)).

^{1}H NMR(400 MHz, $C_2F_3O_2D$ + $CDCl_3$ (2:3), δ): 1.42 (t, J = ? Hz, 4 CH, H-C (4), H-C (4'), H-C (7), H-C (7')), 2.17 (s, 4CH, H-C (2), H-C (2'), H-C (9), H-C (9')), 2.22 (s, 2NH_2, H-N (9), H-N (9')), 2.35 (s, 8OH, OH-C (3), OH-C (6), OH-C (3'), OH-C (6'), OH-C (8), OH-C (12), OH-C (8'), OH-C (12')), 2.40 (d, J = ? Hz, 4CH, H-C (3), H-C (3'), H-C (8), H-C (8')), 4.02 (s, 4 CH, H-C (5), H-C (5'), H-C (11), H-C (11')), 4.25 (q, J = ? Hz, 4CH_2, H-C (6), H-C (6'), H-C (12), H-C (12')), 4.48 (q, J = ? Hz, 4CH, H-C (1), H-C (1'), H-C (10), H-C (10')), 8.91-7.37 (m, 8 Ar-H, H-C (13), H-C (14), H-C (17), H-C (18), H-C (19), H-C (20), H-C (23), H-C (24)).

CH-PNI:

Figure 5.3. NMR Analysis of CH-PNI

^{13}CNMR OF CH-PNI(400 MHz, $C_2F_3O_2D$ + $CDCL_3$ (1:1)) δ (ppm): 67.80 (4 CH_2, C (6), C (6'), C (12), C (12')), 102.96 (4 CH, C (1), C (1'), C (7), C (7'), 142.49-122.05 (10 Ar (C), C (13-20) , C (25), C (26),), 162.14 (4 C=O, C (21), C (22), C (23), C (24)).

^{1}HNMR OF CH-PNI(400 MHz, $C_2F_3O_2D$ + $CDCL_3$ (1:1)) δ (ppm): 1.27 (t, J = ? Hz, 4 CH, H-C (4), H-C (4'), H-C (7), H-C (7')), 2.14 (s, 4CH, H-C (2), H-C (2'), H-C (9), H-C (9')), 2.37 (s, 2NH₂, H-N (9), H-N (9')), 2.67 (s, 8OH, OH-C (3), OH-C (6), OH-C (3'), OH-C (6'), OH-C (8), OH-C (12), OH-C (8'), OH-C (12')), 2.88 (d, J = ? Hz, 4CH, H-C (3), H-C (3'), H-C (8), H-C (8')), 3.92 (s, 4 CH, H-C (5), H-C (5'), H-C (11), H-C (11')), 4.27 (q, J = ? Hz, 4CH₂, H-C (6), H-C (6'), H-C (12), H-C (12')), 4.33 (q, J = ? Hz, 4CH, H-C (1), H-C (1'), H-C (10), H-C (10')), 9.48-7.85 (m, 4 Ar-H, H-C (14), H-C (15), H-C (18), H-C (19))

5.5 Analyses of Photophysical Properties

5.5.1 Photophysical Properties of CH-PPI

Photo-physical properties of the CH-PPI were investigated in different polarity of the solvents (apolar, polar aprotic and polar protic) with UV-vis absorption, excitation and fluorescence emission which are depicted in Figures 4.38 to 4.47 and Table 4.5 to Table 4.12 that summarize the spectral data. The emission and excitation spectra of CH-PPI were taken at λ_{exc} = 485 and λ_{ems} = 620 nm, respectively. And also, the relative fluorescence quantum yields were determine in various solvents by using N,N' –didodecyl-3,4,9,10-perylenebis(dicarboximide) in chloroform as the reference. All other information regarding optical properties are presented in Table 4.13, featuring the maximum absorption wavelength λ_{max} (nm), stoke shifts (cm^{-1}), ratios of absorption intensities $A^{0\rightarrow0}$/ $A^{0\rightarrow1}$, extinction coefficients ε_{max} (L mol^{-1} cm^{-1}), oscillator strength f , fluorescence quantum yields ϕ_f (λ_{exc} = 485 nm), radiative lifetimes τ_0 (ns), fluorescence lifetimes τ_f (ns), fluorescence rate constants k_f (10^7 sec^{-1}), rate constant of radiationless deactivation k_d and singlet energy E_s (kcal mol^{-1}) data of CH-PPI. The optical band gap of 2.28 eV was calculated from the onset of absorption at 544 nm in chloroform solution. This is consistent with the measured band gap using cyclic voltammetry (1.91 eV).

As can be seen Figure 4.63 and Figure 4.67, the absorption and emission bands of CH-PPI are substantially unchanged when treated in apolar solvents and shows typical π–π* transition of perylene bisimide with increasing intensity at higher wavelengths. These bands are strong and well-resolved that are assigned to the vibronic components of the $S_0 \rightarrow S_1$ transition which is in agreement with literature. The most intense absorption peak at 525 nm represents the lowest energy transition from the ground state to the first excited state (0 → 0) while other smaller two

maxima peaks at 488 and 461 nm attribute to the $0 \rightarrow 1$ and $0 \rightarrow 2$ vibronic energy transitions, respectively. The quantum yield of CH-PPI was very high in non-polar solvent. One reason for this effect, CH-PPI can have an internal charge transfer between perylene's carbonyl groups and chitosan's functional groups as acceptor and donor group, respectively. The excitation bands for CH-PPI in apolar solvents showed no significant changes compared with those in other solvents.

Regarding the absorption in polar aprotic solvents (Figure 4.64), the absorption maximum was slightly bathochromic shifted (9 nm) in comparison with that in ethyl acetate and DMSO. In DMSO, the intensity of the $0 \rightarrow 0$ absorption band was diminished and it was almost equal to the intensity of the $0 \rightarrow 1$ absorption band. Also, the intensity of the $0 \rightarrow 0$ excitation band in DMAc and DMF is almost equal to the intensity of the $0 \rightarrow 1$ excitation band and the shape of the spectra is broader than the others. This variation has been attributed to the weak molecular interactions with the solvent molecules. When solvent polarity increases in polar aprotic solvents, maximum emission bands of CH-PPI red shifted from 526 nm in ethyl acetate to 545 nm in DMSO (Figure 4.68). And also the intensity of the $0 \rightarrow 0$ emission band become weaker and showed broad "excimer-type emission" spectrum. Additionally the latter, quenching of fluorescent emission of CH-PPI in DMSO ($\Phi_f = 0.38$) was more obvious than the other solvents which can be explained by $\pi - \pi$ stacking with the formation of excimer in solution. Another reason for this effect could be electron or energy transfer from perylene moiety to its environment thus increasing non-radiative decay in which the low energy excited state is not radiatively coupled to the ground state.

CH-PPI in polar protic solvents showed hypsochromic absorption bands comparing to the other solvents; the $0 \rightarrow 0$ absorption bands at 515 nm in methanol and at 518

nm in ethanol had a dramatic decrease comparing to the intensity of $0 \rightarrow 1$ absorption band at 487-489 nm in both solvents (Figure 4.65). The excitation spectra of CH-PPI in protic solvents are the super-imposed image of the absorption spectrum (Figure 4.73). Further, CH-PPI showed red shifted emission bands in protic solvents comparing to the other solvents (expect DMSO) (Figure 4.70). The $0 \rightarrow 0$ emission band at 541 nm in methanol was almost equal to the intensity of the $1 \rightarrow 0$ emission band at 567 nm. These spectral changes were most likely due to intra- and intermolecular hydrogen-bonding interactions took place between perylene moiety and its environment (chitosan polymer and solvent molecules). On the other hand, while fluorescence quenching in polar media suggested that efficient photoinduced electron/charge transfer takes place between perylene moiety and solvent molecules as well as between perylene and chitosan polymer.

Each molecular unit has their own characteristic force field, and when another molecular entity surpasses this area, the possibility that two units will interact, increases considerably. About the radius of such a force field for perylenes is estimated to be between 90-120 Å. Eventually, aggregation associated with intramolecular attraction (folding) or intermolecular attraction (self-assembly) are observed when these circumstances are met in solution. Both folded and self-assembled π-stacks contribute shifting from $0 \rightarrow 0$ into $0 \rightarrow 1$ transition of perylene absorption spectrum. In this manner, a new model for quantifying degree of aggregation in perylene containing polymers was deducted by optical absorption ratio between the $0 \rightarrow 0$ and $0 \rightarrow 1$ transitions while free (un-folded) perylene diimides show normal Franck–Condon progression with $A^{0 \rightarrow 0} / A^{0 \rightarrow 1} \approx 1.6$ whereas folded perylenes have an inverse intensity distributions among their vibronic states, $A^{0 \rightarrow 0} / A^{0 \rightarrow 1} = 0.7$. Despite CH-PPI is very slightly aggregated in non-polar and aprotic solutions between 1.10–1.27, in the case of protic solvents such as ethanol and

methanol $A^{0 \to 0}/A^{0 \to 1}$ values are 0.92 and 0.89, respectively implying that CH-PPI is strongly aggregated and most likely exist as a dimer in solution. It was also observed that aggregation promote the CH-PPI emission shift from $0 \to 0$ emission (541 nm) to $1 \to 0$ emission (567 nm) which is red-shifted with respect to the monomer CH-PPI. At the same time, absorption spectrum of the CH-PPI in solid films changed massively comparing with their absorption spectra in solution. The most intense peak observed at 499 nm and second at 538 nm with $A^{0 \to 0}/ A^{0 \to 1}$ value of 0.90. However, absorption peak became wider (400–800 nm) than those in solution. Moreover, no emission and excitation peak was detected in solid-state film for newly synthesized polymer. All these spectral changes may be caused by the strong π-π aggregation of the perylene dyes in solid film state which makes them attractive structure for energy transfer applications. Many perylene derivatives have been demonstrated to aggregate in solid films where head-to-tail interaction and face-to-face packing induced bathochromic and hypsochromic shifts, respectively. As a consequence the photophysical properties of the CH-PPI confirmed again that perylene was blended into the chitosan polymer. The evidence of energy transfer could be also confirmed by the fluorescence excitation spectrum. Although energy transfer process was not very significant in this system, the fluorescence excitation spectra well matched with the corresponding visible absorption spectra in both polar and nonpolar solvents. In general, the energy transfer process does not depend on solvent polarity whereas divergent spectra profiles observed with the increasing of polarity. These differences might arise from the stabilization of the ground electronic state of perylene chromophore by the polar solvent that could be induced energy transfer. It is anticipated that effective electron transfer reactions can be found in a covalently linked donor-acceptor system. The fluorescence quenching in different polar solvents can indirectly denote the existence of that case.

5.5.2 Photophysical Properties of CH-PNI

Photo-physical properties of the CH-PNI were investigated in different polarity of the solvents (apolar, polar aprotic and polar protic) with UV-vis absorption, excitation and fluorescence emission which are depicted in Figure 4.48 – 4.62 and Table 4.5 – 4.12 that summarize the spectral data. The emission and excitation spectra of CH-PNI were taken at λ_{exc} = 360 and λ_{ems} = 620 nm, respectively. And also, the relative fluorescence quantum yields were determine in various solvents by using anthracene (Φ_f = 0.27) as reference by exciting at 360 nm in ethanol. All other information regarding optical properties are presented in Table 4.13, featuring the maximum absorption wavelength λ_{max} (nm), stoke shifts (cm^{-1}), ratios of absorption intensities $A^{0\rightarrow0}/ A^{0\rightarrow1}$, extinction coefficients ε_{max} (L mol^{-1} cm^{-1}), oscillator strength f , fluorescence quantum yields ϕ_f (λ_{exc} = 360 nm), radiative lifetimes τ_0 (ns), fluorescence lifetimes τ_f (ns), fluorescence rate constants k_f (10^7 sec^{-1}), rate constant of radiationless deactivation k_d and singlet energy E_s (kcal mol^{-1}) data of CH-PNI. The optical band gap of 2.72 eV was calculated from the onset of absorption at 414 nm in chloroform solution. This is consistent with the measured band gap using cyclic voltammetry (1.97 eV).

The UV-vis absorption spectra of CH-PNI were recorded in different solvents. Figure 4.75 showed the absorption spectra of CH-PNI in apolar medium with maximum absorbance peaks at 370 ($0 \rightarrow 2$), 396 (394 in dicholoromethane) ($0 \rightarrow 1$) and 414 nm ($0 \rightarrow 0$), respectively which are ascribed to the characteristic π–π* vibronic transitions of naphthalene diimides core. The most intense absorption peak at 396 nm (394 in dicholoromethane) represents the $0 \rightarrow 1$ energy transition from the ground state to the second excited state. In contrast to the classical naphthalene dyes,

the intensities of the vibronic absorption bands of CH-PNI are declining in the order of $0 \rightarrow 1 > 0 \rightarrow 0 > 0 \rightarrow 2$. This variation is attributed to the heavy aggregation of dye molecules at ground state even in less polar solvents originating from network structure of polymer. As shown in Figure 4.80, three emission bands are observed in apolar medium which were not similar to the absorption spectra like CH-PPI. The influence of the polymeric network structure on fluorescence properties is clearly appreciable. It was found that incorporation of naphthalene dyes into the chitosan biopolymer alters the fluorescence properties of CH-PNI. The emission band maximum that was observed at 525 nm in dichloromethane is the most red-shifted one comparing to the other solvents (except 552 nm in DMF). That type of emission is attributed to the excimer type emission which is arising from strong intermolecular interactions of dye molecules arranged through planar polymer chain in solution.

Figure 4.76 reveals that the absorption intensities of typical π–π* transitions of naphthalene core are gradually diminished and are not well-resolved in aprotic solutions (except acetonitrile) when compared to absorption of CH-PNI in apolar ones. Despite that, the absorption of CH-PNI in polar aprotic medium was very broad and extended up to 550 nm which is unusual for naphthalene diimides indicating the presence of strong charge transfer interactions at the ground state. Moreover, a small blue shift occurred in aprotic solvents from 414 nm to 407 nm and new important vibronic band of in the region from 353 to 365 nm observed in polar aprotic spectra at high energy region of electromagnetic spectrum was. The disappearance of vibronic peaks and appearance of new peaks are associated with the heavy π–π aggregation of dye cores within the solvent molecules. The influence of aprotic solvent polarity on emission and polarizability of CH-PNI was also studied. As can

be seen in Figure 4.81, the increasing solvent polarity caused highly bathochromic shifting of emission band maxima from 450 nm to 474 nm (except in acetonitrile) by altering the energy levels of excited states in the novel polyimide. Increasing solvent polarity also cause changing in the spectral shape of the emission where exhibits a single broad excimer type emission band especially in DMAc attributed to the π–π aggregation behaviour.

Similarly to the absorption spectra of aprotic solvents, the absorption intensities of classical π–π* transitions of the dye core in polar protic medium are completely disappeared which seems as shoulder (Figures 4.77) at longer wavelength and new band was also observed at 354 nm. Interestingly, a new another additional band with high absorption intensity was distinguished at 344 nm in methanol and 347 nm in ethanol, respectively. These spectral and vibronic changes of CH-PNI in polar protic solvents are attributed to the possible hydrogen-bonding interactions between functional groups of dye and polymer. Moreover, the solvatochromic effect was also observed by increasing solvent polarity. Figure 4.82 depicts the emission properties of CH-PNI in protic solvents. Similarly to their absorption spectra, the emission characteristics were quite different from the other solvents. As the medium changed from apolar to polar, display broad excimer emissions attributed to the higher degree of hydrogen bond formation. By increasing di-electric constant of protic solvent, the emission band maxima of CH-PPI slightly red shifted from 457 to 461 nm. In addition, a small shoulder peak that observed at 408 in ethanol was disappeared in methanol.

On the other hand, the absorption spectra of CH-PNI in acidic and basic medium were also different from the organic medium indicating the diversity in

intermolecular interactions which were shown in Figure 4.79. In acetic acid, CH-PNI UV-vis spectrum shows two blue shifted absorption bands at 356 and 391 nm. CH-PNI UV-vis spectra in NaOH and KOH show two absorption bands with increasing intensities at lower wavelengths at 401 and 341 nm. The emission spectra of CH-PNI in acidic and basic medium were depicted in Figure 4.83. It is clear that excimer type-emissions exist when considering the spectral shape and broadening of the spectra in these solvents.

To understand the energy transfer phenomena in CH-PNI, fluorescence excitation spectra were also studied in all solvents (Figure 4.89). In general, the excitation spectra of dye molecules are exactly identical with absorption spectra. But here, the fluorescence excitation spectra of CH-PNI are unique and also confirm the existence of different absorbing species in the ground state for instance different type of aggregates (dimer, trimer, and so on).

The low fluorescence quantum yields of CH-PNI in all solvents indicate the quenching of fluorescence originating from highly π–π stacking interactions of naphthalene core which are good aggrement with literature data.

Eventually, it is evident from all the photophysical datas that both of the polyimides perylene and naphthalene dyes are highly electro-active and undergoes specific interactions between neighbouring dye molecules and also content of chitosan and solvent molecules.

5.5.2.1 Effect of Concentration Dependency on Emission Spectra of CH-PNI

Figures 4.90 – 4.97 reveal the effect of concentration on fluorescence spectra and also fluorescence spectra of filtered solution through a 0.2 μm SPR microfilter in different kinds of solvents at different concentrations. Interestingly in chloroform, four charming excimer type-emission bands are observed at 406, 456, 518 and 551 nm, respectively. The wide shape of the emission spectra does not change with increasing concentration, only the intensity slightly increased. In contrast to their initial shape upon filtration of the solutions through 0.2 μm SPR microfilter (Figure 4.90), the emission bands are blue shifted and appearing at 421 and 440 nm with a shoulder at 523 nm. The fluorescence intensity of the micro filtered solutions are much greater (approximately four times higher) than their initial states. This behaviour indicates highly self-aggregation of dye molecules through planar network chain even in nonpolar solvent medium. Despite the emission intensity of CH-PNI does not altered upon increasing concentration in tetrahydrofuran Figure (4.95), the maximum emission peak is red-shifted by about 47 nm with a splitting peak at 490 nm. On the other hand, two significant peaks detected at 388 and 409 nm in the filtered solutions. As can be depict from Figure 4.91-4.93, in polar aprotic solvents (such as DMF, DMAc and DMSO), characteristic broad long and shapeless excimer type emission bands are also observed and these are generally bathochromic shifted both in un-filtered and filtered solutions up to 601 nm and 592 nm, respectively and gradually decreased in intensity at higher concentrations which was assigned as extensive concentration dependent π–π stacking interactions between aromatic cores. Moreover, the shoulder peak at the 405nm (406 nm in DMSO) at lower concentration diminished with increasing concentration indicating the possibility of different type of electronic transitions. Although the shape of the emission spectra in

NMP solvent (Figure 4.94) remained same by altering concentration and microfiltration. As expected, it was the result of heavily aggregation of dye units than the other polar aprotic solvents, the emission peak similarly red shifted and intensity decreased with increasing concentration. Except characteristic emission spectra of CH-PNI in acetic acid and NaOH, there is no significant change upon filtration of the solutions through 0.2 μm SPR microfilter (Figure 4.96 and 4.97). Consequently, there is huge intensive non-covalent interactions exist at excited states dependent on concentration and solvent type.

5.5.3 Photophysical Properties of ENPI

Since ENPI has best solubility in TCE, the photophysical properties of the ENPI were investigated in TCE solvent via UV-vis and fluorescence emission spectroscopies in Figures 4.100 to 4102. All other optical parameter such as maximum absorption wavelength λ_{max}, extinction coefficients ε_{max}, , fluorescence quantum yields ϕ_f, radiative lifetimes τ_0 , fluorescence lifetimes τ_f , fluorescence rate constants k_f , and singlet energy E_s data of ENPI are presented in Table 4.13. In Figure 4.100, ENPI has three characteristic absorption transition at 344, 361 and 382 nm and shows additional blueshifted absorption bands at 296, 312 and 326 nm at 1 x 10^{-6} M concentration which can be attributed to 0→2 transition. As can be seen Figure 4.100, when the concentration was reduced to 5 x 10^{-7} M, more intense and broad absorption band is came to view at 282 nm followed by a shoulder peak at 326nm together with most intense bands at 345, 362 and 382 nm. As can be depicted from the Figure 4.101, the absorption intensiy of 0→0 transition was low comparing to the intensity 0→1 absorption band at five different solutions of different concentrations. Moreover, the molar absorption coefficients of ENPI for the absorption peaks 0→0, 0→1 and 0→2 were found as 972700 mol L^{-1} cm^{-1}, 1021000 mol L^{-1} cm^{-1} and 599000 mol L^{-1} cm^{-1}, respectively. To the best our knownledge, such these kinds of very high molar absortivities is the first time reported for naphthalene based polymers in the literature. The reason for this effects in UV-vis spectra could be conformational structure of high molecular weight polymer that effects π—π* electron transitions and leads strong intermolecular interactions such as π—π stacking, hydrogen-bonding or hydrophobic interactions that directed self-aggregation of the dyes molecules of ENPI. The fluorescence spectra of the naphthalene based polyimide ENPI were shown in Figure 4.102. As compared with the absorption spectrum in TCE, the emission spectrum of ENPI have low two emission bands at 392 and 412 nm together with red-shifted and very broad excimer

peak within high intensity at 492 nm attributed to strong π—π stacking of the conjugated chromophoric units in the polymeric chain. The effect of concentration on emission spectra of ENPI were at variable concentration was also shown in Figure 4.103. Although, the wide shape of emission spectra and position of the excimer type emission bands do not altered by increasing concentration, the maximum intensity of emission bands decreased. This behaviour indicates fluorescence quenching by the concentration and also excimer formation even in very low concentration. Figures 4.104 to 4.107, depict the emission spectra of ENPI at various temperatures and concentrations. The emission spectra in all temperature values do not show any changes in peak shapes and positions. However, the intensities of emission peaks for all four different molarities were decreased by increasing temperature from 0 °C to 70 °C. This result was most probably due to conformational transitions in polymeric chains that leading to decrease in molecular inter- and intra-molecular interactions depends on concentration, temperature and solvent.

5.6 Thermal Stability

The thermal behaviours of the polymeric polyimides were explored by DSC (heating rate 10 °C min^{-1}, Figures 4.108) and TGA technigues (heating rate 10 °C min^{-1}, Figures 4.109). Figure 4.108 indicates the DSC thermograms recorded for polyimides and chitosan biopolymer. In the DSC thermogram, commercial chitosan revealed an exothermic peak at 303 °C which represents the degradation of chitosan, no visible glass transition temperature were observed in the DSC run for CH-PPI and CH-PNI up to 440 °C and for ENPI up to 300 °C in the same atmosphere. The DSC curves of polyimides showed a high starting temperature for decomposition (T_d). Figure 4.109 shows the thermogravimetric analysis of the polyimides. The TGA of chitosan and CH-PPI exhibited that they started decomposing at 270 °C and at 443 °C in oxygen atmosphere, respectively. For chitosan, a rapid weight loss of 55 % of the initial weight was occurred between 250 and 450 °C. When it was heated to 550 °C, all of the initial weight was lost, and almost zero char yield observed. For CH-PPI, no significant weight losses were observed up to 400 °C. A rapid weight lost of 40 % of the initial weight occurred between 450 and 500 °C. When the compound was heated to 750 °C, 95 % of the initial weight was lost and a 5 % char yield was observed. The thermogravimetric analysis of CH-PNI represents that CH-PNI began to lose mass at 310 °C in nitrogen atmosphere. When CH-PNI was heated to 900 °C, 45 % of the initial weight was lost and 55 % char yield was behind. Because of enhancement in π—π staking of hydrophobic naphthalene dyes together with long alkoxy chains, ENPI show also high thermal stability and started to lose its initial weight at 400°C. It is clearly evident that new synthesized polyimides have outstanding thermal stability than their naturally occurred one that could be attributed to the symmetry of the network structure of the polyimides and intermolecular forces.

5.7 Electrochemistry of Novel Polyimides

To manifest the impact of the network structure on the electron/energy transfer was also explored. The electrochemical features of chitosan and new polyimides were investigated in detail using square-wave and cyclic voltammetries in solution (supporting electrolyte: 0.1 M NaBF$_4$) and also in solid state (supporting electrolyte: 1 M HCl). All the measured redox potentials, band gap energy E$_g$, LUMO (lowest unoccupied molecular orbital) and HOMO (highest occupied molecular orbital) values were tabulated between Table 4.14 and 4.23.

5.7.1 Electrochemistry of CH-PPI

The redox properties of CH-PPI were determined by cyclic voltammetry (CV) and squarewave voltammetric (SQWV) measurements. The CVs of CH-PPI were illustrated in Figures 4.113 -4.117 that are studied in DMAc and electrochemical datas were tabulated in Table 4.14 and 4.17. CH-PPI undergoes four quasi-reversible one-electron reductions at -0.29 V, -0.54 V, -0.75 V and -1.27 V (vs. ferrocene/ferrocenium) with a ΔE_p=80-90 mV, in DMAc at 100 mV s^{-1} scan rate. The calculated ΔE_p values of CH-PPI in the rage 80-90 mV demonstrate that reversibility of electron transfers were consistent with perylene based polymers in the literature. The calculated cathodic and anodic peak current ratios (i_{pa}/i_{pc}) were almost equal to unity indicating the high reversibility. Electrochemical stability of CH-PPI was also analyzed at different scan rates by measuring repeated cycles of redox processes thoroughly and the results at the entire scanning rate were tabulated in the Table 4.14. At high scan rate (500 mV s^{-1}), the peak separations are changed in the range of 110-210 mV that indicate prudent reproducibility of current as expected from high polarity solvent medium. In order to elucidate the number of peak potentials of CH-PPI, square wave voltammograms were also measured. Referring to Figure 4.118

Similar to the CV, SQWVs of CH-PPI showed three reversible one-electron reductions at -0.35 V, -0.80 V and -1.32 V (vs. ferrocene/ferrocenium, frequency: 25 Hz) indicating the formation of anions in DMAc. The obtained results confirm the reduction processes and are well agreement with cyclic voltammetry in DMAc.

In order to explore the solid state electrochemistry of CH-PPI, solid state cyclic and square wave voltammetry were also studied. As depicted in Figure 4.120, cyclic voltammagrams of perylene substituted chitosan polymer showed reversible one electron reduction and oxidation steps at -0.568 V and 0.215 V (vs. ferrocene/ferrocenium, scan rate: 100 mV s^{-1}), respectively. This is implied that there was a remarkable interaction between its electro-active entities due to network morphology. Comparing with CV data of chitosan (Figure 4.128), one clear and reversible oxidation wave of CH-PPI was also appeared at the same point ($E_{1/2}^{ox}$ = 0.218 V) in the positive direction with a peak potential ΔE_p^{ox} = 331 mV. Similarly, the square-wave voltammograms of CH-PPI showed reversible oxidation potential at 0.459 mV (vs. ferrocene/ferrocenium, scan rate: 100 Hz). The results of cyclic and square-wave voltammetry were in good agreement. Beside that the reduction of PDI moiety was observed at 0.568 V in the negative direction, corresponding to the formation of radical anion. The electrochemical stability and reversibility of the redox processes of CH-PPI was also examined by measuring repeated cycles of redox processes. CH-PPI showed completely reversible oxidation and reduction steps for the entire scanning rate in a region of 50-1000 mV s^{-1} and 50-2000 Hz at solid state. The electrochemical examination implied that the perylene moiety and the chitosan moiety in new electro-active polymer could show their individual electrochemical properties. This indicated that new system which obtained by direct

connection of perylene and chitosan was concerned as donor-acceptor system at solid state.

In order to calculate the absolute energies of LUMO level of CH-PPI with respect to the vacuum level, the redox data have been standardized to the ferrocene/ferricenium couple which is an absolute value of -4.8 eV. While the LUMO energy levels of CH-PPI in solution and solid state were calculated from cylic voltammograms, as -3.65 eV and -4.23 eV, respectively, the optical band gap Eg values were found as 2.28 eV in solution and 1.91 eV in solid state. Accordingly, the HOMO energy levels of CH-PPI were obtained as -5,02 eV in solution and -6.14 eV in solid state.

5.7.2 Electrochemistry of CH-PNI

The redox properties of CH-PNI were also determined by cyclic voltammetry (CV) and squarewave voltammetric (SQWV) measurements. The CVs of CH-PNI were illustrated in Figures 4.116 -4.117 that are studied in NMP and electrochemical datas were tabulated in Table 4.18 – 4.21. CH-PNI undergoes one reversible one-electron reduction at -1.15 V (vs. ferrocene/ferrocenium) with a ΔE_p=260 mV, in NMP at 100 mV s^{-1} scan rate which is the reduction of the neutral compound to radical anion (CH-PNI$^-$) (Figure 4.116). Although the peak separation (ΔE_p) range was about 250-300 mV for the entire scan rate from 50-1000 mV s^{-1}, the calculated peak currents ratio (i_{pa}/i_{pc}) were equal to the unity which confirms the complete reversibility of reduction process as can be seen in Table 4.19. SQWVs of CH-PPI are much more sensitive than the CV data. Interestingly, additional two reduction peaks were appeared at -0.48 V and -0.71 V near to the reduction peak at -1.15 V (vs. Ag/AgCl, frequency: 25 Hz) (Figure 4.127). The solid-state electrochemical property of CH-PNI was determined with cyclic and square-wave voltammetries. In a similar way to

CH-PPI, the cyclic voltammograms of CH-PNI showed one quasi-reversible reduction wave and one reversible oxidation wave, implying the formation of anions and cations (vs ferrocene/ferrocenium, scan rate:100 mV s^{-1}) with peak potential separations (ΔE_p) -0.53 V and 0.215 V, respectively. The oxidation wave of CH-PNI is almost identical with chitosan moiety. Similar to the SQWV data in solution, CH-PNI has shown additional reduction peak (Figure 4.127) at -0.269 V between oxidation peak at 0.299 V and reduction peak at -0.599 V(vs Ag/AgCl, frequency: 25 Hz). The observation of a new peaks both in solution and in solid-state could be attributed to the existence of electronic interaction between neighbouring chromophore and/or its environment.

The LUMO energies of CH-PNI in NMP and solid-state were determined from cyclic voltammograms as -3.65 eV and -4.27 eV, respectively. The optical band gap (Eg) values of CH-PNI are calculated as 2.45 eV and 1.97 eV in NMP and solid-state, respectively. From these values, the HOMO energies of CH-PNI were estimated as as -5,02 eV in solution and -6.24 eV in solid state..

5.7.3 Electrochemistry of ENPI

The solid-state electrochemical properties of the ENPI were studied by cylic and squarewave voltammetries in 1 M HCl solution as supporting electrolyte with at least three repeated cycles in order to confim the reproducibility of the compound within ± 3mV. The cyclic and squarewave voltammograms of ENPI were depicted in Figure 4.130, Figure 4.131 and Figure 4.132, respectively and detailed electrochemical datas were tabulated in Table 4.22. As can be seen from Figure 4.130, ENPI represents one reversible one-electron reductions at -0.60 V (vs ferrocene/ferrocenium), at scan rate 100 mVs $^{-1}$. Interestingly, the shoulder peak potential at -0.28 V was increased in intensity and become most intense peak at higher scan rates by increasing scan rates for the entire region of 20 to 2000mVs^{-1} as shown in Figure 4.131. As can be depicted in Figure 4.132, this tendency was also confirmed by squarewave voltammogram measurements. The squarewave voltammogram of polymer show one poorly resolved one reversible one reduction at -0.199 V and one well appeared one reversible one reduction with high intensity at -0.299 V at scan rate 25 Hz, similar to the CV measurements at higher scan rates. Upon increasing scan rate form 100 Hz to 500 Hz, ENPI demonstrates only one reversible one electron reduction wave at -0.294 V as shown in Figure 4.132. These multiple reduction peaks at low scan rates in both CV and SQWV voltammogram, indicate multielectron transfer corresponding to the formation of two radical anions. These multielectron transfers are originating from high molecular weight of polyimide that can be attributed $\pi-\pi$ conjugation of the chromophoric naphthalene dyes in the polymer chains. Moreover the peak separation (ΔE_p) range was so low about 30-40 mV for the entire scan rate from 100-2000mVs-1, and also the ratio of calculated peak potentials (i_{pa}/i_{pc}) were equal to the unity which approves the electrochemical stability of reduction process as can be seen in Table 4.23.

Chapter 6

CONCLUSION

In conclusion, a novel of perylene and naphthalene diimide containing chitosan aromatic polyimides were synthesized. The new polyimide dyes were obtained with high yield by substitution reaction and their solubility enchanced where become partially soluble in common organic solvents (such as chloroform, dimethylsulfoxide, and so forth) thus increased the feasibility of the products as next generation semi-conductor material. The structure of the compounds was proved by FTIR and elemental analysis as well. The complete analysis of NMR spectroscopy showed that π–π stacking tendency of the aromatic perylene and naphthalene units was very high in the polymeric network and caused very broad proton signals. The M_w were stated by GPC and in parallel, intrinsic viscosities were determined.

The polyimide structure was found to play a major role on photophysical properties. Incorporation of the hydrophobic perylene and naphthalene diimide units within the hydrophilic chitosan backbone yielded a network-like structure and also provided the extension of π–π conjugation. The photophysical analysis (absorption, emission and excitation) of polyimidies confirmed that challenging properties in both ground and excited states coming from conjugation. Interestingly, the absorption spectra of new naphthalene polyimide showed new bands. In addition, the maximum peaks were red-shifted by increasing polartiy and also dimuniton in the intensity of the 0→0 absorbtion band particularly in high polarity solvent medium corresponding to self assembly aggregates even their ground state. Both aromatic polyimide had very

high molar extinction coefficients that are so unique and makes compounds so special for PV technology. In solid state, broad absorption bands up to the 800 nm were noticed that indicates the high absorption ability of the products which it is essential to collect light effectively from the energy source. The fluorescence spectra of the polyimides manifested concentration depended excimer like emissions which were assigned as π-stacking via neighbouring aromatic unit and hydrogen bonding via chitosan linkage (or protic solvent molecules) thus highlighting the significance of polymer design in inducing self-assembly of supramolecular structures. The quenching of fluoresence quantum yield (especially for naphthalene polyimide) indicated the existence of aggregates owing to extensive π stacking of the aromatic core. Solid state emission and excitation of polyimide compounds could not be obtained attributed to the existence of aggregates and excimers. Similary, the photophysical investigations of ENPI showed very high molar absorption coefficients in the 250 – 400 nm range and also excimer type emissions are dependent on concentration.

Starting decomposition temperature for both compounds was higher than 300 °C implying the high thermal stability.

The electrochemical features of the perylene polyimide and naphthalene polyimide were investigated from diluted solution to solid state. Both the polyimide dyes exhibited three reversible one electron reductions in polar aprotic solvent and undergone only one reversible reduction and oxidation in solid state which make them candidate as Donor/Acceptor polymer for low cost photovoltaic cells. Moreover, the electrochemical investigation on ENPI in solid state also proved the existence of multiple reduction potential waves at low scan rates.

REFERENCES

[1] Woodhouse, M.; Perkins, C. L.; Rawls, M. T.; Cormier, R. A.; Liang, Z.; Nardes, A. M.; Gregg, B. A. Non-conjugated polymers for organic photovoltaics: Physical and optoelectronic properties of poly(perylene diimides). *J. Phys. Chem. C* 114 *(*2010) 6784–6790.

[2] Köber, S.; Michael Salvador, M.; Meerholz, K. Organic photorefractive materials and applications. *Adv. Mater.* 23 (2011) 4725–4763.

[3] Hains, A. W.; Liang, Z.; Woodhouse, M. A.; Gregg, B. A. Molecular semiconductors in organic photovoltaic cells. *Chem. Rev*. 110 (2010) 6689–6735.

[4] Bundgaard, E. and Krebs, F. C. Low band gap polymers for organic photovoltaics. *Solar Energy Materials & Solar Cells* 91 (2007) 954–985.

[5] Kessler, F. and Rudmann, D. Technological aspects of flexible CIGS solar cells and modules. *Sol. Energy* 77 (2004) 685–695.

[6] Spanggaard, H. and Krebs, F. C. A brief history of the development of organic and polymeric photovoltaics. *Solar Energy Materials & Solar Cells* 83 (2004) 125–146.

[7] Tao, M. Inorganic photovoltaic solar cells: silicon and beyond. *The Electrochemical Society Interface*, Winter (2008) 30–35.

[8] Habas, S. E.; Platt, H. A. S.; van Hest, M. F. A. M.; Ginley, D. S. Low-cost inorganic solar cells: from ink to printed device. *Chem. Rev*. 110 (2010) 6571–6594.

[9] Miles, R.W.; Zoppi G.; Forbes, I. Inorganic photovoltaic cells. *Materials Today* 10 (2007) 20–27.

[10] Hagfeldt, A.; Boschloo, G.; Sun, L.; Kloo, L; Pettersson, H. Dye-sensitized solar cells. *Chem. Rev*. 110 (2010) 6595–6663.

[11] Pensack, R. D.; Guo, C.; Vakhshouri, K.; Gomez, E. D.; Asbury, J. B. Influence of acceptor structure on barriers to charge separation in organic photovoltaic materials. *J. Phys. Chem. C* 116 (2012) 4824–4831.

[12] Günes, S.; Neugebauer, H.; Sariciftci, N. S. Conjugated polymer-based organic solar cells. *Chem. Rev*. 107 (2007)1324–1338.

[13] Kippelen, B.; Brédas, J.-L. Organic photovoltaics. *Energy Environ Sci* 2 (2009) 251–261.

[14] Cihaner, A. and Algı, F. A novel neutral state green polymeric electrochromic with superior n- and p-doping processes: Closer to red-blue-green (RGB) display realization. *Adv. Funct. Mater*. 18 (2008) 3583–3589.

[15] Sapagovas, V. J.; Gaidelis, V.; Kovalevskij, V.; Undzenas, A. 3,4,9,10-perylenetetracarboxylic acid derivatives and their photophysical properties. *Dyes and Pigments* 71 (2006) 178–187

[16] Hermenau. M.; Schubert, S.; Klumbies, H.; Fahlteich, J.; Müller-Meskamp, L.; Leo, K.; Riede, M. The effect of barrier performance on the lifetime of small-molecule organic solar cells. *Solar Energy Materials & Solar Cells* 97 (2012) 102–108.

[17] Choi, J. W.; Kulshreshtha, C.; Kennedy, G.P.; Kwon, J. H.; Jung, S-H.; Chae, M. Solution-processed bulk heterojunction organic solar cells with high polarity small molecule sensitizer. *Solar Energy Materials & Solar Cells* 95 (2011) 2069–2076.

[18] Jaballah, N.; Chemli, M.; Hriz, K.; Fave, J-L.; Jouini, M.; Majdoub, M.. Blue-luminescent poly(p phenylenevinylene) derivatives: Synthesis and effect of side-group size on the optical properties. *European Polymer Journal* 47 (2011) 78–87.

[19] Patra, D.; Ramesh, M.; Sahu, D.; Padhy, H.; Chu, C-W.; Wei, K-H.; Lin, H-C. Enhancement of photovoltaic properties in supramolecular polymer networks featuring a solar cell main-chain polymer H-bonded with conjugated cross-linkers. *Polymer* 53 (2012) 1219-1228.

[20] Gruber, M.; Stickler, B. A.; Trimmel, G.; Schürrer, F., Zojer, K. Impact of energy alignment and morphology on the efficiency in inorganic–organic hybrid solar cells. *Organic Electronics* 11 (2010) 1999–2011.

[21] Lin, Y., Cheng, P.; Liu, Y.; Shi, Q.; Hua, W.; Li, Y.; Zhan, X. Small molecules based on bithiazole for solution-processed organic solar cells. *Organic Electronics* 13 (2012) 673–680.

[22] Yang, X. and Loos, J. Toward high-performance polymer solar cells: The importance of morphology control. *Macromolecules* 40 (2007) 1353–1362.

[23] Krebs, F. C.; Tromholt, T.; Jørgensen, M. Upscaling of polymer solar cell fabrication using full roll-to-roll processing. *Nanoscale* 2 (2010) 873–886.

[24] Shoaee, S.; Clarke, T. M.; Huang, C.; Barlow, S.; Marder, S. R.; Heeney, M.; McCulloch, I.; Durrant, J. R. Acceptor energy level control of charge photogeneration in organic Donor/Acceptor blends. *J. Am. Chem. Soc.* 132 (2010) 12919–12926.

[25] Akatsukaa, R.; Momotakea, A.; Shinoharab, Y.; Kannac, Y.; Satoa, T.; Moriyamad, M.; Takahashie, K.; Nishimuraa, Y.; Arai, T. Observation of anthracene excimer fluorescence at very low concentrations utilizing dendritic structures. *Journal of Photochemistry and Photobiology A: Chemistry* 223 (2011) 1–5.

[26] Buruiana, E. C.; Podasca, V.; Buruiana, T. Synthesis of block copolymers derived from N-trityl-(S)-serine and pyrene end-labeled poly(methylmethacrylate) or poly(N-isopropylacrylamide) via ATRP. *Journal of Luminescence* 132 (2012) 2704–2713.

[27] González-Álvarez, M. J.; Méndez-Ardoy, A.; Benito, J. M.; Fernández, J. M. G.; Mendicuti, F. Self-association of a naphthalene-capped-β-cyclodextrin through cooperative strong hydrophobic interactions. *Journal of Photochemistry and Photobiology A: Chemistry* 223 (2011) 25–36

[28] Bagui. M.; Dutta, T.; Zhong, H.; Li, S.; Chakraborty, S.; Keightley, A.; Peng, Z. Synthesis and optical properties of perylene diimide derivatives with triphenylene-based dendrons linked at the bay positions through a conjugated ethynyl linkage. *Tetrahedron* 68 (2012) 2806–2818.

[29] Zhan, X.; Facchetti, A.; Barlow, S.; Marks, T. J.; Ratner, M. A.; Wasielewski, M. R.; Marder, S. R. Rylene and related diimides for organic electronics. *Adv. Mater.* 23 (2011) 268–284.

[30] Veenstra1, S. C.; Loos, J.; Kroon, J. M. Nanoscale structure of solar cells based on pure conjugated polymer blends. *Prog. Photovolt: Res. Appl.* 15 (2007) 657–668.

[31] Tao, Y.; McCulloch, B.; Kim, S.; Segalman, R. A. The relationship between morphology and performance of donor–acceptor rod–coil block copolymer solar cells. *Soft Matter* 5 (2009) 4219–4230.

[32] Rand, B. P.; Genoe,J.; Heremans, P.; Poortmans, J.;. Solar cells utilizing small molecular weight organic semiconductors. *Prog. Photovolt: Res. Appl.* 15(2007) 659–676.

[33] Kulkarni, A. P.; Tonzola, C. J.; Babel, A.; Jenekhe, S. A. Electron transport materials for organic light-emitting diodes.*Chem. Mater. 16* (**2004**) 4556–4573.

[34] Law, K.Y. Organic photoconductive materials: Recent trends and developments. Chem. Rev. 93 (1993) 449–486.

[35] Tipnis, R.; Bernkopf, J.; Jia, S.; Krieg, J.; Li, S.; Storch, M.; Laird, D. Large-area organic photovoltaic module: Fabrication and performance. *Solar Energy Materials and Solar Cells* 93 (2009) 442-446.

[36] Liang, Y.; Xu, Z.; Xia, J.; Tsai,S-T.; Wu, Y.; Li, G.; Ray, C.; Yu, L. For the bright future: Bulk heterojunction polymer solar cells with power conversion efficiency of 7.4%. *Adv. Mater.* 22 (2010) E135–E138.

[37] Lee, J. K.; Ma, W. L.; Brabec, C. J.; Yuen, J.; Moon, J. S.; Kim, J. Y.; Lee, K.; Bazan, G. C.; Heeger, A. J. Processing additives for improved efficiency from bulk heterojunction solar cells. *J. Am. Chem. Soc.* 130 (2008) 3619–3623.

[38] Skompska, M. Hybrid conjugated polymer/semiconductor photovoltaic cells. *Synthetic Metals* 160 (2010) 1–15.

[39] Jeonga, S.; Hana, Y. S.; Kwonb, Y.; Choic, M-S.; Chod, G.; Kime, K-S.; Kim, Y. Effects of n-type perylene derivative as an additive on the power conversion efficiencies of polymer solar cells. *Synthetic Metals* 160 (2010) 2109–2115.

[40] Kima, I. and Jabbour, G. E. Effect of annealing on bulk heterojunction organic solar cells based on copper phthalocyanine and perylene derivative. *Synthetic Metals* 162 (2012) 102–106.

[41] Liawa, D-J.; Wangb, K-L.; Huanga, Y-C.; Leec, K-R.; Lai. J-Y.; Ha, C-S. Advanced polyimide materials: Syntheses, physical properties and applications. *Progress in Polymer Science* 37 (2012) 907–974.

[42] urRehman, S.; Li, P.; Zhou, H.; Zhao, X.; Dang, G.; Chen, C. Thermally and hydrolytically stable polyimides containing naphthalimide units. Polymer Degradation and Stability 97 (2012) 1581–1588.

[43] Chisca, S.; Musteata, V. E.; Sava, I.; Bruma, M.. Dielectric behavior of some aromatic polyimide films. *European Polymer Journal* 47 (2011) 1186–1197.

[44] Yuney, K. and Icil, H. Synthesis, photochemical, and electrochemical properties of naphthalene-1,4,5,8-tetracarboxylic acid bis-(N,N'-bis-(2,2,4(2,4,4)-trimethylhexylpolyimide)) and poly(N,N'-bis-(2,2,4(2,4,4)-trimethyl-6-aminohexyl) 3,4,9,10-perylenetetracarboxdiimide). European Polymer Journal 43 (2007) 2308–2320.

[45] Yang, C-P.; Su, Y-Y.; Guo, W.; Hsiao, S-H. Synthesis and properties of novel fluorinated polynaphthalimides derived from 1,4,5,8-naphthalenetetracarboxylic dianhydride and trifluoromethyl-substituted aromatic bis(ether amine)s. *Eur. Polym. J.* 45 (2009) 721–729.

[46] Balcerzaka, E. S.; Iwanc, A.; Zajaca, M. G.; Krompieca, M.; Podgornaa, M.; Domanskib, M.; Siwyb, M.; Janeczek, H. Characterization, liquid crystalline behavior, optical and electrochemical study of new aliphatic–aromatic polyimide with naphthalene and perylene subunits. *Synthetic Metals* 161 (2011) 1660– 1670.

[47] Arslan, E., and Icil, H.Synthesis and spectroscopic properties of highly pure Perylene fluorescent dyes. *Spectrosc. Lett.* 34 (2001) 355–363.

[48] Boobalan, G.; Imran, P. M.; Nagarajan, S. Self-assembly, optical and electrical properties of fork-tailed perylene bisimides. *Superlattices and Microstructures* 51 (2012) 921–932.

[49] Miasojedovasa, A.; Kazlauskasa, K.; Armonaitea, G.; Sivamuruganb, V.; Valiyaveettilb, S.; Grazuleviciusc, J.V.; Jursenas, S. Concentration effects on emission of bay-substituted perylene diimide derivatives in a polymer matrix. *Dyes and Pigments* 92 (2012) 1285-1291.

[50] Oh, J-D.; Seo, H-S.; Kim, D-K.; Shin, E-S.; Choi, J-H. Device characteristics of perylene-based transistors and inverters prepared with hydroxyl-free polymer-modified gate dielectrics and thermal post-treatment. *Organic Electronics* 13 (2012) 2192–2200.

[51] Yukruk, F.; Dogan, A. L.; Canpinar, H.; Guc, D.; Akkaya, E. U. Water-soluble green perylenediimide (PDI) dyes as potential sensitizers for photodynamic therapy. *Org. Lett.* 7 (2005) 2885-2887.

[52] Hofmann, C. C.; Lindner, S. M.; Ruppert, M.; Hirsch, A.; Haque, S. A.; Thelakkat, M.; Köhler, J. The influence of p–p-stacking on the light-harvesting properties of perylene bisimide antennas that are covalently linked to a [60]fullerene. *Phys. Chem. Chem. Phys.* 12 (2010) 14485–14491.

[53] Qian, H.; Yue, W.; Zhen, Y.; Motta, S. D.; Donato, E. D.; Negri, F.; Qu, J.; Xu, W.; Zhu, D.; Wang, Z. Heterocyclic annelated di(perylene bisimide): Constructing

bowl-shaped perylene bisimides by the combination of steric congestion and ring strain. *J. Org. Chem.* 74 (2009) 6275–6282.

[54] Xue, C.; Chen, M.; Jin, S.. Synthesis and characterization of the first soluble nonracemic chiral main-chain perylene tetracarboxylic diimide polymers. *Polymer* 49 (2008) 5314–5321.

[55] Seibt,J.; Winkler, T.; Renziehausen, K.; Dehm, V.; Würthner, F.; Meyer, H.-D.; Engel, V. Vibronic transitions and quantum dynamics in molecular oligomers: A theoretical analysis with an application to aggregates of perylene bisimides. *J. Phys. Chem. A* 113 (2009) 13475-13482.

[56] Bhosale, S. V.; Janiab, C. H.; Langford, S. J. Chemistry of naphthalene diimides. *Chem. Soc. Rev.* 37 (2008) 331–342.

[57] Bruma, M.; Damaceanu, M.-D.; Rusu, R.-D. Study of thin films made from aromatic polymers containing six-member imide rings. *High Performance Polymers* 24 (2012) 31–39

[58] Guo, X.; Kim, F. S.; Seger, M. J.; Jenekhe, S. A.; Watson, M. D. Naphthalene diimide-based polymer semiconductors: Synthesis, structure property correlations, and n-channel and ambipolar field-effect transistors. *Chem. Mater.* 24 (2012) 1434−1442.

[59] Chen, Z.; Stepanenko, V.; Dehm, V.; Prins, P.; Siebbeles, L. D. A.; Seibt, J.; Marquetand, P.; Engel, V.; Würthner, F. Photoluminescence and conductivity of self-assembled p–p stacks of perylene bisimide dyes. *Chem. Eur. J.* 13 (2007) 436–449.

[60] Jancy, B. and Asha S. K. Synthesis and self-organization properties of copolyurethanes based on perylenediimide and naphthalenediimide units. *J. Polym. Sci. A: Polym. Chem.* 47 (2009) 1224–1235.

[61] Niu, H.-J.; Mu, J.S.; Zhang, M. L.; Luo, J.; Luo, P.-H.; Bai, X.-D.; Wang, W. Naphthalene-containing polyimides: Synthesis, characterization and photovoltaic properties of novel donor-acceptor dyes used in solar cell. *Trans. Nonferrous Met. Soc. China* 19 (2009) 587–593.

[62] Ego, C.; Marsitzky, D.; Becker, S.; Zhang, J.; Grimsdale, A. C.; Müllen, K.; MacKenzie, J. D.; Silva, C.; Friend, R. H.. Attaching perylene dyes to polyfluorene: Three simple, efficient methods for facile color tuning of light-emitting polymers. *J. Am. Chem. Soc.* 125 (2003) 437–443.

[63] Yan, H.; Chen, Z.; Zheng, Y.; Newman, C.; Quinn, J. R.; Dötz, F.; Kastler, M.; Facchetti, A. A high-mobility electron-transporting polymer for printed transistors. *Nature* 457 (2009) 679–687.

[64] Wang, Y.; Chen, Y.; Li, R.; Wang, S.; Su, W.; Ma, P.; Wasielewski, M. R.; Li, X.; Jiang, J. Amphiphilic perylenetretracarboxyl diimide dimer and its application in field effect transistor. *Langmuir* 23 (2007) 5836–5842.

[65] Dhara, M. G. and Banerjee, S. Fluorinated high-performance polymers: Poly(arylene ether)s and aromatic polyimides containing trifluoromethyl groups. *Progress in Polymer Science* 35 (2010) 1022–1077.

[66] King, S.; Sommer, M.; Huettner, S.; Thelakkat, M.; Haque, S. A. Charge separation and recombination in self-organizing nanostructured donor–acceptor block copolymer films. *J. Mater. Chem.* 19 (2009) 5436–5441.

[67] Shim, H.-K.; Ahn, T.; Song, S.-Y. Synthesis and LED device properties of carbazole and naphthalene contained conjugated polymers. *Thin Solid Films* 417 (2002) 7–13.

[68] Qiu, Z.; Wu, S.; Li, Z.; Zhang, S.; Xing, W.; Liu, C. Sulfonated poly(arylene-co-naphthalimide)s synthesized by copolymerization of primarily sulfonated monomer and fluorinated naphthalimide dichlorides as novel polymers for proton exchange membranes. *Macromolecules* 39 (2006) 6425–6432.

[69] Gregg, B. A.; Sprague, J.; Peterson, M. W. Long-range singlet energy transfer in perylene bis(phenethylimide) films. *J. Phys. Chem. B* 101 (1997) 5362–5369.

[70] Elemans, J. A. A. W.; Hameren, R.; Nolte, R. J. M.; Rowan, A. E. Molecular materials by self-assembly of porphyrins, phthalocyanines, and perylenes. *Adv. Mater.* 18 (2006) 1251–1266.

[71] Barbieria, A.; Venturaa, B.; Ziessel, R.. Photoinduced energy-transfer dynamics in multichromophoric arrays containing transition metal complexes and organic modules. *Coordination Chemistry Reviews* 256 (2012) 1732–1741.

[72] Kazmaier, P. M. and Hoffman, R. A theoretical study of crystallochromy. quantum interference effects in the spectra of perylene pigments. *J. Am. Chem. Soc.* 116 (1994) 9684–9691.

[73] Cho, E. H.; Kim, M. S.; Park, D. H.; Jung, H.; Bang, J.; Kim, J.; Joo, J. Evolution of light absorption and emission characteristics of organic perylene nanoparticles through hydrothermal process: Application to solar cells. *Adv. Funct. Mater.* 21 (2011) 3056–3063.

[74] Gregg B. A. Evolution of photophysical and photovoltaic properties of perylene bis(phenethylimide) films upon solvent vapor annealing. *J. Phys. Chem.* 100 (1996) 852–859.

[75] Castro, F. L.; Santos, J. G.; Fernandes, G. J. T.; Araújo, A. S.; Fernandes Jr., V. J.; Politi, M. J.; Brochsztain, S. Solid state fluorescence of a 3,4,9,10-perylenetetracarboxylic diimide derivative encapsulated in the pores of mesoporous silica MCM-41. *Microporous and Mesoporous Materials* 102 (2007) 258–264.

[76] Liu, T.; Wang, K.-R.; Guo, D.-S.; Jiang, B.-P. Supramolecular assembly of perylene bisimide with β-cyclodextrin grafts as a solid-state fluorescence sensor for vapor detection. *Adv. Funct. Mater.* 19 (2009) 2230–2235

[77] Sundararajana, P. R.; Sacripantea, G.; Wang, Z. Y. The possibility of intra-molecular nematic order via chain folding in perylene-containing polyimides: a molecular dynamics study. *Computational and Theoretical Polymer Science* 10 (2000) 219–220.

[78] Balcerzaka, E. S.; Zajaca, M. G.; Krompieca, M.; Niestroja, A.; Janeczek, H. New low band gap compounds comprised of naphthalene diimide and imine units. *Synthetic Metals* 162 (2012) 543–553.

[79] Piyakulawata, P.; Keawprajaka, A.; Wlosnewskia, J.; Forsterb, M.; Asawapirom, U. Low band gap copolymer containing naphthalene-1,4,5,8-tetracarboxylic bisimide: Synthesis, properties and organic solar cell applications. *Synthetic Metals* 161 (2011) 1238–1244.

[80] Qia, G.; Li, R.; Wanga, L.; Li, X.. Linear perylenetetracarboxylic monoanhydried derivatives for the sensitization of dye-sensitized solar cells. *Journal of Photochemistry and Photobiology A: Chemistry* 239 (2012) 28–36.

[81] Würthner, F. Perylene bisimide dyes as versatile building blocks for functional supramolecular architectures. *Chem. Commun*. 2004, 1564–1579.

[82] Archer, E. A.; Gong, H.; Krische, M. J. Hydrogen bonding in noncovalent synthesis: selectivity and the directed organization of molecular strands. *Tetrahedron* 57 (2001) 1139–1159

[83] Barooah, N. and Baruah, J. B. Effect of phenyl group on the self assembly of N,N'-bis-(2-phenylglycinyl)pyromellitic diimide with aromatic hydrocarbons. *Journal of Molecular Structure* 872 (2008) 205–211.

[84] Hoeben, F. J. M.; Jonkheijm, P.; Meijer, E. W.; Schenning, A. P. H. About Supramolecular Assemblies of π-Conjugated Systems. *Chem. Rev.* 105 (2005) 1491–1546.

[85] Junga, y.; Seo, J.; Kima, J. H.; Whang, D. R.; Gihm, S. H.; Park, C. R.; Park, S. Y. Fabrication of aligned microwire arrays of perylene bisimide by micromolding in capillary. *Synthetic Metals* 160 (2010) 1287–1290.

[86] Ajayaghosh, A.; George, S. J.; Schenning, A. P. H. J. Hydrogen-Bonded Assemblies of Dyes and Extended π-Conjugated Systems.Topics in Current Chemistry 258 (2005) 83–118.

[87] Kola, S.; Sinha, J.; Katz, H. E.Organic transistors in the new decade: toward n-channel, printed, and stabilized devices. *Journal of Polymer Science Part B: Polymer Physics* 50 (2012) 1090–1120.

[88] Kozma, E.; Kotowski, D.; Bertini, F.; Luzzati, S.; Catellani, M. Synthesis of donoreacceptor poly(perylene diimide–altoligothiophene) copolymers as n-type materials for polymeric solar cells. *Polymer* 51 (2010) 2264–2270.

[89] Rodnikova, M. N. A new approach to the mechanism of solvophobic interactions. *Journal of Molecular Liquids* 136 (2007) 211–213.

[90] Bodapati, J. B. and Icil, H. A new tunable light-emitting and p-stacked hexa-ethyleneglycol naphthalene-bisimide oligomer: synthesis, photophysics and electrochemical properties. *Photochem. Photobiol. Sci*. 10(2011) 1283–1293.

[91] Chen, Y.; Feng, Y.; Gao, J.; Bouvet, M. Self-assembled aggregates of amphiphilic perylene diimide–based semiconductor molecules: Effect of morphology on conductivity. *Journal of Colloid and Interface Science* 368 (2012) 387–394.

[92] Arnaud, A.; Belleney, J.; Boué, F.; Bouteiller, L.; Carrot, G.; Wintgens, V. Aqueous supramolecular polymer formed from an amphiphilic perylene derivative. *Angew. Chem. Int. Ed.* 43 (2004) 1718–1721.

[93] Schanze, K. S. and Shelton, A. H. Functional Polyelectrolytes. *Langmuir* 25 (2009), 13698–13702.

[94] Berth, G.; Voigt, A.; Dautzenberg, H.; Donath, E.; Möhwald, H. Polyelectrolyte complexes and layer-by-layer capsules from Chitosan/Chitosan Sulfate. *Biomacromolecules* 3 (2002) 579–590.

[95] Shang, J.; Shao, Z.; Chen, X. Electrical behavior of a natural polyelectrolyte hydrogel: Chitosan/Carboxymethylcellulose hydrogel. *Biomacromolecules* 9 (2008) 1208–1213.

[96] Ma, G.; Qian, B.; Yang, J.; Hu, C.; Nie, J. Synthesis and properties of photosensitive chitosan derivatives(1). *International Journal of Biological Macromolecules* 46 (2010) 558–561.

[97] Amidi, M. and Hennink, W. E. Chitosan-based formulations of drugs, imaging agents and biotherapeutics. *Advanced Drug Delivery Reviews* 62 (2010) 1–2.

[98] Singh, P. K.; Bhattacharya, B.; Nagarale, R. K.; Kim K.-W.; Rhee, H.-W. Synthesis, characterization and application of biopolymer-ionic liquid composite membranes. *Synthetic Metals* 160 (2010) 139–142.

[99] Pavinatto, F. J.; Caseli, L.; Oliveira Jr., O. N. Chitosan in nanostructured thin films. *Biomacromolecules* 11 (2010) 1897–1908.

[100] Liu, Z.; Liu, J.; Chen, T. Facile synthesis, characterization, and potential applications of two kinds of polymeric pH indicators: Phenolphthalein formaldehyde and o-cresolphthalein formaldehyde. *Journal of Polymer Science Part A: Polymer Chemistry* 43(2005) 1019–1027.

[101] Tripathi, B. P. and Shahi, V. K. Functionalized organic-inorganic nanostructured n-p-carboxy benzyl chitosan-silica-PVA hybrid polyelectrolyte complex as proton exchange membrane for DMFC applications. *J. Phys. Chem. B* 112 (2008) 15678–15690.

[102] Zhao, K.; Zhang, X.; Zhang, L. The first BiOI-based solar cells. *Electrochemistry Communications* 11 (2009) 612–615.

[103] Lin, W.-J.; Hsu, C.-T.; Tsai, Y.-C. Dye-sensitized solar cells based on multiwalled carbon nanotube–titania/titania bilayer structure photoelectrode. *Journal of Colloid and Interface Science* 358 (2011) 562–566.

[104] Buraidah, M. H.; Teo, L. P.; Majid, S. R.; Arof, A. K. Characteristics of TiO2/solid electrolyte junction solar cells with Γ=Γ_3 redox couple. *Optical Materials* 32 (2010) 723–728.

[105] Mohamad, S. A.; Yahya, R.; Ibrahim, Z. A.; Arof, A. K. Photovoltaic activity in a ZnTe/PEO–chitosan blend electrolyte junction. *Solar Energy Materials & Solar Cells* 91 (2007) 1194-1198.

[106] Mucha, M. Rheological properties of chitosan blends with poly(ethyleneoxide) and poly(vinyl alcohol) in solution. *Reactive & Functional Polymers* 38 (1998) 19–25

CURRICULUM VITAE

Home Adress: Okyanus Sokak, No. 17, Yenikent, Gönyeli, TRNC.
Phone: +90 392 630 10 26
Fax: +90 392 365 16 04
E-mail: ilke.yucekan@emu.edu.tr

Personal Information

Name& Surname: İlke Yücekan
Marital status: Married
Nationality: Turkish Cypriot
Date of Birth: 26/04/1984
Place of Birth: Nicosia, Cyprus.

Education

1995 – 1998   Junior High School, Şehit Hüseyin Ruso Ortaokulu, Nicosia, Cyprus.

1998 – 2001   High School, Turk Maarif College, Nicosia, Cyprus.

2001 – 2005   BS in Biochemistry, Biochemistry Department, Faculty of Science, Ege University, Izmir, Turkey.

2005 – 2008   MSc in Biochemistry, Biochemistry Department, Institute of Science, Ege University, Izmir, Turkey.

2008 – present   PhD in Organic Chemistry, Chemistry Department, Eastern Mediterranean University, Famagusta, North Cyprus.

Work Experience

- Two-month summer practice as a assistant in Dr. Burhan Nalbantoglu Hospital, in Biochemistry and Hemathology Laboratories (July – August 2004).

- Research Assistant, Chemistry Department, Eastern Mediterranean University (Fall 2009 – present).

- Author, in "Entellektüel" magazine (November 2010 – present)

Teaching Experience

- Attenden to CHEM 101/General Chemistry lab and tutorial sesssions (2009-present).

List of publications:
BS Thesis

İlke Yücekan, Azmi Telefoncu, "İnsulinin in-vitro Glikasyonunun Araştırılması", *Ege University*, Izmir, Turkey, June 2005.

MSc Thesis

İlke Yücekan, Seçil Önal, "Purification of Invertase Enzyme by Affinity Techiques", *Ege University*, Izmir, Turkey, July 2008.

(SCI, SCI-expanded Journals)

1- Mustafa Özser, **İlke Yücekan**, Jagadeesh B. Bodapati, Huriye İcil, "New Naphthalene Polyimide with Unusual Molar Absorption Coefficient and Excited State Properties: Synthesis, Photophysics and electrochemistry", Journal of Luminescence., 2013, *article in press*.

1- İlke Yücekan, Seçil Önal, "**Physicochemical Properties of Invertase Partitioned in an Aqueous Two-Phase System of Poly(Ethylene Glycol)/Sodium Sulfate**", Hacettepe J. Biol. & Chem., 2012, 40 (2), 139–147.

2- İlke Yücekan, Seçil Önal, "Partitioning of invertase from tomato in poly(ethylene glycol)/sodium sulfate aqueous two-phase systems", *Process Biochemistry*, 46 (2011) 226 – 232. (Impact Factor: 2.444, 5-Year Impact Factor: 3.344) Times cited:10

International Congress Presentations:

1- Uzun, D., Pasaogullari, N., Asir, S., Bodapati, J.B., Refiker, H., **Yucekan, I.,** Pakseresht, M., Icil, H., "The Synthesis and Characterization of Novel Fluorescent pH Sensor Based on Perylene Diimide with Benzopurpurin 4B Substituents: Photophysics, Photochemical and Sensor Properties", 19th International Conference on Photochemical Conversion and Storage of Solar Energy (IPS-19), California Institute of Technology, Pasadena, CA, USA, July 29 – 3 August 2012.

2- Abu Reesh, M.,**Yücekan, I.,** Icil, H., "Synthesis and Characterization of a Novel Fluorescent and Amphiphilic Chitosan Polymer: Optical and Electrochemical Properties", 19th International Conference on Photochemical Conversion and Storage of Solar Energy (IPS-19), California Institute of Technology, Pasadena, CA, USA, July 29 – 3 August 2012.

3-Yücekan, I., Icil, H., "Synthesis and Characterization of a Novel Fluorescent and Amphiphilic Chitosan Polymer: Optical and Electrochemical Properties", XXIV IUPAC Symposium on Photochemistry, Coimbra, Portugal, 15-20 July 2012.

4-Yucekan, I., Icil, H., "Synthesis and Properties of a Novel Semiconductor", **International Summer School - Supramolecular Chemistry - Experimental and Theoretical Methods for Investigations, Sofia, Bulgaria, 21-23 May 2012.**

5-I. Yücekan, Huriye İcil,
"Synthesis and Properties of Low Band Gap Organic Semiconductors For Solar Cell Applications", The David G. Whitten Symposium, Albuquerque, New Mexico, USA (August 19 – 20, 2010).

6- I.Yücekan, S. Önal,

"Partitioning and Purification Of Tomato Invertase In Poly (Ethylene Glycol) and Sodium Sulfate Aqueous Two-Phase Systems", International Enzyme Engineering Symposium, Kusadasi, Turkey (October 2008).

National Congress Presentations:

1-Ilke Yücekan, S. Önal,

"Sulu ikili Faz Sistemi İle Domatesten Saflaştırılan İnvertaz Enziminin Karakterizasyonu", XXII. National Chemistry Congress, Famagusta, North Cyprus, (October 2008).

Participation of Congress and Symposium:

2005   I. Aegean Genetic Symposium

2006   Aegean Symposium of Cancer Biochemistry

Scholar: Researcher in Research Project, TUBİTAK (2010 – 2012, TBAG-110T201), Turkey.

Memberships:

- BILTED
- Turkish Biochemistry Association (2005 – present)
- European Photochemistry Association (2009 – present)